Journal of METALS

SEPTEMBER, 1953

VOL. 5, NO. 9, IN TWO SECTIONS — SECTION TWO

TRANSACTIONS SECTION

Electrical Resistivity of Liquid Metals and of Dilute Liquid Metallic Solutions	E. Scala, W. D. Robertson	1141
Effect of Grain Size Upon Temper Brittleness	L. D. Jaffe, F. L. Carr, D. C. Buffum	1147
A Rationalization of Measured High Temperature Properties of Fe-Cr-Co-Ni Alloys	J. D. Nisbet, W. R. Hibbard, Jr.	1149
Subgrain Formation in High Purity Aluminum During Creep at High Temperatures	A. M. Gervais, J. T. Norton, N. J. Grant	1166
Inhomogeneity in Creep Deformation of Coarse Grained High Purity Aluminum	H. C. Chang, N. J. Grant	1175
Plastic Stress-Strain Relations for Aluminum Alloy 14S-T6 Subjected to Combined Tension and Torsion	J. Marin, H. A. B. Wiseman	1181
Crystallographic Angles for Orthorhombic (Alpha) Uranium	R. B. Russell	1190
Deformation Mechanisms in Alpha Titanium	E. A. Anderson, D. C. Jillson, S. R. Dunbar	1191
Filler Material for the Brazing of Titanium	M. A. DeCecco, H. M. Meyer	1197
Effects of Solid Solution Alloying on the Cold-Rolled Texture of Titanium	C. J. McHargue, S. E. Adair, Jr., J. P. Hammond	1199
Structure of the Phase TiMn and the Indexing of Powder Patterns of Sigma-Type Phases	R. P. Elliott, W. Rostoker	1203
The Ternary System Ti-Te-C	J. G. McMullin, J. T. Norton	1205
System Titanium-Chromium-Iron	R. J. Van Thyne, H. D. Kessler, M. Hansen	1209
Plastic Deformation of Rectangular Zinc Monocrystals	J. J. Gilman	1217
Detection of Microcracks in Steel	W. L. Jensen, R. F. Campbell	1222
Variation of Plastic Properties with Annealing Procedure in Zinc Single Crystals	C. H. Li, J. Washburn, E. R. Parker	1223

Table of Contents Continued

Recovery in Single Crystals of Zinc R. Drouard, J. Washburn, E. R. Parker **1226**

Relation Between Initial Creep Rate and Resolved Shear Stress in Zinc Single Crystals N. Brown, J. Washburn, E. R. Parker **1229**

Plastic Deformation of Single Crystals of Copper J. J. Becker, J. N. Hobstetter **1231**

Orientation Relationships in the Recrystallization of Deformed Copper Single Crystals J. J. Becker, J. N. Hobstetter **1235**

Thermal Conductivity, Electrical Resistivity, and Thermoelectric Power of Uranium W. W. Tyler, A. C. Wilson, Jr., G. J. Wolga **1238**

Age Softening of Beta Brass H. Green, N. Brown **1240**

Plastic Deformation of Iron Between 300° and 77.2°K D. F. Gibbons **1245**

A Corrected Interpretation of the Mechanism of Growth of Magnetite During Oxidation M. H. Davies, M. T. Simnad, C. E. Birchenall **1250**

Rate of Propagation of Martensite R. F. Bunshah, R. F. Mehl **1251**

Decay of Lattice Defects Frozen Into an Alloy by Quenching A. E. Roswell, A. S. Nowick **1259**

Measurement of Approximately Cylindrical Particles in Opaque Samples R. L. Fullman **1267**

Electrical Resistivity of Liquid Metals and of Dilute Liquid Metallic Solutions

by E. Scala and W. D. Robertson

Electrical resistivity of a number of pure liquid metals and alloys has been measured as a function of temperature and composition. The data show a close correspondence between the liquid and solid states with respect to thermal, structural, and compositional relationships.

STUDY of diffuse scattering of X-rays by liquid metals[1] has demonstrated that some degree of order persists above the melting point and that the atomic constitution of liquids is more analogous to the solid state than to a gas. Consideration of the change in various thermodynamic properties that accompanies transformation from solid to liquid leads to the same general conclusion.[2] Nevertheless, specific knowledge of the constitution of the liquid state is limited when compared with that of the solid and gaseous states owing, in part, to the difficulty of interpreting the X-ray data and in part to the indirect character of deductions based on thermodynamic data.

Of the structure-sensitive physical properties, electrical resistivity of liquid metals is perhaps the most easily interpretable, particularly when comparison is made with the solid state. According to the available data, most of which was obtained prior to 1914, cubic metals exhibit a normal linear and positive temperature dependence in the liquid state and the data have been accepted without question. The divalent metals, zinc and cadmium, are apparently exceptional in that resistivity is not linear with temperature and it passes through a minimum. Mercury also exhibits a nonlinear temperature dependence but the slope is always positive. Important comparisons with magnesium could not be made at the time the following work was undertaken because the necessary experimental data were not available.

Data on liquid solutions are very limited and are largely from a single source.[3-6] Based on Bornemann's work, Norbury[7] pointed out that the resistivity of liquid copper alloys appeared to be dependent on the valence of the solute and that the increase due to the solute was of the same order as in the solid state. However, large extrapolations were involved and no quantitative relationship was developed.

Therefore, before proceeding with additional deductions regarding the resistivity of liquid metals and interpretation in terms of structure, it appeared necessary to verify and extend the previous work with particular emphasis on divalent metals and the effect of alloying elements of different valence in dilute liquid solutions.

The present work includes: 1—A determination of the resistivity of high purity liquid magnesium, tin, indium, copper, zinc, and cadmium as a function of temperature. 2—The effect of 1 atom pct of copper, cadmium, aluminum, tin, antimony, and

E. SCALA, Junior Member AIME, is associated with Chase Brass and Copper Co., Waterbury, Conn., and W. D. ROBERTSON, Member AIME, is associated with Hammond Metallurgical Laboratory, Yale University, New Haven, Conn.

Discussion on this paper, TP3598E, may be sent, 2 copies, to AIME by Dec. 1, 1953. Manuscript, March 27, 1953. Cleveland Meeting, October 1953.

This paper is based on a thesis by E. Scala submitted in partial fulfillment of requirements for the degree of Doctor of Engineering to the School of Engineering, Yale University.

The Transactions papers appearing in the Journal of Metals during 1953 will subsequently appear in AIME Transactions, Volume 197, and may be permanently referenced to that volume.

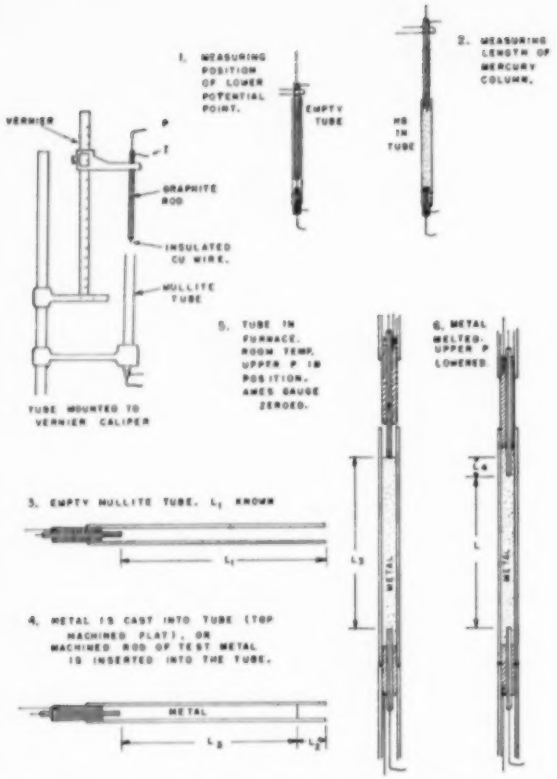

Fig. 1—Determination of the cross-sectional area of the liquid metal container and the distance between potential points.

bismuth on the resistivity of liquid zinc. 3—The effect of 1 atom pct of zinc, aluminum, indium, tin, and phosphorus on the resistivity of liquid copper.

Experimental Procedure

The principle employed in all determinations was to pass a measured current through a known cross section of liquid metal and measure the potential difference between two points at an accurately known distance from each other.

Except in the case of magnesium, the liquid metal was contained in a refractory insulating tube, approximately 0.6 cm ID by 13 cm long. The effective cross section of the tube was determined before each experiment by measuring the electrical resistance of triple distilled mercury at room temperature over a known length determined to 0.001 in. This was done by attaching one of two potential contacts to a vernier caliper as illustrated in Fig. 1.

Potential contacts were made of molybdenum wire cemented in small refractory insulating tubes which passed through graphite (spectrographic carbon) plugs carrying the current leads. Current and potential contacts were separated by about 1 cm from each other, as detailed in Fig. 3a.

After determining the geometry of the container and locating the lower potential contact with respect to the top of the ceramic tube, Fig. 1, the tube was filled by either of two methods: 1—Melting and casting metal in argon after previous evacuation in the unit illustrated in Fig. 2. A flat face was subsequently machined on the top surface of the solidified metal which then served to define the position of the lower potential contact. This method was used for the low melting point metals and the zinc alloys. 2—The copper alloys were poured under argon into graphite molds and then swaged and machined to fit the refractory tubes.

The tube containing the metal and lower contacts was cemented to a long refractory supporting tube. When placed inside the temperature equalizing graphite block mounted in the furnace, shown in Fig. 3, the supporting tube rested on the alundum blocks at the base of the furnace. The upper potential and current leads were placed in position and the height adjusted with respect to the machined face of the specimen by means of an ammeter indicator to determine contact, and a dial gage. Subsequent changes in length accompanying thermal expansion and fusion were followed with the dial gage acting as a dilatometer. The distance between the potential points was thereby known at all times. Correction for the linear thermal expansion of the entire unit was obtained by calibration with pure solid nickel. Calculated corrections were made for the increase in cross-sectional area of the refractory tube at elevated temperatures.

The uniformity of temperature over the length of the specimen was determined with three thermocouples at top, middle, and bottom, touching the ceramic tube. Temperature differences were generally less than 1°C and were determined together with each measurement of resistance.

Potential measurements were made with a precision potentiometer and current was determined by potential drop across a calibrated resistance. The current density employed was 1.7 amp per sq cm. An atmosphere of dried argon gas was maintained at all times. Measurements were made at constant temperature after equilibrium was obtained in both heating and cooling cycles.

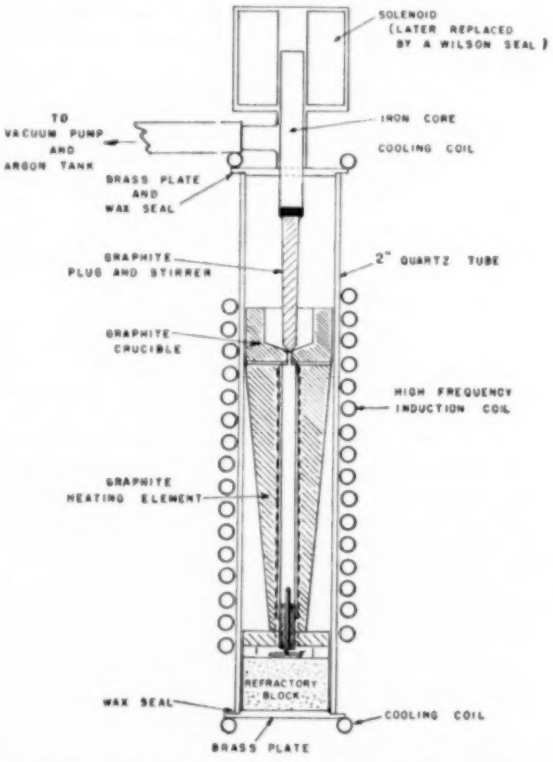

Fig. 2—The casting unit for low temperature metals and alloys.

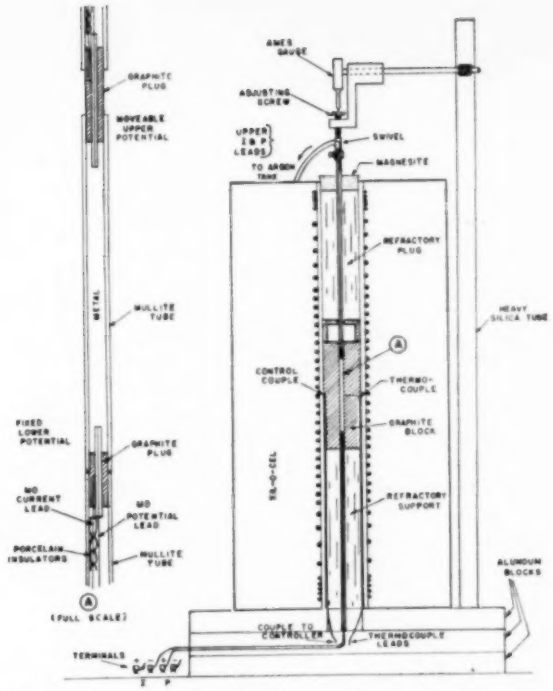

Fig. 3—The testing furnace and assembly of the testing unit. Right-hand drawing one quarter scale, entire figure reduced one half for reproduction.

Except for magnesium, the molten metals did not attack the refractory tubes. In the case of magnesium the procedure was modified by the use of a graphite container in place of ceramic tubes, avoiding contamination of the metal and change of dimensions. Machined graphite tubes were employed and their inside diameters were determined by weighing the mercury required to fill the tubes. The cell constant required for the conducting container was determined over the entire temperature range to be covered by measuring the resistance of high purity tin in identical graphite tubes. This procedure eliminated any assumption regarding a difference in temperature coefficient between magnesium and tin and because the resistivity of both metals is of the same order, the current distribution could be assumed to be similar.

Table I. Chemical Analysis of Metals and Alloys

Metal	Source	Purity, Wt Pct	Major Impurities, Wt Pct
Tin	Commercial	99.96+	0.01% Fe, In, Sb
Tin	Vulcan Detinning	99.9957	0.0015% Fe, 0.0005% Pb
Cadmium	A. S. & R.	99.9976	0.0015% Cu, 0.0009% Pb
Zinc	A. S. & R.	99.9978	0.0006% Cd, 0.0007% Pb
Indium	Indium Corp.	99.98+	0.01% Pb
Magnesium	Dominion Mag. Ltd.	99.975	0.01% Cd, 0.004% Al, 0.003% Si, Pb
Copper	A. S. & R.	99.999	0.0002% As, Te; 0.0001% Pb, Sn, Ni, Se and S

	Chemical Analysis, Atomic Pct	Major Impurities, Wt Pct
Zinc Alloys, Nominal		
1 at. % Cu in Zn	0.996% Cu	Pb, Si <0.001%
1 at. % Cd in Zn	0.89 % Cd	Pb, Si <0.001%
1 at. % Al in Zn	1.13 % Al	Pb, Si <0.001%
1 at. % Sn in Zn	1.03 % Sn	Pb, Si <0.001%
1 at. % Bi in Zn	1 % Bi	
1 at. % Sb in Zn	1 % Sb	
Copper Alloys, Nominal		
1 at. % Zn in Cu	1.25 % Zn	<0.001% Si, Mg, Fe
1 at. % In in Cu	1.00 % In	<0.001% Si, Mg, Pb, Fe
1 at. % Al in Cu	0.95 % Al	<0.001% Si, Mg, Sn, Fe
1 at. % Sn in Cu	1.03 % Sn	<0.001% Si, Mg, Fe
1 at. % P in Cu	0.94 % P	<0.001% Si, Pb, Bi, Fe

At an early stage in the work it was found that with all possible precautions there was an internal source of electromotive force in the liquid metal container. The magnitude of this effect was independent of current (polarization) and temperature difference across the cell within the experimental limits. It was, however, dependent on the temperature level as shown in Fig. 4, obtained with cadmium at zero current. It was found that one half the difference in potential across the cell with current passing in opposite directions ($\Delta E/2$, Fig. 4) was exactly equal to the internal electromotive force measured in the absence of any outside source of current. Consequently, all data are the arithmetic average of sets of readings obtained with reversed current, which effectively eliminates the internal electromotive force. Similar procedures have been adopted in previous work[8-6, 11] but the magnitude of the effect observed was not reported.

All metals and alloys were analyzed chemically and spectrographically before and after determinations. There was no significant accumulation of impurities or detectable solution of molybdenum contacts. The data are summarized in Table I.

Experimental Results

High Purity Metals: The results for tin, indium, magnesium, cadmium, and zinc are shown in Figs. 5 and 6, as a function of temperature. The data interpolated from the smooth curves are sum-

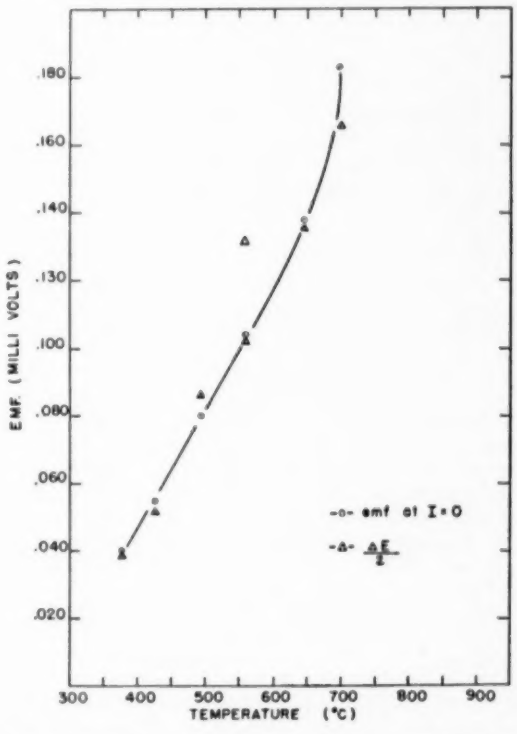

Fig. 4—Electromotive force in liquid cadmium as a function of temperature.

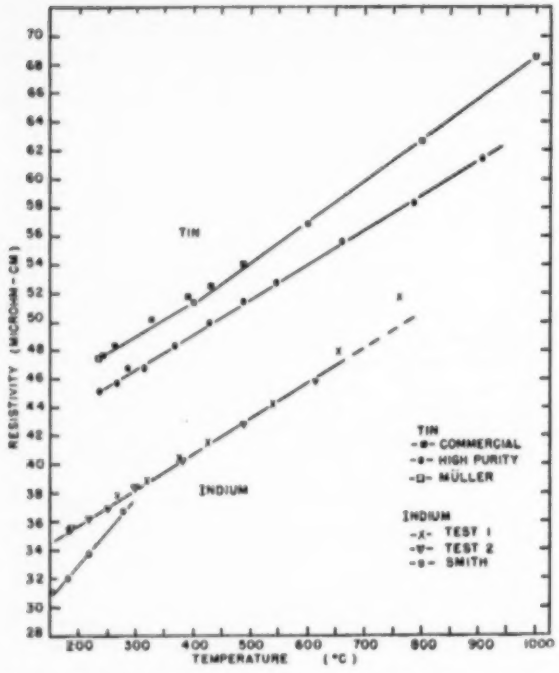

Fig. 5—Resistivity of liquid tin (commercial and high purity) and indium.

marized in Table II at integral values of temperature.

With regard to tin, essentially identical results were obtained with 99.96 pct Sn, containing antimony and iron as principal impurities, as were reported by Müller,[3, 4] and Northrup and Suydam.[5] In view of the relative simplicity of experiments with tin and the availability of two previous determinations, the agreement obtained was taken as an indication of the general adequacy of the present technique which differed from both of the previous experiments. However, with higher purity tin (99.996 pct Sn), the values fall definitely below those for tin of commercial grade and the temperature coefficient is accurately linear from the melting point.

The only available data for indium[10] appear to be considerably in error, both in magnitude and temperature coefficient. As shown in Fig. 5, two independent determinations gave similar results except at the highest temperatures where two points are evidently anomalous.

At the time this investigation was in progress, no resistivity data were available for liquid magnesium. Values have since been published by Horn[11] which are essentially in agreement with those reported here, Fig. 6. In view of the different methods employed (ceramic cell and graphite cell) the agreement may be taken as a verification of procedure and results. The only point of difference is that the present work indicates a small but significant negative temperature dependence, constant over the range investigated.

Previous work with zinc indicated some disagreement between Northrup and Suydam[5] and Müller.[4] The present redetermination confirms the results of Northrup and Suydam in all respects except at the highest temperatures where the resistivity appears to be slightly higher than reported. The temperature dependence at the melting point is negative and changes to positive at a temperature about 230°C above the melting point.

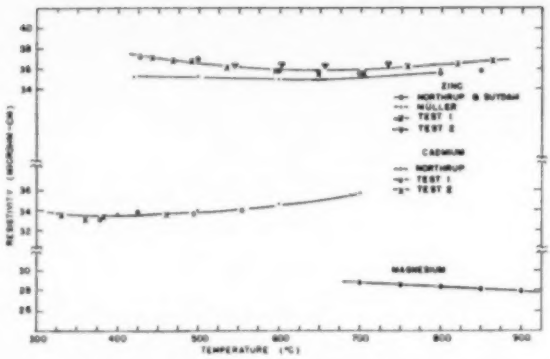

Fig. 6—Resistivity of liquid zinc, cadmium, and magnesium.

The results for cadmium are also in exact agreement with those of Northrup and Suydam.[5] The temperature coefficient at the melting point is small and negative, increasing to zero at about 50°C above the melting point and becoming increasingly positive with rising temperature.

In summary, the unusual dependence of resistivity on temperature for cadmium and zinc is confirmed, as is the magnitude of the values previously reported by Northrup and Suydam. The remaining close-packed hexagonal metal, magnesium, has a small negative temperature dependence which is constant to 200°C above the melting point. Indium has a higher resistivity and smaller linear temperature coefficient than was previously reported. Finally, the resistivity of high purity liquid tin appears to be about 5 pct lower at all temperatures than the previously available values.

Copper Alloys: The results for dilute liquid solutions of zinc, indium, aluminum, tin, and phosphorus in copper are shown in Fig. 7 as a function of temperature, together with experimental data for pure copper.

The high temperatures at which the measurements are necessarily made increase the experimental difficulties and produce some scatter in

Table II. The Resistivity of High Purity Liquid Metals

Temperature, °C	Microhm — Cm						
	Sn*	Sn	Zn	Cd	In	Mg	Cu
200					33.8		
250	48.3	45.4			35.0		
300	49.6	46.7			36.2		
350	50.8	47.8		33.6	37.4		
400	52.0	49.1		33.5†	38.7		
450	53.2	50.3	37.1	33.6	39.9		
500	54.5	51.5	36.5	33.8	41.2		
550	55.7	52.7	36.2	34.0	42.4		
600		54.0	36.0	34.4	43.7		
650		55.2	35.9		44.9		
700		56.4	36.1‡			28.8	
750		57.7	36.2			28.6	
800		58.9	36.4			28.4	
850		60.1	36.7			28.2	
900		61.3				28.0	
1100							22.9
1150							24.0
1200							25.1
1250							26.2
1300							27.3

* Commercial Tin, 99.96 pct.
† Minimum on curve at about 375°C.
‡ Minimum on curve at about 670°C.

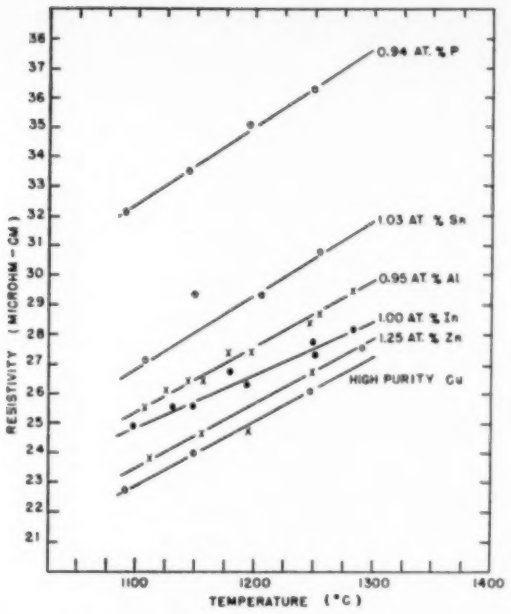

Fig. 7—Resistivity of liquid copper alloys (one atom pct solute).

values. The resistivity of copper determined in these experiments is about 5 pct higher than reported by Northrup[9] as it is for copper alloys when compared to values computed at 1 atomic pct from Bornemann's data on more concentrated solutions. In summary: 1—The introduction of a small number of solute atoms increases the resistivity to the same degree as in the solid state. 2—The change in resistivity is dependent on the valence of the solute, specifically on the square of the difference in valence of solute and solvent as in the solid state. 3—The rate of change of resistance with respect to temperature for all dilute copper alloys is the same, with the possible exception of indium. This temperature dependence is in accordance with Matthiessen's rule which was formulated for the solid state.

Zinc Alloys: Fig. 8 shows the results for liquid zinc solutions containing 1 atomic pct copper, cadmium, aluminum, tin, antimony, and bismuth compared with pure zinc as a function of temperature.

In alloys of zinc containing copper and tin, some difficulty was experienced at high temperatures due to an unexplained increase in resistivity that occurred on heating as compared with the corresponding resistivity-temperature curve followed when cooling, indicated by the dotted lines in Fig. 8. Duplicate runs with cadmium and aluminum did not show this effect whereas the effect was always present in the case of copper and tin. In drawing the curves greater weight was given to the points obtained on cooling that are in accord with those for high purity zinc, in which this effect was never observed.

Unlike copper alloys, the addition of 1 atomic pct copper, cadmium, aluminum, or bismuth to liquid zinc does not significantly affect the resistivity at any temperature. The addition of tin or antimony, however, increases the resistivity and to about the same extent in both cases. Tin and antimony apparently also increase the negative temperature coefficient at the melting point and

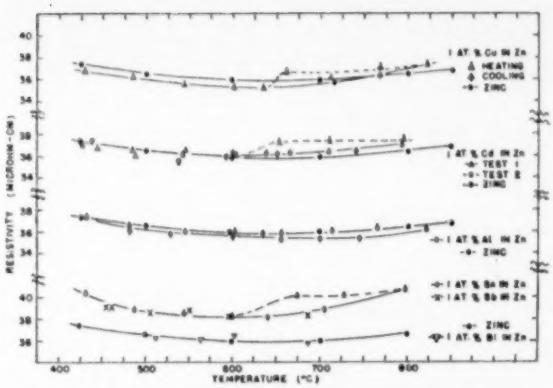

Fig. 8—Resistivity of liquid zinc alloys (one atom pct solute).

correspondingly lower the temperature of the minimum in the resistivity curve by about 50°C.

Discussion

The preceding data indicate that there is a one-to-one correspondence between solid and liquid copper solutions with respect to resistivity-temperature and compositional relationships. It appears, therefore, that insofar as the conduction of electricity is concerned the atomic constitution of the liquid state is very similar to that of the solid state. The differences between the two states appear to be a matter of degree rather than the result of any unique property peculiar to the liquid state.

Mott[12] has shown that it is possible to represent quantitatively the ratio of conductivity in the solid and liquid states at the melting point by the expression

$$\frac{\sigma_L}{\sigma_S} = \left(\frac{V_L}{V_S}\right)^3 = e^{-\frac{mL}{T_M}}$$

where V_L and V_S are vibrational frequencies of atoms in the liquid and solid states respectively; L is the heat of fusion in kilo-joules per gram atom, and T_M°K is the melting point. The essential agreement between observed and calculated values for a variety of close-packed metals indicates that the principal assumption is probably correct; namely, that the atoms in the liquid state vibrate about mean positions with a frequency V_L and that the positions, while moving in time, do so with velocities slow compared with the velocity associated with the vibration of the atoms. Implicit in this assumption is the idea that the resistivity in the liquid state is not primarily a function of disorder, relative to the solid state, but of thermal vibration amplitude and, therefore, the dependence of resistivity in the liquid state on temperature and composition should be similar to that in the solid state. The data in Fig. 7 on copper alloys appear to provide a critical test and confirmation of this hypothesis.

Thus, the increase in resistivity of liquid copper resulting from the addition of 1 atomic pct of various solutes is essentially the same as that for copper solid solutions as reported by Linde.[13] Furthermore, Linde showed that the increase in resistivity per atomic percent solute is proportional to the square of the difference in charge between solute and solvent. Fig. 9 demonstrates that this relationship holds for liquid solutions as well as for

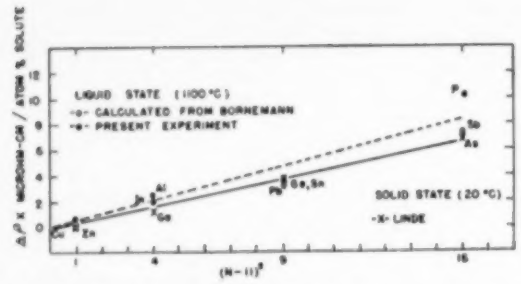

Fig. 9—The application of Linde's rule to dilute copper alloys in the liquid state compared with the solid state.

the substitutional solid solutions with which it is compared. The magnitude of the change in resistivity is similar in both cases, and is independent of temperature.

The introduction of small concentrations of atoms of different size and charge results in the same increase in resistivity and dependence on scattering charge as applies to the solid state. Apparently, then, the disorder in the liquid state, relative to the solid state, cannot be large. Otherwise, it would seem that the effect of one foreign atom in one hundred would be lost in comparison with the effect of extensive disorder.

In this connection, the linear temperature dependence of liquid metals and alloys, except zinc, cadmium, and mercury, appears to indicate that the same type of thermal dependence applies in the liquid state as in the solid state. Furthermore, in the case of both copper and silver, the resistivity in the liquid state extrapolates to zero at 0°K, within the limits of accuracy of the data from the present work on copper and that of Northrup[15] for liquid silver. While the present data do not permit definitive conclusions, it may be inferred that at least a part of the change in resistance associated with lattice expansion and melting can be accounted for by a change in Debye temperature.

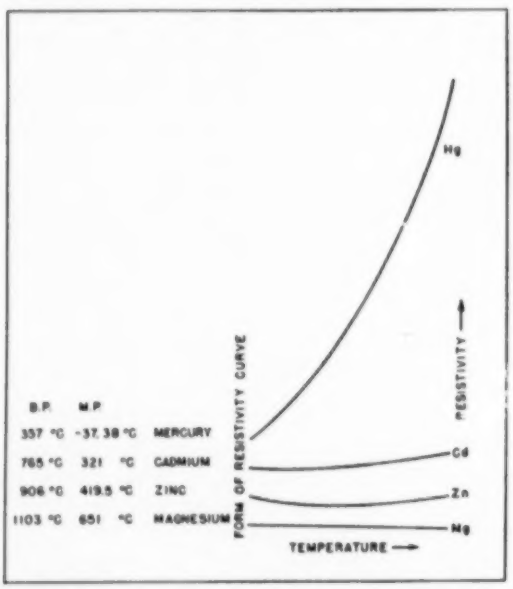

Fig. 10—A schematic drawing of the form of the resistivity temperature curves of liquid magnesium, zinc, cadmium, and mercury.

The resistivity of polyvalent liquid tin and indium, while linear with temperature, do not extrapolate to zero at 0°K, indicating some significant difference between the monovalent and polyvalent metals in the liquid state.

On the other hand, the resistivity of the divalent metals, cadmium, zinc, and magnesium (and mercury), behaves quite differently with respect to temperature. The increase in resistivity on melting, except for mercury, is again of the magnitude indicated by considerations based on the amplitude of displacement about a mean position. However, in the solid state the number of electrons that are available for conduction in these divalent metals is limited and conduction is crystallographically anisotropic owing to scattering at the surfaces of energy discontinuity, the Brillouin zone boundaries. Thus, in addition to the component of resistivity arising from thermal vibration, there is also a structural component in divalent metals.

The negative temperature coefficient at the melting point of the three hexagonal metals and alloys may be accounted for by assuming that the limitation on conduction, imposed by zone boundary overlap, is relaxed in the liquid state.[12] In the case of cadmium and zinc, the change in slope from negative to positive at 50° and 230°C above the melting point, respectively, may be interpreted as a superposition of structural and thermal effects with the latter predominating at temperatures above the minimum.

In this connection, a comparison may be made between the four divalent metals, mercury, cadmium, zinc, and magnesium, Fig. 10. Assuming that the minimum represents a balance of structural and thermal scattering, the thermal component appears to take over in the four metals at a temperature relative to the melting point that increases in the same order as the melting and boiling points, or, in other words, with bond strength. This hypothesis implies that there is not only a degree of order in the liquid state but also a significant degree of order in the crystallographic sense, over short distances and effective in scattering electron waves. The effective order persists above the melting point and disappears with rising temperature in accordance with the respective bond strengths of the four metals. In the case of magnesium, the temperature of the minimum was evidently not attained.

Further evidence that structural factors are controlling resistivity of divalent metals may be derived from the effect of alloying elements added to zinc. It has already been observed, Fig. 8, that unlike copper there appears to be no systematic change in resistance with the valence of the solute; tin and antimony increasing resistance to the same degree, bismuth and aluminum leaving it unchanged as do copper and cadmium. If the effective number of electrons alone were involved, independent of structure, it might be anticipated that the addition of at least some of these solutes would decrease the resistance, as they do in mercury,[14] instead of either increasing it without respect to scattering charge, or leaving it unchanged. Unfortunately, comparison with zinc solid solutions appears to be excluded by the limited solubility of most metals in zinc and, therefore, the effect of solutes on the resistivity of the hexagonal close-packed zinc lattice is unknown.

In the preceding discussion it may appear that

there is some conflict of interpretation with respect to the structure of the liquid state as deduced from electrical measurements and that provided by X-ray evidence which indicates a close-packed aggregate without long range order. It may be concluded that in the liquid state the two methods of observation are not recording precisely the same thing. This is best illustrated by the fact that the radial distribution functions obtained from X-ray data for the cubic and hexagonal metals are exactly similar in form while the properties as observed by resistivity are entirely different. To avoid misunderstanding, all preceding statements regarding structure have been qualified by reference to resistivity.

Conclusions

Redetermination of the resistivity of pure liquid tin, zinc, and cadmium shows that the available data is essentially correct except that the present work indicates that the resistivity of pure tin is about 5 pct lower than has been reported. A new set of values is proposed for the resistivity of pure indium as a function of temperature. The resistivity of pure magnesium has been determined and is in essential agreement with recently published data.

Investigation of dilute liquid solutions of copper shows that the effect of alloying elements on the resistivity of simple metallic liquid solutions is identical with that of similar solid solutions; specifically, 1—the increase in resistivity due to the addition of solutes is proportional to the square of the difference in valence of solute and solvent; 2—the increase in resistivity due to the solute is independent of temperature; and 3—the magnitude of the increase is the same in both solid and liquid states.

The resistivity of liquid zinc, cadmium, and magnesium appears to be dependent on structure and, except for tin and antimony which increase resistivity equally, the resistivity of zinc is unaffected by the addition of 1 atomic pct of copper, cadmium, aluminum, or bismuth.

It is suggested that temperature dependence of resistivity of the divalent metals may be explained by a superposition of structural dependence associated with bond strength, and thermal vibration.

Insofar as electrical conduction is concerned, it may be concluded that there is essentially complete correspondence between the liquid and solid states of metals including thermal, structural, and compositional relationships.

Acknowledgments

We wish to thank Dr. D. K. Crampton, whose cooperation enabled us to undertake this project, and to acknowledge the help and assistance of many people at Chase Brass and Copper Co. We are also grateful to the Indium Corp. of America for supplying the indium used in the experiments and to Dominion Magnesium, Ltd., for the high purity magnesium.

References

[1] N. S. Gingrich: *Revue of Modern Physics* (1943) **15**, p. 90.
[2] O. Kubaschewski: *Trans.* Faraday Soc. (1949) **45**, p. 931.
[3] K. Bornemann and P. Müller: *Metallurgie* (1910) **7**, p. 396.
[4] P. Müller: *Metallurgie* (1910) **7**, pp. 730, 755.
[5] K. Bornemann and G. Von Rauschenplat: *Metallurgie* (1912) **9**, p. 473.
[6] K. Bornemann and G. Wagenmann: *Ferrum* (1913-1914) **11**, pp. 276, 289.
[7] A. L. Norbury: *Trans.* Faraday Soc. (1920-1921) **16**, p. 570.
[8] E. F. Northrup and V. A. Suydam: *Journal* Franklin Inst. (1913) **175**, p. 153.
[9] E. F. Northrup: *Journal* Franklin Inst. (1914) **177**, p. 1.
[10] A. W. Smith: *Ohio Journal of Science* (1916) **16**, p. 244.
[11] F. H. Horn: *Physical Review* (1951) **84** (2), p. 855.
[12] N. F. Mott: *Proc.* Royal Soc. (1934) **146A**, p. 465.
[13] J. O. Linde: *Ann. Physik* (1932) **15**, p. 219.
[14] H. Feninger: *Handbuch der Metallphysik* (1935) Vol. 1, Part I, p. 344. Leipzig.
[15] E. F. Northrup: *Journal* Franklin Inst. (1914) **178**, p. 85.

Technical Note

Effect of Grain Size Upon Temper Brittleness

by L. D. Jaffe, F. L. Carr, and D. C. Buffum

SINCE the temper brittleness of steels is generally considered to be a grain-boundary phenomenon[1, 2] it would be expected that austenitic grain size would affect temper brittleness. Several investigators[3-6] reported that temper brittleness, as measured by room-temperature impact tests, increased as the austenitizing temperature was raised. It was subsequently pointed out that conclusions as to temper brittleness based upon room-temperature impact tests are likely to be misleading.[1, 6] Hurlich[7] used a range of testing

L. D. JAFFE and D. C. BUFFUM, Members AIME, are associated with Watertown Arsenal, Watertown, Mass., and F. L. CARR, formerly with Watertown Arsenal, is now with National Research Corp., Cambridge, Mass.

TN 174E. Manuscript, April 20, 1953.

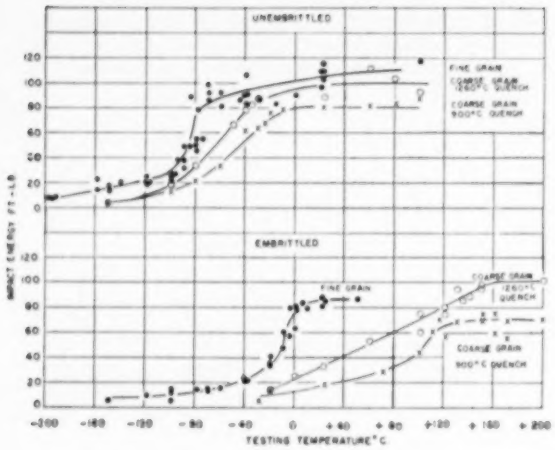

Fig. 1—Impact energy vs testing temperature.

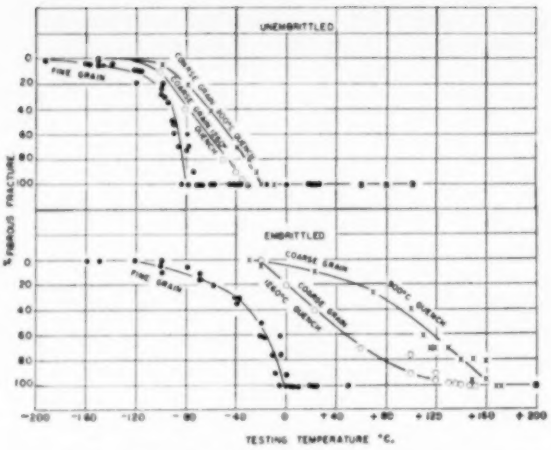

Fig. 2—Percentage of fibrous fracture vs testing temperature.

temperatures which was unfortunately too narrow to permit evaluation of his data on the basis of any single criterion of transition from tough to brittle failure. Craig[9] pointed out that quenching from different austenitizing temperatures might introduce differences in respects other than grain size; for example, in stresses resulting from quenching. Accordingly, experimental work was planned in which the austenitizing treatment would be varied with and without changing the temperature from which the steel was quenched.

The steel used was SAE 3140, ⅝ in. round hot-rolled bar stock from a heat previously studied.[10] About 100 blanks 2 3/16 in. long were austenitized for 1 hr at 900°C, then water-quenched, giving an austenite grain size of ASTM 8. Another 100 blanks were austenitized for 4 hr at 1260°C. Half of these were water-quenched. The other half were quenched into salt at 900°C and held 1 hr and 40 min, then water-quenched. The austenite grain size resulting from both of these treatments was predominantly ASTM 0, with some larger grains. In all cases the structure was 100 pct martensite with no visible carbides.

All blanks were tempered 1 hr at 675°C, then water-quenched to room temperature. Half of the tempered blanks from each of the three austenitizing treatments were next isothermally embrittled in salt at 500°C for 48 hr, then water-quenched. The blanks were machined into standard V-notched Charpy bars which were broken at various temperatures on a 217 ft-lb impact machine (16.8 ft per sec striking velocity). The data, presented in Figs. 1 and 2, show that an increase in austenite grain size results in an increase in transition temperature. This confirms earlier work.[7, 11]

It is likewise evident that the shift in transition temperature due to temper embrittlement is greater for large grain size than for small grain size. This is in agreement with the view of Herres and Lorig[8] that temper brittleness should become more apparent the larger the grain size. Lowering the quenching temperature did not reduce the transition temperature of the coarse-grained specimens but rather raised it slightly, at least on the basis of fracture behavior, Fig. 2. This is contrary to the theory of temper brittleness suggested by Spretnak and Speiser,[12] as previously pointed out.[13]

The impact energy level of the unstabilized coarse-grain specimens quenched from 1260°C was higher than that of the coarse-grained specimens quenched from 900°C. The fracture of all coarse-grained specimens at temperatures producing 0 pct fibrous fracture was predominantly transcrystalline in the unembrittled state and intercrystalline in the embrittled state. Microscopic examination revealed some intercrystalline fracture with the transcrystalline and vice versa.

It is concluded that an increase in austenitic grain size increased the shift in transition temperature associated with temper brittleness. At fixed grain size, lowering the quenching temperature had little effect upon the transition temperature, perhaps raising it slightly.

The authors acknowledge with thanks the metallographic work performed by M. R. Norton for this investigation.

References

[1] J. H. Hollomon: Temper Brittleness. *Trans.* ASM (1946) **36**, pp. 473-542.

[2] L. D. Jaffe: What to do about Temper Brittleness of Steels. *Steel* (Nov. 29, 1949) **125**, No. 21, pp. 86-89, 114.

[3] R. H. Greaves and J. J. A. Jones: Temper-Brittleness of Nickel-Chromium Steels. *Journal* Iron and Steel Inst. (1920) **102**, pp. 171-222.

[4] W. Bischof: Contribution to the Question of Temper Brittleness. *Arch. Eisenhuttenw.* (1935) **8**, pp. 293-301.

[5] E. Maurer, O. H. Wilms, and H. Kiessler: Influence of Phosphorus and of Various Alloying Elements on the Temper Brittleness of Structural Steel. *Stahl u. Eisen* (1942) **62**, pp. 81-89, 115-121.

[6] H. Jolivet and G. Vidal: The Temper Brittleness of Steel. *Comptes Rendus* (1943) **216**, pp. 664-666.

[7] A. Hurlich: Discussion on ref. 8. *Trans.* ASM (1948) **40**, pp. 805-809.

[8] S. A. Herres and C. H. Lorig: Influence of Metallurgical Factors on the Mechanical Properties of Steel. *Trans.* ASM (1948) **40**, pp. 775-805.

[9] W. F. Craig, Jr.: Private communication, 1949.

[10] L. D. Jaffe, D. C. Buffum, and F. L. Carr: Effect of Various Heat Treating Cycles upon Temper Brittleness. *Trans.* ASM (1953) **45**, pp. 725-731.

[11] L. D. Jaffe and J. F. Wallace: Discussion on ref. 8. *Trans.* ASM (1948) **40**, p. 809.

[12] J. W. Spretnak and R. Speiser: *Trans.* ASM (1951) **43**, pp. 734-758.

[13] D. C. Buffum: Discussion on ref. 12. *Trans.* ASM (1951) **43**, pp. 748-750.

A Rationalization of Measured High Temperature Properties Of Fe-Cr-Co-Ni Alloys

by J. D. Nisbet and W. R. Hibbard, Jr.

The high temperature properties of Fe-Cr-Co-Ni base alloys and the effects of hardening element additions on these properties are rationalized on the basis of general principles of alloying.

DURING the past few years the base elements in high temperature austenitic alloys have gradually been changed from iron-rich materials to nickel-rich, then to cobalt-rich and more recently to various iron, cobalt, and nickel combinations, all with an approximately constant chromium content of 20 pct. Concurrently, the hardening additions of the incongruous* elements, have been shifted from small amounts of a single element to various ratios of molybdenum, tungsten, columbium, carbon, titanium, and aluminum with the percentages of these constituents continually increasing.

* Elements having a relatively low solubility in Fe-Ni-Cr-Co solid solutions.

It has been known that the typical soft high temperature alloy (such as Inconel) consisted of face-centered cubic austenite, but the effect of varying the composition of the base elements, iron, chromium, nickel, and cobalt, has not been broadly analyzed. Therefore, it was reasoned that the first major problem in the understanding of the properties or the further development of high temperature alloys was to study systematically the effect of composition upon the mechanical properties of face-centered cubic Fe-Ni-Co-Cr austenitic solid solutions.

The matrix of the strong high temperature alloys (such as Inconel X) is usually also a face-centered cubic solid solution of iron, nickel, chromium, and cobalt but with additional phases which can be generally classified as intermetallic compounds and carbides. It is usually observed that combinations of the hardening elements, tungsten, molybdenum, columbium, tantalum, titanium, aluminum, carbon, and others have been used in these strong high temperature alloys. Thus, it was reasoned that a second major problem in studying these alloys was to understand the effect on mechanical properties of adding

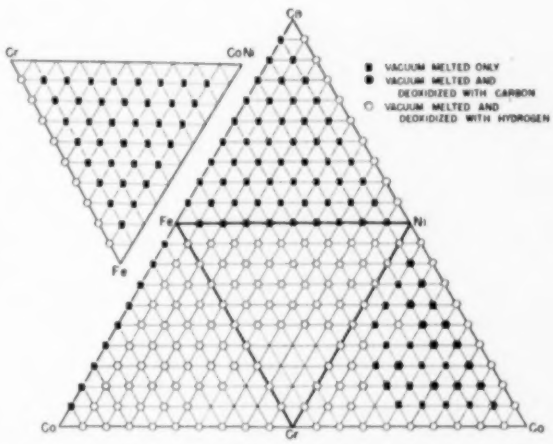

Fig. 1—Nominal compositions in atomic percent and melting practices of the base alloys investigated. CoNi indicates alloys in which the CoNi content is 50 pct Co and 50 pct Ni.

J. D. NISBET, Associate Member AIME, formerly with General Electric Co., is now associated with Universal Cyclops Steel Co., Bridgeville, Pa., and W. R. HIBBARD, Jr., Member AIME, is associated with the Metallurgy Research Dept., Research Lab., General Electric Co., Schenectady.

Discussion on this paper, TP 3618E, may be sent, 2 copies, to AIME by Dec. 1, 1953. Manuscript, Sept. 16, 1952; revision, April 16, 1953. Cleveland Meeting, October, 1953.

Table I. Chemical Compositions of Incongruous Elements Added to Different Base Alloys

Nominal Base Analysis	Base Classification	Incong. Alloy	Nominal and Analyzed (in Parentheses) Atomic Percentages of Incongruous Element Added							
20%Cr-80%Ni	Unsaturated	Ta	1	(1.2)	5	(3.9)	8	(7.2)	10	(9.7)
		Cb	1	(0.76)	5	(3.5)	8	(6.1)	10	(7.9)
		W	1	(1.3)	5	(4.5)	8	(7.0)	10	(7.9)
		Mo	2	(2.4)	4	(3.3)	8	(6.4)	12	(9.6)
		Zr	1	(0.39)	3	(1.6)	6	(3.2)	9	(7.4)
		Ti	1	(0.50)	4	(2.8)	8	(6.3)		
		Al	1	(0.34)	3	(1.2)	6	(4.1)		
		Be	1	(0.45)	2	(0.77)	4	(1.9)	8	(3.2)
		C	0.5	(0.19)	1	(0.25)	2	(1.4)	3	(1.8)
									4	(2.9)
		O	1 min.	(0.086)	5 min.	(0.079)				
			10 min.	(0.136)						
		N	1 min.	(0.734)	5 min.	(0.621)				
			10 min.	(0.509)						
30%Cr-30%Co-40%Ni	Saturated	Ta	2	(1.6)	4	(3.4)	8	(6.7)		
		Zr	1	(0.11)	2	(1.0)	4	(2.1)		
40%Cr-20%Co-40%Ni	Supersaturated	Mo	2	(1.8)	4	(3.4)				
		V	2	(1.3)	4	(3.4)	8	(6.6)		
20%Fe-30%Cr-25%Co-25%Ni	Saturated	Cb	2	(1.3)	4	(2.9)	8	(5.8)	10	(7.2)
		Mo	2	(1.8)	4	(3.9)	8	(7.2)	10	(8.9)
									12	(11)
		Zr	6	(2.7)	8	(3.5)	10	(6.6)		
		Ti			2	(0.30)	4	(1.84)	6	(2.8)
					8	(3.5)	10	(5.2)		
		C	0.2	(0.14)	0.4	(0.10)	0.8	(0.42)	1.5	(0.46)*
							2	(0.75)	1	(1.3)*
		Ta	10	(7.91)						
		V	10	(9.16)	12	(11.13)				
20%Fe-40%Cr-20%Co-20%Ni	Supersaturated	Be	1	(0.2)	2	(0.3)	4	(0.6)		
		W	2	(1.9)	4	(4.0)	8	(6.8)		
		Al	2	(0.39)	4	(3.5)	8	(5.6)		
20%Fe-20%Cr-60%Ni	Unsaturated	C	5	(0.19)	10	(0.24)				
		Al	2	(0.36)	4	(1.2)	6	(2.2)		
		Ti	2	(1.04)	4	(2.3)	6	(3.3)		
30%Fe-20%Cr-50%Ni	Unsaturated	Al	6	(4.9)	8	(6.8)	10	(8.2)	12	(10.1)
50%Fe-20%Cr-30%Ni	Saturated	C	5	(0.23)	10	(0.23)				
		Al	2	(0.66)	4	(1.5)	6	(2.2)		
		Ti	2	(2.4)	4	(2.5)	6	(4.1)		
80%Fe-20%Cr	Unsaturated	C	5	(0.45)	10	(0.69)				
60%Fe-40%Ni	Unsaturated	Al			5	(4.10)	10	(6.78)	15	(11.11)
		Cb	1	(0.56)	5	(4.00)	10	(8.33)	15	(12.02)
		Ti	1	(0.60)	5	(3.48)	10	(6.44)	15	(10.27)

All alloys vacuum melted and hydrogen treated except two (*) carbon alloys which were vacuum melted only.

various compounds of different composition and characteristics to various face-centered cubic solid solutions. Therefore, a systematic exploratory research was started in 1946 to study the metallurgy of alloys at high temperatures from these viewpoints. Certain principles have been deduced from this research. It is the purpose of this paper to present data leading to these principles.

Experimental Procedure

More than two hundred alloys consisting of binary, ternary, and quaternary combinations of iron, chromium, cobalt, and nickel were made to evaluate and compare the properties of the base alloys. The elements varied in steps of 10 atomic pct** as illustrated schematically in Fig. 1. More than a hundred supplementary alloys with incongruous additions listed in Table I were tested in the second part of the work. Typical of analysis of the four starting materials used in the base alloys are those listed in Table II. The hardening elements were added in the purest form available, as follows: Al, 99.996 pct; Be, 99.8; Mo, 99.9; Cb, 99.4; Ta, 99.9+; titanium hydride, 94.0; W, 99.9; Va, 99.7; and zirconium hydride 96.0. Since these elements were added in amounts no larger than 12 pct, it is believed that the impurities are not significant.

** Compositions are expressed in atomic percent throughout the paper.

All alloys were produced by a vacuum-melting technique[1,2] to reduce the amounts of extraneous impurities. Certain alloys were deoxidized with carbon or hydrogen as indicated symbolically in Fig. 1, or as noted in Table I. All alloys were centrifugally cast, in vacuum, into a permanent molybdenum or copper segmented mold to yield castings of the form shown in Fig. 2. Each casting was homogenized at 2100°F for 15 hr in hydrogen and water quenched. Mechanical tests were performed with the material in this initial condition. Hardness tests were made on quenched specimens aged 2 hr at 400°, 800°, 1200°, 1400°, 1600°, 1800°, and 2000°F, respectively. This type of data is shown plotted in Fig. 3a. All heat-treating and testing temperatures were maintained within 5°F.

Both tensile and rupture tests were made on button-head cylindrical specimens machined to a gage length of 1⅛ in. and a gage diameter of 0.160

Table II. Analysis of Base Components

	C	S	Si	Mn	P	O	H	N	Fe	Cr	Pb	Ni	Cr	Co
Electrolytic nickel	0.02	0.006	Nil	None	Trace	0.006	0.0003	0.0000	ND	ND	—	Rem.	—	—
Electrolytic chromium	0.01	0.019	—	—	—	0.41	0.034	0.007	0.054	0.01	0.001	—	Rem.	—
Electrolytic iron	0.03	0.004	Trace	Trace	0.02	0.061	0.0004	0.0018	Rem.	Trace	—	Nil	Trace	Nil
Rondell's cobalt	0.02	0.003	0.22	Trace	—	0.119	0.0001	0.0000	Nil	Nil	—	Trace	Nil	Rem.

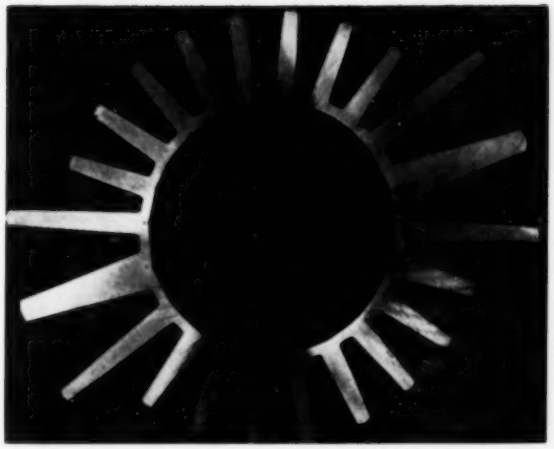

Fig. 2—Cross section of permanent mold centrifugally cast specimen. X0.6. Area reduced approximately 80 pct for reproduction.

±0.0005. Tensile tests were made on a Baldwin-Southwark testing machine adapted for elevated temperature testing. Tests were run at a rate of 0.050 in. per min at room temperature, 600°, 1200°, 1400°, 1600°, 1800°, and 2000°F in air. An example of the tensile data is shown plotted in Fig. 3b. The time of tensile testing varied with the elongation to fracture. For this paper, however, an average value of 0.1 hr is used. This value is typical of that obtained for tests at temperatures near 1500°F.

Two types of rupture apparatus were used: a large 48-bar unit[5] and a single-bar apparatus of a common design. Constant-load rupture tests were carried out at 1000°, 1200°, and 1500°F. Three to five samples were tested at each temperature and loaded so that the fracture time was between 1 and 1000 hr. An example of the type of data obtained is shown in Fig. 3c.†

† In this paper, since the results of both tensile and rupture tests are plotted together, the term "breaking strength" is used to indicate the maximum load divided by the initial cross-section area. This value for tensile tests is the conventional ultimate strength, and for rupture tests is the initial stress.

Metallographic samples of each alloy were examined to evaluate cleanliness in the vacuum melting and casting process, and to determine the microstructure. Typical micrographs are shown in Fig. 4a, b, and c. The grain size varied from about ASTM No. 1 for solid solution alloys to about No. 7 for multiphase alloys, usually in typical progression, as shown in Fig. 4a. Since grain size is a dependent variable, the effects of composition reported in this paper include the effects of grain size. The significance of grain size in elevated temperature tests has never been clearly and undisputably evaluated, since the heat treatment and changes in procedure required to control grain size also change other factors which affect the strength. The types of microstructures encountered in this investigation are illustrated in Fig. 4b and c, including solid solution alloys and alloys undergoing allotropic transformation during quenching (Fig. 4b, left), mixed-phase alloys of approximately equal proportions (Fig. 4b, center and right), and the effects of incongruous additions where a second phase is formed in a massive condition (Fig. 4c, first three micrographs), or where the second phase appears interdendritically (Fig. 4c, last three micrographs).

A chemical analysis of the principal elements was made on approximately every tenth alloy, except for those containing incongruous additions as noted below. The melting practice was developed to a high degree of reproducibility; therefore, deviations from the nominal compositions were minor. Variations of as much as 1 or 2 pct in the composition of any one of the four elements iron, chromium, cobalt, and nickel were found to produce only small differences in mechanical properties. The analyses made indicated that variations were usually less than this amount. Chemical analyses of impurities were made frequently to establish the effectiveness of the purifying treatments carried out during vacuum melting. An analysis typical of alloys prepared is 0.0006 atomic pct H, 0.021 O, 0.005 N, and 0.08 to 0.13 C. Since all the alloys were prepared in a similar manner and checked wherever practicable, it is believed that in all alloys the impurity contents are under control. Chemical analyses were run on all incongruous addition elements. The nominal and actual compositions are listed in Table I.

The base compositions used in the investigation of incongruous elements are listed in Fig. 5, together with the 1500°F phase boundaries. All alloys are face-centered cubic solid solutions except 80 pct Fe-20 pct Cr, which is body-centered cubic as-quenched from 2100°F. They include base alloys which are unsaturated solid solutions such as 80 pct Ni-20 pct Cr, nearly saturated solutions such as 30 pct Cr-30 pct Co-40 pct Ni and supersaturated solid solu-

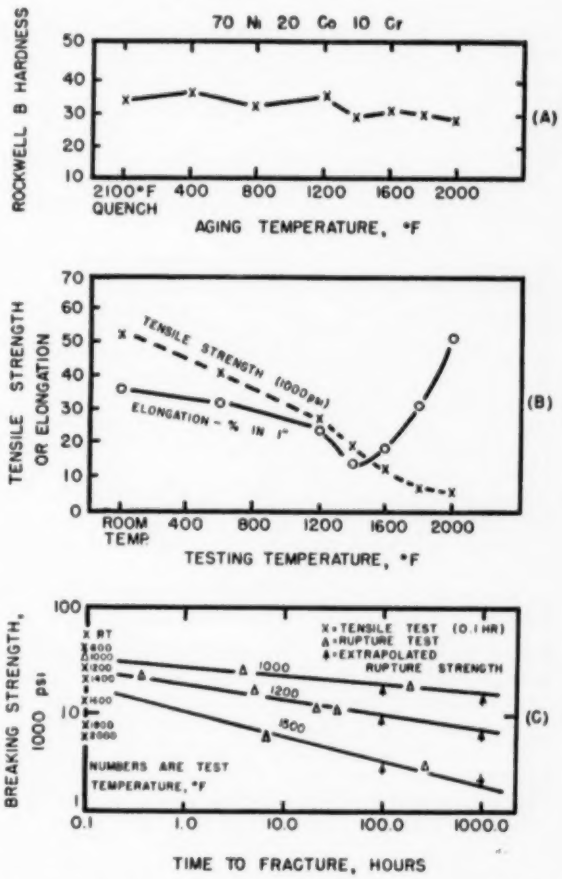

Fig. 3—Hardness, tensile, and rupture data for 70 pct Ni-20 pct Co-10 pct Cr base alloy plotted conventionally. Breaking strength is defined as the maximum load divided by the original cross-section area.

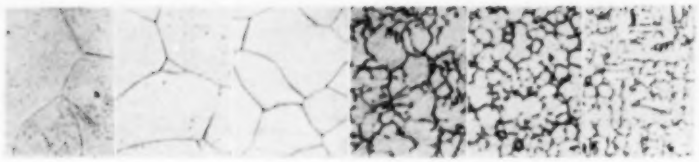

No added C Grain size No. 2-3 | 0.19 pct C No. 3-4 | 0.25 pct C No. 4-5 | 1.4 pct C No. 6-7 | 1.8 pct C No. 7-8 | 2.9 pct C —

Fig. 4a—80 pct Ni-20 pct Cr base alloy. Effect of carbon additions on microstructure. Electrolytic (oxalic acid) etch. X100.

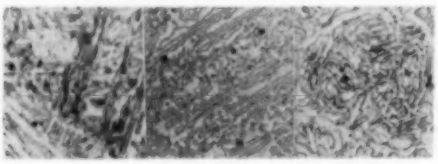

80 pct Fe-10-pct Cr-10 pct Ni Gamma—alpha Allotropic transformation Picric acid etch | 50 pct Cr-40 pct Co-10 pct Ni Gamma + sigma Electrolytic (chromic acid) etch | 60 pct Fe-30 pct Cr-10 pct Ni Alpha + gamma HCl + H_2O_2 etch

Fig. 4b—Multiphase base alloys. Etchants as indicated. X100.

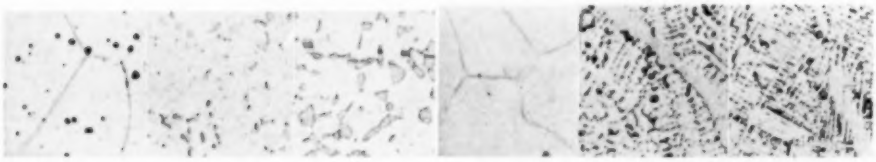

20pctFe-40pct Cr-20pctCo-20pctNi Electrolytic (chromic acid) etch | 20pctFe-40pct Cr-20pctCo-20pctNi plus 0.2 pct Be HCl + HNO_3 etch | 20pctFe-40pct Cr-20pctCo-20pctNi plus 0.6 pct Be HCl + HNO_3 etch | 30pctCr-30pct Co-40pctNi Electrolytic (chromic acid) etch | 30pctCr-30pct Co-40pctNi plus 1.0 pct Zr Cupric chloride etch | 30pctCr-30pct Co-40pctNi plus 2.1 pct Zr Cupric chloride etch

Fig. 4c—Effects of incongruous additions on microstructure. Etchants as indicated. X100.

tions such as 40 pct Cr-20 pct Co-40 pct Ni as indicated in Table I. Although several of the alloys are supersaturated solid solutions as-quenched from 2100°F, there was no indication of age hardening in terms of hardness tests on specimens subsequently aged at various temperatures. These base compositions cover the range of high temperature strength found for the Fe-Cr-Co-Ni solid solution alloys.

Incongruous elements having a variety of melting points, atomic diameters, compressibilities, and crystal structures, as listed in Table III, were chosen for alloying with the selected base materials. A series of compositions with increasing amounts of incongruous additions was prepared in an attempt to include unsaturated, supersaturated, and multiphase alloys.

Technique of Plotting: Time Temperature Parameter

The customary procedure for presenting time-temperature breaking strength data consists of plotting the logarithm of the breaking strength as a function of the logarithm of the time to failure at each testing temperature. This method of plotting, Fig. 3c, is clumsy to use for comparing the effects of wide varieties of time and temperature upon the fracture strength of alloys. A more useful method in which time and temperature are interrelated as a single-valued function of breaking strength has been found to facilitate the comparison of the properties of different alloys.[4,5] This time-temperature function which will be referred to as a parameter may be expressed as follows:

$$T\ (C + \log t)$$

where T is temperature in degrees Rankine,†† t is time in hours, and C is a constant equal to 11 in the present work.‡ When the logarithm of the breaking strength is plotted against this parameter, a single line as shown in Fig. 6 replaces the customary sets of curves and can include both short-time tensile strengths at different temperatures and stress-rupture strengths at different times and temperatures. For parameter numbers above about 19,000, this line is straight for data such as those shown in Fig. 6 (19,000 corresponds to a tensile test—0.1 hr—at 1340°F, or a 1000-hr rupture test at about 900°F). The 1000-hr rupture strength at 1500°F (a parameter number of 27,400) is more accurately defined in Fig. 6 than in Fig. 3c, primarily because more data points are used in the parameter plot. This strength is used as a basis of comparison of different alloys in this paper. For purposes of evaluating the parametric method, interpolated and extrapolated rupture values from conventional log stress-log

†† °F plus 459.4.

‡ The constant was determined by trial and error. By plotting log time against $1/T°K$ for various constant strengths and extrapolating to a convergence point at $1/T = 0$, a value of C may be determined graphically. Since data at any given strength level are limited by the nature of the alloys and the difficulties of running very short and very long-time tests, the extrapolation is so long as to preclude any accurate determination of C. A single average value of the constant was used. For further discussion, see ref. 4.

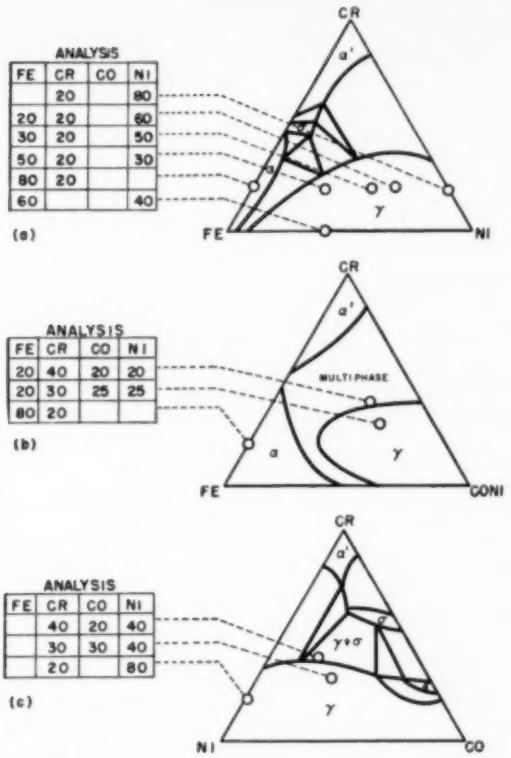

Fig. 5—Composition and 1500°F phase boundaries for base alloys selected for alloying with incongruous additions.

time plots are included on the parametric plots to illustrate the similarities of the values obtained by the two methods. These values are labeled "extrapolated rupture strength" for purposes of brevity, but were not used in fitting lines to the data points. An important advantage of the parametric method is that all types of data are included on the same plot. Other advantages and disadvantages of the parametric method of plotting are discussed in subsequent sections.

Results of Tests

Parametric plots were constructed from tensile and rupture strength data determined from specimens of all alloys considered. A few examples will be discussed in detail to illustrate the correlation between the parametric plots and different types of alloys.

Solid Solutions. An important experimental generalization‡‡ is that the high temperature data for all single-phase cobalt-containing alloys of the Fe-Cr-Co-Ni type can be represented on parametric plots by a straight line having a slope of −0.117 (illustrated in Fig. 6) and that the high temperature data for single-phase Fe-Cr-Ni or cobalt-free austenitic alloys (except alloys having allotropic phase changes) can be represented by a straight line with a slope of −0.133 (illustrated in Figs. 7 and 8). This finding is empirical and not understood, but is convient for the analysis of data. It is interesting to note that, since the slope is empirically defined by the composition, the straight-line portions of the parametric plots used in this investigation may be reconstructed from the 1000-hr 1500°F rupture strengths (parameter No. 27,400) in Fig. 17 by the point-slope method. In addition, because of the similarities of slopes, similar composition-strength contours will result from any constant parameter number (condition of testing time and temperature), provided it lies on the straight-line portion of the plot.

‡‡ Lines were independently fitted to experimental data points for a large number of alloys. Subsequent inspection of these plots lead to the recognition of the common slopes.

Supersaturated Solid Solutions: When metallurgical changes which affect properties occur as functions of time and temperature different from the $T(C + \log t)$ parameter, the strength is not a single-valued function of the parameter. Under these conditions, several strength values can occur at a

Table III. Some Characteristics of Alloying Elements

Element	Melting Point, °F	Atomic Diam., Å	Compress. 10^6 Cm²/Kg	Valence	Crystal Structure
W	6170	2.82	0.293	*	BCC
Ta	5425	2.95	0.479	*	BCC
Mo	4760	2.80	0.347	*	BCC
Cb	4380	2.94	0.570	*	BCC
Cr	3430	2.57	0.600	*	BCC
Ti	3300	2.93	0.797	*	CPH-BCC
Zr	3200	3.19	1.097	*	CPH-BCC
V	3150	2.71	0.609	*	BCC
Fe	2802	2.52	0.587	*	FCC-BCC
Co	2723	2.50	0.539	*	CPH-FCC
Ni	2651	2.49	0.529	*	FCC
Be	2340	2.25	0.855	2	CPH
Al	1220	2.80	1.34	3	FCC
C	6700			4	Hex.
O	−362			6	Orth.
N	−346			5	Cubic

* Transition.

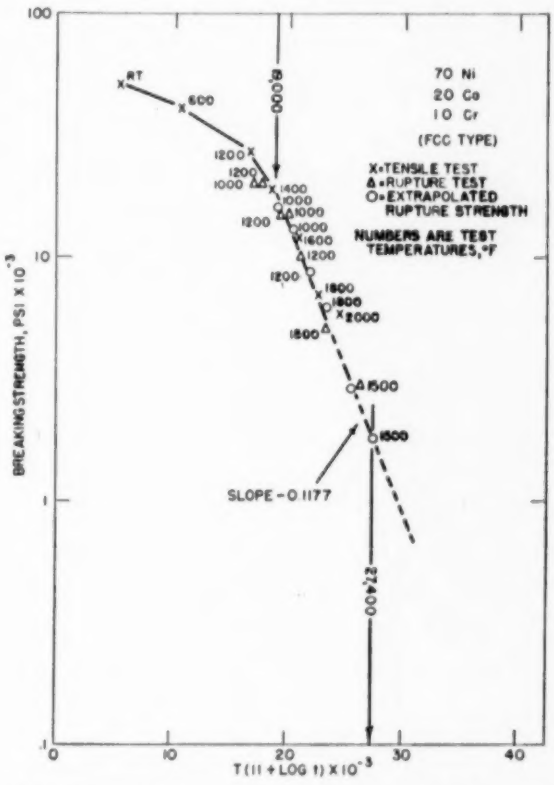

Fig. 6—Parametric plot of the tensile and rupture data of Fig. 3 for 70 pct Ni-20 pct Co-10 pct Cr base alloy, illustrating the characteristic slope for cobalt-containing alloys.

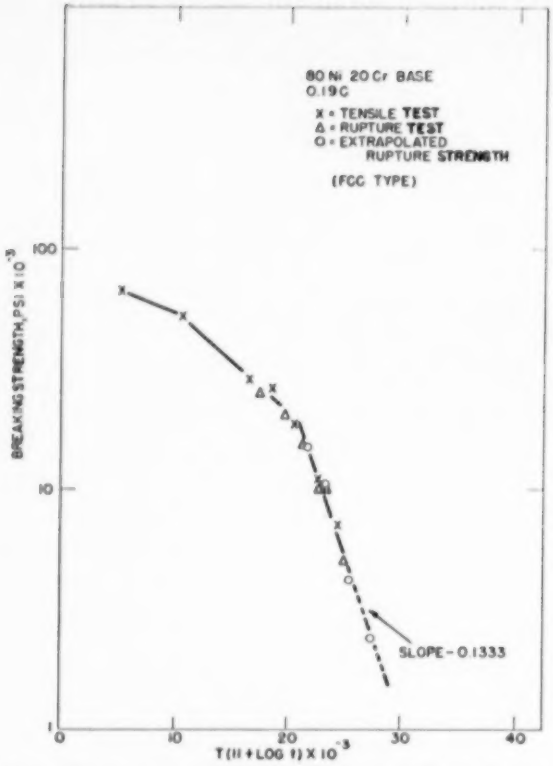

Fig. 7—Parametric plot of data for the 80 pct Ni-20 pct Cr base alloy of the face-centered cubic solid solution type, illustrating the characteristic slope for cobalt-free alloys.

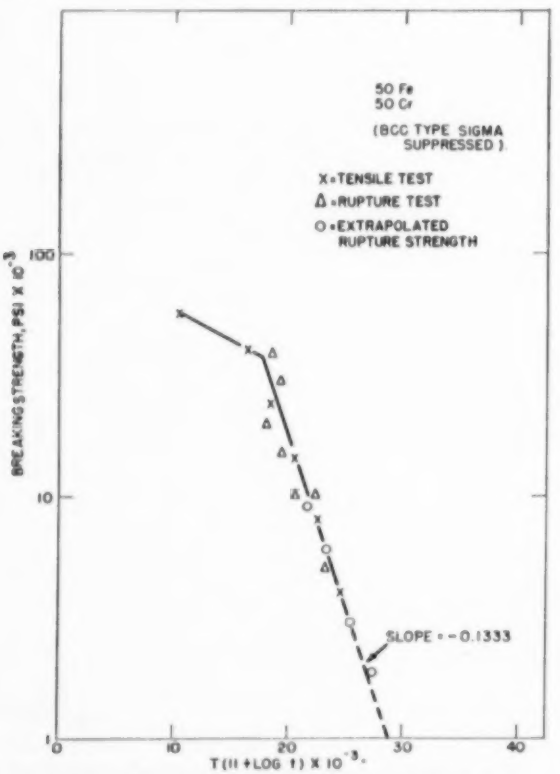

Fig. 8—Parametric plot of data for the 50 pct Fe-50 pct Cr base alloy of the body-centered cubic supersaturated solid solution type.

single parameter number which includes different combinations of time and temperature causing varied properties.

Thus, the parametric plots for supersaturated solid solutions of age-hardening alloys varied from a well-defined single line to a band of strength values. For specimens which fractured at values of the parameter at times and temperatures such that no measurable age-hardening occurred, a single-line parametric plot resulted. If the times and temperatures of tests were such that significant age-hardening occurred, a band of strength values was found, depending upon the amount of hardening. Data from different types of alloys exhibited certain characteristic behaviors.

The binary 50 pct Fe-50 pct Cr body-centered cubic alloy represents one type of behavior. In this alloy σ phase exists up to 1500°F under equilibrium conditions, but there was no evidence of σ phase

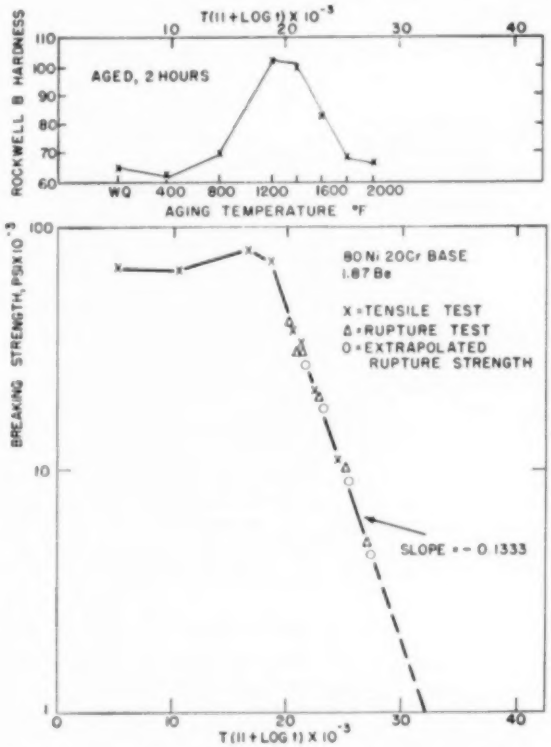

Fig. 9—Hardness data and parametric plot of data for the 1.87 pct Be addition to the 80 pct Ni-20 pct Cr base alloy, illustrating the results for an alloy which age hardens to a maximum at temperatures below 1500°F.

revealed by metallographic examination of specimens in the cast or quenched condition or in stress-rupture specimens after 1000 hr at either 1200° or 1500°F. Thus, this supersaturated solid solution alloy did not transform during the tests and the parametric plot of test data shown in Fig. 8 is a single-line characteristic of solid solutions, although there is some spread of data. In other experiments it was found that σ did occur in the samples of this alloy cold-worked 60 to 70 pct at room temperature and heat-treated to cause age hardening. Since it is known that age-hardened materials are stronger than the supersaturated solutions at temperatures where the precipitated phase is stable, an even

wider spread of data than that shown in Fig. 8 would be expected for results of tests of this alloy under all possible structural conditions.

For some age-hardenable alloys such as shown in Fig. 9, data from both long and short-time tests at high temperatures could be represented by a single line at high parameter values. Based on the hardness-temperature curves in Fig. 9, this Ni-Cr-Be alloy did age-harden in the temperature range of 1200° to 1400°F. Data points from stress-rupture tests and tensile tests, however, showed no measurable deviations from a single line, probably because none of these tests were carried out under conditions of time and temperature associated with measurable age hardening. When tested under conditions promoting maximum age hardening below the straight-line part of the curve, a wide band could be obtained, as was experimentally determined for several alloys of this type.

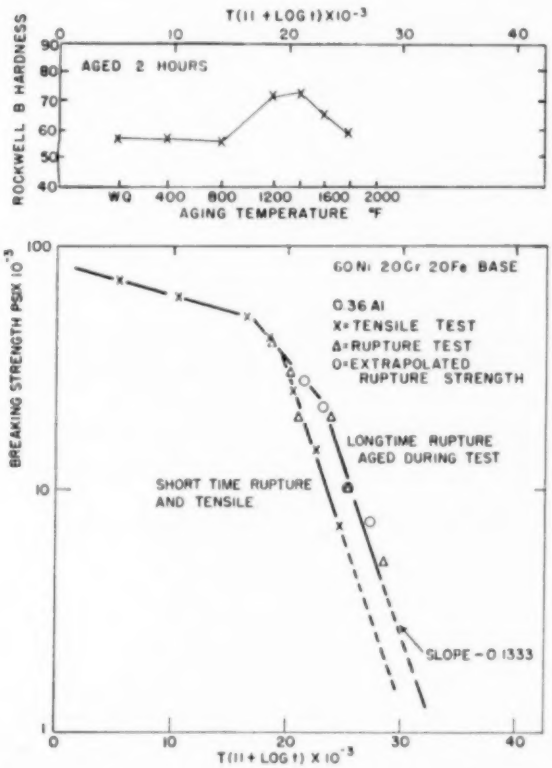

Fig. 10—Hardness data and parametric plot for the 0.36 pct Al addition to the 60 pct Ni-20 pct Cr-20 pct Fe base alloy, illustrating the band formed for an alloy which age hardens to a maximum near 1500°F.

For other age-hardenable alloys for which maximum hardening occurred near 1500°F, data from long-time tests causing age hardening did not conform to the straight line which fitted data from short-time tests at high parameter values. Data for a Ni-Cr-Fe alloy of this type is shown in the parametric plot in Fig. 10. For this alloy, the long-time (>100 hr) rupture values for 1200° and 1500°F fall along a single line of characteristic slope, while the tensile test data and short-time rupture data at 1200°and 1500°F form a single parallel line at a lower strength level.

These results indicate that data for age-hardening

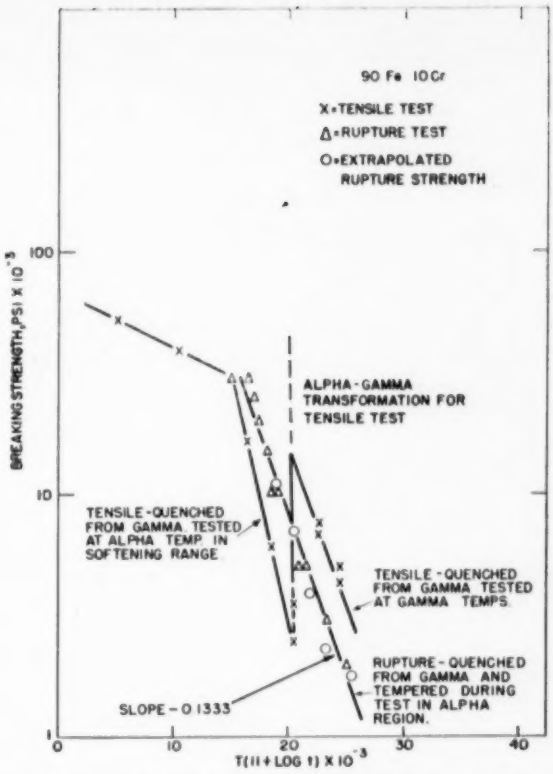

Fig. 11—Parametric plot of data for the 90 pct Fe-10 pct Cr base alloy, illustrating the effects of an allotropic transformation.

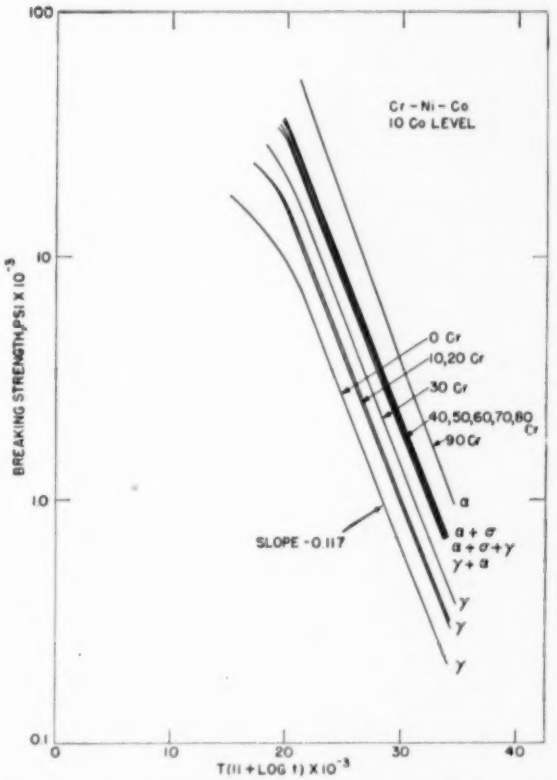

Fig. 12—Parametric plots of data for Cr-Ni-Co alloys with 10 pct Co constant, illustrating the effects of stable multiple-phase alloys.

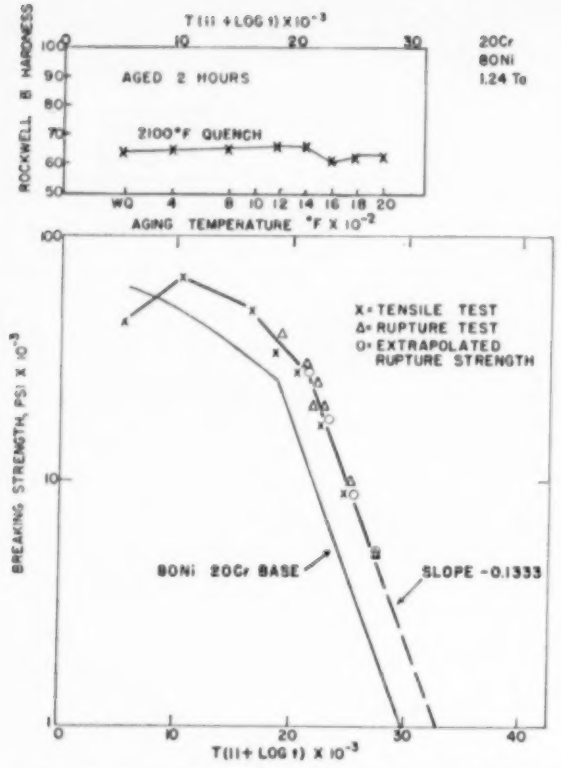

Fig. 13—Hardness data and parametric plot for data from alloy with 1.24 pct Ta addition to 80 pct Ni-20 pct Cr base.

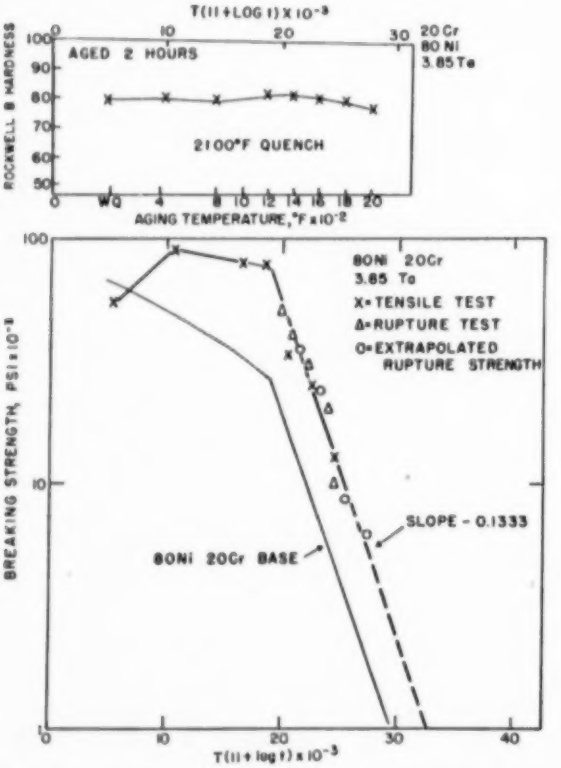

Fig. 14—Hardness data and parametric plot for data from alloy with 3.85 pct Ta addition to 80 pct Ni-20 pct Cr base.

alloys may form a band of strength values for each of the parameter values depending upon the prior metallurgical history and the effect of time and strain upon the strength at the testing temperature. The possible ramifications are extensive. The exact pattern of the data for various temperatures within the parameter band is not definite. It is believed that more complete strength data for different testing temperatures might form families of curves with the extremes of strength values falling on parallel lines. It is significant, however, that two parallel straight lines of characteristic slope‡ can be used to approximate the limiting strengths for the times, temperatures, and, in turn, the parameter numbers used in this analysis. This convenience will be used for determining the range of strengths of the alloys studied.

‡ 0.117 for cobalt-containing alloys; −0.133 for cobalt-free alloys.

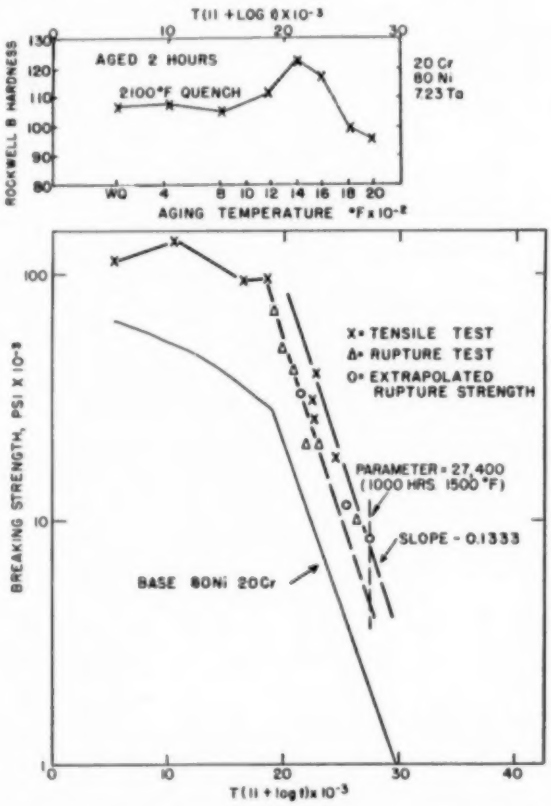

Fig. 15—Hardness data parametric plot for data from alloy with 7.23 pct Ta addition to 80 pct Ni-20 pct Cr base.

Allotropic Transformations: Iron-rich and cobalt-rich alloys of the Fe-Cr-Co-Ni system undergo allotropic changes on heating. For alloys where a single parameter number covers a range of temperature and time including both allotropic modifications, the parametric plot may consist of a broad band rather than a single line, depending upon the relative properties and amounts of the phases. A 1000-hr test at 755°F of a specimen of ferritic iron would result in a strength different from that of a tensile test (0.1 hr) of austenitic iron at 1800°F, although both tests correspond to a parameter number of 22,600. Data from specimens of an Fe-Cr alloy

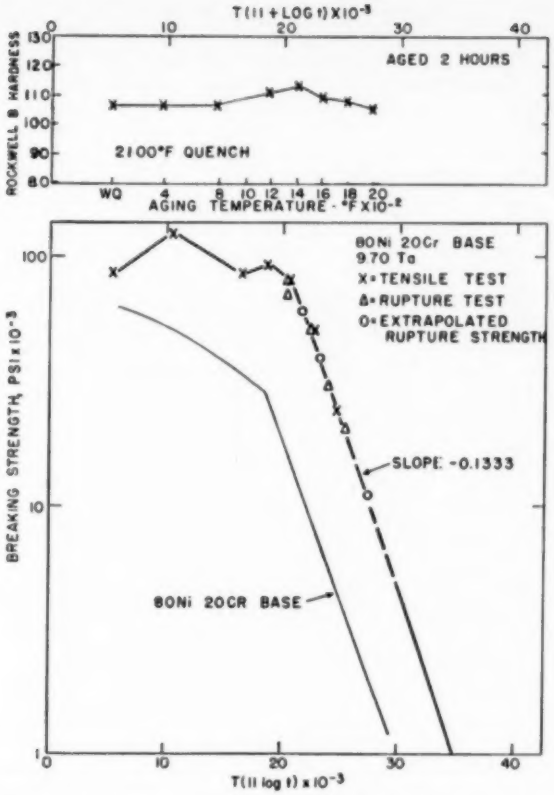

Fig. 16—Hardness data and parametric plot for data from alloy with 9.70 pct Ta addition to 80 pct Ni-20 pct Cr base.

which undergoes an allotropic transformation within the range of testing temperatures are plotted in Fig. 11. The line for points corresponding to the high temperature phase is at a higher strength than the line for points corresponding to the low temperature phase. When allotropic transformation of a martensitic type occurs, the parametric plot can be further complicated by nonequilibrium conditions. This alloy was quenched from 2100°F and was subsequently tempered during testing at elevated temperatures. Under these conditions it became stronger, which is the expected behavior.[6]

Multiple Phases and Crystal Structure: Single-line parametric plots were obtained for data from stable multiple-phase alloys. In Fig. 12, single-line parametric plots are reconstructed in composite for the purpose of comparing the strengths of alloys in the Cr-Co-Ni system consisting of α, γ, α-γ, and α-γ-σ phases with 10 pct Co and varying chromium contents. The strength of these alloys increases with increasing chromium contents and the appearance of a second phase. The γ solid solution alloys with less than 40 pct Cr are relatively weak. The stronger alloys with 40 pct Cr or more (Fig. 12) contain the more complex σ or α chromium phases and are brittle at low temperatures.

Single Additions of Incongruous Elements: With progressively increasing amounts of additions of a single incongruous element to a given solid-solution alloy, the following three characteristic types of alloys were recognized by relating microstructure, parametric plots and age-hardening data: 1—single-phase alloys, 2—supersaturated solid solutions which age hardened, and 3—multiphase alloys at all testing temperatures. This behavior is shown in Figs. 13 through 16 for tantalum additions to 80 pct Ni-20 pct Cr and can be rationalized as follows:

1—For small tantalum additions, the hardness of the base was increased, but no large change in hardness occurred during aging tests. The data for this type of alloy will form a single line on the parametric plots as shown in Figs. 13 and 14.

2—When the amount of incongruous addition was increased and maximum age hardening occurred near 1500°F, the corresponding strength data on a parametric plot developed a band characteristic of age-hardening alloys which age at high temperatures as shown in Fig. 15.

3—As the amount of incongruous addition was increased further beyond the optimum addition so that the age-hardening peak in the hardness-temperature plot became smaller, or disappeared, the corresponding strength data on parametric plots formed a single line in the high temperature range, as shown in Fig. 16, similar to Fig. 13.

Fig. 17—1000 hr, 1500°F rupture strengths (1000 psi) of Fe-Ni-Cr-Co base alloys determined from parametric plots. 1500°F phase boundaries superimposed.

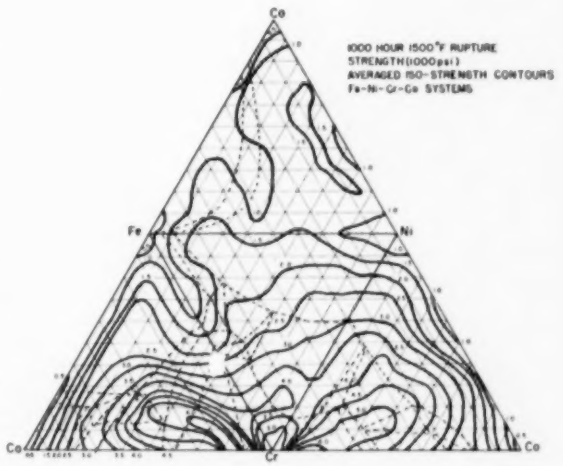

Fig. 18—Iso-strength contours for Fe-Ni-Cr-Co ternary systems indicating 1000 hr, 1500°F rupture strength (1000 psi).

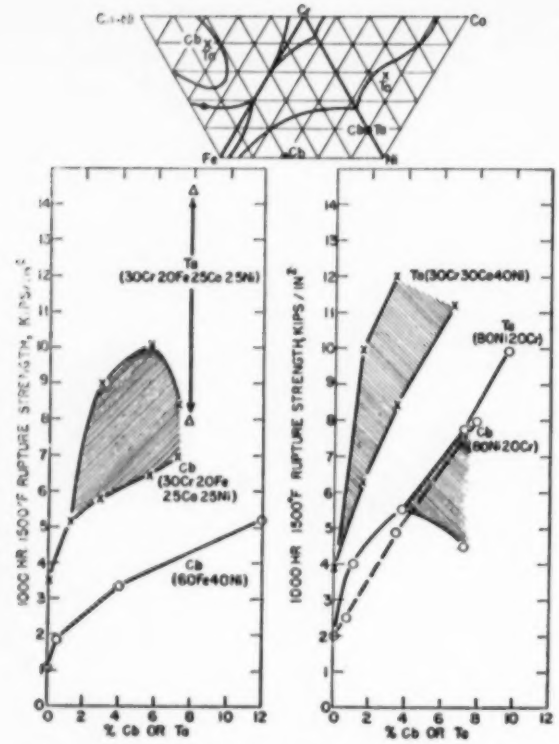

Fig. 19—Effect of single additions of columbium or tantalum on the 1000 hr, 1500°F rupture strength of selected base alloys. Location of base alloys with respect to 1500°F solubility limits indicated on phase isotherms at top.

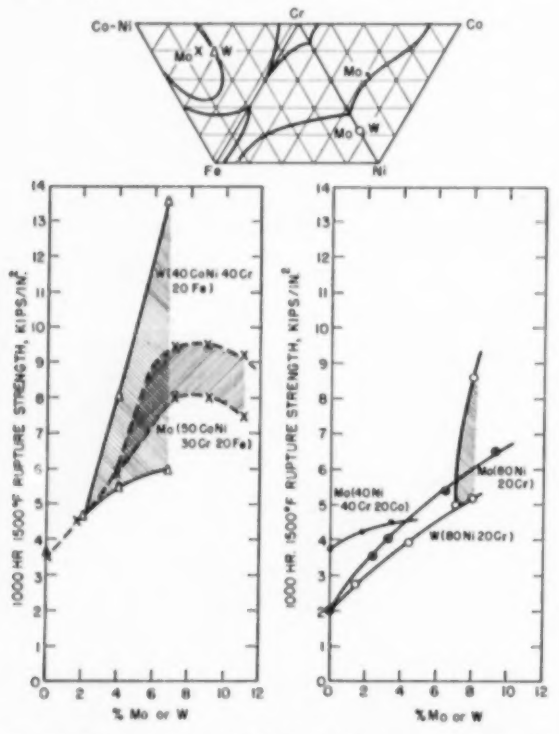

Fig. 20—Effect of single additions of molybdenum or tungsten on the 1000 hr, 1500°F rupture strength of selected base alloys. Location of base alloys with respect to 1500°F solubility limits indicated on phase isotherms at top.

Comparative Rupture Strength

From the parametric plots, a value of 1000 hr, 1500°F rupture strength (P = 27,400) was determined for each alloy. These values of strength are used throughout as a basis for comparing the high temperature properties of the alloys, in order to develop some principles of alloy design and not merely to report property data.

Fe-Ni-Cr-Co Alloy Bases: Data for the strength of alloy bases determined from parametric plots are shown in Fig. 17 on ternary plots of the Ni-Cr-Fe, Ni-Cr-Co, and Fe-Ni-Co systems. Where available, 1500°F equilibrium phase boundaries are indicated based on refs. 7 through 13. Fig. 18 is an iso-strength plot based on the averaged values from three intersecting plots of strength as a function of the percentages of two of the elements for a constant amount of the third element. Similar data for quaternary alloys are not included since the data for the ternary alloys adequately illustrates the principles involved. The strongest alloys in Fig. 17 could not be investigated in detail because alloys with large amounts of σ are too brittle to test accurately.

Incongruous Additions: For alloys containing incongruous additions which resulted in parametric plots having a band of strength values, two parallel lines, as shown in Fig. 15, were drawn to approximate the range of available strength from the unaged to the fully-hardened conditions. From these plots, two values of strength were obtained at the single parameter number of 27,400. It should be emphasized that these two values do not represent scatter but do represent the variability of strength resulting from heat treatment or changes in structure.

The 1000-hr, 1500°F strengths obtained from additions of tantalum and columbium are plotted in Fig. 19 as a function of composition, together with the ternary diagrams indicating the base alloy compositions. Where a single-strength value is indicated for a given composition, a single-line parametric plot was obtained. For alloys where a range of strength values is indicated by shading, a parametric plot with a band of strength values was obtained. In each case, the data represent lines fitted to the experimental points, and not experimental scatter. It should also be noted that a given addition element has very different effects on different base alloys, as illustrated in Fig. 19 by comparing the columbium curves for 60 pct Fe-40 pct Ni and 30 pct Cr-20 pct Fe-25 pct Co-25 pct Ni. These observations suggest an advantage of using a supersaturated alloy base as compared with an unsaturated alloy base. It should be noted also that there is a question as to whether these alloys were solution treated to obtain maximum solubility.

The range of strength obtained from the parametric plots are plotted against the percentage of molybdenum or tungsten additions in Fig. 20, together with ternary diagrams showing the location of the base alloys. Three characteristic types of plots are shown as follows:

1—For all molybdenum additions to the 80 pct Ni-20 pct Cr base, single strength values were obtained.

2—In the case of tungsten additions to the 80 pct Ni-20 pct Cr base, it was evidently soluble in the base up to about 7 atomic pct, forming a single strength-composition line. Near the solubility limit, the plot branches into a band indicative of age hardening.

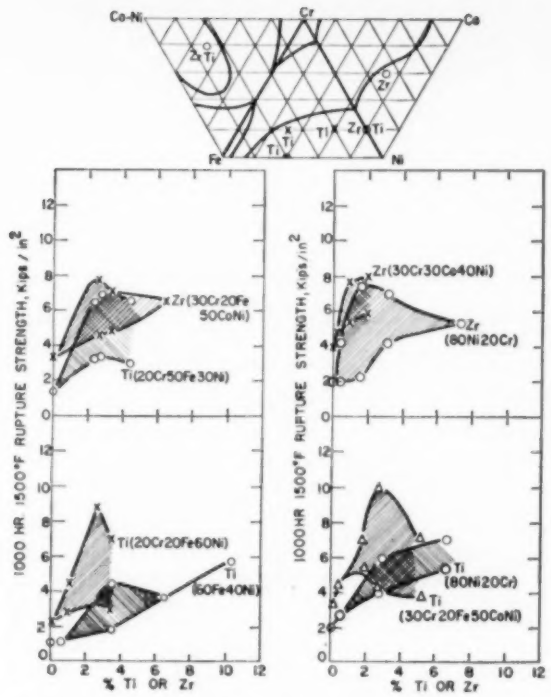

Fig. 21—Effect of single additions of titanium or zirconium on the 1000 hr, 1500°F rupture strength of selected base alloys. Location of base alloys with respect to 1500°F solubility limits indicated on phase isotherms at top.

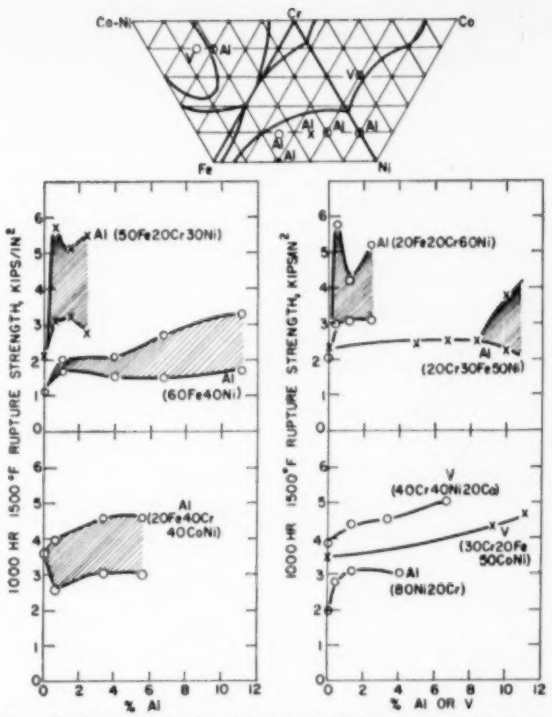

Fig. 22—Effect of single additions of aluminum or vanadium on the 1000 hr, 1500°F rupture strength of selected base alloys. Location of base alloys with respect to 1500°F solubility limits indicated on phase isotherms at top.

3—For molybdenum additions to the 40 pct Ni-40 pct Cr-20 pct Co base the alloy is probably a stable two-phase structure, but the data did not produce any measurable deviations from single strength values characteristic of age hardening. There is a question as to whether or not these alloys

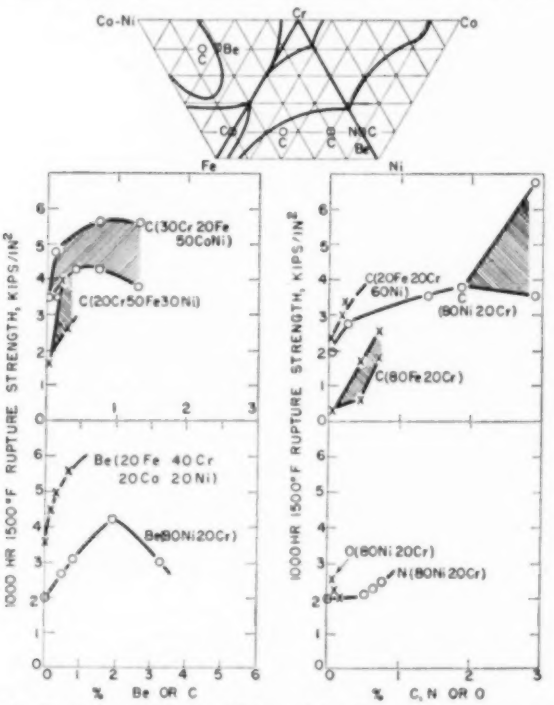

Fig. 23—Effect of single additions of beryllium, carbon, nitrogen, or oxygen on the 1000 hr, 1500°F rupture strength of selected base alloys. Location of base alloys with respect to 1500°F solubility limits indicated on phase isotherms at top.

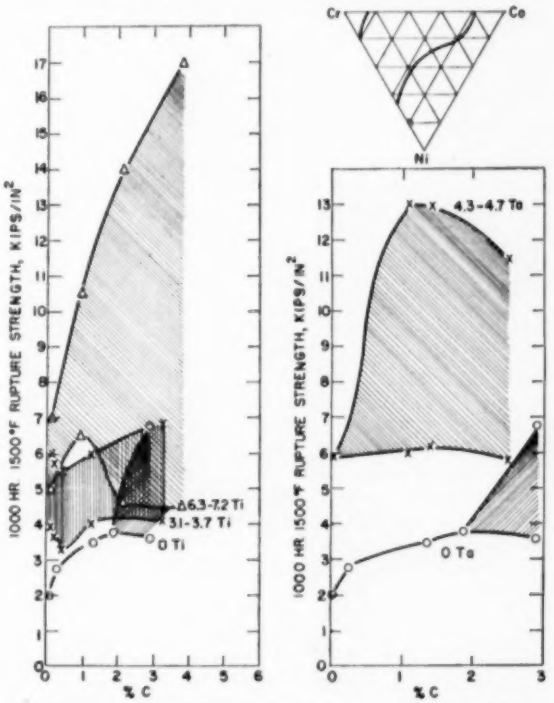

Fig. 24—Effect of additions of carbon and tantalum or titanium on the 1000 hr, 1500°F rupture strength of 80 pct Ni-20 pct Cr base alloy. Location of base alloy with respect to 1500°F solubility limit indicated on phase isotherm at top.

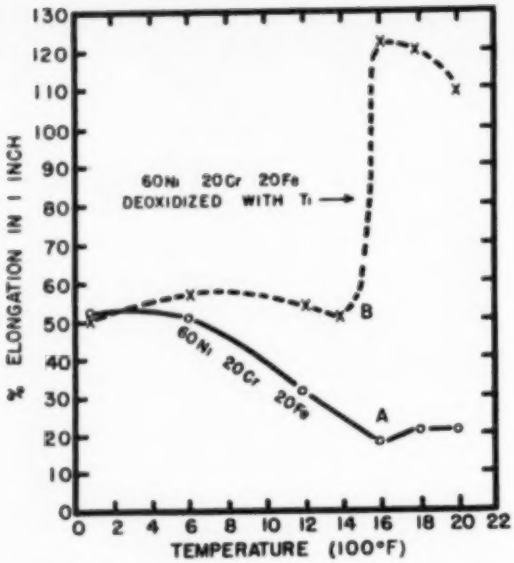

Fig. 25—Elongation data from tensile tests of the 60 pct Ni-20 pct Cr-20 pct Fe base alloy as a function of temperature, illustrating the improved ductility obtained from deoxidation with titanium.

were properly solution treated—2100°F is not sufficiently high a temperature to obtain maximum solution for all these alloys. Both of these elements, molybdenum and tungsten, are similar, but are different in atomic characteristics from the base elements.

The strengths resulting from titanium or zirconium additions to various base alloys are shown in Fig. 21 and again with reference ternary diagrams. These alloys age hardened and the extent is indicated by the spread in parametric plots. It is somewhat less than for tantalum, tungsten, or molybdenum.

The effect of aluminum or vanadium on the 1000-hr 1500°F rupture strength of selected bases is plotted in Fig. 22. For the limited amount of data available for vanadium, the effect of this element is very small as might be expected because of its similarity to chromium (Table III). In the case of aluminum there is a pronounced age-hardening effect for two of the base alloys, 50 pct Fe-20 pct Cr-30 pct Ni and 20 pct Fe-20 pct Cr-60 pct Ni, but in both cases the alloy contained small amounts of carbon. Three other aluminum additions produced small age-hardening effects. In the case of the 20 pct Fe-40 pct Cr-20 pct Co-20 pct Ni base, the minimum strength obtained from the age-hardening alloys was lower than that for the alloy base. This decrease suggests that aluminum had a purifying effect on the base material which caused the strength of the alloy to be lower than that of the base. Apparently, this effect is similar to that reported by Lacy and Gensamer for chromium added to iron.[14]

The effects of single additions of beryllium, carbon, nitrogen, or oxygen on various bases are shown in Fig. 23. The data for alloys of oxygen and nitrogen are somewhat limited; however, for nitrogen additions the strength obtained for various compositions extrapolated to a lower base value than that obtained for the base itself. Oxygen appears to have a large strengthening effect in very small amounts which then decreases with increasing additions. The difficulty of accurately analyzing for gases in metals should be recognized in considering these results.

Fig. 24 shows the effects of simultaneous additions of carbon with titanium or tantalum on the strength of the 80 pct Ni-20 pct Cr base. Carbon, in this case, is combined with strong carbide formers, titanium or tantalum, which produces large age-hardening effects due to the precipitation of these carbides. The strong interaction effects resulting from this carbide formation would suggest that the effects of these simultaneous additions would be considerably different from the sum of the effects of each element independently.

Ductility: The percentage of elongation at fracture in tensile tests is plotted in Fig. 25 (curve *A*) as a function of temperature for an Fe-Ni-Cr alloy. This plot is typical of those found in the Fe-Cr-Co-Ni face-centered cubic alloys with a minimum elongation in the high temperature range related to the transition from transgranular to intergranular fracture. The minimum does not occur in data from alloys thoroughly deoxidized with hydrogen and 2 pct Ti[15] as illustrated in curve *B* of Fig. 25. Above 1200°F, where fracture even in short-time tests was intergranular, the ductility of these alloys becomes low except at very high testing temperatures. For certain alloys, such as Ni-Cr binary alloys and the Fe-Ni-Cr alloys, the minimum point in the elongation curve moves toward lower ductility levels and higher temperature levels with increasing chromium composition, and it is believed to follow approximately with the recrystallization temperature. In comparison, for alloys such as 90 pct Fe-10 pct Cr which undergo allotropic changes, the highest elongation occurred at temperatures corresponding to the allotropic transformation region. Likewise, at temperatures below the minimum where the fracture is transgranular the ductility of Fe-Cr-Co-Ni face-centered cubic solutions tended to be very high near the saturation limit in chromium-rich alloys. Precipitation hardening alloys showed low ductility at a temperature causing rapid precipitation near the transgranular-to-intergranular transition and below the recrystallization temperature.

Discussion of Results

The variation in strength of alloys is believed to be related to the melting temperature, the crystal structure, and other alloying characteristics. For solid solutions relative atomic size, relative valency, and relative compressibility are important. For multiple-phase alloys, phase interaction (for example, coherency), together with the relative strengths, size, shape, and distribution of the phases should be considered. These factors, known to affect the strength of alloys, are used to rationalize the strengths of the materials studied.

Melting Point: The greater the difference between the testing temperature and the melting temperature (where the interatomic bond of the solid crystal is thermally broken) the stronger an alloy should be.[16]

By considering the relative strengths of the Fe-Cr-Co-Ni alloys at a constant fraction of the absolute melting temperature (a homologous temperature), differences in melting temperature (the melting point effect) are equalized to a first approximation.

From a plot of the liquidus temperature for these systems shown in Fig. 26, the temperatures cor-

responding to 0.6 of the absolute melting temperature were calculated for each alloy, and the 1000-hr rupture strength at these temperatures determined from its parameter plot. The resulting averaged iso-strength contours are shown in Fig. 27. The contours of Fig. 27 can now be considered on the basis of the other factors affecting strength.

Crystal Structure: This factor is probably related to the ease of deformation and can be considered on the basis of the number of possible slip systems (a stable function of the slip direction, since the slip plane may vary). On the basis of the number of possible slip directions, increasing hardness should occur in the order given in Table IV, assuming equality of all other factors.

Westbrook[18] has shown that, based on extrapolated hardness at 0°K within experimental error, the differences in strength between pure nickel, iron, chromium, and cobalt due to crystal structure should be small, with the complex σ phase having a strength possibly several times greater. Experimentally, from Fig. 27, cobalt, iron, nickel, and chromium have similar strengths ranging from about 500 to 1300 psi. The complex Cr-Co σ structure is associated with two peaks at strengths of 8000 to 9000 psi.

Solid Solution Strengthening: Fundamental alloying characterististics of solid solutions are believed to be related to:

1—Relative Atomic Size of Constituents: Qualitatively, at least, larger differences in atom size, or more specifically, larger percentage of changes in lattice parameter per atomic percentage of solute addition, cause larger strengthening effects.[16, 17-19] Solutes which decrease the lattice parameter appear to be more effective strengtheners than those which increase it.[20]

2—Relative Compressibility of the Atoms: The smaller the compressibility of the solute atom with respect to the solvent atom, the greater the strain introduced in the lattice by solution and the strengthening is greater. The effect is probably a function of whether the change in lattice parameter is positive or negative. A large negative change in lattice parameter and a large negative difference in compressibility between the solvent and solute would have greatest effects.[21, 22]

Each of the factors (atomic size and compressibility) vary periodically when plotted against the atomic number of the pure element. It is interesting to note that the solution-hardening effect can also be related periodically to the atomic number of the solute element.[22]

In the Fe-Ni-Co system in Fig. 27, except for a small region near iron and extending toward cobalt, the alloys are entirely γ with the existing α near its maximum temperature (i.e., by raising the homologous fraction to 0.7 α would disappear), and for all other factors listed in Table II, the elements are very similar. Thus, a flat strength plateau is reasonable in this system.

Table IV. Order of Increasing Hardness

No.	Structure	No. of Slip Directions
1.	Face-centered cubic	6
2.	Body-centered cubic	4
3.	Hexagonal close-packed, c/a 1.6	3
4.	Hexagonal close-packed, c/a 1.9	3
5.	Other complex	3

The reason for the lack of a high peak in the equilibrium σ region of the Fe-Cr system in Fig. 27 is believed to be a result of the fact that iron and chromium form a nearly complete solid solution at this temperature (except for a small region of σ under equilibrium conditions at 50/50 ratio of Fe-Cr which was suppressed) and thus approach Fe-Ni-Co in character.

The Cr-Co maximum in Fig. 27 is associated with the σ phase existing at very high temperatures and, also, because chromium and cobalt are different with respect to the factors affecting solution hardening listed in Table III. Chromium is also an active element and combines readily with oxygen and nitrogen to form stable compounds which are difficult to reduce and, thus, impurities remain. Therefore, some hardening would be expected from impurities which represent an unisolated alloying factor.

The maximum strength in the Cr-Ni system in Fig. 27 is believed to be due to the alloying effect, since nickel and chromium are the most different of the metals considered in Table III, with limited mutual solubility.

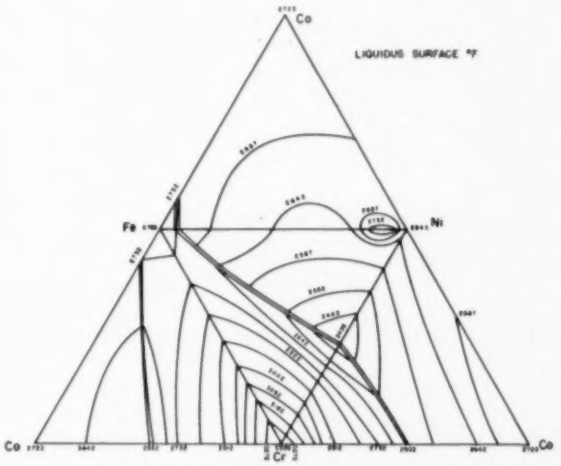

Fig. 26—Isothermal contours of liquid surface for ternary Fe-Ni-Cr-Co systems based on data of Kase,[9] Pugh and Nisbet,[11] and Koster.[12] Eutectic troughs indicated by double lines.

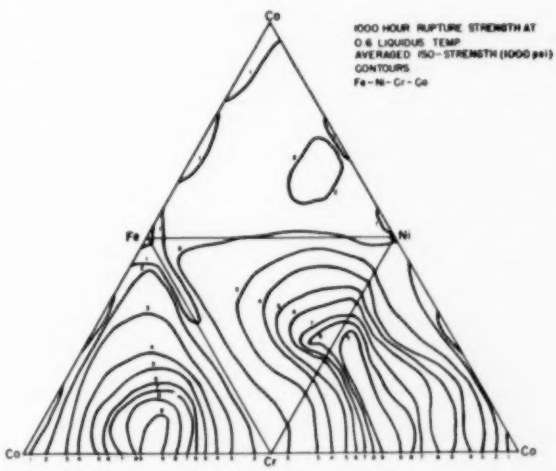

Fig. 27—Iso-strength contours for Fe-Ni-Cr-Co ternary systems indicating 1000 hr rupture strength at 0.6 liquidus temperature (°K) from parametric plots.

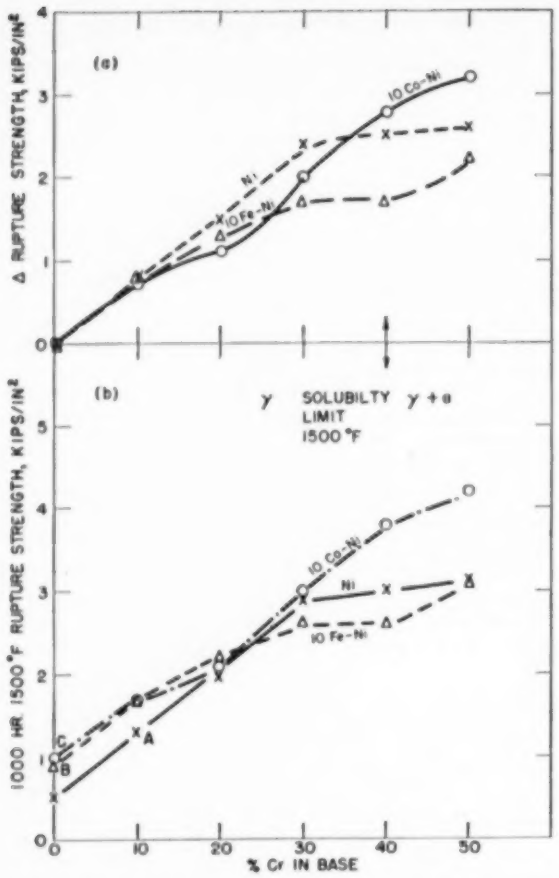

Fig. 28—Effect of chromium additions on the 1000 hr, 1500°F rupture strength of nickel with and without 10 pct Fe or 10 pct Co.

The factors controlling solution hardening also may be those which affect the limit of solid solubility. Solubility limits at 1500°F are approximately as follows:

Ni-Co, Complete face-centered cubic
Ni-Fe, Nearly complete face-centered cubic, small amount body-centered cubic Fe
Ni-Cr, 35 pct Cr face-centered cubic
Co-Cr, 18 pct Cr face-centered cubic
Cr-Fe, Nearly complete body-centered cubic, small amount of σ
Co-Fe, 22 pct Fe face-centered cubic.

According to these data, chromium is the element least soluble in nickel and consequently should be the most effective binary hardener. The solubility of chromium in cobalt is half of the solubility of chromium in nickel. Consistent with the concept that more limited solubility leads to more extensive solution hardening, in the presence of cobalt the strengthening of nickel due to chromium should increase. Iron, however, is extensively soluble in chromium, nickel, and cobalt at 1500°F. Larger amounts of more potent hardeners such as chromium or cobalt should be required in nickel to reach a given strength level with iron present than when iron is absent. This concept is consistent with the findings that alloy additions are not independent of one another, but that there are interactions between solutes as well as between the solvent and solute, as illustrated in Fig. 28. Chromium is the most effective hardener of nickel (compare point *A* with points *B* and *C*). The strengths of the ternary Ni-Cr-Fe alloys with 10 pct Fe fall below the strengths of the binary Ni-Cr alloys of comparable alloy content. The strengths of the Ni-Cr-Co alloys with 10 pct Co reach values one-third higher than the Ni-Cr or Ni-Cr-Fe alloys. The strengths of these base alloys are least different from each other at the 20 pct Cr level found in many commercial alloys. This interaction effect indicates that when iron is used in large amounts compensatory additions of chromium and/or cobalt are necessary to maintain a given strength.

The interaction effects are more significant for the most effective addition elements and will be discussed in subsequent sections.

Relative Strengthening Effects of Incongruous Additions: For multiphase alloys, all of the above factors for solid solutions will apply to determine the inherent strength of each phase. Relative strengths, amounts, and distribution and condition of the phases will determine the strength of the alloy and will be modified by temperature and strain history, as they control the several factors such as strain aging, strain hardening, allotropic transformation, precipitation hardening, recovery, recrystallization and grain size.[17, 28-29]

The strengthening of the various incongruous additions was obtained by subtracting the base strength from the strengths of the alloys containing incongruous elements. These results reflect the general relative strengthening effects of the various additions.¶

¶ It is clear that the experimental work did not include a sufficiently wide composition range of all incongruous alloys for their maximum effects to be considered comparable. In addition, the order of strengthening when compared on the basis of the maximum effects (regardless of amount) is not the same as that when the comparative strength is considered at low concentrations and at constant amounts. It is also believed that the strengthening effect reaches a maximum and usually falls off at higher concentrations of incongruous elements.

From these data on the basis of comparing maximum effects the decreasing order of effectiveness appears to be as follows: 1—tantalum and tungsten, 2—columbium and molybdenum, 3—zirconium and titanium, 4—carbon, 5—aluminum which has been treated with carbon, 6—beryllium and aluminum, 7—vanadium, and 8—oxygen and nitrogen. The greatest strengthening effects come from the *high melting* incongruous additions, tungsten, tantalum, columbium, and molybdenum. Among these four, the element with the *largest atomic diameter*, tantalum, is most effective. The next most effective additions are titanium and zirconium which are widely different from the base alloy in terms of atomic diameter, but similar in terms of melting point. This order suggests that the most important characteristic, aside from *melting point*, is a difference in *atomic diameter*. Beryllium which has a lower melting point than the base elements is the next in order of effectiveness and aluminum which has the lowest melting point and vanadium which has the smallest difference in atomic diameter are least effective. The effects of carbon, nitrogen, and oxygen are somewhat uncertain because deoxidizing effects partly mask the true strengthening and the data are limited. Also, they are probably interstitial and exhibit characteristics different from the substitutional incongruous elements. The results on simultaneous additions of carbon with titanium or tantalum clearly emphasize the complex effects

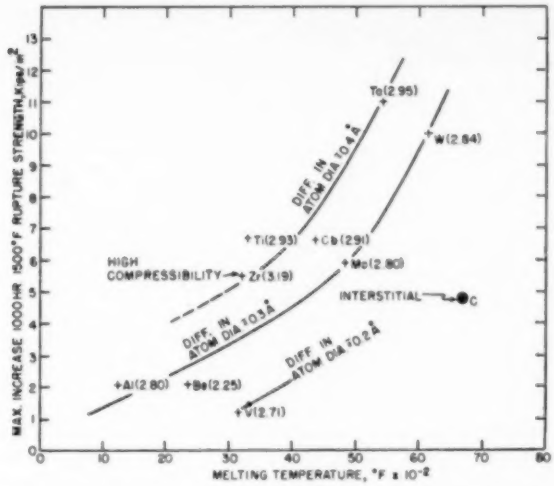

Fig. 29—Correlation between the maximum increase in 1000 hr, 1500°F rupture strength due to single addition of incongruous elements to selected base alloys with the melting temperature and atomic diameter of the incongruous element.

possible from multiple alloy additions found in commercial alloys. They also suggest that the best commercial alloys may be those where the interaction effects are most pronounced. The multiple incongruous elements added should have high melting points, high compound forming tendencies and low solubility in each other as well as low solubilities in the base elements, and the compounds formed should be very stable.

In Fig. 29, the maximum strengthening effect of each incongruous element obtained in these tests is plotted against its melting point. The data points are connected according to the difference in atomic diameter between the incongruous element and the base (except for the interstitial element carbon, for which the atomic diameter is not certain). This family of curves clearly indicates the strengthening effects of high melting elements with large differences in atomic size. Zirconium has a somewhat lower strengthening effect than would be predicted from its melting point or atomic diameter, probably because of its high compressibility. The effect of valence is not apparent, probably because most of these elements are transitions or because valence difference for these elements is a less important factor in hardening.

The significance of the relationship in Fig. 29 may be further clarified by reference to studies of magnesium alloy systems, where the phase diagrams are well documented. Fig. 30 is based on magnesium alloy binary systems in which the terminal magnesium-rich solid solution is in equilibrium with intermetallic compounds forming directly from the liquid. For these systems, the melting temperature of the intermetallic compound is related directly to the melting temperature of the addition element (with the exceptions Mg_2Sn and Mg_2Cu). It has been shown[29] that the higher melting point compounds (and from Fig. 30 high melting point alloying elements) are associated with high eutectic temperatures, low eutectic compositions, and low maximum solubility limits. Thus, the results in Fig. 29 suggest that the addition of higher melting point elements results in the formation of higher melting point compounds which are more effective hardeners at 1500°F than lower melting point elements which form lower melting point compounds.

Alloying Principles

The complex alloys used at high temperatures may be considered as consisting of a solid solution matrix or base alloy to which incongruous elements are added to saturate and strengthen the solution and to form second phases.

In this paper, the strength of the base alloys has been explained in terms of the relative solution-hardening effects of solute elements on the strength of the solvent element. It has been shown that the largest strengthening effect is obtained by the addition of solute elements which are least soluble in the solvent element and most unlike it with respect to atomic diameter, compressibility, and crystal structure. Supplementary strengthening results from interaction effects due to combinations of solute elements which are unlike each other and emphasize these mutual differences with the solvent element. Addition elements, on the other hand, which are completely soluble with all other constituent elements at high temperatures and are intermediate among them in atomic characteristics, tend to decrease the strengthening characteristics of more potent hardeners.

The crystal structure is an important factor associated with the differences in strength of alloys as it is related to the ease of deformation and to allotropic transformations. Strong alloys result from complex crystal structures which are stable at operating temperatures.

Other things being equal, the strength of an alloy is significantly influenced by the testing temperature in terms of the fraction of the absolute melting point. A careful compromise in composition is usually necessary since alloy additions usually lower the melting temperature.

The largest strengthening effects were obtained from incongruous elements with high melting points and large differences from the base elements with respect to atomic diameter. These elements have low compressibility and tend to form compound-

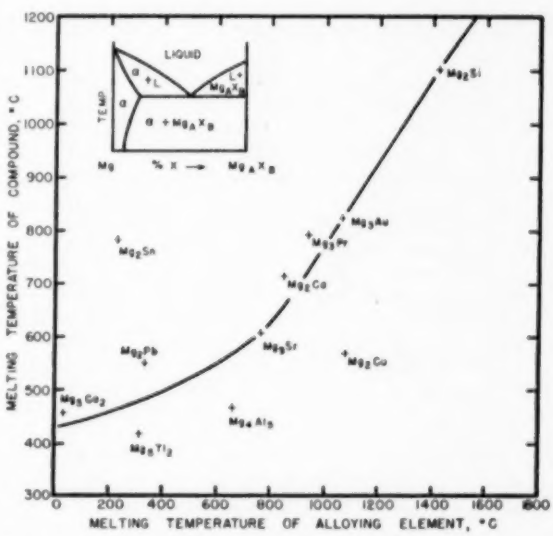

Fig. 30—Correlation between the melting temperature of magnesium compounds of the type indicated in the phase diagram and the melting temperature of the alloying elements.

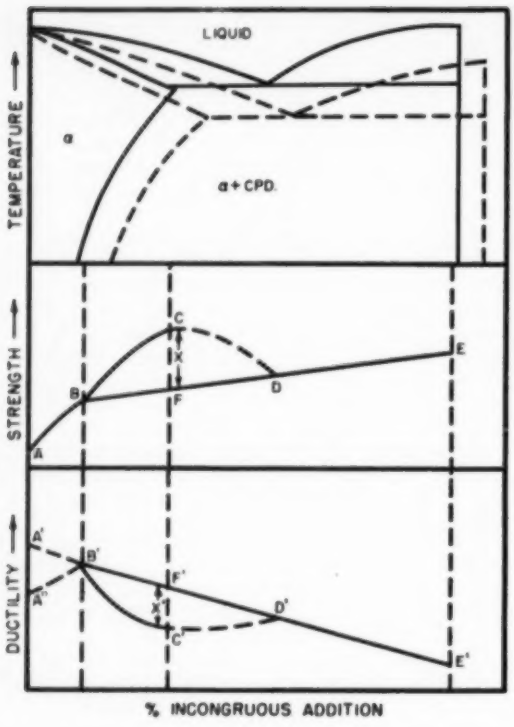

Fig. 31—Schematic relationships between the phase diagrams, strength, and ductility of base alloys with incongruous additions.

type phases with the base metals. Although pertinent phase diagrams are not available for discussion, it appears that the effective incongruous elements are relatively insoluble in the base alloys and small additions serve to complete the saturation of the matrix phase with a more prominent solution-hardening effect than that associated with any of the base elements at saturation compositions. In addition, these elements form supplementary phases which produce age hardening. The most effective age-hardening temperatures were higher for alloys having higher melting incongruous elements which maintained their hardening effects at the test temperature as compared to lower melting incongruous elements whose structures usually overaged and softened at the test temperature. Alloys which age harden at temperatures well above the test temperature exhibit improved ductility as compared to those which age harden at the test temperature. The strengthening effect of some incongruous elements passed through a maximum as a function of composition in a manner which suggests that the presence of insoluble stable second phases is not necessarily desirable for age-hardening-type alloys. (The ductility of these "overalloyed" materials is very low and this brittleness may result in an apparent low strength.) Maximum strength may occur near the maximum limit of solubility and this suggests the advantages of strengthening by age hardening as compared to the strengthening associated with equilibrium multiple phases. The phenomenom emphasizes the apparent effectiveness of small optimum amounts of incongruous elements within the maximum solid solubility limit as compared to large additions producing massive second phases. The latter may be considered as overalloying. These considerations lead to generalizations relating strength, ductility, and composition presented in Fig. 31.

In Fig. 31a, the solid line represents the constitution diagram formed with a high melting element as compared to the dashed lines which represent the diagram formed with a low melting element. Fig. 31b is based on the ideal relationships of Mehl and Jetter[8] for age hardening of alloys from the phase diagram in Fig. 31a (solid lines). *AB* represents solution hardening, *BDE* represents the overaged or equilibrium strengthening excluding the possible effect of particle size. *BCD* represents the age-hardening effect, and *X* is the maximum strengthening due to age hardening. It is possible, therefore, to obtain strengths within the range *BD* to *BCD*, depending upon the treatment used or the stability at high temperatures. The corresponding changes in ductility are indicated in Fig. 31c. In the range of solid solubility, sometimes the ductility is increased with increasing additions ($A''B'$) and in some systems it is decreased ($A'B'$). In any case, the optimum combinations of strength and ductility probably occur in alloys near the maximum solubility limit.

These schematic diagrams are substantiated by the findings of this research that high melting incongruous addition elements are associated with low maximum solubilities occurring at high temperature, which are related to pronounced solution-hardening and age-hardening effects. The age-hardening peak in the strength plot is also related to the maximum limit of solubility and for high melting additions should occur at a high aging temperature and thus be stable at a high service temperature. The schematic ductility plot suggests that little strength is gained and considerable ductility is lost beyond the composition of the maximum solubility limit. In addition, forging difficulties might be more pronounced with alloys which are multiple phase at forging temperatures. These effects can be derived with some consistency from the effects of single incongruous additions considered in this paper. The application of these principles to complex multiple-component commercial high temperature alloys with uncertain phase diagrams and interactions with respect to strengthening and embrittling effects are as yet obscure and require considerably more fundamental data than are now available.

Summary

1—The high temperature properties of binary ternary, and quaternary Ni-Cr-Co-Fe alloys and the effects of single additions of incongruous elements have been analyzed using the $T(C + \log t)$ parameter, (a) to determine the 1000 hr, 1500°F rupture strength from tensile and rupture tests from room temperature to 2000°F, (b) to characterize the variety of alloys as follows: (1) solid solution alloys, (2) allotropic transformation alloys, (3) precipitation hardening alloys, and (4) multiple phase alloys, and (c) to emphasize the importance of such factors as relative melting points, relative atom sizes, recrystallization and recovery, and their interactions.

2—The strength of these alloys can be rationalized on the basis of strengthening effects related to fundamental characteristics of the components and their possible phasial relationships.

3—Nickel-rich solid solutions are hardened more

effectively by chromium than by cobalt or iron. Solute additions are not mutually independent, but interaction effects, generally positive for cobalt and negative for iron, indicate that variations in base composition require quantitative compensation to maintain a given strength.

4—Several factors influence ductility, including: alloy content, crystal structure, temperature at which fracture changes, temperature dependence of precipitation hardening, temperature of allotropic transformation, deoxidation practice, recovery, and recrystallization.

5—In the design of alloys for high temperature applications, it appears that the characteristics of the base alloy should include: (a) Solid solutions as nearly as possible saturated at the temperatures of maximum solubility with the most potent solution-hardening elements (i.e., large differences in atom diameter, valency, compressibility, and minimum solubilities). (b) The most complex structures consistent with acceptable ductility. (c) The highest melting alloys, preferably for service at temperatures < 0.5 melting temperature. (d) Since solution-hardened alloys are usually lower melting unless they form peritectics and since complex structures are not readily fabricated, the optimum compromise between all of these factors should be sought. In seeking this compromise, it should be remembered that solution-hardening elements in addition to raising the base strength also increase the amount of strain hardening and raise the recrystallization temperature. These factors in part counteract the lowering of the melting point.

6—The relative strengthening effects of various incongruous additions appear to be related to the melting point of the incongruous addition, to the difference in atom diameter between the incongruous addition and the base and probably to the compressibility. The high melting point of the incongruous addition probably reflects itself in the melting point of the compound formed during age hardening. This effect was particularly apparent in the simultaneous additions of carbon and titanium or tantalum which formed high melting carbides and produced the largest amount of strengthening found.

7—A limited amount of data on simultaneous additions of carbon and titanium or tantalum suggests that when the incongruous elements have large interaction effects their strengthening effect upon a base will be considerably different from that obtained from individual elements.

8—It was found that several of the alloy additions had purifying effects on the base as indicated by a lowering of the base strengths.

Acknowledgment

The authors wish to express their appreciation to members of the Metallurgy Research Dept. of the General Electric Research Laboratory and particularly to the many laboratory assistants who performed most of the tests and compiled a great deal of the data reported. The advice of W. E. Ruder, A. H. Geisler, and J. H. Westbrook is particularly appreciated.

References

[1] J. D. Nisbet: Producing High Purity Metals with Vacuum. *Iron Age* (June 19, 1947) p. 56.

[2] J. D. Nisbet: Vacuum Melting Techniques. *Iron Age* (March 18, 1948) p. 79.

[3] J. D. Nisbet: Rupture Testing in a 48-Bar Furnace. *Iron Age* (February 12, 1948) p. 81.

[4] F. R. Larson and J. Miller: A Time-Temperature Relationship for Rupture and Creep Stresses. *Trans.* ASME (1952) **74** (5) p. 765.

[5] J. H. Hollomon and L. D. Jaffe: Time-Temperature Relations in Tempering Steel. *Trans.* AIME (1945) **162**, p. 223.

[6] P. Grün: Creep of Steels as a Function of Alloy Content and Heat Treatment. *Arch. Eisenhutt.* (1934) **8**, p. 205.

[7] A. R. Elsea and C. C. McBride: The Effects of Nitrogen, Iron or Nickel Upon the Alpha-Beta Transformation and Gamma Precipitation in Cobalt-Chromium Alloys. *Trans.* AIME (1950) **188**, p. 154; JOURNAL OF METALS (January 1950).

[8] *Metals Handbook.* Sections on constitution diagrams. (1948) Cleveland, ASM.

[9] T. Kasé: On the Equilibrium Diagram of the Iron-Nickel-Cobalt System. *Sci. Rpt.* Tohoku Univ. (1927) **16**, p. 496.

[10] W. D. Manley and P. A. Beck: The Sigma Phase in Ternary Cr-Co-Fe and Cr-Co-Ni Alloys. *Trans.* AIME (1949) **185**, p. 354; JOURNAL OF METALS (June 1949).

[11] J. W. Pugh and J. D. Nisbet: A Study of the Iron-Chromium-Nickel System. *Trans.* AIME (1950) **188**, p. 268; JOURNAL OF METALS (February 1950).

[12] W. Köster: The System Iron-Cobalt-Chromium. *Arch. Eisenhutt.* (1932) **6**, p. 113.

[13] S. Rideout, W. D. Manley, E. L. Kamen, B. S. Lement, and P. A. Beck: Intermediate Phases in Ternary Alloy Systems of Transition Elements. *Trans.* AIME (1951) **191**, p. 872; JOURNAL OF METALS (October 1951).

[14] C. Lacy and M. Gensamer: The Tensile Properties of Alloyed Ferrites. *Trans.* ASM (1944) **32**, p. 88.

[15] U. S. Patent 2,564,498.

[16] J. H. Westbrook: Temperature Dependence of the Strength of Pure Metals. *Trans.* ASM (1953) **45**, p. 221.

[17] O. D. Sherby, R. A. Anderson, and J. E. Dorn: Effect of Alloying Elements on the Elevated Temperature Plastic Properties of Alpha Solid Solutions of Aluminum. *Trans.* AIME (1951) **191**, p. 643; JOURNAL OF METALS (August 1951).

[18] R. M. Brick, D. L. Martin, and R. P. Angier: Effects of Various Solute Elements on the Hardness and Rolling Textures of Copper. *Trans.* ASM (1943) **31**, p. 675.

[19] J. E. Dorn, P. Pietrowsky, and T. E. Tietz: The Effect of Alloying Elements on the Plastic Properties of Aluminum Alloys. *Trans.* AIME (1950) **188**, p. 933; JOURNAL OF METALS (July 1950).

[20] A. P. Gulyeav and E. F. Trusova: Relationship in the Variations of the Properties of Solid Solutions. *Zhur, Tekhn, Fiziki* (1950) **20** (1) p. 66.

[21] R. F. Mehl: Interatomic Forces in Metals and Alloys. *Trans.* AIME (1928) **78**, p. 405.

[22] J. H. Frye, J. W. Caum, and R. M. Treco: Hardness and Lattice Stress in Solid Solutions. *Trans.* AIME (1943) **152**, p. 83.

[23] A. P. Gulyeav: Periodicity of the Influence of Alloys on the Mechanical Properties of Metals. *Doklady Akad, Nauk. SSSR* (1950) **75**, p. 25 (cf. *Chemical Abstracts* (1950) **44**, 8710f).

[24] J. D. Lubahn: Strain Aging Effects. *Trans.* ASM (1952) **44**, p. 643.

[25] J. D. Lubahn: Simultaneous Aging and Deformation in Metals. *Trans.* AIME (1949) **185**, p. 702; JOURNAL OF METALS (October 1949).

[26] B. L. Averbach: The Effect of Plastic Deformation on Solid Reactions. Part I Diffusion Reactions. *Trans.* ASM (1949) **41A**, p. 262.

[27] A. Beck: *Magnesium and Its Alloys.* (1940) London. R. A. Hughes and Co.

[28] L. A. Carapella: Fundamental Alloying Nature of Magnesium. *Metals Progress* (August 1945) p. 297. (A review of investigations primarily by W. Hume-Rothery and G. V. Raynor.)

[29] R. F. Mehl and L. K. Jetter: The Mechanism of Precipitation from Solid Solution. The Theory of Age Hardening. *Symposium of Age Hardening* (1940) Cleveland. ASM.

Subgrain Formation in High-Purity Aluminum During Creep At High Temperatures

by Andre M. Gervais, John T. Norton, and Nicholas J. Grant

An investigation of the creep deformation of coarse-grained high-purity aluminum at temperatures approaching the melting point permitted the formulation of a theory of subgrain formation. Subgrain boundaries were found to be formed by two different processes: kinking and polygonization. Polygonization is considered as the main factor in subgrain formation.

SINCE "slipless flow" was first discussed in detail by Hanson and Wheeler,[1] many studies have been undertaken to determine how metals deform at high temperatures. Several types of observations have been reported. Jenkins and Mellor,[2] working on the creep of mild steels and various grades of commercial irons, found metallographic evidence of a kind of substructure within the grains after deformation at high temperatures. Homes[3] observed after creep deformation of steel at high temperatures that the original X-ray spots were sharply divided into several small ones. The same phenomenon was reported by Hirst[4] from his studies on lead and later by Crussard[5] from his work on aluminum.

The works of these investigators demonstrated beyond any doubt that the splitting of the X-ray spots was due to the fact that the grains underwent a division into subgrains during deformation at high temperatures.

Since then, numerous experiments have been undertaken on aluminum in order to determine the mechanism of formation of subgrains. Research workers can be divided, for the purpose of discussion, into two different groups as regards thinking on subgrain formation.

On one hand, based on the work on polygonization by Cahn,[6] Guinier and Lacombe,[7] Greenough and Smith,[8,9] Crussard,[10,11] and Servi, Norton, and Grant,[12] it was concluded that subgrain formation was a consequence of the simultaneous effects, first, of inhomogeneous deformation which produced bending of the lattice, and second, polygonization.

On the other hand, Wood and coworkers[13–16] based their work on the results of an earlier report[17] which dealt with crystallite size and a fragmentation theory. It is interesting to note that while Greenough and Smith[8] and Wood et al. performed similar experiments, their conclusions were quite different. Wood et al. did not recognize polygonization as a fundamental mechanism and said that aluminum, at the beginning of the deformation, fragmented immediately into subgrains in order to permit deformation of the metal, the number of these subgrains being a function of strain rate and temperature. They concluded that deformation of grains occurred by flow along the subgrain boundaries.

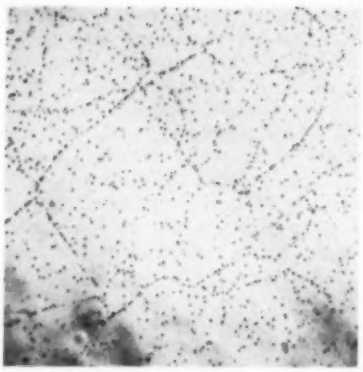

Fig. 1—Region in a grain of specimen 2 deformed by creep at 1150°F and at a stress of 45 psi. Total elongation 4.7 pct. Surface as revealed by etch pit technique after electrolytic polishing. The etch pit network represents the subgrain boundaries. X50. Area reduced approximately 50 pct for reproduction.

In view of the contradictory conclusions, it would appear that the data were not explicit enough to provide an unambiguous conclusion. It appears that the techniques by which most of the results were obtained, namely, X-ray work, were not enough by themselves to solve the problem.

Another approach was needed. In the present research, therefore, an extensive metallographic study was planned to supplement the X-ray work. The importance of revealing the subgrain boundaries metallographically was realized, and this will explain the extensive development and use of etching techniques. In order that subgrains would be considerably larger and therefore more readily visible under a microscope, the creep experiments were performed at very high temperatures approaching the melting point of aluminum.

Development of Experimental Technique

Creep tests were run at constant load on high purity (99.995 pct) aluminum specimens having a very coarse grain size. None of the specimens was run to fracture. The specimens were originally round (diameter, 0.187 in.; gage length, 1 in.) and had parallel flats milled in the gage section to permit

A. M. GERVAIS, Student Associate AIME, formerly Research Assistant MIT, is now with the Societe Commentry-Fourchambault et Decazeville, Imphy (Nievre), France, and J. T. NORTON and N. J. GRANT, Members AIME, are Professor and Associate Professor, respectively, Dept. of Metallurgy, Massachusetts Institute of Technology, Cambridge, Mass.

Discussion on this paper, TP 3620E, may be sent, 2 copies, to AIME by Dec. 1, 1953. Manuscript, April 14, 1953. Cleveland Meeting, October 1953.

This paper is based on a thesis by A. M. Gervais submitted in partial fulfillment of the requirements for the degree of Doctor of Science in Metallurgy to the Massachusetts Institute of Technology, February 1953.

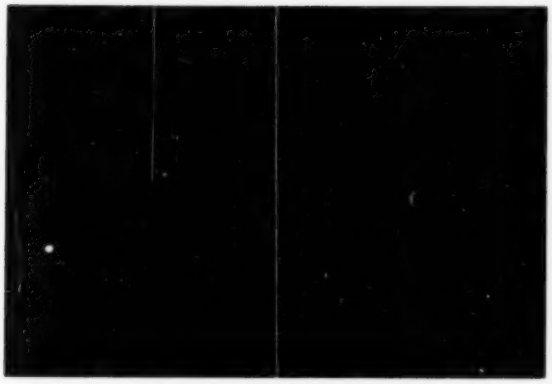

a—Film to specimen distance was 3 cm. b—Film to specimen distance was 15 cm.

Fig. 2—Laue back-reflection photographs with X-ray beam located in the region indicated by Fig. 1. No division of spots is observed, only marked asterism in Fig. b.

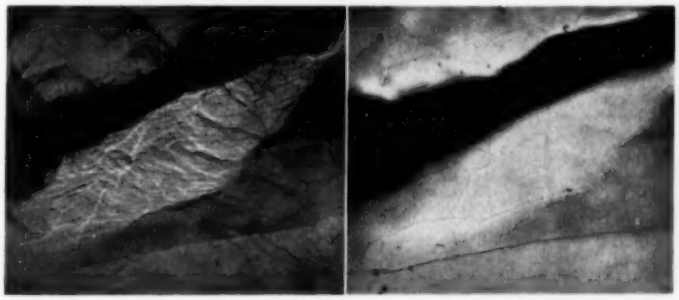

Fig. 3—Region of specimen 11 deformed by creep at 1150°F and at a stress of 90 psi. Total elongation 4.2 pct. Agreement between patterns is seen in both pictures (the black band, shadow, is due to grain boundary sliding and migration). X50. Area reduced approximately 50 pct for reproduction.

a (left)—Surface after deformation (very fine black markings are cracks in the oxide skin).

b (right)—Same location after careful electrolytic polishing and electrolytic etching.

easier metallographic and X-ray observations. The final thickness between the milled flats was 0.120 in. and the final gage length 0.85 in.

The specimens were annealed at 1150°F for at least 15 hr to obtain a coarse grain size. This coarse grain size was obtained by direct grain growth and not by strain-annealing, to avoid the introduction of any deformation which would affect the results. In order to prevent bending of the gage length during annealing, the specimens were placed flat on a bed of alumina powder contained in a boat.

Extensive grain boundary migration during creep at high temperatures was minimized by using such coarse grained specimens. Due to the limited amount of grain boundary migration with respect to the size of the grains, metallographic and X-ray observations were easily performed on the same grain during a series of several experiments.

Many tests were run but only the typical cases are reported. Among the several hundreds of micrographs and X-ray patterns taken during this research only those related to the typical cases are presented.

At the beginning of this research some effort was devoted toward improving X-ray techniques. Monochromatic radiation was not suitable for very refined work on this subject. In agreement with Bragg's law, spots produced by some elements could appear or disappear with a slight change in orientation of these elements during deformation. Consequently, it was not possible to follow step by step the evolution of a spot, that is to say, of the element of the structure that produced this spot. Therefore, the Laue technique using white radiation was adopted in these investigations. The grains were considerably larger than the X-ray beam itself, which permitted the beam to be located entirely within a single grain, if desired.

Guinier and Tennevin[15] refined the X-ray technique by using a focusing Laue transmission technique so that neighboring elements differing in orientation by even 10 sec of arc could be resolved. In the present work the above technique could not be used because it requires very thin specimens having thicknesses of the order of less than 0.5 mm. Such thin specimens were not adequate for creep work because the specimen surface was too large with respect to its volume and consequently the influence of the surface would be too great. Furthermore, the handling of such thin specimens during creep testing could result too easily in bending and thus modify and color the results.

Therefore, the Laue back-reflection technique had to be used, but in such a case no focusing was possible. The ordinary method was improved for some of the determinations by increasing the film to specimen distance from 3 to 15 cm. The collimator length was also increased to decrease the divergence of the X-ray beam. The first problem with this apparatus was the very long exposure time (about 10 hr) which was required. The second was that the resolving power was not high enough in all cases to reveal the subgrains. A clear example of this is shown in Figs. 1 and 2. Fig. 1 shows the microstructure of a typical test specimen, the subgrains being revealed by an etch pit technique which will be described later. Fig. 2a is a Laue back-reflection

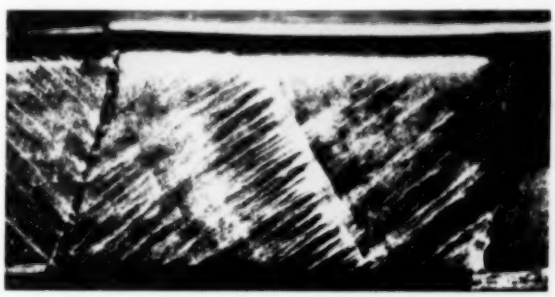

a—Surface after deformation (oblique illumination).

Fig. 4—Kink band in a grain of specimen 10 deformed by creep at 1150°F and at a stress of 90 psi. Total elongation 4.3 pct. X11. Area reduced approximately 50 pct for reproduction.

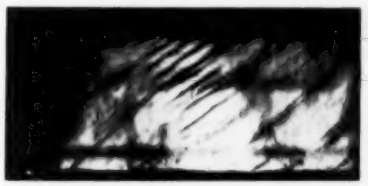

b—Surface after careful electrolytic polishing and electrolytic etching (direct illumination). Kink band boundaries are clearly revealed by electrolytic etching.

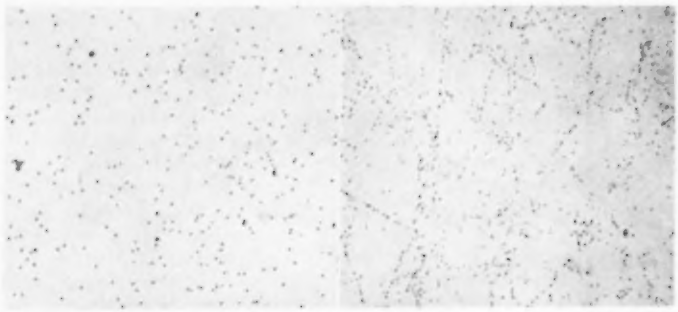

Fig. 5—Region of a grain of specimen 13 as revealed by etch pit technique after electrolytic polishing. X50. Area reduced approximately 50 pct for reproduction.

a (left)—After annealing at 1150°F, before deformation.

b (right)—After deformation by creep at 1150°F and at a stress of 70 psi. Total elongation 5.1 pct. Note the etch pit network.

photograph (film to specimen distance of 3 cm) with the X-ray beam located in the same region shown in Fig. 1. Fig. 2b is a Laue back-reflection photograph (film to specimen distance of 15 cm) with the X-ray beam located at the same spot. The asterism is marked in the second case, but still no subgrains are indicated by this refined technique in spite of the fact that subgrains are quite evident (Fig. 1). From this it can be concluded that the Laue back-reflection technique alone is inadequate to measure or detect all the changes taking place. An X-ray microbeam technique[19] was not used because its resolving power does not seem to be superior to that of the other techniques.

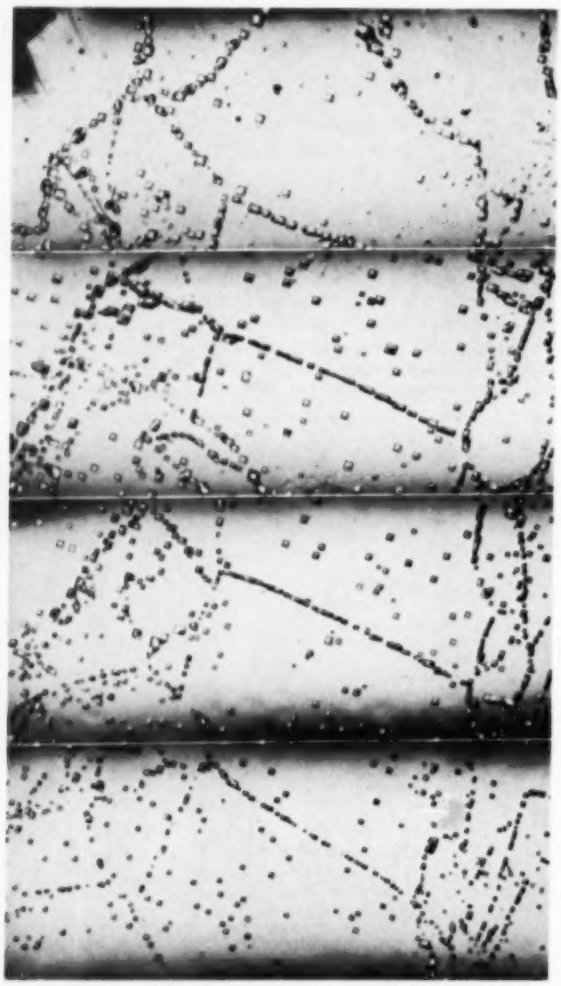

Fig. 6—Gradual change in substructure as 0.001 inch of metal is removed successively from the surface after each repolish and etch. HCl, HF, HNO_3 in alcohol. a—top. b—second from top. c—second from bottom. d—bottom. X100. Area reduced approximately 50 pct for reproduction

Polarized light,[20, 21] used for similar research, was not utilized here because it appeared that the results obtained with this very delicate technique were approximately identical to those obtained by electrolytic etching, a very simple technique. After electrolytic polishing of the specimens in the Jacquet solution[22] (2/3 acetic anhydride + 1/3 perchloric acid) at a voltage of about 30 v, the specimens were kept in the same solution at a temperature of about 20°C and at a very low voltage of about 2 v for 1 hr or more.

After deformation, the untouched surface of the specimen revealed boundaries as shown in Fig. 3a. These boundaries are revealed more precisely by the electrolytic etching as seen in Fig. 3b, but do not have the same intensities indicated in Fig. 3a. This is due to the fact that there is a selective appearance of these boundaries which is related to the difference in angle between the blocks. The greater the difference, the more distinct do the boundaries appear. Electrolytic etching, when applied similarly to grains containing kink bands,[23] revealed that the kink band boundaries were sharp and that rather important differences in orientation were present as shown in Fig. 4. This relationship between sharp bending and kinking will be discussed later.

The etch pit technique was a modification of the one devised by Lacombe and Beaujard[24] to show subgrain boundaries in the case of polygonization.[25] The specimens were etched after careful electrolytic polishing. The chemical composition of the etching reagent was as follows: methyl alcohol, 50 cc; hydrochloric acid, 32 cc; nitric acid, 50 cc; and hydrofluoric acid, 2 cc.

The reagent was cooled in an ice bath during preparation and a fresh solution was made each time. The etching was performed at a temperature of about 10°C. As established before[24] the rate of growth of the etch pits varied with the orientation of the surface of the grain; very fast for a surface parallel to (111), slow for a surface parallel to (100). Consequently, no specific etching time could be defined, every grain having its own optimum etching time. Therefore, this method was sometimes tedious.

A reproducible network was not revealed by the etch pits on a specimen after annealing at 1150°F and before deformation (Fig. 5a) but after creep deformation at the same temperature of 1150°F a very clear reproducible network is apparent (Fig. 5b). Consequently the relation between deformation and the etch pit network is very evident.

The main question was whether etching with this reagent revealed the existing structure accurately. Fig. 6 shows a region of a specimen deformed at 1200°F and then polished and etched four times so

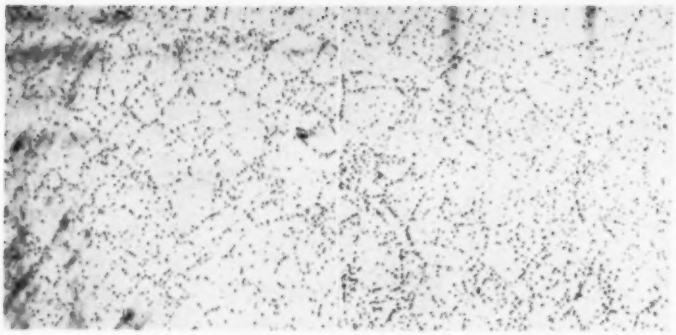

Fig. 7—Specimen 1 deformed by creep at 1150°F and at a stress of 50 psi. Total elongation 6 pct. Etch pit technique after electrolytic polishing. X50. Area reduced approximately 50 pct for reproduction.

a—Region of a grain on the surface of the specimen.

b—Region of the same grain in cross section. Note similarity of subgrain size in both directions.

that after each electrolytic polishing, about 1/1000 in. was removed. The four pictures show the substructure of the same area located by a small prior identification scratch. It is easy to recognize the same etch pit subgrain network and to follow the progressive changes in depth. Fig. 7a shows the front surface of a creep deformed specimen after being etched by the etch pit technique and Fig. 7b shows the surface of the cross section at right angles to this area. This shows that subgrains are formed through the whole thickness of the specimen, and are on the average about the same size.

Another example of the nature and utility of this network of etch pits is given by the following experiment. A very coarse-grained specimen was slightly bent under its own weight during annealing at 1150°F, the axis of bending being parallel to the flat milled surface of the specimen and perpendicular to the axis of the specimen. Fig. 8 shows the two opposite surfaces of one of the grains of the specimen after polishing and etching, Fig. 8a showing the convex side and Fig. 8b the concave side. The lines of etch pits are perpendicular to the axis of the specimen, that is, parallel to the bending axis.

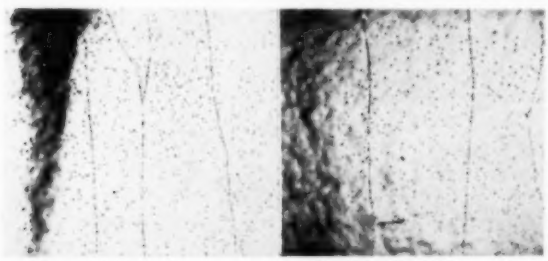

a—Convex side. b—Concave side.

Fig. 8—Grain of specimen slightly bent by sagging during annealing at 1150°F, polished and etched. The etch pit boundaries are perpendicular to the axis of the specimen. X25. Area reduced approximately 50 pct for reproduction.

X-ray diffraction confirmed that the etch pits in Fig. 8 were located at the boundaries of two blocks which had a slight difference in orientation caused by the curvature of the specimen due to bending. Every spot of the Laue back-reflection photograph (Fig. 9a) taken on the convex side was sharply divided into two parts and this separation line was perpendicular to the specimen axis, that is to say, parallel to the etch pit lines. A schematic explanation of the division of the X-ray spots is given in Fig. 9b. In such an experiment no errors were introduced because the X-ray beam could not hit more than two subgrains delineated by the etch pits.

This illustrates very well the process of polygonization as described by Cahn[6] where dislocations move to surfaces (walls of dislocations) in order to occupy a state of lower energy.[26] Ramsey[27] was opposed to polygonization because he did not believe that dislocations of the same sign could move in opposite directions toward these surfaces. Actually the dislocations can move in any direction since their final state would be one of lower energy.

Because etch pits have a certain size, or range of sizes, the minimum subgrain size that could readily be detected under a microscope after etching with the reagent had to be much larger than the etch pit size. In the present work, therefore, the range of deformation temperatures for which subgrains could be easily observed and studied was rather limited; that is, it was only above a certain minimum temperature that the subgrain size was large enough to be revealed distinctly by the etch pit technique.

It must be pointed out that, at first, it was quite difficult to see any relation between the results of the two different etching techniques (etch pit and electrolytic) because of the high density of subgrain boundaries shown by the etch pit technique with respect to that indicated by electrolytic etching.

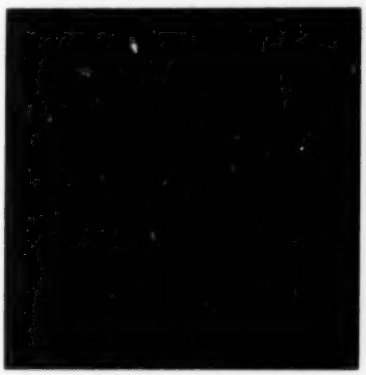

Fig. 9a—Laue back-reflection photograph of the convex side of the grain in Fig. 8a. Spots are sharply divided in their middle.

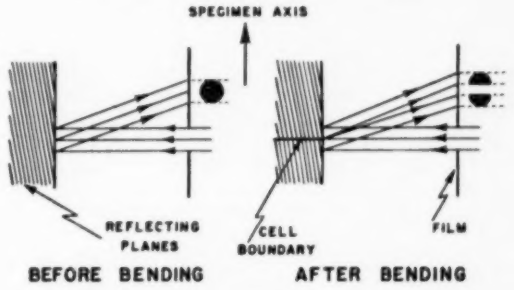

Fig. 9b—Schematic representation of the division of the X-ray spots of Fig. 9a.

Fig. 10—Region of a grain of specimen 10 deformed by creep at 1150°F and at a stress of 35 psi. Total elongation 6.9 pct. Boundary network in Fig. a is confirmed in Fig. b (indicated by arrows in several more prominent locations). X50. Area reduced approximately 50 pct for reproduction.

a (left)—Electrolytic etching after careful electrolytic polishing.

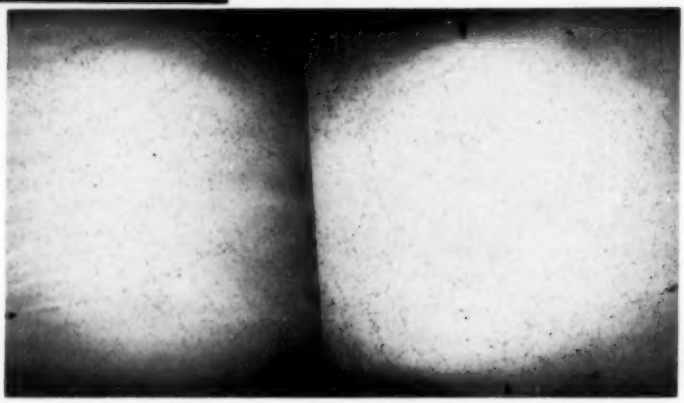

b (right)—Etched with the etch pit reagent after careful electrolytic polishing.

However, a relation was found between these two types of networks, as shown in Fig. 10. It is possible, as indicated by the arrows, to identify the pattern of subgrain boundaries revealed by electrolytic etching within the pattern of subgrain boundaries revealed by using the etch pit technique.

Fig. 11 shows three micrographs of an area after deformation, after polishing and electrolytic etching, and after polishing and etching with the etch pit technique. In this case it was not as easy to match the patterns obtained by the two etching techniques as it was for the case presented in Fig. 10, where the subgrain size was much larger (i.e., the number of subgrain boundaries and hence the number of etch pits were less).

Since it had been indicated before that the boundaries revealed by electrolytic etching were related to the boundaries seen on the surface after deformation, it is, consequently, possible to correlate these boundaries with those revealed by the etch pit technique.

Mechanism of Subgrain Formation

After deformation, when one looks at a region in a grain, the boundaries appear to separate dark regions from light regions, this difference in illumination being due to the sudden change in orientation across these boundaries. This type of boundary is somewhat similar in appearance to the ideal kink band boundaries previously described,[28] but is different in that the boundaries of the ideal kink bands cross the entire width of the specimen, the cross section being occupied by only one grain. In the case where a smaller grain size is involved, the quantity of grain boundary with respect to the volume of the grain is greater; therefore, the bending moments are not so homogeneously distributed in the smaller grains during heavy grain boundary sliding.[28] On the other hand, there is a unique bending moment in a large grain with kink bands crossing the width of the specimen. In the case of smaller grain size the kinking process is not regular and results in the formation of blocks (as contrasted to bands). The boundaries produced by the process of kinking are the locations of sharp changes in orientation of the lattice, but the bending in this case was sharp from the very beginning of the deformation. This initial difference in orientation then increased with a progressive tilt of the neighboring block (rotation as in the case of kink bands).[28, 29]

These metallographic observations are in contradiction to the theory of Wood and coworkers on the flow between subgrains to permit deformation of the grain.[10, 14, 30] Fig. 12 shows schematically why Wood's idea cannot be accepted in the case of such boundaries. In case II of Fig. 12, flow along subgrain boundaries, as suggested by Wood et al., would produce the same effect as that along grain boundaries (see for example, Figs. 3 and 11); that is to say, dark bands would be observed to separate two neighboring blocks which would have about the same intensity. On the contrary, case I of Fig. 12 would be observed with a sharp change in orientation at the boundary, that is, kinking with no movement of the boundary during the process of rotation of one block with respect to the other. It may be seen from a study of the micrographs in Figs. 3a and 11a that case II is not applicable to the observations.

Boundaries revealed by electrolytic etching correspond to the kinks observed on the surface after deformation due to selective etching based on the difference in angle between the blocks on each side of the boundary. As these kinking boundaries present a greater difference in orientation they were

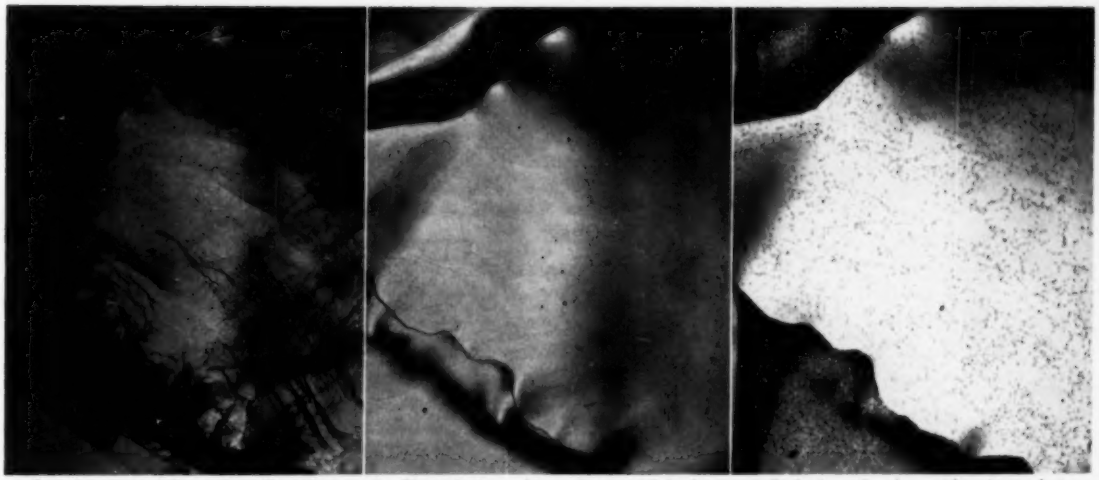

a—Surface after deformation (boundaries inside the grain separate regions of completely different illumination). Forked black markings are cracks in the oxide.

b—Electrolytic etching after careful electrolytic polishing.

c—Etched with the etch pit technique after careful electrolytic polishing (small subgrain size).

Fig. 11—The same region of a grain of specimen 11 deformed by creep at 1150°F and at a stress of 90 psi. Total elongation 4.2 pct. X50. Area reduced approximately 50 pct for reproduction.

revealed first by electrolytic etching. In Fig. 11b the subgrain boundaries revealed by electrolytic etching are apparently only those boundaries of higher difference in orientation of the lattice because frequently they join the grain boundaries at points where the grain boundaries change their orientation. This is due to their higher energy with increasing difference in orientation of the lattice.[20, 21]

On the other hand, the magnitude of the difference in orientation of the lattice on each side of the subgrain boundaries, as revealed by the etch pit technique, does not seem to have an influence on the appearance of the boundary. Opposite results are found when boundaries are revealed by electrolytic etching (Fig. 10). The result of etching with the etch pit technique is that boundaries separating subgrains having only a small difference in orientation are virtually identical in appearance to boundaries separating blocks which have a larger difference in orientation.

It appears, therefore, that the etch pit technique is a more sensitive method of detecting the first appearance of subgrains but does not differentiate on the basis of the angular difference between subgrains. Electrolytic etching, on the other hand, does not detect subgrain boundaries with small angular difference between subgrains, but is capable of delineating orientation differences at fairly large angles, for example due to kinking. Consequently, electrolytic etching can quite easily give erroneous information on the number of subgrains and on the real subgrain size, as for example, in Rachinger's work.[22]

In the work on kink band formation,[23] it was shown that in addition to sharp bending along the kink band boundaries, X-rays revealed a smooth bending in the bands themselves or in regions outside the kink bands. These results were observable primarily because of the large size of the kink bands;[23] but this phenomenon remains the same in the case of smaller blocks formed by kinking in the present work on subgrain formation, namely, that in addition to the sharp bending produced by kinking, a smooth bending occurred inside the blocks formed by kinking.

In observations of the formation of kink bands,[23] as compared with observations of general substructures revealed by etching methods and by observations of the microstructures after deformation, it is possible to distinguish two processes of subgrain boundary formation: 1—By kinking, which forms sharp boundaries from the very beginning of the deformation process; 2—By polygonization of the smoothly bent regions within the zones formed by prior kinking.

In opposition to the case of ideal smooth bending about a single axis, the boundaries formed by polygonization, as revealed by etch pits inside the zones formed by kinking, are not parallel to each other because the amount of bending and the axes of bending vary from one spot to another due to the

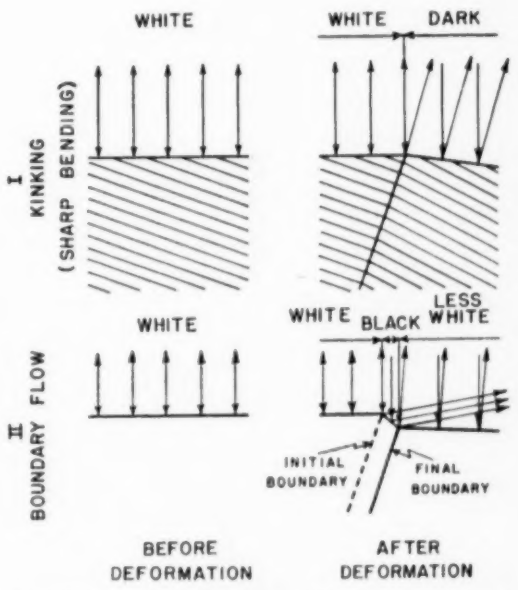

Fig. 12—Schematic representation of the appearance of boundaries in microscopic observations as produced by kinking or fragmentation and boundary flow.

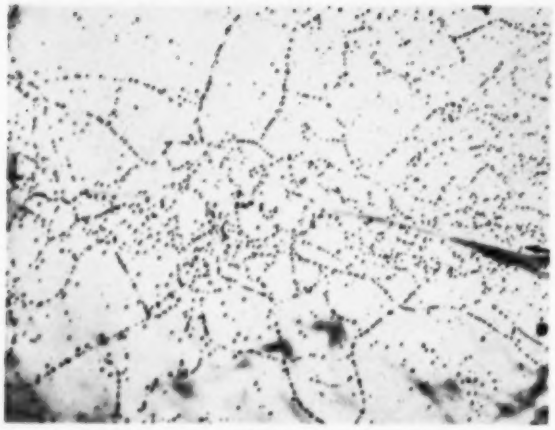

Fig. 13—Subgrains near a grain boundary of specimen 2 deformed by creep at 1150°F and a stress of 45 psi. (Grain boundary indicated by arrows). Electrolytically polished and etched (etch pit technique). Note greater density of subgrains near the grain boundary. X50. Area reduced approximately 50 pct for reproduction.

Fig. 14a (left)—Laue back-reflection photograph with X-ray beam at a point removed from the grain boundary indicated in Fig. 13.

Fig. 14b (right)—Laue back-reflection photograph with X-ray beam located just along the grain boundary indicated in Fig. 13. Higher bending of the lattice is noticeable near the grain boundary.

extensive inhomogeneity of deformation in creep testing.

Fig. 11 shows that the number of subboundaries as revealed by the etch pit technique was much greater than the number of subboundaries which could be seen on the unetched surface either after deformation or after electrolytic etching. Such observations indicate that the number of subboundaries formed by polygonization is much higher than that which is formed by kinking. Consequently, polygonization appears to be the main factor responsible for subgrain formation.

In the present work which was performed at high temperatures not far from the melting point, diffusion rates are high and dislocations can move easily and reach stable positions very rapidly. Hence, if polygonization is really the main factor in subgrain formation, it is reasonable to believe that the subgrain size would be primarily a function of the total amount of bending and of temperature, namely, smaller subgrain size with higher bending and lower temperature.[20] Results found in the present investigation agree with this theory, and the typical cases are presented below.

It is known that at high temperatures, because of heavy sliding along grain boundaries, deformation initially is greater along grain boundaries than inside the grains.[20, 21] Fig. 13 shows such a grain boundary (indicated by arrows) and the neighboring regions. The subgrains are considerably finer adjacent to the grain boundary. Fig. 14a is a Laue back-reflection photograph of a region far from the grain boundary shown in Fig. 13, and Fig. 14b is a Laue back-reflection photograph of a region just along the grain boundary. Fig. 14b clearly supports the etch pit evidence in Fig. 13 of higher bending of the lattice adjacent to the grain boundary.

In another test specimen 5 was successively elongated by 1, 3, and 12 pct in a creep test at the same initial stress and temperature. Fig. 15 indicates that the subgrain size decreased with increasing elongation. In the third step of the creep test heavy duplex slip took place during increased deformation in the grain (Fig. 15c). Increasing deformation re-

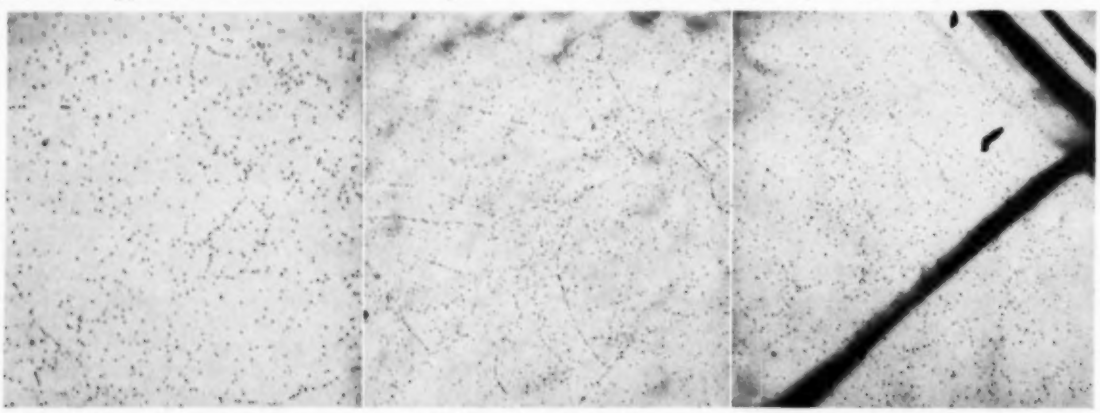

a—After 1 pct elongation.

b—After 3 pct elongation.

c—After 12 pct elongation. (Slip and conjugate slip occurred inside the grain for such a total elongation).

Fig. 15—Same region of specimen 5 deformed by creep at 1150°F and at a stress of 50 psi, electrolytically polished and etched (etch pits). Note the decrease in subgrain size with the greater deformation of the grain. X50. Area reduced approximately 50 pct for reproduction.

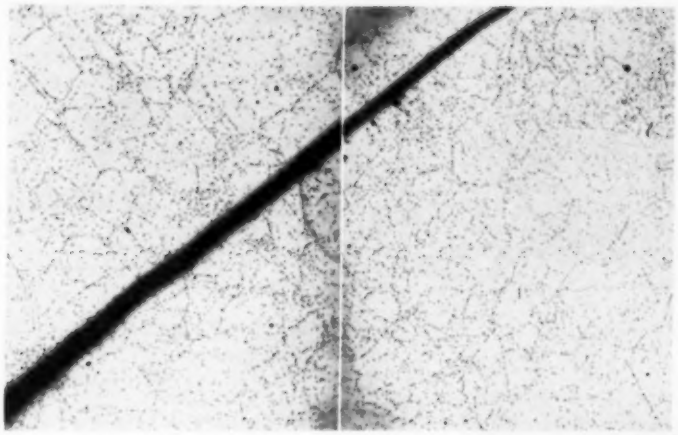

Fig. 16—Same region of a grain of specimen 10 deformed by creep at 1150°F, electrolytically polished and etched (etch pits). X50. Area reduced approximately 50 pct for reproduction.

a (left)—Deformed at a stress of 90 psi. Strain rate: $3.2 \times 10^{-1} hr^{-1}$. Total elongation from 0 to 4.3 pct.

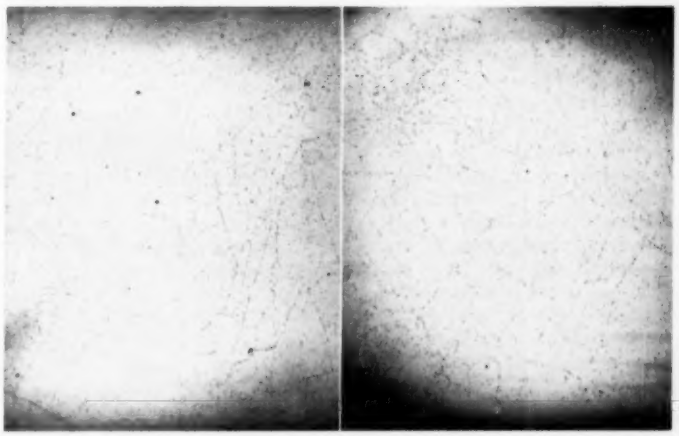

b (right)—Further deformed at a stress of 35 psi. Strain rate: $4 \times 10^{-1} hr^{-1}$. Total elongation from 4.3 to 6.9 pct.

No distinct change in subgrain size. Subgrain size varies markedly within the grain.

sulted in greater bending and consequently in diminishing the subgrain size.

In a test to evaluate the role of strain rate, specimen 10 was first deformed by creep at 1150°F at a stress of 90 psi; later a small additional increase in strain was obtained by creep at 1150°F and at a decreased stress of 35 psi. In the second portion of the test the strain rate was 800 times smaller than in the first. The metallographic results are shown in Fig. 16, and an important change in subgrain size is not evident. This result does not agree with the assumption that the subgrain size largely determines the mechanical strength exhibited by the metal during deformation.[15, 16] Furthermore, it must be pointed out that in the micrographs of Fig. 16 the subgrain size is not the same all over the grain, and this fact is not in agreement with the theory of strength as a function of the subgrain size. On the contrary, bending can vary in different parts of a grain and the explanation of subgrain size as a function of local bending seems more feasible.

Finally, the influence of temperature on subgrain size was very striking, as shown in Fig. 17. In this case the tests were run on the same specimen at the same initial stress but at three different temperatures. It will be noted that the subgrain size increased markedly with temperature at these high temperatures.

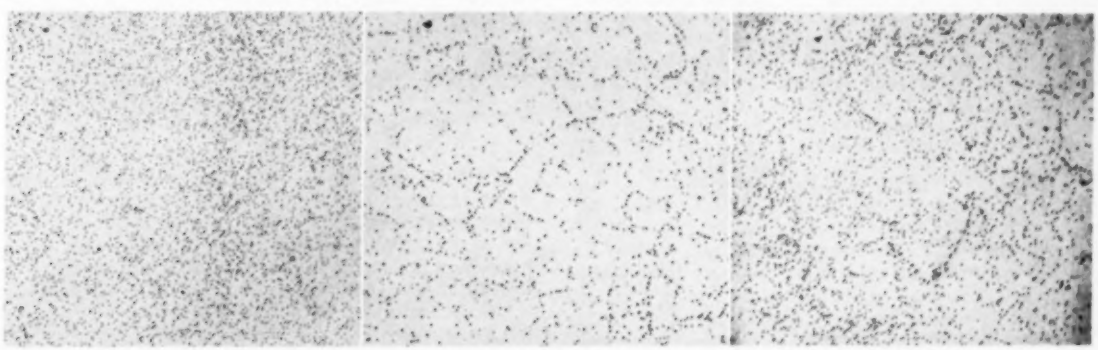

a—Deformed at 1075°F. Strain rate: 1.1×10^{-1}. Total elongation from 0 to 5.2 pct.

b—Deformed at 1150°F. Strain rate: 3.8×10^{-1}. Total elongation from 5.2 to 10.8 pct.

c—Deformed at 1100°F. Strain rate: 1.02×10^{-1}. Total elongation from 10 to 17.3 pct.

Fig. 17—Same region of specimen 15 deformed by creep under a stress of 90 psi, electrolytically polished and etched (etch pits). Note the change in subgrain size as a function of temperature in spite of the fact that the specimen was deformed at the same stress. X50. Area reduced approximately 50 pct for reproduction.

Conclusions

A theory of subgrain formation has been proposed. The striking fact is that this theory bridges the gap between the theory based on fragmentation on the one hand and that based on polygonization on the other.

Wood and coworkers were not entirely wrong in saying that fragmentation was taking place if fragmentation is synonymous with kinking. Due to kinking, a small number of boundaries are formed which are sharp from the very beginning of the deformation process. Contrary to Wood et al.'s argument, however, significant sliding has not been noted to occur along this type of boundary but primarily rotation.

In addition, the idea that polygonization was the only process of subgrain formation, while subject to some modification, is essentially correct since most of the subgrain boundaries are formed by polygonization of the smoothly bent regions delineated by kinking.

X-ray and metallographic evidence indicate that polygonization was the main factor in subgrain formation. The subgrain size was found to be a function of the extent of bending and of temperature. The experiments, which had to be performed at high temperatures where diffusion rates were very high, showed temperature to be a very important factor. Since polygonization is indicated to be chiefly responsible for subgrain formation, subgrains must form as a consequence of deformation and are not a main cause of deformation.

Acknowledgments

The authors wish to express appreciation to H. C. Chang and A. R. Chaudhuri for frequent helpful discussions. Thanks are also extended to the Flight Research Laboratory (WCRRL) Wright Air Development Center, for sponsoring this research under Contract AF 33 (038) -23281.

References

[1] D. Hanson and M. A. Wheeler: The Deformation of Metals Under Prolonged Loading. Part I: The Flow and Fracture of Aluminum. *Journal* Inst. Metals (1931) **45**, p. 229.

[2] C. H. M. Jenkins and G. A. Mellor: Part I: Structural Changes in Mild Steels and Commercial Irons During Creep. *Journal* Iron and Steel Inst. (1935) **132**, p. 179.

[3] G. A. Homes: Recherches sur le Mecanisme structurale du Comportement Mecanique des Metaux aux Temperatures elevees. *Revue de Metallurgie* (1939) **36**, p. 373.

[4] H. Hirst: Deformation of Single Crystals of Lead by Creep. Part IV: Process of Deformation During Creep. *Proc.* Australasian Inst. of Mining and Metallurgy (1941) **121**, p. 11.

[5] C. Crussard: Le Role des Joints Intergranulaires dans la Deformation des Metaux. Application au Fluage et a la Fatigue. *Revue de Metallurgie* (1946) **43**, p. 307.

[6] R. W. Cahn: Recrystallization of Single Crystals after Plastic Bending. *Journal* Inst. Metals (1949) **76**, p. 121.

[7] A Guinier and P. Lacombe: L'etat "polygonise" du Cristal Metallique. *Metaux et Corrosion* (1949) **23**, p. 212.

[8] G. B. Greenough and E. M. Smith: The Mechanism of Creep as Revealed by X-ray Methods. *Journal* Inst. Metals (1950) **77**, p. 435.

[9] G. B. Greenough, C. M. Bateman, and E. M. Smith: X-ray Diffraction Studies in Relation to Creep. *Journal* Inst. Metals (1952) **80**, p. 545.

[10] C. Crussard: Discussion on Ref. 13. *Journal* Inst. Metals (1949) **75**, p. 1125.

[11] G. Wyon and C. Crussard: Modifications de Structure de l'Aluminium au cours du Fluage. *Revue de Metallurgie* (1951) **48**, p. 121.

[12] I. S. Servi, J. T. Norton, and N. J. Grant: Some Observations of Subgrain Formation During Creep in High Purity Aluminum. *Trans.* AIME (1952) **194**, p. 965; JOURNAL OF METALS (September 1952).

[13] G. R. Wilms and W. A. Wood: Mechanism of Creep in Metals. *Journal* Inst. Metals (1949) **75**, p. 693.

[14] W. A. Wood and W. A. Rachinger: The Mechanism of Deformation in Metals with Special Reference to Creep. *Journal* Inst. Metals (1949) **76**, p. 237.

[15] W. A. Wood and R. F. Scrutton: Mechanism of Primary Creep in Metals. *Journal* Inst. Metals (1950) **77**, p. 423.

[16] W. A. Wood, G. R. Wilms, and W. A. Rachinger: Three Basic Stages in the Mechanism of Deformation of Metals at Different Temperatures and Strain Rates. *Journal* Inst. Metals (1951) **79**, p. 159.

[17] W. A. Wood: The Lower Limiting Crystallite Size and Internal Strains in Some Cold-worked Metals. *Proc.* Royal Soc., London (1939) **172A**, p. 231.

[18] A. Guinier and J. Tennevin: Sur deux Variantes de la Methode de Laue et leurs Applications. *Acta Crystallographica* (1949) **2**, p. 133.

[19] P. Gay and P. B. Hirsch: An X-ray Technique for the Study of Substructures in Materials. *Acta Crystallographica* (1951) **4**, p. 284.

[20] D. McLean: Creep Processes in Coarse-grained Aluminum. *Journal* Inst. Metals (1952) **80**, p. 507.

[21] J. Hino, P. G. Shewmon, and P. A. Beck: Effect of Simultaneous Strain on Subgrain Growth. *Trans.* AIME (1952) **194**, p. 873; JOURNAL OF METALS (August 1952).

[22] P. Jacquet: Sur une Nouvelle Technique de Polissage Electrolytique de l'Aluminum et de ses Alliages. *Metaux et Corrosion* (1943) **18**, p. 198.

[23] A. M. Gervais, J. T. Norton, and N. J. Grant: Kink Band Formation in High Purity Aluminum During Creep at High Temperatures. Unpublished.

[24] P. Lacombe and L. Beaujard: The Application of Etch-Figures on Pure Aluminum (99.99%) to the Study of Some Micrographic Problems. *Journal* Inst. Metals (1947) **74**, p. 1.

[25] P. Lacombe: "Sub-boundary" and Boundary Structures in High Purity Aluminum. *Report of a Conference on Strength of Solids.* University of Bristol, July 7-9, 1947. Published by the Physical Society, 1948.

[26] F. R. Nabarro: The Mathematical Theory of Stationary Dislocations. *Advances in Physics* (July 1952) **1**, p. 315.

[27] J. A. Ramsey: The Recovery of Polycrystalline Aluminum. *Journal* Inst. Metals (1952) **81**, p. 61.

[28] H. C. Chang and N. J. Grant: Observations of Creep of the Grain Boundary in High Purity Aluminum. *Trans.* AIME (1952) **194**, p. 619; JOURNAL OF METALS (June 1952).

[29] H. C. Chang and N. J. Grant: Inhomogeneity in Creep Deformation of Coarse Grained High Purity Aluminum. This issue, p. 1175.

[30] K. T. Aust and B. Chalmers: Surface Energy and Structure of Crystal Boundaries in Metals. *Proc.* Royal Soc., London (1950) **204A**, p. 359.

[31] C. G. Dunn, F. W. Daniels, and M. J. Bolton: Relative Energies of Grain Boundaries in Silicon Iron. *Trans.* AIME (1950) **188**, p. 1245; JOURNAL OF METALS (October 1950).

[32] W. A. Rachinger: The Effect of Grain Size on the Structural Changes Produced in Aluminum by Slow Deformation. *Journal* Inst. Metals (1952) **80**, p. 415.

[33] C. G. Dunn and F. W. Daniels: Formation and Behavior of Subboundaries in Silicon Iron Crystals. *Trans.* AIME (1951) **191**, p. 147; JOURNAL OF METALS (February 1951).

[34] E. A. Calnan and B. D. Burns: Some X-ray Observations on the Nature of Creep Deformation in Polycrystalline Aluminum. *Journal* Inst. Metals (1950) **77**, p. 445.

Inhomogeneity in Creep Deformation of Coarse Grained High Purity Aluminum

by H. C. Chang and N. J. Grant

Creep of very coarse grained high purity aluminum was studied at 400°, 700°, and 1100°F at initial stresses of 50 to 1200 psi. Local strain measurements were made across the grain boundaries and in different regions of various grains during creep, thereby permitting the drawing of component creep curves. The relative amounts of elongation as measured across a grain boundary and in the grains adjacent to the boundary depend on the temperature of testing. The significance of creep curve equations and activation energies is discussed.

THIS paper presents some of the results of a research program devoted to the study of the mechanism of creep in high purity aluminum. Previous publications have dealt with the cyclic processes of alternating grain boundary sliding and migration, and the deformation in the grains caused by these processes;[1] the direction and the driving force of grain boundary sliding and migration;[2] the deformation in the grains and the restricting effects of the grain boundaries on this deformation.[3] These previous papers were based mainly on either microscopic observations or X-ray data, or both. Sometimes creep curves across two closely spaced reference marks (about 0.6 to 0.7 mm apart) were also presented with a view to correlating the elongation values with the optical observations in general, and with certain deformation processes in particular. These curves shall henceforth be referred to as component creep curves. No attempts were made, however, to compare either the component creep curves which were obtained in different regions of a specimen, or those obtained from different specimens subjected to different creep test conditions.

It is the purpose of this paper to present these component creep curves. Among the factors influencing the behaviors of these curves, those studied were stress, temperature, and grain arrangements in the specimens. It is proposed to show how greatly the deformation can vary from grain to grain and within an individual grain in a coarse grained specimen.

H. C. CHANG, Associate Member AIME, is associated with the DIC Staff, and N. J. GRANT, Member AIME, is Associate Professor, Dept. of Metallurgy, Massachusetts Institute of Technology, Cambridge, Mass.

Discussion on this paper, TP3629E, may be sent, 2 copies, to AIME by Dec. 1, 1953. Manuscript, Sept. 15, 1952; revision, June 19, 1953. Cleveland Meeting, October 1953.

The experimental technique and procedure have been presented.[1] It remains necessary to emphasize that the reference marks were produced by pressing a thin sewing needle into the surface of the specimen before the final annealing at 900°F for 24 hr and at 1150°F for 12 hr. The cold work around the needle indentations was therefore removed. The depth of these holes after electropolishing the annealed specimens was about 0.01 mm. This depth and area were negligible in comparison with the thickness of the specimens, 2.3 mm, and hence would not affect the creep behavior.

Results

Fig. 1 shows a development diagram of specimen P-8. The dots on the surface locate the needle point reference marks used to obtain the component creep curves. A curve obtained between two dots across a grain boundary measures not only the boundary deformation but also the deformation associated with boundary sliding occurring in the grains in the region between these indents. The original distance between two reference marks was about 0.6 to 0.7 mm. The maximum error of measurement was 0.01 mm, or in terms of percentage elongation, of the order of ± 1.5 pct.

Whereas the component creep curves shown in the figures to follow were drawn as a gross average of the points, in view of the fineness of some of the steps of grain boundary sliding and migration, as shown in the previous publications,[1, 2] it appears logical to expect that some of the finer cycles of movement have not been delineated for the strain sensitivity of the measuring system. It seems justifiable to say that the curves are not as smooth as shown.

700°F Tests: Fig. 2 shows component creep curves across four of the grain boundaries in specimen P-8, tested at 700°F and 85 psi. These curves clearly show alternate cycles of increasing and decreasing

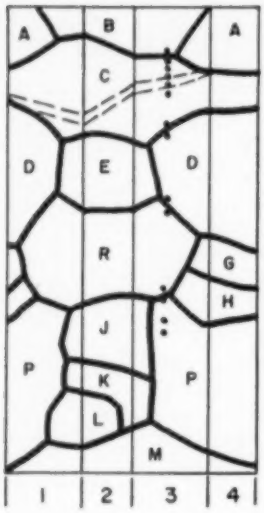

Fig. 1—Structural development drawing of specimen P-8, tested at 700°F and 85 psi. Dashed line indicates the course of heavy slip bands. The black dots indicate reference marks for component creep curves. 1—Back surface. 2—Left edge. 3—Front surface. 4—Right edge.

creep rates. It has been shown[1] that these cycles are associated with the consecutive processes of grain boundary sliding and migration.

It can be seen from Fig. 1 that the boundary between grains *B* and *C* lies about 75° to the direction of applied stress. This boundary was not too favorably oriented for sliding; the component creep curve obtained across this boundary is shown as curve IV in Fig. 2. After one cycle of increasing and decreasing creep rates in the early stages of the test, the creep rate settled down to a low fairly constant value in the later stages of creep. The elongation across this boundary at the time when the test was stopped was only 7.5 pct which is low compared to the values for the other three boundaries.

As shown in Fig. 1, the boundary between grains *C* and *D* at the reference marks was favorably oriented for sliding; however, the balance of the boundary was curved at the start of the creep test. After an initial period of about 15 hr, during which time creep deformation was small, this grain boundary became relatively straight as a result of boundary migration. As this boundary straightened out, the blocking effect at the triple point of grains *C*, *D*, and *E*, Fig. 1, on the front surface was overcome, and rapid deformation occurred as shown by creep curve III, Fig. 2, the elongation increasing sharply for the next 20 to 25 hr. A period of recovery followed

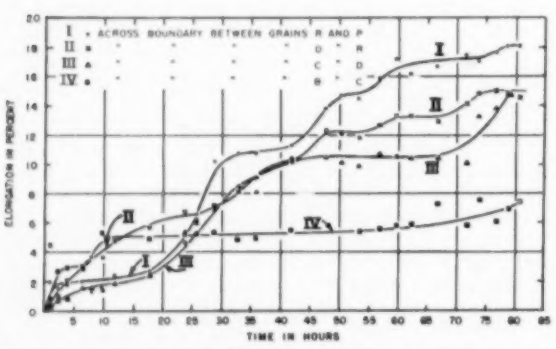

Fig. 2—Specimen P-8, 700°F, 85 psi. Component creep curves across grain boundaries of various orientations with respect to the specimen axis. See Fig. 1 for location of markers.

before another period of increasing creep rate could occur after about 65 hr.

The grain boundary between grains *D* and *R*, with two small grains *E* and *G* (Fig. 1) at its ends offering relatively small resistance, was favorably oriented for sliding. Extensive deformation occurred from the very beginning, showing a fairly continuous increase in elongation, curve II, Fig. 2.

Curve I, Fig. 2, shows the component creep curve across the boundary between grains *R* and *P*. This boundary at the reference marks, Fig. 1, is a short straight boundary close to 45° to the stress axis. Furthermore, this region of the specimen contains more grains (finer grain size) than the rest of the specimen. It was shown previously[2] that the extent of grain boundary sliding and migration increases with decreasing grain size at high temperatures. The large initial creep deformation and the final large deformations are the result of this particular grain arrangement. After about 80 hr, at a time

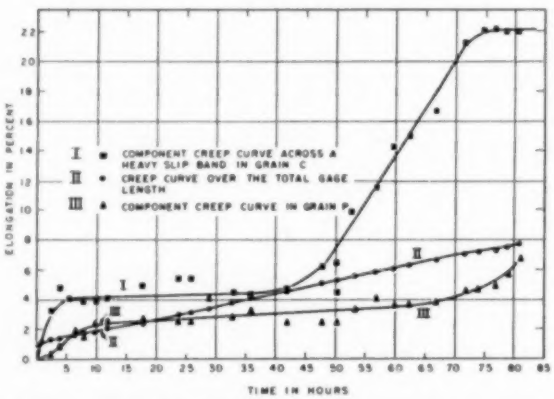

Fig. 3—Specimen P-8, 700°F, 85 psi. Component creep curves in the grains and a creep curve over the total gage length. See also Fig. 1.

when the total deformation for the specimen was about 8 pct, this was 18 pct elongation across boundary *RP* and as little as 7.5 pct across boundary *BC*.

It is interesting to note from the curves in Fig. 2, curves I and II in particular, that the periodicity of decreasing and increasing rates gets smaller as the amount of creep increases.

Many component creep curves were also obtained in the grains of specimen P-8. Two typical examples of these are shown in Fig. 3, curves I and III.

Curve I was obtained across a heavy slip band in grain *C*. The nature of a component creep curve across such a band has been discussed.[3] It is shown here for the purpose of comparison with curve III, which was obtained in a region of grain *P* where subgrains, instead of heavy slip bands, were formed. The amount of extension in a region in which subgrains were formed, as curve III demonstrates, is very much less than that in a region in which heavy slip bands were formed. However, they are qualitatively similar in that they show a cyclic behavior.

In Fig. 3 is also shown the creep curve over the entire gage length of the specimen, curve II. Regardless of the step-wise nature of component creep curves obtained from this specimen, P-8, curve II is not only similar to the conventional creep curve but is also surprisingly smooth.

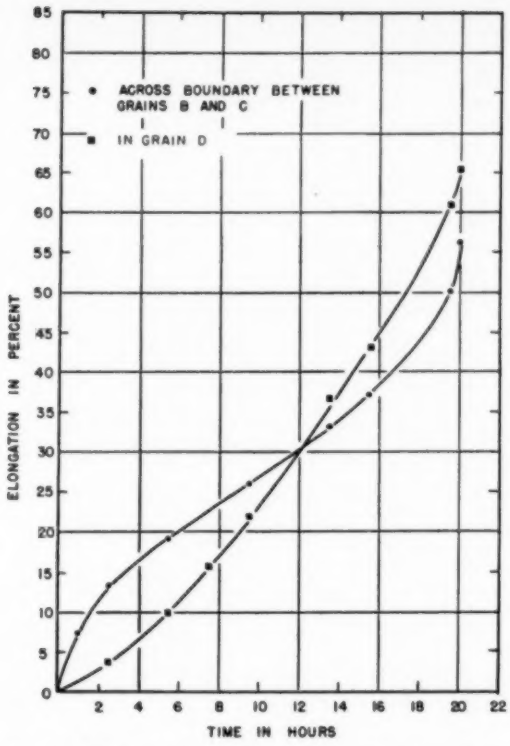

Fig. 4—Specimen P-6, 700°F, 200 psi. Component creep curves. See Fig. 6.

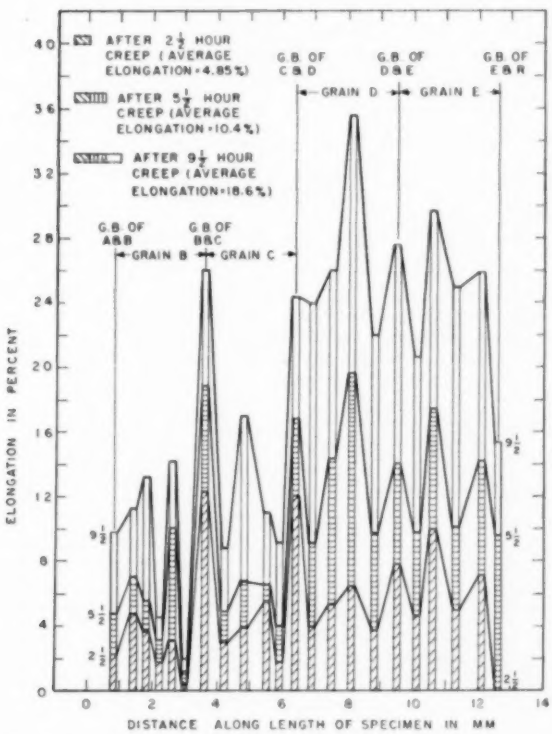

Fig. 5—Specimen P-6, 700°F, 200 psi. Deformation along the gage length of specimen P-6 (see Fig. 6) after fixed intervals of time, comparing relative creep across grain boundaries and within grains.

In order to show the effect of higher stresses on the form of component creep curves, two typical component creep curves, one across a grain boundary and the other for a grain, obtained from specimen P-6, are shown in Fig. 4. The development diagram of this specimen is shown in Fig. 5. Specimen P-6 was subjected to creep at 700°F and 200 psi (fractured in about 22 hr), whereas P-8 was at 700°F and 85 psi. The initial period of rather rapid increase of creep strain across a grain boundary, curve I, was in accord with the optical observations during the test which showed that boundary sliding and migration were primarily responsible for the deformation in the early period at 700°F. Comparison of curves I and II, Fig. 4, shows that deformation in the grains can overtake the deformation across the grain boundaries, in the later stages of creep.

It appears that the step-wise nature of component creep curves at high stresses, Fig. 4, is less distinct than at low stresses, Figs. 2 and 3; however, the infrequency of measurements relative to the creep rate of this specimen is very probably one of the reasons.

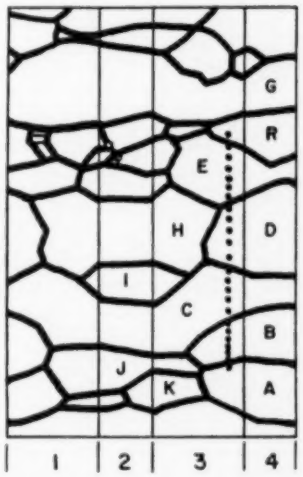

Fig. 6—Structural development drawing of specimen P-6, tested at 700°F and 200 psi. Black dots indicate reference marks for component creep curves. 1—Back surface. 2—Left edge. 3—Front surface. 4—Right edge.

Fig. 5 shows a plot taken from specimen P-6 of percentage elongation, represented by blocks between consecutive markers along the gage length of the specimen (see Fig. 6) at three different time intervals during the course of the creep test. Each column along the abscissa is at the midpoint between two reference markers, the distances being taken with respect to grain boundary *AB* as a reference. The areas between the various time levels show the deformation which has occurred in that time interval. The elongation at a grain boundary was arbitrarily considered as the elongation between two reference marks across the grain boundary. Fig. 5 also shows that boundaries, oriented favorably for the application of shear stress, such as the boundaries of grains *B* and *C*, and *D* and *E*, show greater deformation than less favorably oriented ones. That the elongation across the boundary between grains *E* and *R* is relatively small in comparison with the other three equally favorably oriented boundaries may be the result of a slight orientation difference across this grain boundary in addition to the complicated arrangement of the grains in that part of the specimen.

The point mentioned above in connection with Fig. 4, that the amount of deformation in the grains

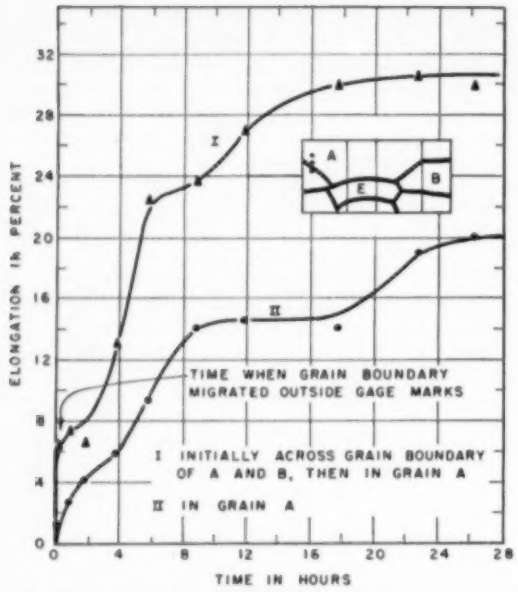

Fig. 7—Specimen P-10, 1100°F, 50 psi. Component creep curves showing large initial deformation due to grain boundary sliding and migration. Insert shows a portion of the development diagram of specimen P-10.

overtakes that across the grain boundary in the later stages of creep, is more clearly illustrated in the case of grain *D*, Fig. 5. It can be seen from this figure that after 2½ hr of creep, the largest elongation in grain *D* was about 7 pct whereas the elongation across the boundary between grains *C* and *D* was 12.5 pct. However, after the specimen was subjected to creep for 9½ hr, the largest elongation in grain *D* increased to 36 pct whereas that across the boundary between grains *C* and *D* increased only to 24.5 pct.

Another point of interest in connection with Fig. 5 is that the elongation in that part of the grain which is close to a grain boundary favorably oriented for sliding is often less than the deformation close to the center of the grains, or across the grain boundaries. It is interesting to compare these results with those obtained by Boas and Hargreaves who measured the local strains of tensile deformed specimens (at room temperatures) of coarse grained commercially pure aluminum.[6] They found that the deformation tends to be continuous across the grain boundaries, and that the grain boundaries, in general, restrict the deformation in the grains. This restricting effect of the boundaries on the deformation in the grains still exists under creep conditions of testing both at high and low temperatures, and results in an elongation, measured in the neighborhood of the grain boundaries, which is often smaller than that in the center of the grains, depending on geometry.

1100°F Test: As shown in a previous publication,[7] a grain boundary in a specimen subjected to creep at 1100°F, migrated quickly in a step-wise manner to a position almost perpendicular to the specimen axis during the early stage of the test, each step of migration being accompanied with small amounts of sliding. Fig. 7 shows two component creep curves obtained on this specimen

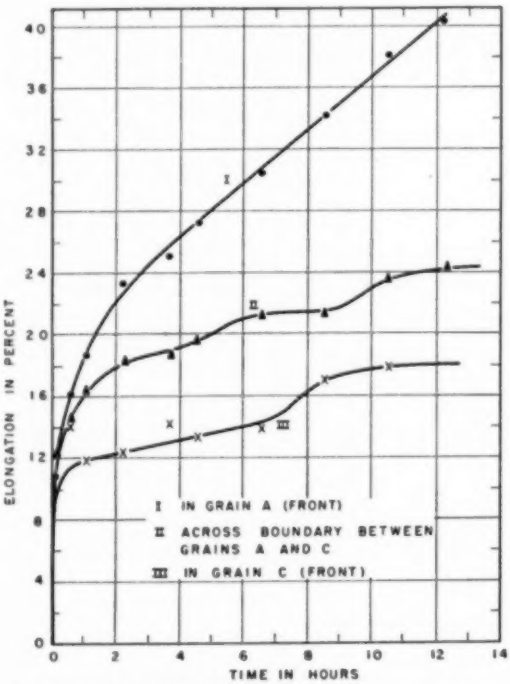

Fig. 9—Specimen P-7, 400°F, 1200 psi. Component creep curves across and adjacent to grain boundary of grains A and C, Fig. 10, representing the case where slip can be transmitted across the grain boundary.

(P-10, tested at 1100°F, 50 psi). Curve I represents a component creep curve obtained across the original boundary between grains *A* and *B* (represented by the two lower reference marks in the insert of Fig. 7). Curve I shows that an elongation of about 7 pct occurred in the first ½ hr period. During this time the grain boundary between grains *A* and *B* slid and migrated down and out of the field covered by the two noted reference marks. In comparison with the upper curve, the balance of which was actually obtained in grain *A*, curve II (the two upper dots are reference marks) shows a relatively small amount of creep in the first ½ hr period. Thereafter, both curves represent the deformation in grain *A* by slip and subgrain formation. Both curves show a cyclic behavior as did those obtained from specimen P-8 tested at 700°F.

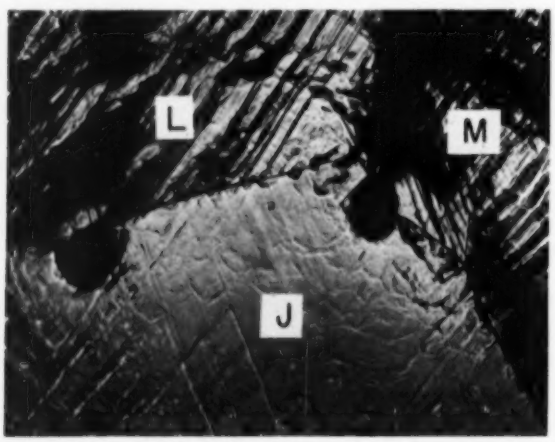

Fig. 8—Specimen P-11, 400°F, 400 to 750 psi. Illustration of restriction of deformation due to orientation and geometry effects. Note especially grain J. X100. Area reduced approximately 50 pct for reproduction.

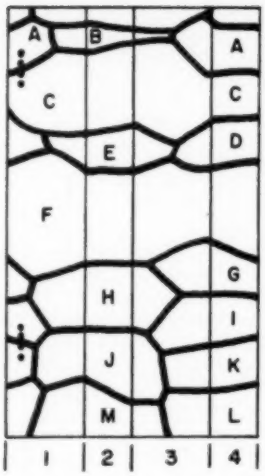

Fig. 10—Structural development drawing of specimen P-7, tested at 400°F and 1200 psi. Black dots indicate the reference marks for component creep curves. 1—Front surface. 2—Right edge. 3—Back surface. 4—Left edge.

As in the previous instances the deformation throughout the specimen, as measured by component creep curves, is severely inhomogeneous.

400°F Test: It has been shown[8] that creep deformation at 400°F, in contrast to that at 700° to 1100°F, is characterized by slip band formation in the early stages of creep and by slip and subgrain formation in the later stages of creep. Grain boundaries slid slightly only in the late stages of creep. Clear steps of boundary migration were not observed at this temperature. Thus the characteristics of deformation at this temperature are more similar to those of room temperature deformation.

The behavior of the grain boundaries at 400°F can be divided into two types based on grain and grain boundary orientation relationships. The first depends on whether the orientation difference across the grain boundary is small, so that deformation in one grain can be easily transmitted to the other grain; the second type depends on whether the adjacent grains are of such orientation that the deformation in both grains is restricted, see grains *L* and *J*, Fig. 8.

The nature of the creep curve for the case where deformation can continue across the grain boundary is shown in Fig. 9 for specimen P-7, tested at 400°F and 1200 psi. Curve II shows the elongation across the boundary between grains *A* and *C*, Fig. 10. The elongation values shown in curve II lie in between those of curves I and III. Curves I and III represent the creep in grains *A* and *C*, respectively, in the vicinity of the boundary. The case wherein the deformation in both grains is restricted, is shown in Fig. 11. The extent of deformation across the grain boundary is smaller than that in either grains. A creep curve over the whole gage length is also shown in Fig. 11 for specimen P-7, and again a smooth creep curve was obtained.

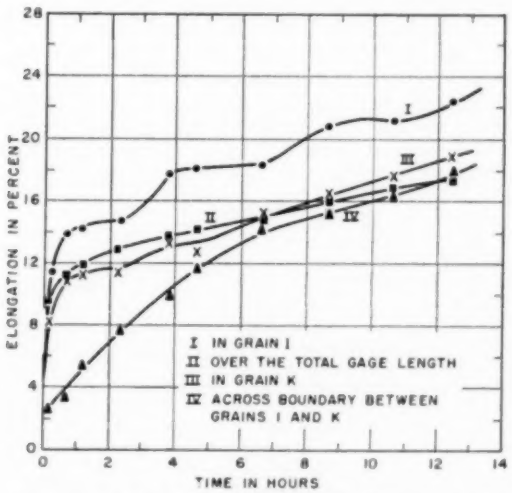

Fig. 11—Specimen P-7, 400°F, 1200 psi. Component creep curves across and adjacent to grain boundary of grains I and K, Fig. 10, representing the case where orientation difference across the grain boundary is large.

Fig. 12 was prepared in the same way as Fig. 5. It can be seen that the deformation in the grains follows the same general trend at two different times. The peaks and valleys appeared to correspond respectively to regions between reference marks which included heavily slipped bands and

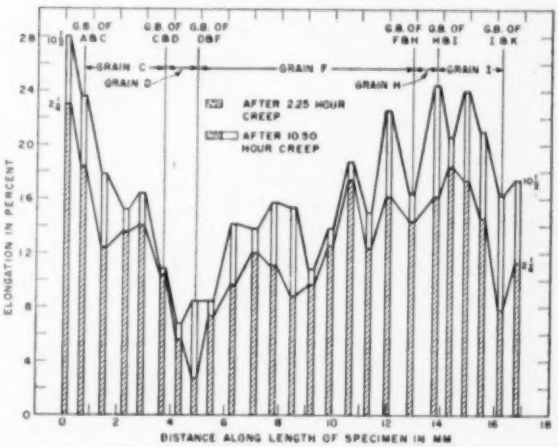

Fig. 12—Specimen P-7, 400°F, 1200 psi. Deformation along the gage length of specimen P-7 (see Fig. 10) after fixed intervals of time, comparing relative creep across grain boundaries and within grains.

regions between markers where deformation was less noticeable. While the initial deformation across grain boundaries was relatively small, the amount of deformation became more significant in the later stages of creep, as for example across the boundaries between grains *D* and *F* and between grains *H* and *I*, Fig. 12. This corresponds to the optical observation that at 400°F boundary sliding occurs in the later stages of creep with the initial deformation occurring primarily in the grains.

Fig. 12, for the 400°F, 1200 psi creep test, when compared with the same kind of plot for specimen P-6 tested at 700°F, Fig. 5, shows that in general the grain boundary regions show more restricted deformation than regions removed from the grain boundary. The phenomena which have been described above in connection with Figs. 9 and 11 are also clearly revealed in Fig. 12.

Thus, at 400°F, although the relative contributions of the grains and grain boundaries are significantly different from 700° and 1100°F, it is still to be noted that the component creep curves still show extreme inhomogeneity of creep deformation in the various portions of the specimen.

Discussion

It has been shown that when a specimen is subjected to creep at 700°F, the deformation in the

grains may eventually overtake the deformation across the grain boundaries, Fig. 4. It is thought that this phenomenon is associated with the nature of the grain boundaries in the later stages of creep. As shown previously,[1] heavy boundary sliding causes the grain boundary to become strongly irregular and angular after boundary migration. Consequently, the angular nature of the grain boundary might be expected to make further sliding difficult or at least to occur in shorter cycles. Whereas it could be expected that the angular grain boundary might decrease the creep rate, the angularities could also initiate slip bands or deformation bands at those places where sharp changes of curvature of the boundary had taken place. This is shown in Fig. 13

The observation that the periodicity of the cyclic processes of boundary creep increases with increasing deformation, Fig. 2, may also be explained by the development of the angular grain boundaries as creep progresses. It is obvious that the more angular the grain boundary becomes the shorter the distance the grain boundary can slide, and therefore the more frequently the cycles of grain boundary migration, i.e., recovery needed for further boundary sliding.

Fig. 13—Specimen P-6, 700°F, 200 psi, front surface. Deformation bands started from that part of the grain boundary where sharp curvature occurred as a result of uneven boundary sliding and migration. X100. Area reduced approximately 25 pct for reproduction.

It must be evident from the data that creep is a complex process, even in high purity materials. The component creep curves show that while the deformation in the grains and across grain boundaries must balance, the relative amounts are a function of the strain, of temperature, of time, and of orientation relationship among the grains and grain boundaries. At 400°F the initial deformations appear to be greater in the grains than in the grain boundaries, whereas at 700° and 1100°F the initial deformation is generally greater along the grain boundary regions. But, equally important, the deformation after a given time varies vastly from one grain boundary to another and from one grain to another. On the other hand, even for these coarse grained test specimens, the overall creep curves have been surprisingly smooth and conventionally shaped to encourage the seeking of equations to describe them.

Thus, while it is admitted that processes of an activation type take place during creep, the cyclic nature of the component creep curves and the large variations in creep rates between adjacent zones in any one specimen make it difficult, if not impossible, to believe that either a single activation process can describe creep behavior or that a single activation process exists. Certainly a different value of activation energy must exist for grain and for grain boundary creep.

It has been suggested by many that such a single activation energy can be determined for creep, however the activation energy is probably a statistical summation of a number of activation processes.

Since the total creep is made up of many dissimilar component creep curves, the creep curve exists only in a statistical sense. The applicability of certain equations to the creep curve must therefore depend on the material tested, time, temperature, etc. No one equation could ever be expected to apply in all instances. The assignment of physical significance[5] to constants in such equations is without basis since the creep curve equation is a statistical equation.

Conclusions

Based on many component creep curves measured between closely spaced consecutive gage marks, in tests run at 400°, 700°, and 1100°F, the following conclusions are drawn:

1—A cyclic behavior is exhibited both across grain boundaries and in the grains. The periodicity of these cycles obtained across grain boundaries appears to increase as creep progresses, but the deformation per cycle decreases.

2—Boundary deformation is very significant in creep from the start of the test for specimens tested at 700° and 1100°F. At 400°F, boundary sliding becomes noticeable only in the later stages of creep.

3—In view of the inhomogeneity of high temperature creep, as exemplified by component creep curves along the length of a test bar, it is unlikely that a single activation process can be considered for creep.

4—Any equation intended to define a conventional creep curve must be considered to be a statistical summation of equations describing the various component processes of creep.

Acknowledgments

The authors wish to express appreciation to A. R. Chaudhuri who contributed significantly to this research. Thanks are also due to the Bureau of Ships for sponsoring this research.

References

[1] H. C. Chang and N. J. Grant: Observations of Creep of the Grain Boundary in High Purity Aluminum. *Trans.* AIME (1952) **194**, p. 619; JOURNAL OF METALS (June 1952).

[2] H. C. Chang and N. J. Grant: Grain Boundary Sliding and Migration and Intercrystalline Failure Under Creep Conditions. *Trans.* AIME (1953) **197**, p. 305; JOURNAL OF METALS (February 1953).

[3] H. C. Chang and N. J. Grant: Mechanism of Creep in Coarse Grained High Purity Aluminum. Unpublished.

[4] W. Boas and M. E. Hargreaves: On the Inhomogeneity of Plastic Deformation in the Crystals of an Aggregate. *Proc.* Royal Soc. (1948) **A193**, p. 89.

[5] T. H. Hazlett and E. R. Parker: Nature of the Creep Curve. *Trans.* AIME (1953) **197**, p. 323; JOURNAL OF METALS (February 1953).

Plastic Stress-Strain Relations for Aluminum Alloy 14S-T6 Subjected to Combined Tension and Torsion

by Joseph Marin and H. A. B. Wiseman

This paper presents results of an experimental study dealing with the plastic stress-strain relations of aluminum alloy 14S-T6 subjected to combined biaxial tension and compression stresses. Plastic stress-strain relations for both constant and various types of variable stress ratios were determined and a comparison made with the simple flow theory of plasticity.

THIS investigation was undertaken for two main purposes: 1—to obtain plastic stress-strain relations for Alcoa 14S-T6 when subjected to various combinations of biaxial stresses, and 2—to determine the validity of the flow theory in predicting plastic stress-strain relations for combined stresses. The biaxial stresses used were tension combined with compression. These stresses were produced by subjecting a thin-walled tube to axial tension and torsion.

Various types of combined stress conditions were investigated. To provide control test data and information on the influence of biaxial stresses on the strength, the usual constant stress ratio type tests were made. These tests showed that the biaxial yield strength agrees approximately with the distortion energy theory. However, the Prager semi-empirical theory agrees best with the test results. For these constant stress ratio tests the plastic stress-strain relations were found to agree approximately with the flow theory. (For constant stress ratio the flow and deformation type theories are identical.)

In view of the fact that the constant stress ratio tests cannot distinguish between the flow and deformation theories, a number of variable and special biaxial stress tests were made. These tests showed that the flow theory is inadequate, since large differences exist between the experimental and theoretical results.

Special tests were also conducted to check the validity of the isotropic yielding assumption. This assumption is made in the linear-type flow theory. In these tests specimens were loaded in tension to predetermined values beyond the proportional limit stress. The tension load was removed from the specimen and the specimen was subsequently loaded in torsion to fracture. Other tests were applied with the order of torque and tension loading reversed. The nominal stress-strain curves for these two tests approximately coincide indicating that the assumption of isotropic yielding is valid. In addition, these tests verified the requirement by the slip theory of plasticity that prestraining below 140 pct of the proportioned limit stress in either torsion or tension did not influence the subsequent plastic stress-strain relations in tension or torsion.

Another type of test was conducted to check the assumption that the axes of principal stress and strain coincide during plastic flow and variable stress conditions. These tests were conducted by applying combinations of axial tension, internal pressure, and torsional loads such that the axes of maximum principal stress could be rotated through 90° during the loading path. The results of those tests showed that the angle between the axes of principal stress and strain varied greatly and that the assumption of coincidence between axes of principal stress and strain is not valid.

Introduction

In various metal processes including forming of sheets, rolling of bars, and extrusion of rods, metals are subjected to stresses beyond the yield strength of the material. Often these stresses are not simple stresses acting in one direction, but are combined stresses acting in more than one direction. Structural and machine members are often subjected to combined stresses. To adequately determine the factors of safety for these members, it is necessary to know the plastic stress-strain relations of the material used for various combined stress conditions.

Various theories have been proposed for predicting the plastic stress-strain relations for combined stress in terms of the simple tension plastic stress-strain relation for the material. To determine which theory might be adequate, test results must be obtained for various combined stress conditions, in order to compare the actual with the assumed theoretical behavior. Although there is considerable test data available for combined stress conditions in which the principal stress ratios are constant, relatively little test information is available for vari-

J. MARIN and H. A. B. WISEMAN are associated with the Dept. of Engineering Mechanics, The Pennsylvania State College, State College, Pa.

Discussion on this paper, TP 3605E, may be sent, 2 copies, to AIME by Dec. 1, 1953. Manuscript, Sept. 10, 1952; revision, March 17, 1953. Cleveland Meeting, October 1953.

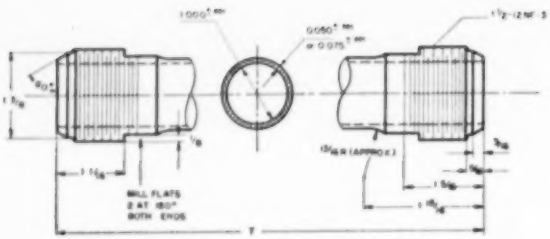

Fig. 1—Tubular specimen tension diagram.

able stress conditions. In order to determine the adequacy of the flow theory,* constant stress ratio tests are inadequate since for the case of constant stress ratios the flow and deformation theories coincide. This paper gives the results of an investigation for both constant and variable combined stress conditions. Special tests are also reported in which the validity of basic assumptions made in flow theory are checked.

* When reference is made to the flow theory the simple isotropic theory based on the octahedral or significant stress and strain is intended.

Test Procedure

Material Tested and Specimens: The material tested was an aluminum alloy designated as 14S-T6. The material was supplied in the form of hot-rolled machined cylinders 7¼ in. long with a 1⅝ in. OD and a 11/16 bore. The normal composition in addition to aluminum and normal impurities, consists of 4.4 pct Cu, 0.8 pct Si, 0.8 pct Mn, and 0.4 pct Mg. The Research Laboratories of the Aluminum Co. of America supplied control data on the yield strength, tensile strength, and ductility. These data were obtained primarily to provide information on the degree of anisotropy of the specimens. For this purpose, specimens taken from the cylinders were tested in the axial, lateral, and diagonal directions. The average values of the properties were: yield strength 62,400 psi ±3 pct, tensile strength 69,100 psi ±4 pct, elongation in 4 diameters 6.5 to 12 pct. The data supplied showed that only about one-half the percentage variations in strength was due to anisotropy, the remaining differences being due to normal variations in the material.

The dimensions of the machined specimen are given in Fig. 1. Both the inside and outside surfaces of the specimens were machined. The wall thicknesses of the tubular specimens were measured using the apparatus previously described.[1] The ratio of the wall thickness to diameter was selected so as to delay buckling as much as possible and at the same time to yield an essentially uniform stress distribution throughout the wall of the specimen.

Testing Machine: The special tension-torsion machine as shown in Fig. 2 was designed to conduct the tests described in this report. The axial tensile load is applied to the tubular specimen (*S*) by means of the hydraulic jack (*H*) through the pulling rod (*R*). The axial load is measured by the SR-4 dynamometer (D_a). The twisting moment is applied by a ¾ hp dc motor (*M*) and speed reducer (*SR*). Variation in rate of application of torque load is provided by rheostat (*RH*) and a motor generator set. A disk (*D*) is attached to the lower part of the specimen to which cables are connected passing over frictionless pulleys to the bar (*B*). The torque is measured by the calibrated bar (*B*) using SR-4

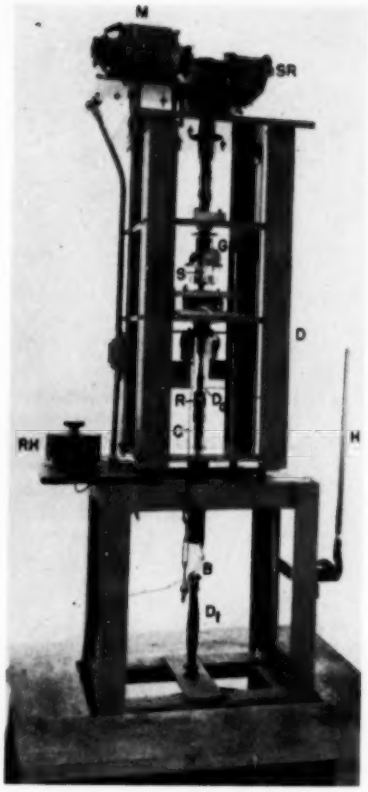

Fig. 2—Tension-torsion testing machine.

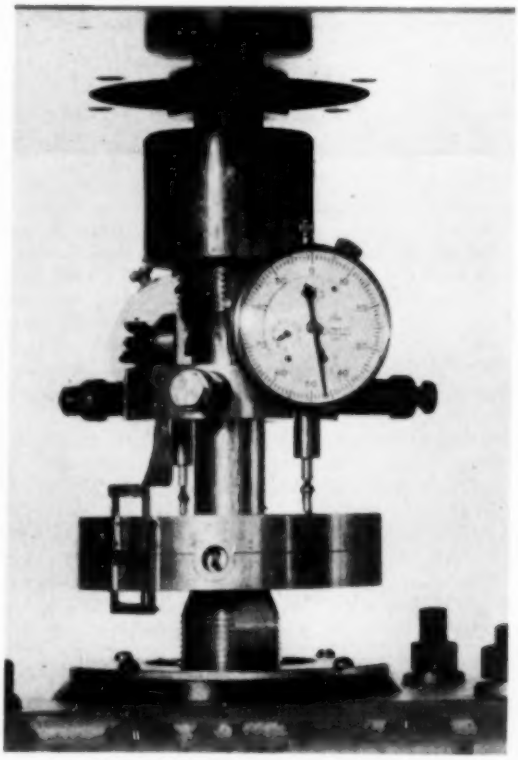

Fig. 3—Tension-torsion strain gage.

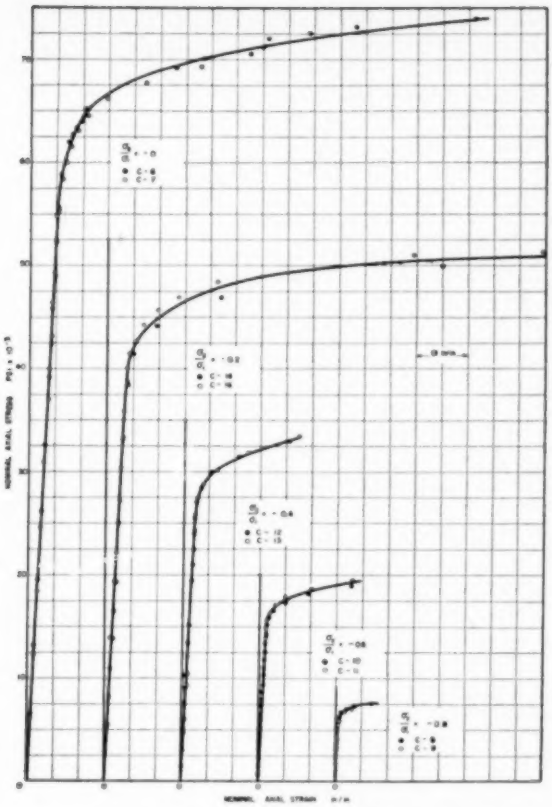

Fig. 4a (above)—Stress-strain relations for constant stress ratio tests, nominal axial stress and strain.

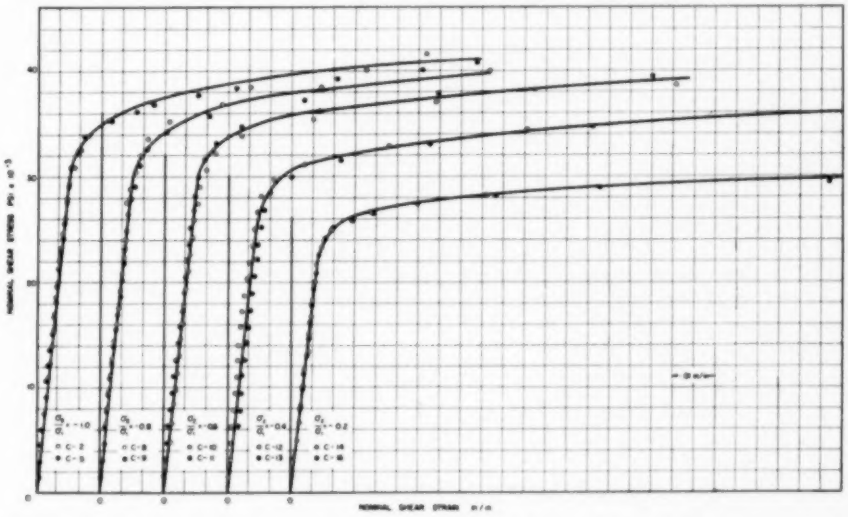

Fig. 4b (right)—Stress-strain relations for constant stress ratio tests, nominal shear stress and strain.

strain gage to the specimen during plastic flow was maintained by rods which bear on the specimen at one end and are connected by preloaded springs to the strain gage at the other end. By adequate initial spring pressure, the gage remained attached to the specimen without slipping even in cases where the specimen had considerable reduction in diameter.

Method of Testing: The specimen is first assembled in the testing machine with the elastic SR-4 gages and the special mechanical gage as shown in Fig. 3. Increments of axial tensile load and torque are then applied as prescribed by the particular test. For each load increment applied, axial strain and angle of twist readings are recorded.

Constant Stress Ratio Tests

Plastic stress-strain relations for various constant values of the biaxial stress ratios were obtained to provide information on the influence of biaxial stresses on the plastic stress-strain relations and on the yield strength.

Conventional Stress-Strain Results: The average conventional stress-strain curves for various principal stress ratios and for the axial and shear stress components are shown in Fig. 4a and b. The values of the nominal axial and average shear stresses used in Fig. 4 were determined respectively from the approximate relations.

$$\sigma_a^1 = \frac{P}{\pi t(d+t)} \qquad [1]$$

and

$$\tau_{ay}^1 = \frac{2M_t}{\pi t(d+t)^2} \simeq \frac{2M_t}{\pi dt(d+2t)} \qquad [2]$$

strain readings to indicate the load. A 2000 lb dial-type dynamometer (D_b) is attached to the bar (B) to check the foregoing torque value. In some tests in addition to axial tension and torsion, internal pressure was applied by a specially built pump unit not shown in the Fig. 2.

Method of Measuring Strains: A special mechanical-type strain gage was designed for the measurements of plastic angles of twist and axial strains as shown in Fig. 3. By this mechanical gage, axial strains were measured for a 2 in. gage length by two 0.0001 in. dials placed 180° apart. The angles of twist were measured for a 2 in. gage length by the twistmeter part of the gage. Attachment of the

where P is the axial load; M_t, the twisting moment; d, the internal diameter of the specimen; and t, the wall thickness.

The nominal axial and shear strains for the above stresses in terms of the measured strains are, respectively,

$$e_a = \frac{\delta_{1a} + \delta_{2a}}{2L_o} \qquad [3]$$

$$\gamma_{ay}^1 = \frac{\pi}{360}\,\frac{(d+t)}{L_o}\,\rho \qquad [4]$$

where δ_{1a}, δ_{2a} are the measured axial strains on op-

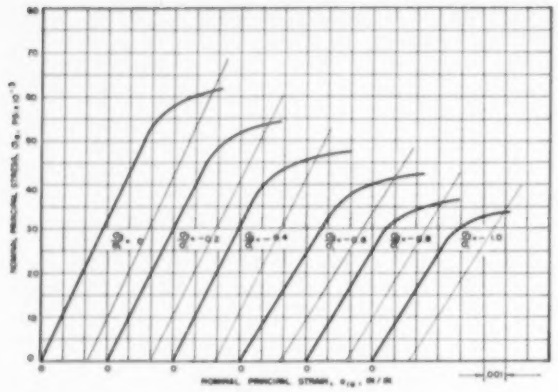

Fig. 5a—Elastic stress-strain relations for constant stress ratio tests for maximum principal yield stress.

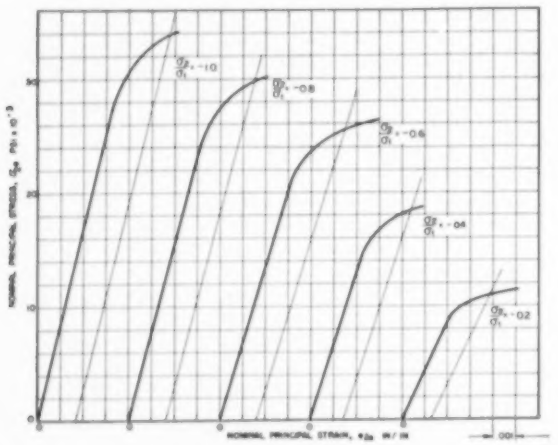

Fig. 5b—Elastic stress-strain relations for constant stress ratio tests for minimum principal yield stress.

posite sides of the specimens; L_o is the gage length; and p, the angle of twist in degrees.

The initial elastic part of the nominal stress-strain diagrams are shown in Fig. 5a and b for the maximum and minimum nominal principal stress values. The values of the nominal principal stresses and strains used for plotting Fig. 5a and b have been shown to be, respectively,

$$\left.\begin{matrix}\sigma_{1e}\\ \sigma_{2e}\end{matrix}\right\} = \frac{\sigma_x^1}{2} \pm \sqrt{\left(\frac{\sigma_x^1}{2}\right)^2 + (\tau_{xy}^1)^2} \qquad [5]$$

$$\left.\begin{matrix}e_{1e}\\ e_{2e}\end{matrix}\right\} = \frac{e_x + e_y}{2} \pm \tfrac{1}{2} \sqrt{(e_x - e_y)^2 + (\gamma_{xy}^1)^2} \qquad [6]$$

To define elastic failure or yielding, the yield strength in simple tension will be determined based on an offset strain of 0.002 in. per in., as shown in Fig. 5. For combined stresses an equivalent offset strain value was used to determine yielding.[7]

Plastic Stress-Strain Results: To determine the plastic stress-strain relations, the changes in the dimensions of the specimens must be considered and the true stresses and strains calculated. Fig. 6a and b gives the average true plastic stress-strain relations considering the change in gage length and dimensions in the plastic range. The values of the true stress components in terms of the nominal stresses can be shown to be,[8] respectively,

$$\sigma_x = \sigma_x^1 (1 + e_x) \qquad [7]$$

$$\tau_{xy} = \tau_{xy}^1 (1 + e_x)^{3/2} \qquad [8]$$

Ref. 2 also shows that the true strain components are in terms of the nominal strains

$$\epsilon_x = \ln (1 + e_x) \qquad [9]$$

$$\gamma_{xy} = \frac{\gamma_{xy}^1}{(1 + 1.5e_x)} \qquad [10]$$

The true stresses and strains used in plotting Fig. 6 are those defined in Eqs. 7 to 10.

Analysis and Discussion: A comparison of the experimental and theoretical values of the yield strength for various biaxial stress ratios is given in Fig. 7. The theories shown in Fig. 7 include the distortion energy, and shear theories and a semi-empirical theory by Prager[3] based on the second and third stress invariants. A comparison of the theoretical values and the test results shows that the yield strengths can best be defined by the Prager theory.

A comparison of the flow theory and experimental results was made by plotting the significant stress-strain relations,[4] where the significant stress and strain are, respectively,

$$\bar{\sigma} = \sqrt{\sigma_x^2 + 3\tau_{xy}^2} \qquad [11]$$

$$\bar{\epsilon} = \sqrt{(\epsilon_x)_p^2 + \frac{1}{3}(\gamma_{xy})_p^2} \qquad [12]$$

The total strains and not the increments are considered in the interpretation of these tests, since for constant stress ratio tests the flow theory reduces to the deformation theory. Values of the stress components used in calculating the significant strain are the plastic strains or the total strains less the elastic strains. Fig. 8 gives the significant stress-strain relations for various principal stress ratios. By the flow theory all these relations should coincide with the simple tension plastic stress-strain relation. An examination of Fig. 8 shows that the relations agree approximately and that the flow theory is therefore a good approximation.

In Fig. 6 the plastic stress-strain relations are compared with the values predicted by the flow theory. These results show that the theory gives a reasonable approximation to the test results.

In plotting the theoretical stress and strain values in Fig. 6, the following procedure is used. It is first noted that for constant stress ratios, the deformation and flow theories coincide and the strain components can be shown to be[4]

$$(\epsilon_x)_p = \frac{1}{D}\left[\sigma_x - \frac{1}{2}\sigma_y - \frac{1}{2}\sigma_z\right] = \frac{\sigma_x}{D} \qquad [13]$$

$$(\gamma_{xy})_p = \frac{3}{D}\tau_{xy} \qquad [14]$$

where D is the plasticity modulus.

The total strains in terms of the stress components then become

$$\epsilon_x = \frac{\sigma_x}{E} + \frac{\sigma_x}{D} \qquad [15]$$

$$\gamma_{xy} = \frac{2(1 + u)}{E}\tau_{xy} + \frac{3}{D}\tau_{xy} \qquad [16]$$

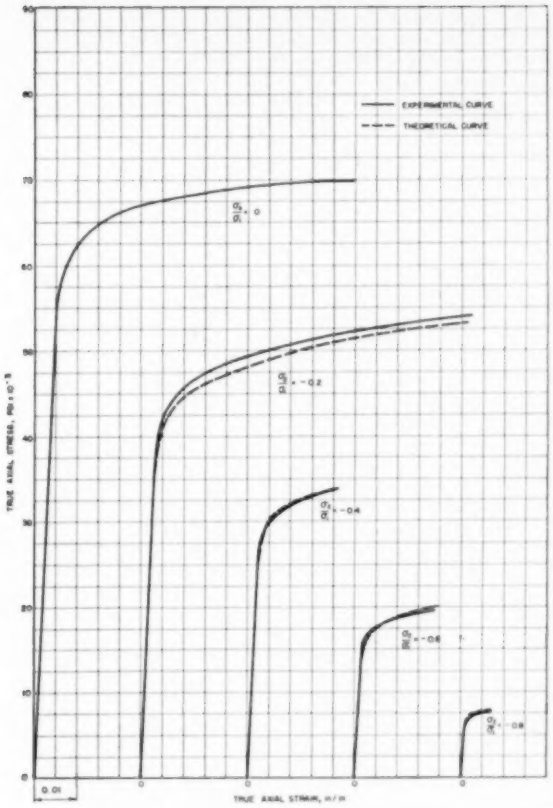

Fig. 6—Comparison of true plastic stress-strain relations with deformation theory for constant stress ratios.
a (above)—True axial stress and strain.
b (right)—True shear stress and strain.

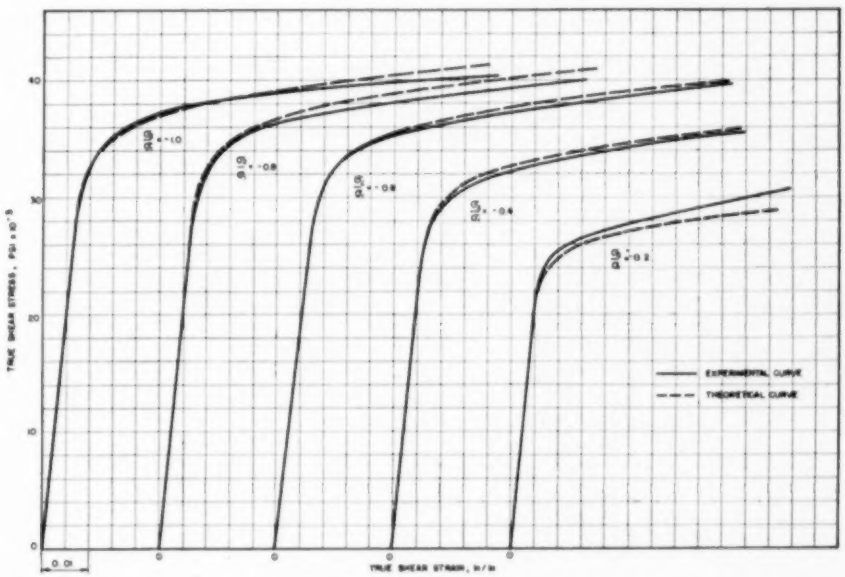

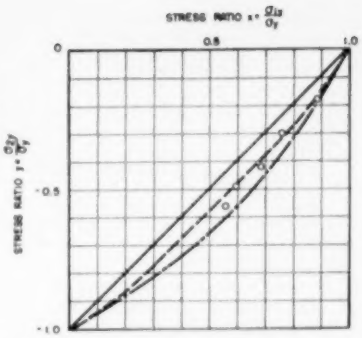

Fig. 7—Comparison of yield strengths with theories of failure. Solid line, shear theory; dashed line, Prager's theory; dash-dot line, deformation theory; circles, test points.

the theoretical strains can be calculated by Eqs. 13 and 14 and the theoretical stress and strain components may then be plotted as shown in Fig. 6.

Variable Stress Ratio Tests Without Unloading—Type A

The foregoing constant stress ratio tests cannot determine the validity of the flow theory, since for constant stress ratios the flow and deformation theories coincide. For this reason, variable stress ratio tests were conducted by applying a stress in one direction followed by stressing in the other direction. Two sets of variable stress ratio tests were made—Set A, in which an axial tensile stress was applied followed by twisting moment and Set B, in which a twisting moment was applied followed by axial tension. In both series of tests various initial amounts of straining in the plastic range were used. Sample nominal stress-strain diagrams for both the axial and torsional stresses are shown in Figs. 9 and 10. The manner of loading and the amount of initial uniaxial stress and strain are also shown in Figs. 9 and 10. The stage of loading is also indicated by points labeled P_0, P_1, and P_2.

Analysis and Discussion: A comparison of the actual true plastic stress-strain relations with the theoretical relations as given by the flow theory for both Set A and B tests are shown in Figs. 11 and 12 for the sample tests. The determination of the theoretical values for the deformations based on the uniaxial tension test results is described in the fore-

From Eqs. 11 and 12, for simple tension, $\bar{\sigma}/\bar{\epsilon} = \sigma/\epsilon_p$ and by Eq. 13 for simple tension $\sigma/\epsilon_p = D$ or

$$\frac{\bar{\sigma}}{\bar{\epsilon}} = D \qquad [17]$$

Eqs. 11, 13, 14, and 17 can now be used to find the theoretical stress-strain relations. For given values of σ_x and τ_{xy}, $\bar{\sigma}$ can be found by Eq. 11. Using the simple tension plastic stress-strain relations in Fig. 8, for a given stress $\bar{\sigma}$ the strain $\bar{\epsilon}$ can be found from the curve and $D = \bar{\sigma}/\bar{\epsilon}$ determined. With D known,

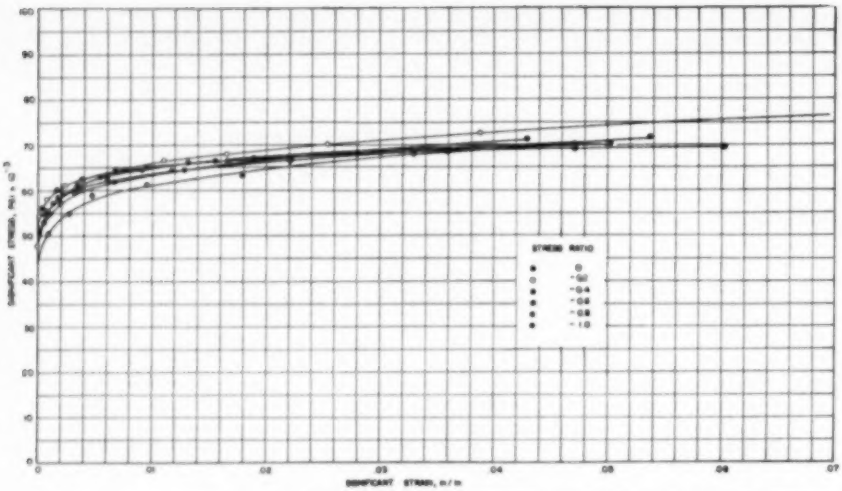

Fig. 8—Comparison of significant stress-strain relations with uniaxial stress-strain values for constant stress ratio tests.

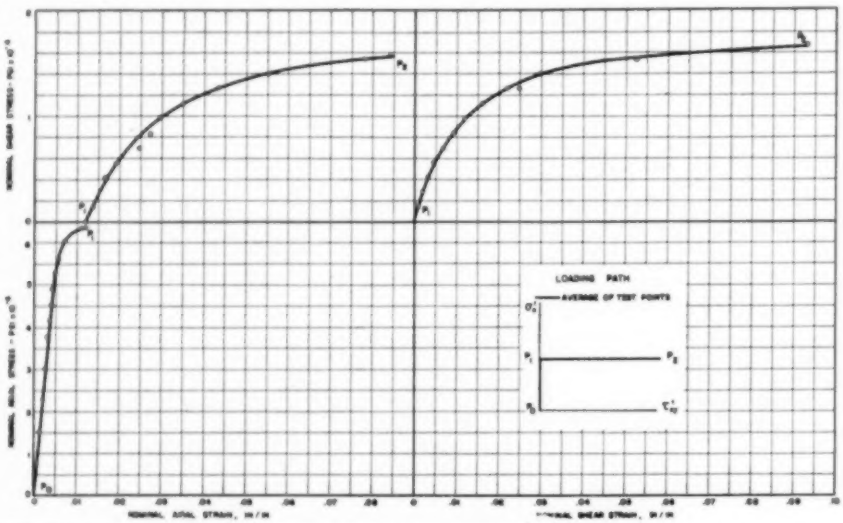

Fig. 9—Nominal stress-strain relations for variable stress ratio tests. Set A.

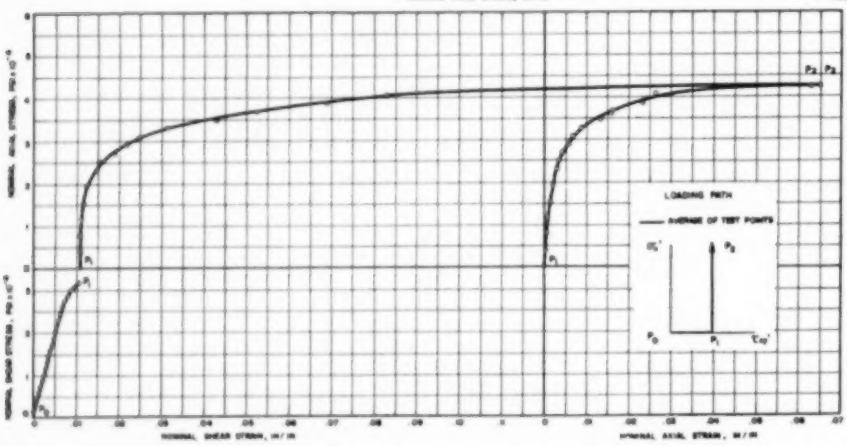

Fig. 10—Nominal stress-strain relations for variable stress ratio tests. Set B.

going section. The theoretical values based on the flow theory were computed as discussed in the appendix. From Figs. 11 and 12 it is seen that the flow theory is in poor agreement with the test results. An empirical relation is also shown in Figs. 11 and 12 based upon the equation

$$\bar{\sigma}^2 = \sigma_s^2 + 3\tau_{xy}^2 + e^{-k\alpha}\,\sigma_s\,\tau_{xy} \qquad [18]$$

where e is the Naperian base and k and α are experimental constants. Although this empirical relation proposed has no theoretical basis, it appears to agree well with the test results. The foregoing conclusion was also noted for three other sets of data not included herein because of space limitations. The deformation theory is mathematically inconsistent for variable stress ratios and Figs. 11 and 12 show that this theory is in poor agreement with the test results.

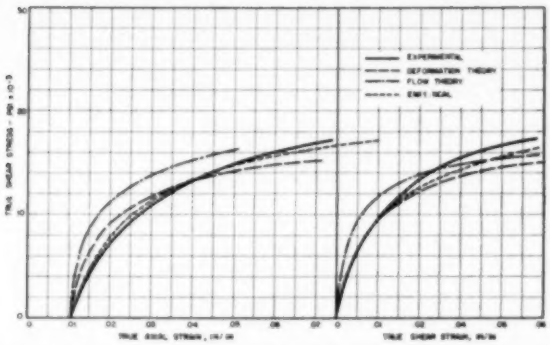

Fig. 11—Comparison of true stress-strain diagrams with plasticity theories for variable stress ratio tests. Set A.

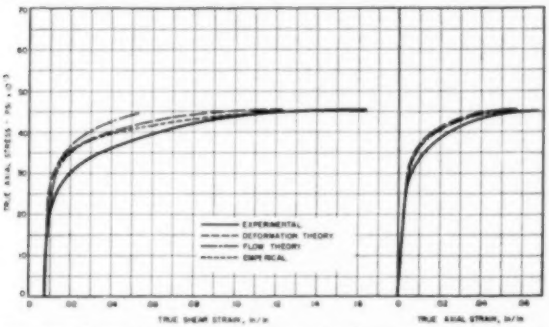

Fig. 12—Comparison of true stress-strain diagrams with plasticity theories for variable stress ratio tests. Set B.

Variable Stress Ratio Tests Without Unloading—Type B

Another type of variable stress ratio test conducted in this study consisted in loading first in tension then torsion followed by tension as indicated in Fig. 13. Four different tests were made in which true initial axial stresses were 54,250, 56,000, 57,100, and 58,100 psi, followed by a shear stress of 14,400 psi in each test prior to final stressing to failure in tension. Another group of four tests illustrated in Fig. 14, consists of loading in the order torsion, tension, and torsion. In these tests initial torsional stresses were selected equal to one-half the initial tensile values and the subsequent tensile stresses were taken as twice the torsional stress used above or 28,800 psi. The nominal stress-strain relations for one sample of each of these tests are illustrated in Figs. 13 and 14. Figs. 15 and 16 give the true stress-strain relations corresponding to Figs. 13 and 14. The theoretical plastic stress-strain results based on the flow theory are also shown in Figs. 15

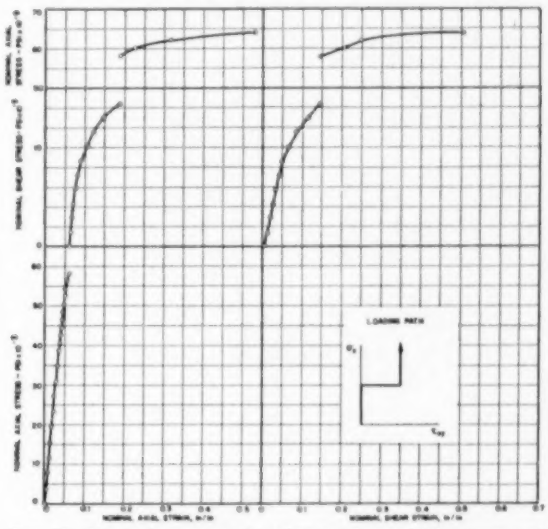

Fig. 13—Nominal stress-strain relations for variable stress ratio tests. Set C.

and 16. All four sets of test results show poor agreement with the flow theory. However, an empirical relation based upon Eq. 18 gives, as indicated in Figs. 15 and 16, a good representation of the test results.

Special Unloading Tests

It is assumed in the isotropic linear flow theories that initial prestrains will not produce anisotropy. In other words, it is assumed that isotropic yielding occurs. To determine the accuracy of this assumption a test was made in which a specimen was stressed first in the axial tension direction to a specified strain value. This axial stress was removed

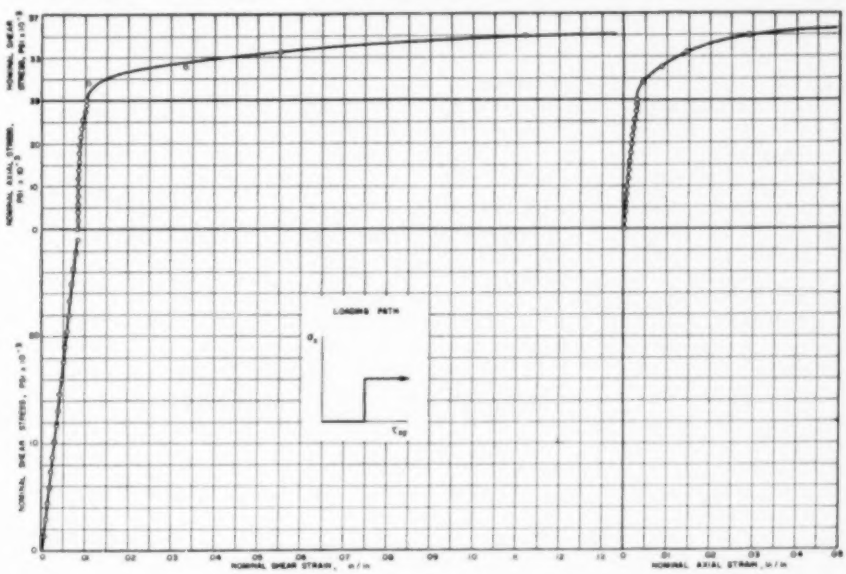

Fig. 14—Nominal stress-strain relations for variable stress ratio tests. Set D.

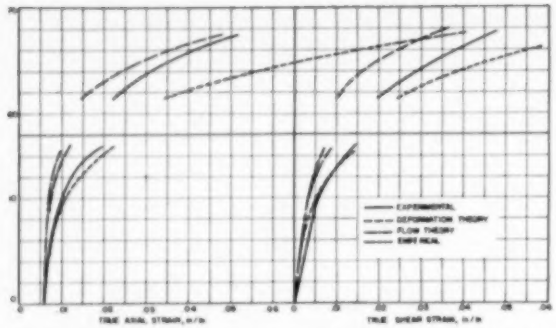

Fig. 15—Comparison of true stress-strain diagrams with plasticity theories for variable stress ratio tests. Set C.

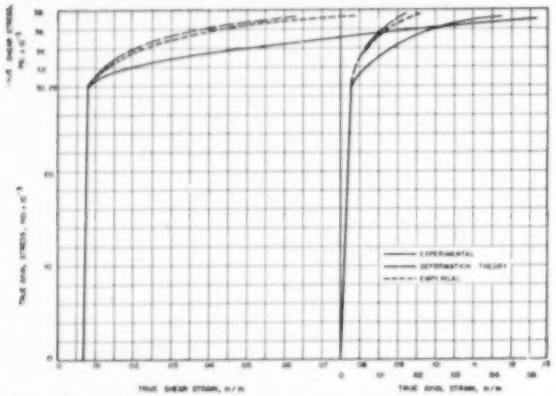

Fig. 16—Comparison of true stress-strain diagrams with plasticity theories for variable stress ratio tests. Set D.

and the specimen was stressed in torsion until failure occurred. Another specimen was initially stressed in torsion to an equivalent initial strain value as used in the first specimen. The torsional stress was then removed and axial tension stress was applied to failure. For the assumption of isotropic yielding to be valid, the nominal stress-strain curves for each of the foregoing tests should coincide.

Two sets of tests were made as described for initial stresses in tension and torsion equal to 120 and 140 pct of the proportional limit stress. A comparison of the stress-strain relations with the nominal stress-strain relations based on pure torsion and simple tension respectively are shown in Figs. 17 and 18. Since these stress-strain relations are in approximate agreement it may be assumed that the assumption of isotropic yielding is verified by these tests.

Variable Stress Ratio Tests

Tests were conducted to determine if the directions of the principal stresses and strains coincide during plastic flow under conditions where the principal stress ratio is variable. For this purpose four tests were conducted in which the significant stress was maintained constant throughout the combined stress loading, but the maximum principal stress direction was varied from 0° to 90° by changing the relative magnitudes of the axial tension, internal pressure, and torque applied. The four tests conducted were for significant stress values of 55,000, 57,500, 59,000, and 60,000 psi. For each load increment the strain components were measured and the directions of the maximum principal strain were computed. The differences between the directions of the maximum principal stress and principal strain are represented as a function of the principal stress direction in Fig. 19. An examination of these results shows a variation between about 2° and 18°, indicating that the direction of the principal stresses and strains cannot be assumed to coincide.

Conclusions

For the Alcoa 14S-T6 tested and for biaxial stresses obtained in combined tension and torsion the main conclusions that can be made based on the results obtained are:

1—The plastic stress-strain relations for combined stresses and constant stress ratios can be approximately defined by the flow theory.

2—Two types of variable stress ratio tests indicate that the flow theory is inadequate for defining the plastic stress-strain relations.

3—Special unloading tests confirm the assumption of isotropic yielding made in the linear flow theories.

4—The assumption that the direction of the principal stresses and strains coincide is disproved by the test results obtained.

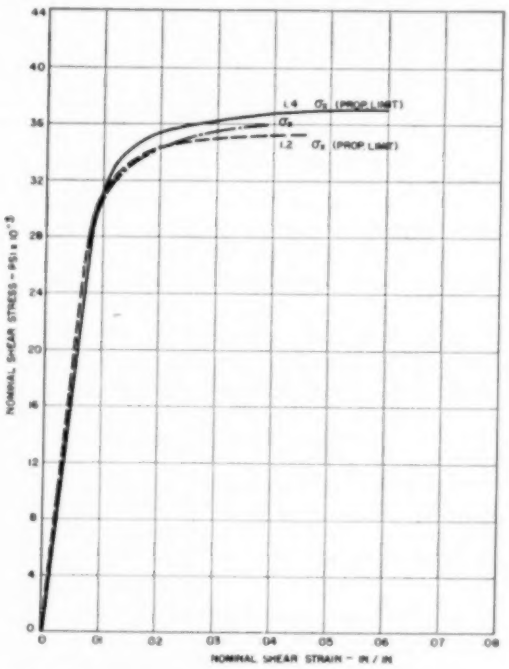

Fig. 17—Comparison of stress-strain relations for special tests with pure torsion.

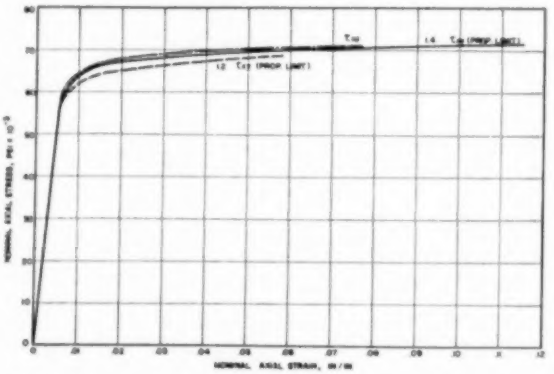

Fig. 18—Comparison of stress-strain relations for special tests with simple tension.

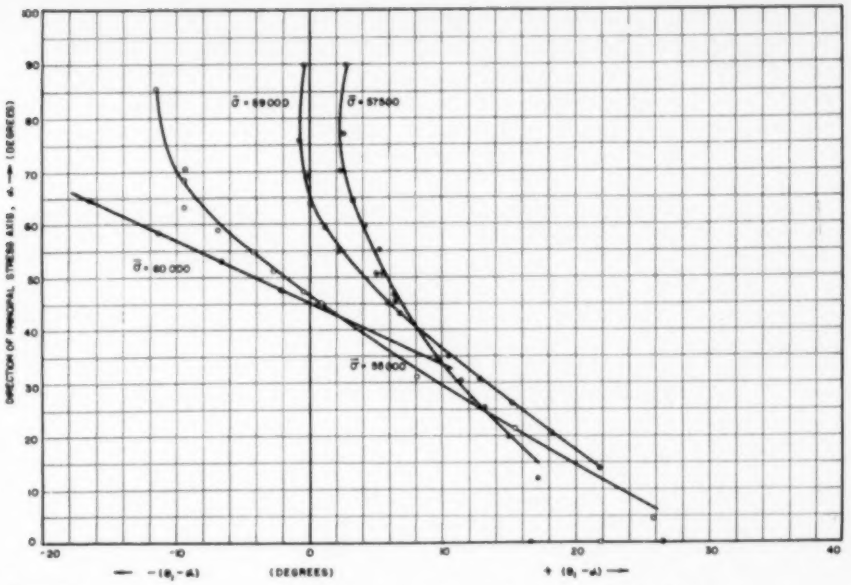

Fig. 19—Comparison of the direction of the principal stress axis with the difference between the direction of the principal strain axis and the direction of the principal stress axis.

Acknowledgments

The research described in this paper was performed in the Plasticity Laboratory of The Pennsylvania State College under the sponsorship and with the financial assistance of the Office of Ordnance Research of the Army Department. H. A. B. Wiseman, L. W. Hu, and J. Hamburg of the Plasticity Laboratory staff conducted the tests. H. A. B. Wiseman also made the necessary calculations for the interpretation of the test results. The testing machine and test specimens were made by S. S. Eckley and L. H. Johnson of the Engineering Mechanics Dept. The assistance given by Office of Ordnance Research and the foregoing individuals in making possible this investigation is greatly appreciated.

Appendix

Determination of Plastic Strain Components by the Flow Theory for Variable Stress Ratios

For an element subjected to normal stresses σ_x, σ_y and σ_z, and shear stress τ_{xy}, τ_{yz} and τ_{zx}, it has been shown[5] that for the simple type isotropic flow theory the increments of strain are defined as

$$\left.\begin{aligned} \delta\epsilon_x &= \left(\frac{\delta\epsilon}{\bar{\sigma}}\right)\left[\sigma_x - \frac{1}{2}(\sigma_y + \sigma_z)\right] \\ \delta\epsilon_y &= \left(\frac{\delta\epsilon}{\bar{\sigma}}\right)\left[\sigma_y - \frac{1}{2}(\sigma_z + \sigma_x)\right] \\ \delta\epsilon_z &= \left(\frac{\delta\epsilon}{\bar{\sigma}}\right)\left[\sigma_z - \frac{1}{2}(\sigma_x + \sigma_y)\right] \end{aligned}\right\} \qquad [19]$$

where

$$\bar{\sigma} = \sqrt{\tfrac{1}{2}\{[(\sigma_x - \sigma_y)^2 + (\sigma_y - \sigma_z)^2 + (\sigma_z - \sigma_x)^2] + 6[\tau_{xy}^2 + \tau_{yz}^2 + \tau_{zx}^2]\}} \qquad [20]$$

and

$$\delta\epsilon = \sqrt{(\delta\epsilon_x)^2 + (\delta\epsilon_y)^2 + (\delta\epsilon_z)^2} \qquad [21]$$

For many engineering materials, including the alloy reported herein, the simple tensile plastic stress-strain relation can be approximately defined by $\epsilon = K\sigma^n$ where ϵ is the plastic strain; σ, the stress; and K and n are experimental constants. For simple tension and by Eqs. 20 and 21, $\bar{\sigma} = \sigma$ and $\bar{\epsilon} = \epsilon$, and since $\epsilon = K\sigma^n$

$$\bar{\epsilon} = K\bar{\sigma}^n \qquad [22]$$

Placing the value of $\bar{\epsilon}$ from Eq. 22 in Eqs. 19

$$\left.\begin{aligned} \delta\epsilon_x &= Kn\bar{\sigma}^{n-2}\left[\sigma_x - \frac{1}{2}(\sigma_y + \sigma_z)\right]\delta\bar{\sigma} \\ \delta\epsilon_y &= Kn\bar{\sigma}^{n-2}\left[\sigma_y - \frac{1}{2}(\sigma_z + \sigma_x)\right]\delta\bar{\sigma} \\ \delta\epsilon_z &= Kn\bar{\sigma}^{n-2}\left[\sigma_z - \frac{1}{2}(\sigma_x + \sigma_y)\right]\delta\bar{\sigma} \end{aligned}\right\} \qquad [23]$$

For the stress state considered in this investigation $\sigma_y = \sigma_z = \tau_{yz} = \tau_{zx} = 0$ and then by Eq. 20

$$\bar{\sigma} = \sqrt{\sigma_x^2 + 3\tau_{xy}^2} = \sigma_x\sqrt{1 + 3\alpha^2} \qquad [24]$$

where $\alpha = \tau_{xy}/\sigma_x$.

From Eqs. 23 and 24

$$\epsilon_x = \int\delta\epsilon_x = Kn\int_{\alpha_1}^{\alpha_2}\sigma_x^n\,(1 + 3\alpha^2)^{\frac{n-2}{2}}\,\delta(1 + 3\alpha^2)^{1/2} \qquad [25]$$

Similarly it can be shown that

$$\gamma_{xy} = 3Kn\int_{\alpha_1}^{\alpha_2}\sigma_x^n\,(1 + 3\alpha^2)^{\frac{n-2}{2}}\,\alpha\delta(1 + 3\alpha^2)^{1/2} \qquad [26]$$

For the case in which σ_x is constant and the stress ratio α is variable Eqs. 25 and 26 become

$$\epsilon_x = \frac{Kn}{n-1}\sigma_x^n\left[(1 + 3\alpha^2)^{\frac{n-1}{2}}\right]_{\alpha_1}^{\alpha_2} \qquad [27]$$

and

$$\gamma_{xy} = \frac{3Kn}{n-1}\sigma_x^n\left[\alpha(1 + 3\alpha^2)^{\frac{n-1}{2}} - \int_{\alpha_1}^{\alpha_2}(1 + 3\alpha^2)^{\frac{n-1}{2}}\,d\alpha\right] \qquad [28]$$

The integral in Eq. 28 can be evaluated by expansion into a Taylor's series. Then for known values of α_1 and α_2 the strains ϵ_x and γ_{xy} can be evaluated.

For the case in which τ_{xy} is constant and the stress ratio α is variable Eqs. 25 and 26 become

$$\epsilon_x = \frac{Kn}{n-1}\tau_{xy}^n\left[\beta(\beta^2 + 3)^{\frac{n-1}{2}} - \int_{\beta_1}^{\beta_2}(\beta^2 + 3)^{\frac{n-1}{2}}\,d\beta\right] \qquad [29]$$

$$\gamma_{xy} = \frac{3Kn}{n-1}\tau_{xy}^n\left[(\beta^2 + 3)^{\frac{n-1}{2}}\right]_{\beta_1}^{\beta_2} \qquad [30]$$

where $\beta = \sigma_x/\tau_{xy} = 1/\alpha$

The integral in Eq. 29 can be evaluated by use of Taylor's series expansion. Then for specific values of β_1 and β_2, the strains ϵ_x and γ_{xy} can be determined using Eqs. 29 and 30.

References

[1] J. Marin, J. H. Faupel, V. L. Dutton, and M. W. Brossman: Biaxial Plastic Stress-Strain Relations for 24S-T Aluminum Alloy: N.A.C.A. T.N. 1536 (1948).

[2] J. Marin, D. H. Ulrich, and W. P. Hughes: Plastic Stress-Strain Relations for 75S-T6 Aluminum Alloy Subjected to Biaxial Tensile Stresses. N.A.C.A. T.N. 2425 (1951).

[3] J. Marin: Stress-Strain Relations in the Plastic Range for Biaxial Stresses. *Journal* Franklin Inst. (September 1949) **248**, No. 3, pp. 231-249.

[4] W. Prager: Strain Hardening Under Combined Stresses. *Journal of Applied Physics* (December 1945) **166**, No. 12, pp. 837-840.

[5] A. Nadai: *Theory of Flow and Fracture of Solids.* Vol. 1, Second Edition (1950) New York. McGraw Hill Book Co.

[6] L. W. Hu and J. Marin: Determination of Theoretical Plastic Stress-Strain Relations for Variable Combined Stress Ratios. *Journal of Applied Mechanics* (December 1952) **19**, No. 4, pp. 485-488.

Technical Note

Crystallographic Angles for Orthorhombic (Alpha) Uranium

by R. B. Russell

SINCE Cahn's[1] paper on plastic deformation in orthorhombic (α) uranium an increasing amount of work is to be expected on orientation of single crystals and preferred orientation in this metal. It would seem desirable to have a table of angles (ϕ) between crystallographic planes (hkl) and (HKL). Table I shows these angles as distances from (100), (010), and (001), and in Fig. 1 as a standard (001) stereographic projection. Only the locations of poles whose diffracting planes produce Cu Kα reflections up to $\theta = 70.5°$ (i.e. (154)) are given.* The relative powder diffraction intensities from the lowest order reflection of these planes are represented by circle diameters. It is hoped that the projection may also be used in making inverse pole figures, originally suggested by Harris.[2]

Table I. Angles Between Crystallographic Planes in Orthorhombic (α) Uranium Calculated from the Data in Ref. 3

	HKL				*HKL*		
hkl	(100)	(010)	(001)	*hkl*	(100)	(010)	(001)
h00	0°	90°	90°	130	55.6°	34.4°	90°
0k0	90	0	90	131	57.5	38.4	71.9
001	90	90	0	132	61.7	46.3	56.9
hk0	—	—	90	133	66.2	53.9	45.6
h0l	—	90	—	134	69.9	55.9	37.5
0kl	90	—	—	135	72.8	64.5	31.5
101	30.0	90	60.0	150	67.6	22.4	90
102	49.1	90	40.9	151	68.2	25.4	77.6
				152	69.6	32.1	66.3
310	9.2	80.8	90	153	71.5	39.4	56.7
311	14.1	81.0	79.3	154	73.4	46.0	48.7
312	29.5	81.9	69.2				
313	30.9	82.0	60.4	172*	74.5	24.2	72.0
110	25.9	64.1	90	061	90	11.2	78.8
331	27.6	64.5	80.2	041	90	16.5	73.5
221	29.5	65.0	75.5	031	90	21.6	68.4
111	37.0	67.2	62.6	021	90	30.7	59.3
223	44.8	69.8	52.1	043	90	41.7	48.3
112	51.4	72.3	44.0	011	90	49.9	40.1
113	60.9	76.3	32.7	045	90	56.0	34.0
114	67.0	79.1	25.8	023	90	60.7	29.3
115	71.1	81.0	21.1	012	90	67.1	22.9
				025	90	71.4	18.6
120	44.2	45.8	90				
241	45.4	46.9	78.3				
121	52.2	49.9	67.5				
243	52.5	53.8	58.2				

* Does not appear with Cu Kα x-radiation.

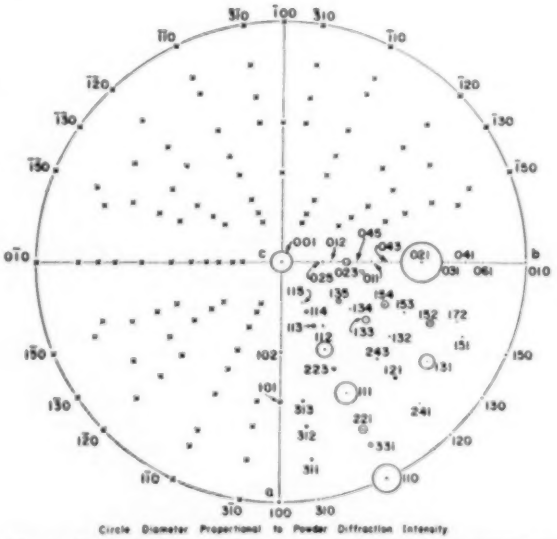

Fig. 1—Standard (001) projection for uranium based on parameters and Cu Kα intensities given by Jacob and Warren.[3]

Values of ϕ were calculated from the expression

$$\cos\phi = d_{hkl}\, d_{HKL} \left(\frac{hH}{a^2} + \frac{kK}{b^2} + \frac{lL}{c^2} \right)$$

where the lattice parameters a, b, c, and the spacings d were taken from the work of Jacob and Warren.[3] (They report $a = 2.852$ kX (2.8578 Å), $b = 5.865$ kX (5.8768 Å), $c = 4.945$ kX (4.9550 Å).) The parameters reported by them may be subject to revision,[4, 5] accordingly the interplanar angles are listed to only the nearest tenth of a degree.

References

[1] R. W. Cahn: *Acta Metallurgica* (1953) **1**, p. 49.

[2] G. B. Harris: *Philosophical Magazine* (1952) **43**, p. 113.

[3] C. W. Jacob and B. E. Warren: *Journal* ACS (1937) **59**, p. 2588.

[4] J. S. Lukesh: *Acta Crystallographica* (1949) **2**, p. 420.

[5] J. Thewlis: *Nature* (1951) **168**, p. 198.

* (172) which does not appear with Cu Kα radiation is also shown (ref. 1).

R. B. RUSSELL is associated with the Division of Industrial Cooperation, Massachusetts Institute of Technology, Cambridge, Mass.

TN 179E. Manuscript, June 19, 1953.

Work performed as MIT Metallurgical Project under Contract No. At(30-1)-981 with the United States Atomic Energy Commission.

Deformation Mechanisms in Alpha Titanium

by E. A. Anderson, D. C. Jillson, and S. R. Dunbar

THE present work was undertaken to furnish information, lacking in the literature, on the deformation mechanisms active in pure titanium at room temperature. Since it was started, Rosi, Dube, and Alexander[1] have indicated that slip can occur in coarse-grained (2 to 6 mm diameter) titanium on the $\{10\bar{1}0\}$ and $\{10\bar{1}1\}$ planes and twinning can take place on the $\{10\bar{1}2\}$, $\{11\bar{2}2\}$ and $\{11\bar{2}1\}$ planes. Liu and Steinberg,[2] working with titanium flakes produced by fused salt electrolysis, found evidence of twinning on the $\{10\bar{1}2\}$, $\{11\bar{2}1\}$, $\{11\bar{2}2\}$, $\{11\bar{2}3\}$, and $\{11\bar{2}4\}$ planes.

The crystals used in the present work were substantially longer (up to nearly 2 in. in length) and possibly purer.

Production of Large Crystals

It was the purpose of this part of the work to provide single crystal or large grain specimens for use in the deformation studies rather than to study the mechanism of crystal growth. Accordingly, all further exploratory studies on methods were abandoned when it was found that cold-rolled bars sealed in vacuo in individual Vycor tubes and given three or more cycles of 4 hr at 1200°C and three to five days at 850°C, gave large grains. Eighteen specimens about 0.2 in. square x 2 in. long yielded 33 useful grains, ranging from ¼ in. to nearly 2 in. in length, with an agreeably wide range of orientations, Fig. 1.

The 0.25 in. thick strip from which the starting specimens were cut had been reduced 67 pct on 18 in. diameter rolls from a scalped, hot-forged (950° to 1000°C), arc-melted, iodide titanium ingot. The bar was at room temperature, but the rolls were at 200°C. Reductions of about 0.03 in. per pass were used. The bar was cut into four segments, each of which was rolled in a somewhat different manner. No effect on the growth of large grains was noted.

E. A. ANDERSON, Member AIME, and S. R. DUNBAR, Associate Member AIME, are associated with the Research Dept., The New Jersey Zinc Co. (of Pa.), Palmerton, Pa., and D. C. JILLSON, Member AIME, formerly with The New Jersey Zinc Co. (of Pa.), is now with General Electric Co., Syracuse, N. Y.

Discussion on this paper, TP 3594E, may be sent, 2 copies, to AIME by Dec. 1, 1953. Manuscript, April 1, 1953. Cleveland Meeting, October 1953.

Table I. Analysis of Titanium Ingot

Element	Pct	Element	Pct
Oxygen	0.027	Molybdenum	Not detected
Nitrogen	0.002	Lead	0.006
Hydrogen	0.0076	Nickel	Not detected
Carbon	0.05	Copper	0.015
Manganese	0.02	Tin	0.008
Iron	0.02	Magnesium	0.006
Aluminum	0.03	Tungsten	Not detected

Note: Metallic elements determined spectrographically; nitrogen by modified Kjeldahl method; oxygen and hydrogen by vacuum fusion on piece of machined, forged bar; carbon by combustion.

The composition of the titanium, determined on turnings from the ingot scalping operations, is given in Table I. The Rockwell A hardness of the ingot was 26.

The standard starting specimens, about ¼x¼x2 in., were milled on all four sides, hand polished on 280 and 400 mesh emery papers, etched for 3 min in a 50 HF-50 glycerine solution, rinsed, and dried in alcohol and ether just before sealing them in Vycor tubes. The average specimen weight was 7.5 g, and the tube volume was 6.5 cc. A vacuum of less than 1 micron pressure was applied.

The specimen tubes were placed in an evacuated Inconel muffle to minimize the danger of collapse of the glass tubes at temperature. In practice the specimens were first heated to 1200°C for 4 hr and then transferred fairly quickly to an 850°C furnace where they were held for three to five days. This cycle was repeated at least three times before the specimens were cooled, removed from the tubes, lightly polished and etched on one surface for examination. Those in which large grains had not developed were resealed in Vycor and returned to the cycling.

Satisfactory specimens (about one out of every four cycled) were polished with emery paper on all four sides, then metallographically polished using etching between wheels to remove distorted metal and, finally, given a very light etch to reveal the grain boundaries. This was necessary because the surface was roughened by the sublimation of titanium under high temperature vacuum conditions.

Specimens were identified by TiXI numbers using supplementary letters to designate specific grains.

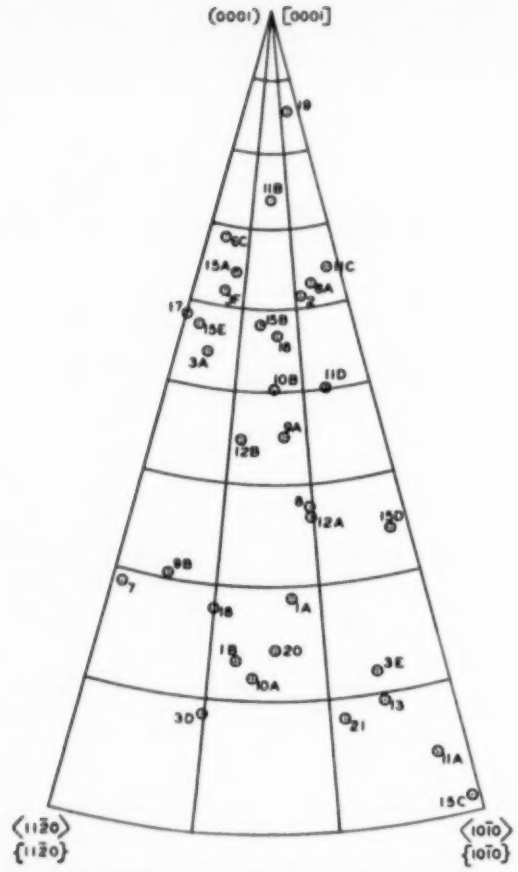

Fig. 1—Orientations of useful large crystals of titanium. Points indicate stereographic projections of specimen axes.

The orientations of the crystals relative to the specimen axis as determined by standard Laue X-ray back-reflection methods are shown stereographically in Fig. 1.

Table III. Effect of Glass Contact on Oxygen Contamination

Specimen No.	Treatment	Sample Location	Oxygen, Pct
Ti-138-1	As forged	—	0.04
Ti-138-2, 3, 4	(a)	Middle	0.036(d)
Ti-138-5, 6, 7	(b)	Middle	1.08(d)
Ti-138-8, 9	(c)	Middle	0.068(e)

(a) Cycled once in 1/5 atm of argon out of contact with glass tube.
(b) Cycled once in 1/5 atm of argon — specimen immersed in soft glass beads.
(c) Cycled once in 1/5 atm of argon — specimen in contact with glass tube.
(d) Average of three runs.
(e) Average of two runs.

Cycling in vacuo had the disadvantage that the specimen surfaces became roughened and the section thickness reduced by the sublimation of titanium. It had the advantage, however, that the β grain size and shape were revealed by selective evaporation. *When the sublimation was suppressed by admitting 1/5 atm of pure argon to the tubes no large grains were obtained.*

All of the specimens were contaminated with oxygen, as shown in Table II, which also contains information on the crystal lengths obtained. The specimen ends consistently showed higher oxygen contents than the centers. That the source of the oxygen contamination was the glass containers is indicated by the data in Table III.

The reason for the failure of large grains to develop in the presence of argon is not clear. The fact, however, that the specimen surfaces were not detectably altered in the argon treatment while significant amounts of metal were removed in the vacuum cycling suggests that an effect associated with the surface is involved. The presence of unremoved thin distorted layers from the machining operation or of an oxygen gradient are possibilities. Either source would be minimized by the evaporation of the surface layers in vacuo.

No detailed study of the internal perfection of the crystals was made. Visual inspection of the Laue spots on the back-reflection photograms revealed no recognizable evidence of imperfections but such

Table II. Identification, Length and Analysis of Large Titanium Crystals

Specimen No.	Cycled In	Sample Location	Analysis, Pct O	Analysis, Pct H	Analysis, Pct N	Crystal Length, In.
TiX1-2	Vacuum	—	(a)	(a)	(a)	2A ⅜
TiX1-3	Vacuum	X1-3A	0.11	0.012	(a)	3A 1
TiX1-3	Vacuum	X1-3D	0.058	0.015	(a)	3D ⅛-½*
TiX1-6	Vacuum	X1-6A	0.14	0.016	(a)	6A 1¾
TiX1-6	Vacuum	Spec. end	0.39	(a)	(a)	—
TiX1-6	Vacuum	Adjacent to spec. end	0.18	(a)	(a)	—
TiX1-8	Vacuum	X1-8A	0.18	0.008	(a)	8A 1¼
TiX1-9	Vacuum	X1-9A	0.093	0.012	(a)	9A 1⅝
TiX1-9	Vacuum	—	—	—	—	9B 5/16
TiX1-9	Vacuum	Spec. end	0.32	0.012	(a)	—
TiX1-10	Vacuum	X1-10A	0.098	0.011	(a)	10A 1⅜
TiX1-10	Vacuum	—	—	—	—	10B ⅝
TiX1-11	Vacuum	Spec. end	0.26	0.012	(a)	—
TiX1-11	Vacuum	—	—	—	—	11A ⅛-⅜*
TiX1-11	Vacuum	—	—	—	—	11B ¾
TiX1-12	Vacuum	X1-12A	0.16	0.008	(a)	12A 1¼
TiX1-12	Vacuum	—	—	—	—	12B ⅝
TiX1-12	Vacuum	Near end	0.24	0.010	(a)	—
TiX1-17	Vacuum	Adjacent to X1-17A	0.039	0.010	(a)	17A ⅝
TiX1-19	Vacuum	X1-19A	0.17	0.015	(a)	19A 1½
Run 23-1	Argon	Center	0.15	0.011	(a)	—
Run 23-2	Argon	Center	0.13	0.011	(a)	—
Run 22-1	Argon	Center	0.30	0.028	0.002	—
Run 22-2	Argon	Center	0.29	0.019	0.002	—
TiX1-15	Argon	Spec. end	0.16	0.013	(a)	—
TiX1-15	Argon	Other end	0.42	0.007	0.002	—

(a) Not determined.
* Irregular shape.

Table IV. Deformation Mechanisms Observed in Large Titanium Crystals

Crystal No.	Length, In.	Analysis, Pct		Slip Plane	Slip Direction	Critical Resolved Shear Stress, G Per Sq Mm	Twinning Plane	Stress Direction
		O	H					
TiX1-3D	⅛-½	0.058	0.015	{10$\bar{1}$0}	<11$\bar{2}$0>	5,000	None	Tension
TiX1-9A	1⅝	0.093	0.012	{10$\bar{1}$0}	<11$\bar{2}$0>	4,500	None	Tension
TiX1-9B	5/16	(a)	(a)	{10$\bar{1}$0}	<11$\bar{2}$0>	5,500	None	Tension
TiX1-10A	1⅜	0.098	0.011	{10$\bar{1}$0}	<11$\bar{2}$0>	5,000	None	Tension
TiX1-11A	⅛-⅜	(b)	—	{10$\bar{1}$0}	(c)	6,700	None	Tension
TiX1-12A	1⅛	0.16	0.008	{10$\bar{1}$0}	<11$\bar{2}$0>	11,700	None	Tension
TiX1-8A	1⅛	0.18	0.008	{10$\bar{1}$0}	(d)	6,500	None	Compression
TiX1-1A(e)	¼	(a)	(a)	{10$\bar{1}$0}	(d)	(a)	{10$\bar{1}$2} (f)	Compression
TiX1-1B(e)	¼	(a)	(a)	{10$\bar{1}$0}	(d)	(a)	None	Compression
TiX1-2A	⅜	(a)	(a)	{0002}	(g)	(a)	{11$\bar{2}$1}	Tension
TiX1-3A	1	0.058	0.015	{0002}	<11$\bar{2}$0>	10,900	{11$\bar{2}$1}	Tension
TiX1-6A	1¾	0.14	0.016	{0002}	<11$\bar{2}$0>	13,100	(h)	Tension
TiX1-11B	¾	0.17	0.004	{0002}	<11$\bar{2}$0>	13,500	(i)	Tension
TiX1-19A	1½	0.17	0.015	(j)	—	—	{10$\bar{1}$2}	Tension
TiX1-17A	⅝	0.039	0.010	{0002}	(d)	(a)	{11$\bar{2}$2}	Compression

(a) Not determined.
(b) 0.26 at end of specimen — possibly less in test area.
(c) Probably <11$\bar{2}$0> but not determined.
(d) Not determined but probably <11$\bar{2}$0> in opposite sense to tension slip.
(e) From preliminary tests on another iodide titanium bar.
(f) {10$\bar{1}$2} twinning at crystal boundary.
(g) Not determined but probably <11$\bar{2}$0>.
(h) {11$\bar{2}$1} twinning in later stages of deformation.
(i) {11$\bar{2}$1} and {10$\bar{1}$2} twinning in later stages of deformation.
(j) No slip detected.

could have been present undetected by this simple test. Where more than one X-ray examination was made on the same grain, the orientations agreed within experimental error. It was judged that the specimens were reasonably perfect and suitable for use in the deformation studies.

Plastic Deformation Studies

Test Procedures: All deformations were made at room temperature in a 20,000-lb capacity hydraulic testing machine at 0.1 in. per min free head speed. Tension specimens were gripped for a length of about ¼ in. at each end in Templin self-aligning grips. Axiality of loading was judged visually. Gage marks were produced by very fine scratching. Elongations, with load released, were measured at 18X by comparison with a machine-ruled scale graduated in hundredths from which thousandths could be estimated.

For compression testing, the crystals were machined to produce plane, parallel ends on test pieces ½ in. in length, giving a length to width ratio of about 3. Compression was carried out between lubricated polished steel plates. In all testing the load was removed periodically to permit measurement of change in length, identification and study of deformation markings and, where desired, X-ray identification of change in orientation.

While no attempt was made to obtain data from which to construct precise stress-strain curves, the yield points usually were determined with sufficient accuracy to permit the calculation of approximate critical resolved shear stresses.

Initial orientations and changes in orientation due to deformation were determined by standard Laue X-ray techniques using a North American Philips Unicam to line up the specimen surface normal to the X-ray beam to within ½°. Unfiltered copper radiation was used with a specimen-to-film distance of 1 in. and an exposure time of about 1 hr.

A semitransparent zinc sulphide mirror affixed to the specimen surface provided a reflecting surface for the optical setting-up procedure. This was necessary when the surfaces became too distorted for good light reflection. The mirror was left in place during the X-ray exposure. It caused no difficulty and may have produced some improvement in photogram quality.

Examinations of deformation markings were made with the aid of binocular and metallographic microscopes at magnifications up to 1000X. The angles between the markings and an edge were measured with the revolving stage of the latter. Identification of the operating plane was based on measurements on at least two, and frequently all four, surfaces. Many markings could be traced over an edge but in other cases the numbers and fineness of the markings made definite pairings impossible. In these cases, markings, on two or more surfaces, defining a single low-index type plane were considered definite pairs.

Experimental Results: The deformation mechanisms observed are assembled in Table IV together with the calculated critical resolved shear stresses for slip. The observed and probable slip rotations in tension are plotted stereographically in Figs. 2 and 3. Fig. 4 shows probable directions of slip and slip rotation in compression. Characteristic slip and twin markings are shown in Figs. 5 through 10.

Discussion: It is evident from Figs. 2 to 4 that the crystals may be divided into two groups to facilitate the discussion. In Group 1 are those in which the {0002} plane made angles of from about 5° to about 40° with the specimen axis. Group 2 contains those in which this angle exceeded about 40°.

Group 1: The deformation mechanism operating in this group of crystals was slip on the most highly stressed {10$\bar{1}$0} plane in the <11$\bar{2}$0> close-packed direction. While the slip direction in compression was not determined, there seems little doubt that

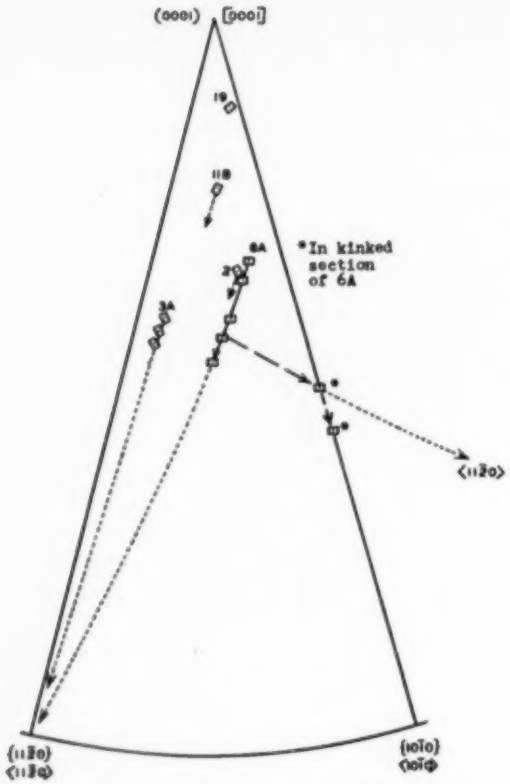

Fig. 2—Rotation due to {0002} slip in <11$\bar{2}$0> direction in tension. (Also probably {10$\bar{1}$0} slip in another <11$\bar{2}$0> direction in part of TiXI-6A.)

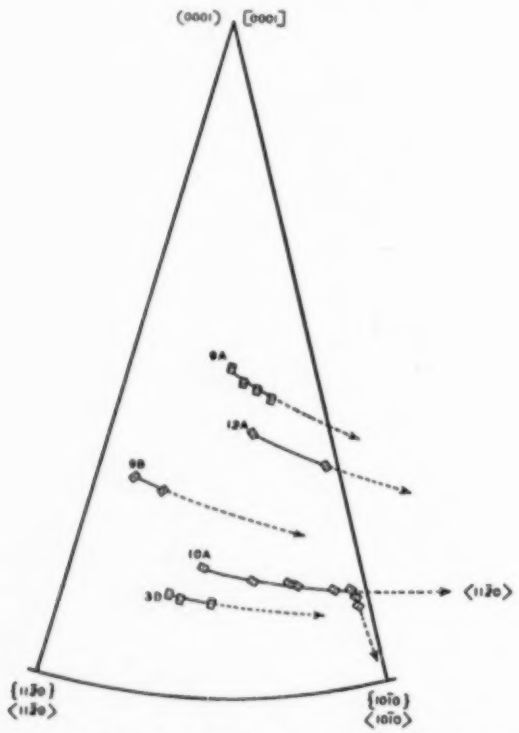

Fig. 3—Rotation due to {10$\bar{1}$0} slip in <11$\bar{2}$0> direction in tension.

it was the <11$\bar{2}$0> direction in the opposite sense to the tensile slip. The only twinning observed in this series was that incident to local restraints.

The experience of TiXI-10A is worthy of comment. As can be seen in Fig. 3, this crystal was subjected to a very large total extension which was sufficient to rotate it to the point where a second {10$\bar{1}$0} plane should become active. Consequent double slip evidently rotated the specimen axis toward the <10$\bar{1}$0> direction. At this time, a kink of the unusual configuration shown in Fig. 11 developed. The Laue X-ray back-reflection patterns establishing the rotation were taken ⅛ to ¼ in. from the kink. No satisfactory patterns were obtained in the kink nor were the markings informative.

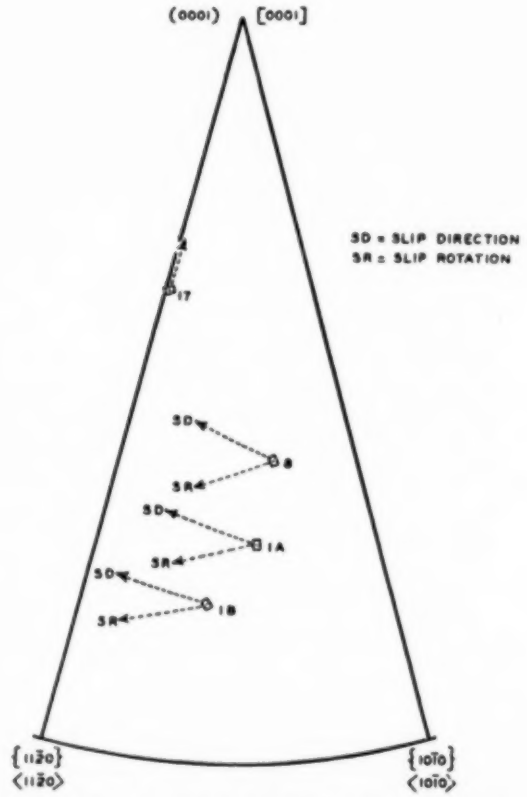

Fig. 4—Probable directions of slip (SD) and slip rotation (SR) due to {0002} and {10$\bar{1}$0} slip in compression.

The critical resolved shear stress for {10$\bar{1}$0} slip in the <11$\bar{2}$0> direction was of the order of 5000 g per sq mm. The higher values noted for TiXI-11A, 12A, and 8A probably reflect the influence of higher gas impurity contents.

Group 2: The deformation behavior of this group (Fig. 2) was somewhat complex, requiring more detailed discussion of the tests on the individual crystals. TiXI-2A, 3A, and 6A constitute a group rather similarly oriented but varying in crystal length. Slip on {0002} was observed in all three crystals and slip in the most highly stressed <11$\bar{2}$0> direction was proved for TiXI-3A and 6A. However, {11$\bar{2}$1} twinning also was observed at extensions which varied with the crystal length. These twins

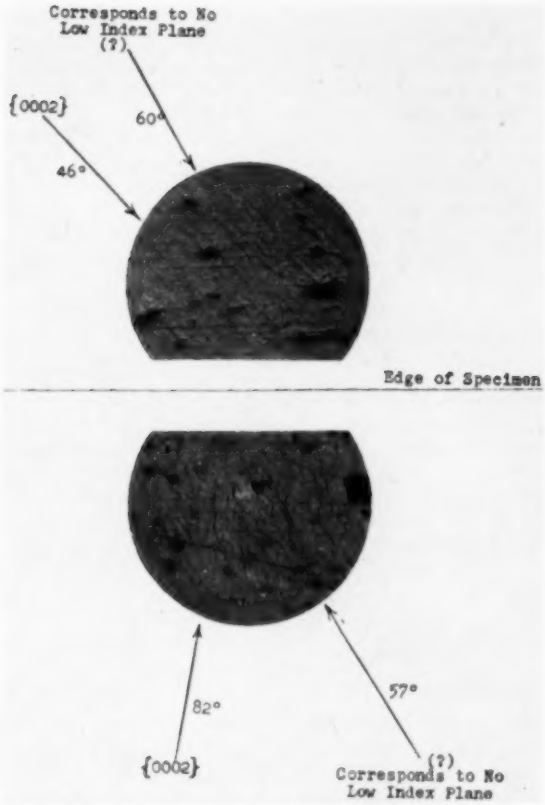

Fig. 5—Micrographs of two adjacent surfaces of TiXI-6A pulled to 10 pct elongation. Note {0002} slip and cross markings. X250. Area reduced approximately 60 pct for reproduction.

developed first near the grip or grain boundary restraints, moving toward the crystal center as the extension was increased and possibly largely replacing the basal slip mechanism as the preferred deformation process. Thus TiXI-2A (⅜ in. long)

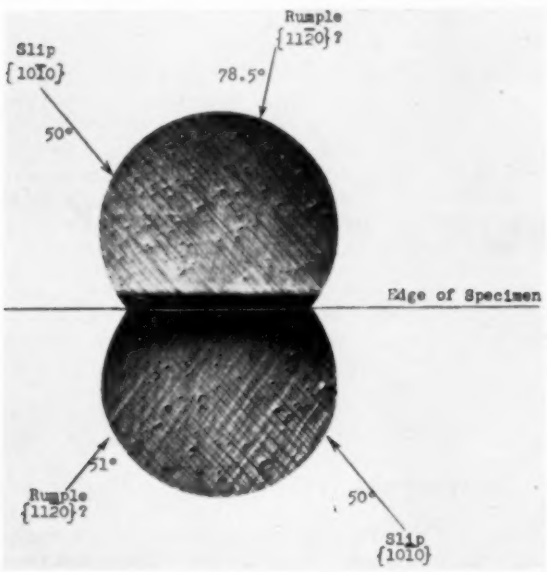

Fig. 6—Micrographs of two adjacent surfaces of TiXI-10A pulled to 12.5 pct elongation. Note {10$\bar{1}$0} slip and {11$\bar{2}$0}? rumple marks. X25. Area reduced approximately 60 pct for reproduction.

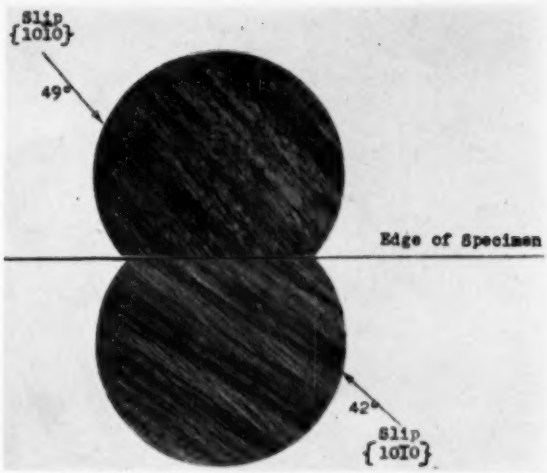

Fig. 7—TiXI-10A pulled to 49.3 pct elongation. Note irregularities in markings. X250. Area reduced approximately 60 pct for reproduction.

showed abundant {11$\bar{2}$1} twinning after small extensions; TiXI-3A (1 in. long) required 9.2 pct extension before twinning at the crystal center was observed; and TiXI-6A (1¾ in. long), while twinned for a distance from each grip, had no twins at the center after 28.2 pct extension.

It seems evident that basal slip is unlikely to be an important mode of deformation in polycrystalline titanium of normal grain size. Perhaps the failure of Rosi, Dube, and Alexander[1] to detect evidence of {0002} slip was due to their use of comparatively small crystals of commercial purity titanium.

The considerable length and desirable orientation of TiXI-6A made it of special interest. It was obvious that the rotation due to {0002} slip would ultimately reorient the crystal sufficiently to bring the stress on a {10$\bar{1}$0} plane to the critical resolved shear

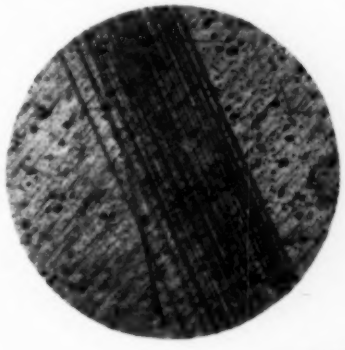

Fig. 8 (left)—TiXI-3A {0002} and {11$\bar{2}$1} twinning. Note slight change in slip direction in twinned area. X75. Area reduced slightly for reproduction.

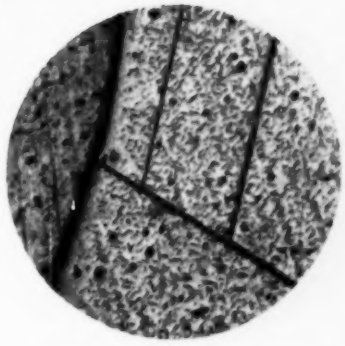

Fig. 9 (right)—TiXI-3E (crystal at right). 2 sets of {11$\bar{2}$2} twins. Crystal at left is 3D showing {10$\bar{1}$0} slip. X75. Area reduced slightly for reproduction.

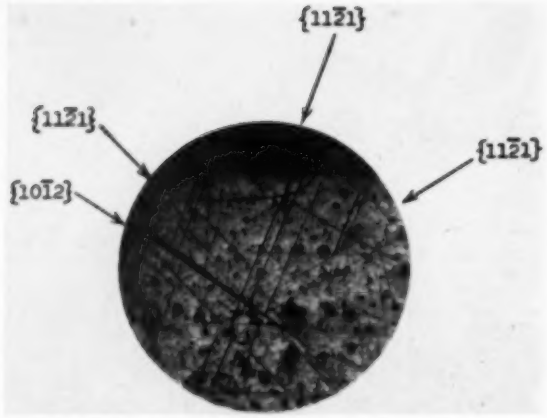

Fig. 10—TiXI-3A showing {10$\bar{1}$2} twin and 3 sets of {11$\bar{2}$1} twins. X75. Area reduced approximately 50 pct for reproduction.

value required to initiate prismatic slip. This apparently happened since a kink developed at the third extension which, from its orientation, seems to have resulted from {10$\bar{1}$0} slip in the <11$\bar{2}$0> direction in a limited volume of the crystal.

After the fourth extension, the main crystal showed only a continuation of the basal glide rotation while the orientation of the metal in the kink indicated double slip with rotation toward the <10$\bar{1}$0> pole. Due, possibly, to the considerable extension applied to the crystal, the deformation markings in the kink were indeterminate.

The critical resolved shear stress for {0002} slip in the <1120> direction was calculated to be about 10,900 to 13,500 g per sq mm. The lower value was obtained on the purest crystal and is probably the more nearly correct one.

TiX1-11B represents a crystal with a somewhat steeper angle between the basal plane and the specimen axis. While only a single small extension (0.8 pct) was applied, markings consistent with {0002} slip and {1121} and {10$\bar{1}$2} twinning were found.

TiX1-19A had the steepest angle of any of the crystals at hand. Extension to the extent of 14.5 pct

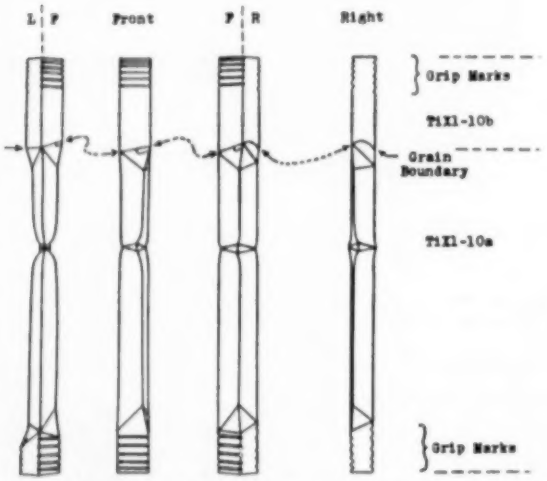

Fig. 11—Appearance of TiXI-10A after final extension. Note kink at center and bend plane adjustments to grips and grain boundary restraints.

resulted in abundant {10$\bar{1}$2} twinning. While final inspection of the crystal was made difficult by the roughening effect of the extensive {10$\bar{1}$2} twinning, no evidence of any other deformation mechanism was observed at this stage or earlier.

TiX1-17A (Fig. 4), tested in compression, showed evidence of {1122} twinning and {0002} slip. The twinning was noted at an earlier stage in the deformation than was the basal slip. This is in contrast with the tension experience with TiX1-2A, 3A, and 6A in which basal slip preceded the {11$\bar{2}$1} twinning.

Slip Markings: While the identification of the slip planes and directions is conclusive, the markings themselves had some peculiarities. Seldom had they the clear-cut appearance of similar markings in zinc. The basal plane slip markings characteristically showed cross linkages, the angles of which with an edge corresponded to no plane of low index (Fig. 5). It is the writers' suggestion that these might represent an unresolved (at 1000X) com-

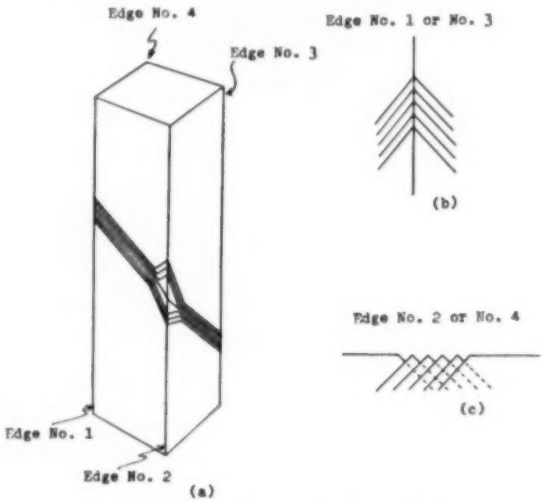

Fig. 12—Effect of edges on {11$\bar{2}$1} twinning.

posite slip between the basal plane and some other, probably pyramidal, plane having a close-packed direction in common.

{10$\bar{1}$0} slip lines appear simple in nature at low extensions but become irregular at greater extensions. This results (Fig. 7) in a light and dark banding of a hill-and-valley type at a small angle to the slip markings. These are quite similar in appearance to the striae observed by Calnan[9] in stretched single crystal aluminum specimens and attributed to areas of complex slip, possibly including rotational (polar) slip. Rumpling or kinking about an <0001> axis giving approximate {1120} markings is apparent at the lower elongations (Fig. 6). The latter bands differ in appearance and probable origin from the former and can be rationalized without assuming complex slips (ref. 4).

Twin Markings: The three twinning planes found in this work have characteristic appearances. {10$\bar{1}$2} twins in titanium resemble those in zinc and magnesium. They are broad and lenticular and appear to increase in width with increase in stress. {11$\bar{2}$1} twins, on the other hand, are narrow and straight. They appear to traverse the entire width of a crys-

Table V. Identification of Deformation Planes

Mechanism	Plane	Rosi, Dube, Alexander	Liu, Steinberg	Present Work
Slip	{10$\bar{1}$0}	X	(a)	X
Slip	{10$\bar{1}$1}	X	(a)	(b)
Slip	{0002}	(b)	(a)	X
Twinning	{10$\bar{1}$2}	X	X	X
Twinning	{11$\bar{2}$1}	X	X	X
Twinning	{11$\bar{2}$2}	X	X	X
Twinning	{11$\bar{2}$3}	(b)	X	(b)
Twinning	{11$\bar{2}$4}	(b)	X	(b)

(a) Not reported — apparently not looked for.
(b) Did not find.

tal. A branching habit near alternate crystal edges appear common. This is shown diagrammatically in Fig. 12. Twinning leaves exposed corners at edges Nos. 2 and 4 (Fig. 12c) but not at edges Nos. 1 and 3 (Fig. 12b). The specimen tends to avoid the high energy condition of Fig. 12c by twinning on an alternative {11$\bar{2}$1} plane that produces the form of Fig. 12b; or perhaps it should be said that the formation of an initial twin changes the stress distribution along the edge sufficiently to change the active plane. {11$\bar{2}$1} twins do not appear to grow with increased specimen stressing; instead new twins appear. {11$\bar{2}$2} twins are intermediate in appearance between the {11$\bar{2}$1} and {10$\bar{1}$2} twins.

Twinning directions and shears were not given close attention, but observations on TiX1-3A suggested that the twinning direction for {11$\bar{2}$1} twinning was perpendicular to the trace of that plane in the basal plane.

Comparison with Other Work: The deformation planes identified by Rosi, Dube, and Alexander, Liu and Steinberg, and the present writers are set forth in Table V.

There is agreement on the identification of {10$\bar{1}$0} slip and {10$\bar{1}$2}, {11$\bar{2}$1} and {11$\bar{2}$2} twinning. Rosi et al. detected {10$\bar{1}$1} slip while the present workers did not. The present workers established the reality of basal slip which Rosi et al., for reasons discussed earlier, did not find. Liu and Steinberg report {11$\bar{2}$3} and {11$\bar{2}$4} twinning which were not observed by Rosi et al. or the present writers at room temperature.

The best conclusion at present seems to be that α titanium is capable of deforming by slip on the {10$\bar{1}$0} and {0002} planes and by twinning on the {10$\bar{1}$2}, {11$\bar{2}$1}, and {11$\bar{2}$2} planes. In view of this unexpectedly large number of operating planes, it should not be surprising to find that additional planes can be active.

Summary

Large grains of α titanium can be grown by cycling several times between 4 hr at 1200°C and three to five days at 850°C in vacuo.

Alpha titanium can deform at room temperature by slip in the <11$\bar{2}$0> direction on the {10$\bar{1}$0} plane at a critical resolved shear stress of about 5000 g per sq mm or on the {0002} plane in the <11$\bar{2}$0> direction at a critical resolved shear stress of about 11,000 g per sq mm.

Alpha titanium can deform at room temperature by twinning on the {10$\bar{1}$2}, {11$\bar{2}$1}, and {11$\bar{2}$2} planes. The choice of deformation mechanism was dependent largely upon the crystal orientation and the direction of stressing but in the case of {0002} slip was also related to crystal size.

Acknowledgments

This work was carried out under contract with the Watertown Arsenal to whom the writers are indebted for permission to publish. They are deeply grateful to C. H. Mathewson for his advice and counsel during the work and to C. B. Tennant for his careful X-ray examinations.

References

[1] F. D. Rosi, C. A. Dube, and B. H. Alexander: *Trans.* AIME (1952) **194**, p. 189; JOURNAL OF METALS (February 1952).

[2] T. S. Liu and M. A. Steinberg: JOURNAL OF METALS (October 1952) p. 1043.

[3] E. A. Calnan: *Acta Crystallographica* (1952) **5**, p. 557; *Trans.* AIME (1952) **191**, p. 526; JOURNAL OF METALS (May 1952).

[4] N. K. Chen and C. H. Mathewson: *Trans.* AIME (1951) **191**, p. 653; JOURNAL OF METALS (August 1951).

Technical Note

Filler Material for the Brazing of Titanium

by N. A. DeCecco and H. M. Meyer

IN the early stages of a titanium brazing investigation, binary titanium systems partially or completely known and fundamental metallurgical data were surveyed to select the pure metal most likely to be satisfactory for producing a ductile high strength joint.

The phase diagrams for the purpose of this survey were classified into two groups: 1—systems with large solubility in β titanium, but negligible solubility in α titanium, and 2—systems with large solubility in α titanium.

Those metals with melting points believed to be too high or too low for titanium brazing (Ti_m = 1730°C) were eliminated from consideration. The melting points of vanadium, tungsten, tantalum, hafnium, zirconium, and the platinum group are too high and those of zinc, lead, cadmium, and tin are too low.

The remaining metals were grouped as follows: 1—large β solubility: Cr,[1] Mn,[2] Fe,[3] Co,[4] Ni,[5] Cu,[6] Be,[7] Si.[8] 2—large α solubility: Al.[9]

N. A. DeCECCO and H. M. MEYER, Member AIME, are associated with the Welding Section, Armour Research Foundation of Illinois Institute of Technology, Chicago.

TN 177E. Manuscript, Feb. 19, 1953; revision, May 18, 1953.

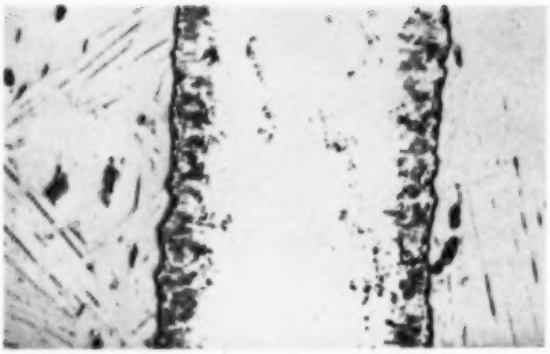

Fig. 1—Silver brazed joint of titanium. Note the columnar grains of the compound growing from the interfaces into the silver. Etchant: 60 cc $C_2H_4O_2$, 20 cc HNO_3, 20 cc HF. X500. Area reduced approximately 50 pct for reproduction.

It was noted that the sequence of elements from chromium through copper follow titanium in the first long period of elements. The corresponding metals in the second and third long period, zirconium through palladium and hafnium through platinum, as well as vanadium, the immediate neighbor, were eliminated because of their melting points. Therefore, only the metals of subgroup I-b, silver and gold, remain from the second and third long periods for consideration as filler materials.

Gold[10-12] and the metals listed in groups 1 and 2 form intermetallic compounds with titanium (Table I) which are known to be brittle. This brittleness is undesirable for a brazing material because the compound formation imparts brittle physical properties to the joint.

The metal remaining is silver. Silver and titanium were either believed to be immiscible in both the liquid and solid states[10, 13] or to have a solubility of at least 2 pct Ag in Ti.[10] Metals of subgroup I-b are known to show frequent similarities in their metallurgical behavior. Furthermore interatomic spacing of silver and titanium differs by only 2 pct and both have close-packed structures; a circumstance which is considered favorable for formation of solid solutions. Therefore the brazing of titanium with fine silver was tried.

Experiments in a helium atmosphere furnace were conducted to determine the wetting properties of molten silver on a heated titanium surface. It was found that silver wet and flowed; metallographic examination of the specimens indicated alloying of the two metals. Subsequently, brazed joints were made with fine silver as the filler metal. The joints were made of 1x⅛ in. strips of commercially pure titanium clamped vertically in a fixture with a ⅛ in. overlap. A length of fine silver wire was placed across the end of one titanium specimen and covered with dry powdered flux composed of 10 pct AgCl, 36 pct KCl, 9 pct LiF, and 45 pct NaCl. The joint was then heated with an oxyacetylene torch, until the fine silver fused and flowed into the capillary space.

Table I. Intermetallic Compounds Known to Form in Binary Titanium Systems

Metal	Compounds	References
Cr	$TiCr_2$	1
Mn	TiMn; $TiMn_2$	2, 10
Fe	TiFe; $TiFe_2$	3, 10
Co	Ti_2Co(?); TiCo; $TiCo_2$	10
Ni	Ti_2Ni; TiNi; $TiNi_3$	10
Cu	Ti_2Cu; TiCu; Ti_2Cu_3; $TiCu_3$	6, 10
Be	TiBe; $TiBe_2$	7
Si	Ti_5Si_3; TiSi; $TiSi_2$	8
Al	TiAl; $TiAl_3$	10
Au	Au_4Ti; Au_2Ti; AuTi	10, 11, 12

The ultimate shear strengths of the joints have a mean value of 31,500 lb per sq in. with a standard deviation of 5400 lb per sq in. All the specimens break with a ductile shear fracture.

Metallographic studies of the Ti-Ag brazed joints indicate the presence of an intermetallic compound which exhibits considerable ductility. This experimental observation contradicts the consideration that an extended solid solubility can be expected. Instead an equiatomic compound forms which is not brittle. It is an open question why this is so. This compound seems to serve as a kind of bridge between the two metal structures because of their structural and geometric similarities. Fig. 1 is a micrograph of a joint cross-section. The black lines at the titanium-brazed metal interface are caused by metallographic etching relief. Adjacent to the black line is the columnar structured compound which formed on the titanium surface and extends into the brazed metal.

It was believed that an investigation to determine the composition and confirm the ductility of the compound was warranted. The details and results of the subsequent study are reported elsewhere.[14]

Acknowledgments

This work was sponsored by Watertown Arsenal, whose permission to publish this paper is gratefully acknowledged. The authors also wish to express their appreciation to C. A. Johnson for the metallographic work.

References

[1] P. Duwez and J. L. Taylor: *Trans.* ASM (1952) **44**, p. 495.

[2] D. J. Maykuth, H. R. Ogden, and R. I. Jaffee: *Trans.* AIME (1953) **197**, p. 225; JOURNAL OF METALS (February 1953).

[3] R. J. Van Thyne, H. D. Kessler, and M. Hansen: *Trans.* ASM (1952) **44**, p. 974.

[4] B. Egeberg: *Abh. Inst. Metallk. Elektromet.;* T. H. Aachen (1915) **1**, No. 1, p. 37.

[5] J. R. Long et al.: U. S. Bur. Mines Publ. *R. I.* 4463 (1949).

[6] A. Joukainen, N. J. Grant, and C. F. Floe: *Trans.* AIME (1952) **194**, p. 766; JOURNAL OF METALS (July 1952).

[7] P. Ehrlich: *Ztsch. anorg. allgem. Chem.* (1949) **259**, p. 1.

[8] M. Hansen, H. D. Kessler, and D. J. McPherson: *Trans.* ASM (1952) **44**, p. 518.

[9] E. S. Bumps, H. D. Kessler, and M. Hansen: *Trans.* AIME (1952) **194**, p. 609; JOURNAL OF METALS (June 1952).

[10] F. Laves and H. J. Wallbaum: *Naturwissensch.* (1939) **27**, p. 674.

[11] E. Raub, P. Walter, and M. Engel: *Ztsch. Metallk.* (1952) **43**, p. 112.

[12] P. Duwez and C. B. Jordan: *Acta Cryst.* (1952) **5**, p. 213.

[13] C. M. Craighead, O. W. Simmons, and L. W. Eastwood: *Trans.* AIME (1950) **188**, p. 485; JOURNAL OF METALS (March 1950).

[14] R. J. Van Thyne, W. Rostoker, and H. D. Kessler: *Trans.* AIME (1953) **197**, p. 670; JOURNAL OF METALS (May 1953).

Effects of Solid Solution Alloying on The Cold-Rolled Texture of Titanium

by Carl J. McHargue, Sam E. Adair, Jr., and Joseph P. Hammond

Cold-rolled sheet textures have been determined for binary solid solutions of aluminum, columbium, tantalum, and zirconium in titanium. An alloy containing 3.8 pct Al had a (0002) [10$\bar{1}$0] texture, whereas alloys with the other elements had rotated (0002) [10$\bar{1}$0] textures similar to that of iodide titanium.

THERE have been relatively few studies of the effect of alloying on deformation textures. A second element may be present in the base metal in solid solution and/or as a second phase. The literature offers no satisfactory explanation for the effects of solid solution alloying on textures noted thus far. For example, there is no satisfactory explanation of the difference in the textures of copper and α brass.

The most complete study of the effects of solid solution alloying on deformation textures has been that of Brick, Martin, and Angier.[1] These investigators reported that the copper texture was retained by alloys of copper with up to 30 pct Ni, less than 5 pct Zn, less than 2 pct Al or Co up to the limit of solubility. Copper containing more than 5 pct Zn, more than 2 pct Al, or the maximum soluble concentration of tin, silicon, or manganese showed the deformation texture of α brass.

Bakarian[2] reported that additions of 0.20 pct Ca to 99.98 pct Mg or 2.0 pct Mn plus 0.15 pct Ca to magnesium resulted in entirely different textures than for the pure magnesium. The texture obtained for high-purity magnesium sheet showed the basal plane to be concentrated parallel to the rolling plane. The texture obtained for the alloy containing 0.20 pct Ca had the basal planes concentrated in elliptical areas whose centers were tilted 15° from the center of the pole figure toward the rolling direction. This split basal orientation was even more pronounced in the alloy containing 2.0 pct Mn and 0.15 pct Ca.

Fuller and Edmunds[3] studied the rolled sheet textures in a zinc alloy containing 1 pct Cu and 0.01 pct Mn. The basal pole figure of this alloy contained a region of strong concentration not found in the pole figure for pure zinc.[4]

In the above cases, results were discussed in terms of possible changes in slip and/or twinning systems and critical shear stresses. However, there were no experimental data to relate these speculations with the observed textures.

It has been suggested that the deformation textures of titanium, zirconium, and beryllium could be directly ascribed to their low c/a ratios. The complex deformation mechanisms of titanium[5] also have been suggested to be characteristic of hexagonal close-packed metals with low c/a ratios. The purpose of this investigation was to study the cold-rolled sheet textures in binary titanium-base α alloys in which the c/a ratios were greater than, less than, and about the same as the c/a for iodide titanium. The annealed textures of these alloys will be reported in a subsequent article.

Materials and Methods

The chemical analyses of the metals used in this investigation are given in Table I.

The alloys were prepared as 15 g buttons on a water-cooled copper block in a vacuum arc-furnace. The furnace was evacuated to pressures of the order of 10^{-5} mm Hg, flushed with 99.98 pct pure argon, and melting was carried out in 0.2 atm pressure argon. Each button was remelted until radiographs and chemical analyses indicated complete solution of the solute elements.

All buttons were forged and homogenized 72 hr at 500°C. The buttons to be rolled were ground and etched to sizes and shapes suitable for the rolling

C. J. McHargue, Junior Member AIME, formerly Research Metallurgist, Dept. of Metallurgical Engineering, University of Kentucky, is now Metallurgist, Oak Ridge National Laboratory, Oak Ridge, Tenn., S. E. ADAIR, JR., Student Associate AIME, formerly Research Associate, Dept. of Metallurgical Engineering, University of Kentucky, is now Engineer, Linde Air Products, Indianapolis, Indiana, and J. P. HAMMOND is Associate Professor of Metallurgical Engineering, University of Kentucky, Lexington, Ky.

Discussion on this paper, TP 3607E, may be sent, 2 copies, to AIME by Dec. 1, 1953. Manuscript, April 15, 1953. Cleveland Meeting, October 1953.

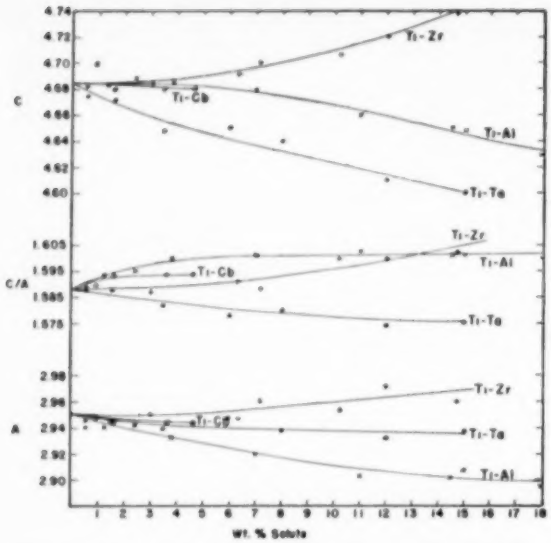

Fig. 1—Variation of lattice parameters with composition of titanium-base alloys.

schedule and vacuum annealed at 700°C. Filings for the parameter studies were annealed at 500°C in titanium capsules which were in turn sealed in evacuated quartz tubes.

The alloyed buttons were cold-reduced 93 pct to 0.007 in. using a 2-high rolling mill with 4 in. diam rolls. A reduction of approximately 10 pct per pass was used, and the rolling direction was changed 180° between passes.

Strips of the rolled sheet were made into small rods for use as the X-ray specimens. A flat strip was placed in a jig, and the edges were ground, polished, and etched away until a rod-shaped specimen was obtained. Transmission X-ray photograms were made with a Laue-type camera using molybdenum radiation (45 kv, 18 ma). It was necessary to insert a zirconium filter between the specimen and film because of the fluorescent radiation. Preliminary exposures were made with the beam perpendicular to the rolling direction at rotations of 0, 11°, 26°, 41°, 56°, 71°, and 79°, and with the beam perpendicular to the cross direction at rotations of 11°, 26°, 56°, 71°, and 79°. Additional exposures were then made where necessary to determine boundaries of intensity regions accurately. The variations in intensity were estimated visually with the aid of an exposure chart.

Films for the a-lattice parameter determinations of the alloys were obtained with a 114.59 mm powder camera with the film mounted according to the method of Straumanis. Nickel filtered copper radiation was used, and a 0.001 in. aluminum foil was placed inside the camera to reduce the high background encountered with titanium. The parameters were calculated by a least squares solution of the

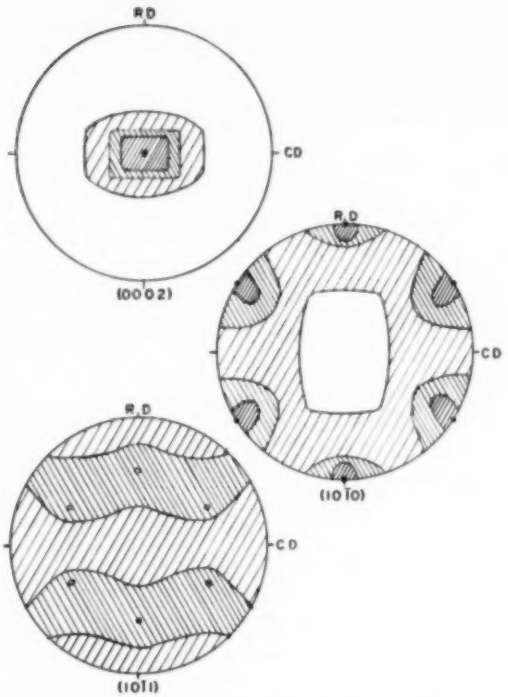

Fig. 2—Cold-rolled sheet texture of alloy containing 3.8 pct Al. O = (0002) [10$\bar{1}$0]

five strongest high angle lines and provided an accuracy of ± 0.005Å or better.

Experimental Results

Titanium-Aluminum: The effect of alloying on the lattice parameters of the Ti-Al alloys is shown in Fig. 1. These results are similar to those published by Rostoker,[6] differing mainly in rapidity of the rise of the c/a curve for low aluminum concentrations. It was desired to determine the texture for an alloy with the greatest possible c/a ratio, but alloys containing more than approximately 5 wt pct Al could not be cold-reduced the desired amount (90 pct or better.) The material selected for study contained 3.8 pct Al and had a c/a ratio of 1.600.

The cold-rolled sheet textures of this alloy are shown in Fig. 2. These pole figures show an "ideal" texture differing from that of iodide titanium (Fig. 3). Fig. 2a and b indicates that the basal planes are concentrated parallel to the rolling plane and that the digonal axis [10$\bar{1}$0] is parallel to the rolling direction, or that the "ideal" texture is (0002) [10$\bar{1}$0]. The major spread is in the cross direction.

Titanium-Columbium: It is seen from Fig. 1 that there are only slight changes in the parameters of the Ti-Cb alloys. The c/a ratio at 4.5 pct Cb has shifted only to 1.592 from 1.588.

Table I. Compositions of Materials Used

	Mn	Fe	Al	Pb	Cu	Sn	Mg	C	W	Cb	N_2
Iodide Ti	0.004	0.0065	0.0065	0.0025	0.01	0.002	—	—	—	—	0.002
Al	—	—	99.983	—	—	—	—	—	—	—	—
Cb	—	Tr.	—	—	—	Tr.	—	0.05	—	—	—
Ta	—	0.02	—	—	—	—	—	0.01	0.04	0.05	—
Zr	0.001	0.04	0.01	0.001	0.01	0.001	0.003	0.001	0.001	—	0.01

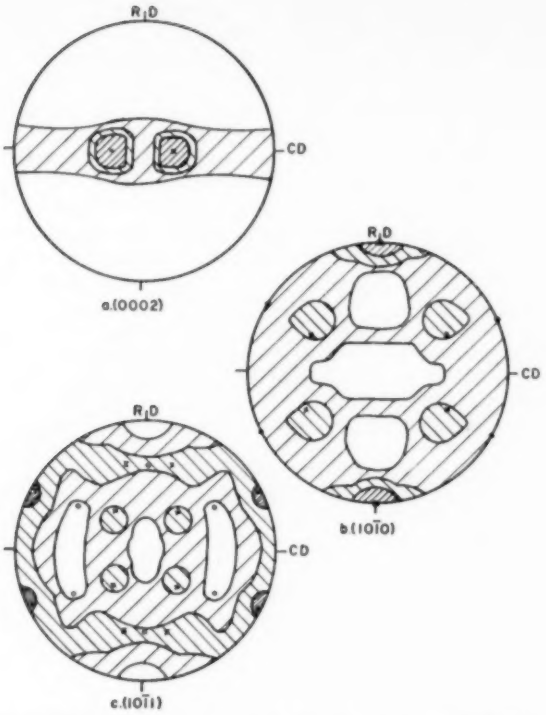

Fig. 3—Cold-rolled sheet texture of iodide titanium. O = (0002) [10$\bar{1}$0]; x = (0002) rotated 27° about rolling direction, [10$\bar{1}$0]

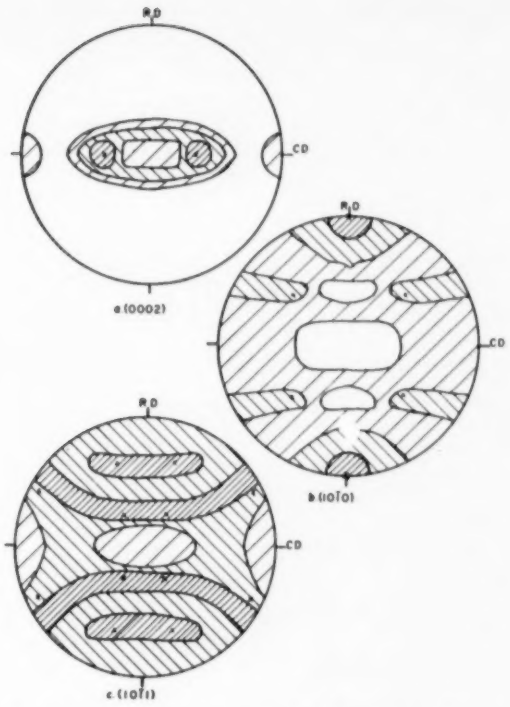

Fig. 4—Cold-rolled sheet texture of alloy containing 3.6 pct Cb. x = (0002) rotated 40° about rolling direction, [10$\bar{1}$0]

The cold-rolled sheet pole figures for an alloy containing 3.6 pct Cb and having c/a = 1.592 are shown in Fig. 4. These are similar in form to those of titanium; however, the maxima in the (0002) pole figure are centered approximately 40° from the center of the pole figure instead of 27° as for titanium. There is a region of second high intensity in the (0002) pole figure approximately 15° to 20° from the center in the rolling direction which did not appear for unalloyed titanium. The lowest intensity region of the (0002) pole figure of the Ti-Cb alloy shows a break near the basic circle, whereas that region for the iodide titanium extended all the way across the figure. The figures for the (10$\bar{1}$0) and (10$\bar{1}$1) planes are consistent with the rotated basal, [10$\bar{1}$0] texture and show very much spread in the cross direction.

Titanium-Tantalum: It was observed that the c/a ratio of the α solid solution decreased with increasing concentrations of tantalum, Fig. 1. Textures were determined for two alloys of titanium with tantalum. One alloy contained 3.6 pct Ta and had a c/a ratio of 1.584 while the other contained 15.4 pct Ta and had a c/a ratio of 1.575.

The pole figures for the 3.6 pct Ta alloy cold-reduced 93.6 pct in thickness are illustrated in Fig. 5 and show the rotated basal, [10$\bar{1}$0] texture. The only differences in the basal pole figures for this alloy and iodide titanium are the absence of (0002) poles near the basic circle and the presence of the region of second high intensity near the center of the figure in the rolling direction. In other respects

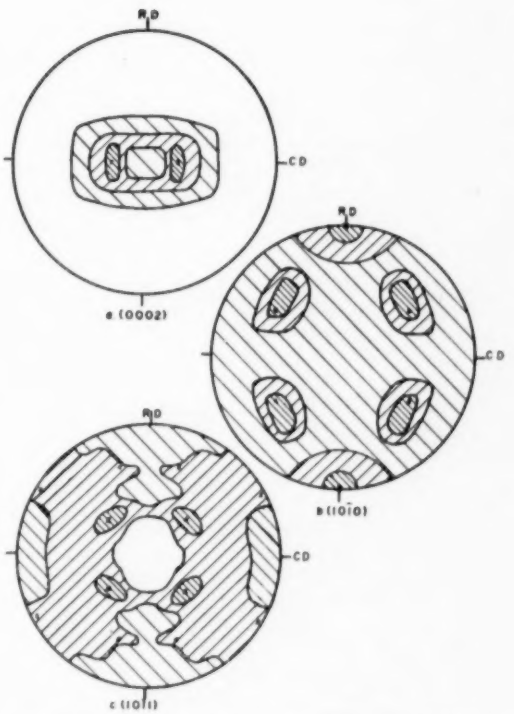

Fig. 5—Cold-rolled sheet texture of alloy containing 3.6 pct Ta. x = (0002) rotated 27° about rolling direction, [10$\bar{1}$0]

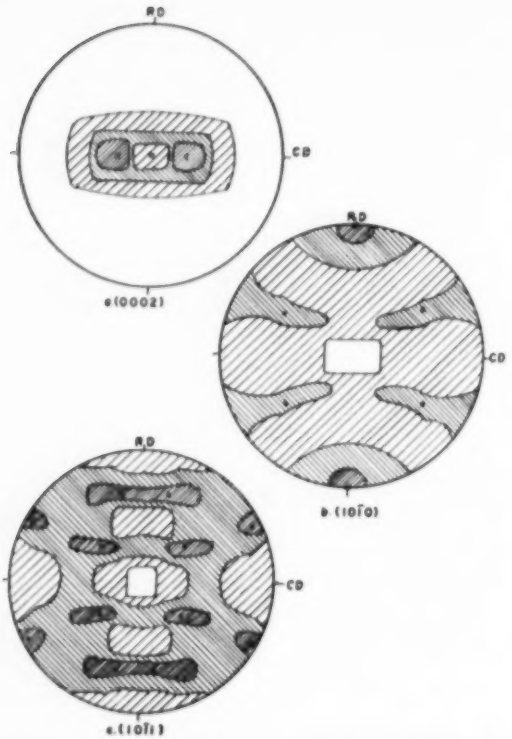

Fig. 6—Cold-rolled sheet texture of alloy containing 7.1 pct Zr. x = (0002) rotated 30° about rolling direction, [10$\bar{1}$0]

the alloyed texture was essentially the same as the unalloyed.

The texture for the 15.4 pct Ta alloy cold-rolled 93.6 pct showed no significant differences from Fig. 5. The regions of maximum intensity in the (0002) pole figure were approximately 25° to 27° from the center in the transverse direction as for iodide titanium and the alloy of 3.6 pct Ta.

Titanium-Zirconium: Titanium and zirconium show complete solid solubility in both crystal forms, and the a lattice parameters have a negative deviation from Vegard's law.[7] The composition parameter results of the present study are shown in Fig. 1.

Textures were studied for alloys containing 7.1 pct Zr (c/a = 1.590) and 14.75 pct Zr (c/a = 1.602) which were cold-reduced 93.6 pct in thickness. Fig. 6 contains the pole figures for the 7.1 pct Zr alloy. The figures for both alloys were similar and differ from those for iodide titanium only in those respects discussed for the Ti-Ta textures. These alloys showed the rotated basal, [10$\bar{1}$0] texture.

Discussion of Results

While a complete explanation of the effects of solid solution alloying on deformation textures cannot be given at this time, some observations can be made as a result of this investigation. Although limited data are available, it appears that the c/a ratio is an equivocal factor in the establishment of deformation textures.

It has been suggested that the deformation mechanisms and deformation textures of hexagonal close-packed metals were peculiar to the deviation of their c/a ratios from the ideal packing. On this basis, it was suggested that the textures of metals or alloys having the same c/a ratio would be similar. However, as can be seen in Table II, the results of this investigation do not justify this belief.

In the cases of the titanium-base alloys containing 3.8 pct Al and 14.75 pct Zr, having c/a ratios of 1.600 and 1.602, respectively, there were entirely different textures. The Ti-Al alloy possessed a cold-rolled texture described as (0002) [10$\bar{1}$0] and the Ti-Zr alloy possessed a rotated (0002) [10$\bar{1}$0] texture similar to that of iodide titanium (c/a = 1.588).

It has been observed that the cold-rolled texture of beryllium,[8] (0002) [10$\bar{1}$0], resembles that of magnesium. However the scatter from this mean orientation is toward the cross direction, whereas that for magnesium is toward the rolling direction. This texture of beryllium is inconsistent with any relationship between c/a and texture since the texture is that which has been associated with higher c/a ratios (near 1.63). Furthermore, an alloy was investigated during this study which has a c/a ratio close to that of beryllium (1.575 and 1.57 respectively). The Ti-Ta alloy had the rotated (0002) [10$\bar{1}$0] texture in contrast to the (0002) [10$\bar{1}$0] texture of beryllium.

The textures of titanium alloyed with columbium (c/a = 1.592), tantalum (c/a = 1.584 and 1.575) and zirconium (c/a = 1.590 and 1.602) have the same basic textures and differ from the texture of iodide titanium only by having areas of second high intensity 15° to 20° from the center of the (0002) pole figure in the rolling direction, shifts in the positions of the basal maxima along the cross direction, and in general, more scatter. In addition to these differences, the basal pole figures of the alloys containing zirconium, columbium, and tantalum did not show the low intensity region extending completely across the figure.

An interesting observation may be made from consideration of the phase diagrams of the systems studied. As indicated in Table II, the Ti-Al system shows a wide a solid solution range and two intermediate phases. The Ti-Cb and Ti-Ta systems show more restricted a regions, and the β phase is stabilized to room temperature for higher concentrations of the solute. The Ti-Zr system shows complete solid solubility. At least in this investigation, the system showing intermediate phases has a deformation texture different from that of the pure solvent, whereas those systems with no intermediate phases retained the texture of the solvent. Eventu-

Table II. Summary of Textures Listing c/a Ratios and Type of Phase Diagrams

	c/a	Texture	Type of Phase Diagram
Ti	1.588	(0002) tilted 27°, [10$\bar{1}$0]	
Zr	1.589	(0002) tilted 40°, [10$\bar{1}$0][5]	
Be	1.57	(0002) [10$\bar{1}$0][8]	
Ti—3.8% Al	1.600	(0002) [10$\bar{1}$0]	Wide a range, intermediate phases
Ti—3.6% Cb	1.592	(0002) tilted 40°, [10$\bar{1}$0]	Narrow a range, β stabilized
Ti—3.6% Ta	1.584	(0002) tilted 27°, [10$\bar{1}$0]	Moderate a range, β stabilized
Ti—15.4% Ta	1.575	(0002) tilted 27°, [10$\bar{1}$0]	Moderate a range, β stabilized
Ti—7.1% Zr	1.590	(0002) tilted 30°, [10$\bar{1}$0]	Complete solid solubility
Ti—14.75% Zr	1.602	(0002) tilted 30°, [10$\bar{1}$0]	Complete solid solubility

ally it may be possible to relate the factors determining the nature of the phase diagram with the choice of deformation mechanisms and deformation textures.

Most rationalizations of textures have been based on considerations of the crystal structure, deformation mechanisms, and relative ease of deformation on various systems. Before a complete analysis of the effect of alloying on textures can be carried out along these lines, it will be necessary to determine the effect of alloying on the deformation characteristics.

Summary

1—The deformation texture of a titanium alloy containing 3.8 pct Al and having c/a equal to 1.600 is very different from that of iodide titanium. The texture of the alloy can be described as (0002) $[10\bar{1}0]$.

2—The cold-rolled textures of a titanium alloy containing 3.6 pct Cb (c/a = 1.592), alloys containing 3.6 and 15.4 pct Ta (c/a = 1.584 and 1.575, respectively), and alloys containing 7.1 and 14.75 pct Zr (c/a = 1.590 and 1.602, respectively) were essentially the same as the cold-rolled texture of iodide titanium.

3—The deformation textures of hexagonal close-packed materials cannot be predicted entirely from a knowledge of the c/a ratios.

Acknowledgment

This work is part of a study of the preferred orientations in titanium and titanium-base alloys sponsored by the Flight Research Laboratory, Wright-Patterson Air Force Base under Contract No. AF 33(038)-19574.

References

[1] R. M. Brick, D. L. Martin, and R. P. Angier: *Trans.* ASM (1943) **31**, p. 675.
[2] P. W. Bakarian: *Trans.* AIME (1942) **147**, p. 266.
[3] M. L. Fuller and G. Edmunds: *Trans.* AIME (1934) **111**, p. 146.
[4] V. Caglioti and G. Sachs: *Metallwirtschaft* (1932) **11**, p. 1.
[5] F. D. Rosi, C. A. Dube, B. H. Alexander: *Trans.* AIME (1953) **197**, p. 257; JOURNAL OF METALS (February 1953).
[6] W. Rostoker: *Trans.* AIME (1952) **194**, p. 212; JOURNAL OF METALS (February 1952).
[7] E. T. Hayes, A. H. Roberson, and O. G. Paasche: Bur. Mines *R.I.* No. 4826 (1951).
[8] R. K. McGeary and B. Lustman: *Trans.* AIME (1951) **191**, p. 994; JOURNAL OF METALS (November 1951).
[9] C. S. Barrett and A. Smigelskas: *Trans.* AIME (1949) **185**, p. 145; JOURNAL OF METALS (February 1949).

Technical Note

Structure of the Phase TiMn and the Indexing of Powder Patterns Of Sigma-Type Phases

by R. P. Elliott and W. Rostoker

TWO intermediate phases enter into equilibrium with the primary solid solutions of titanium.[1] The $TiMn_2$ phase was identified by Wallbaum[2] as of the C14 type isomorphous with $MgZn_2$. Contrary to Maykuth, et al.,[1] the phase occuring at about the 50-50 atomic proportion has been shown to derive from a peritectoid reaction.[3] A 30 day anneal at 900°C of an alloy containing 52 wt pct Mn developed sufficient of the new phase to give a clear and predominant diffraction pattern. The powder pattern was taken in a 14 cm diameter powder camera using filtered Cu Kα radiation. In all, 75 lines were recognized and measured. Interplanar spacing and observed intensities for the first 26 of these are given in Table I.

R. P. ELLIOTT and W. ROSTOKER are Assistant Metallurgist and Senior Metallurgist, respectively, Metals Research Dept., Armour Research Foundation of Illinois Institute of Technology, Chicago.
TN 172E. Manuscript, May 14, 1953.

Table I. Observed Interplanar Spacings of σ-TiMn

	d, kX	Intensity*
1.	2.358	vft
2.	2.301	vft
3.	2.272	vw
4.	2.247	vft
5.	2.215	w
6.	2.191	vft
7.	2.156	vw
8.	2.109	diffuse vft
9.	2.001	ft
10.	1.967	vft
11.	1.945	vft
12.	1.893	diffuse vw
13.	1.819	vft
14.	1.778	vft
15.	1.728	vft
16.	1.685	vft
17.	1.667	vft
18.	1.492	vft
19.	1.433	ft
20.	1.407	vft
21.	1.345	vft
22.	1.331	vft
23.	1.314	vw
24.	1.302	vw
25.	1.290	vw
26.	1.255	vft

* w, weak; vw, very weak; ft, faint; vft, very faint.

Table II. Powder Pattern Lines of Sigma Phases Indexed According to the True Unit Cell (kX Units)

(hkl)	σ-FeCr,[5] d, Observed	σ-CrCo,[5] d, Observed	σ-FeV,[5] d, Observed	σ-CoV,[5] d, Observed	σ-NiV,[5] d, Observed	σ-TiMn d, Observed	σ-TiMn d, Calculated
101		4.00	4.01	4.07	4.10		
111		3.68	3.72	3.68	3.71		
201*			3.22	3.20	3.22		
220				3.10	3.12		
211				3.01			
300			2.97	2.94			
310			2.84	2.79			
221		2.61					
301	2.50						
311	2.38	2.36		2.35		2.358	2.383
002	2.27	2.26	2.31	2.28	2.31	2.272	2.266
102	2.215	2.20				2.191	2.196
400	2.22					2.215	2.215
321	2.16	2.15				2.156	2.161
410		2.124	2.155	2.140	2.160		
112						2.109	2.131
330	2.065	2.062	2.110	2.081	2.087		
202	2.019	2.010	2.050	2.032	2.052	2.001	2.018
212†	1.967	1.958	1.998	1.978	1.997	1.967	1.967
420							
411	1.925	1.922	1.961	1.940	1.959	1.945	1.942
331	1.879	1.878	1.914	1.895	1.911	1.893	1.897
222	1.833	1.827	1.864	1.846	1.859		
421						1.819	1.816
302				1.805			
312	1.757	1.752	1.789	1.769	1.785	1.778	1.772
500-430							
322	1.663	1.655	1.685	1.676	1.687	1.667	1.666
501-431	1.637	1.633	1.665	1.650	1.662		
511	1.608	1.607	1.636	1.621	1.640		

* (201) line does not belong to $D\frac{14}{4h}$ or $C\frac{4}{4v}$ space groups.

† Bracket indicates indistinguishable indices.

Note: The (100), (110), (200), (210), (320), (510), and (520) planes also should reflect in the sigma lattice, but have not been detected.

By inspection, a close resemblance was noted to powder patterns of σ-type phases. Although single-crystal studies by Shoemaker and Bergman,[4, 5] Dickens and Douglas,[6] and Christian and Pearson[7] have shown σ-type phases to be tetragonal (space group $D\frac{14}{4h}$ or $C\frac{4}{4v}$) with an axial ratio of about 0.5, published powder patterns[8] have been indexed on the basis of a tetragonal unit cell of axial ratio ≅ 1.46. For the proper identification of the structure of the new intermediate phase in the system Ti-Mn, it was considered necessary to re-index the powder patterns of Duwez and Baen[8] according to the correct unit cell.

For this purpose, a large Hull-Davey chart was constructed for the tetragonal lattice in the axial ratio range of 0.4 to 0.6. A log d scale of 50 in. per log cycle was used. From the lattice constants for σ-FeCr[4, 5] as derived from the single-crystal studies, it was apparent that the (002) planes possessed an interplanar spacing of 2.27 kX. Duwez and Baen[8] report lines of relatively high intensity at about this spacing for the powder patterns of σ-FeCr, σ-CrCo, σ-FeV, σ-CoV, and σ-NiV. With the use of the Hull-Davey chart and by locating the appropriate line at the (002) position, it was possible to index the rest of the patterns in every case. Calculations of lattice parameters from indices and spacings agreed well with results reported on single crystals. A summary of line spacings and indices is given in Table II.

Using the same procedure, the pattern for the new intermediate phase of the Ti-Mn system was successfully indexed. The results are compiled in Table II to provide a comparison with other members of the σ-phase family. Four very faint lines of the pattern could not be indexed. The lattice parameters of σ-TiMn were calculated by a least squares solution of best fitting lines as follows:

$$c = 4.533 \text{ kX}; \; a = 8.862 \text{ kX}; \; c/a = 0.512$$

Using these lattice parameters, interplanar spacings were calculated for comparison with observed values (see Table II). The agreement was quite satisfactory. It is to be noted that the indices determined for lines of all of the σ-phase patterns obey the systematic extinction requirements for the $D\frac{14}{4h}$ and $C\frac{4}{4v}$ namely, for lines of type $(h0l)$ reflections will not occur unless $(h + l)$ is even.

Acknowledgment

The authors wish to express appreciation for the sponsorships of this work by Ordnance Corps, U. S. Army, Watertown Arsenal, Watertown, Massachusetts, and for permission to publish. The work was performed under Contract DA-11-022-ORD-272.

References

[1] D. J. Maykuth, H. R. Ogden, and R. I. Jaffee: *Trans.* AIME (1953) **197**, pp. 225-230; JOURNAL OF METALS (February 1953).

[2] H. J. Wallbaum: *Ztsch. Metallkunde* (1941) **103**, p. 391.

[3] W. Rostoker, R. P. Elliott, and D. J. McPherson: Discussion on Ref. 1. To be published.

[4] D. P. Shoemaker and B. G. Bergman: *Journal* ACS (1950) **72**, p. 5793.

[5] B. G. Bergman and D. P. Shoemaker: *Journal of Chemical Physics* (1951) **19**, p. 515.

[6] G. I. Dickens and A. M. B. Douglas: *Journal* Iron and Steel Inst. (1951) **167**, p. 27.

[7] J. W. Christian and W. B. Pearson: *Nature* (1952) **169**, p. 70.

[8] P. Duwez and S. R. Baen: ASTM *Tech. Pub. No. 110* (1951) pp. 48-60.

The Ternary System Ti-Ta-C

by John G. McMullin and John T. Norton

An 1820°C isothermal cross section of the Ti-Ta-C ternary diagram was prepared from X-ray diffraction and metallographic data. No phases other than those appearing in the three binary diagrams were observed. At temperatures above the titanium transition temperature titanium and tantalum form a complete series of solid solutions containing up to 2 atomic pct C. The phases TiC and TaC also form a continuous series of solid solutions extending across the diagram.

PREVIOUS work on this alloy system was very limited. Of the three binary constitution diagrams involved, only one, the Ta-C system was available in the literature. Preliminary data on the other two systems was received from the investigators during the course of the investigation and both have been published in recent months. It had been shown that TiC and TaC formed a continuous series of solid solutions, but the range of carbon content in this phase was not known. While Ta_2C had been described, its solubility for or reactions with other carbides had not been reported. It was not known whether or not any ternary compounds occurred in the system.

The present program was undertaken to determine experimentally the general form of the ternary diagram. It is hoped that the results will be of value in furthering the development of sintered carbide cutting materials and high temperature ceramets, many of which contain combinations of TiC and TaC.

The Binary Systems

Of the three binary diagrams involved only that of Ta-C was available at the time this project was started. The diagram of Ellinger[1] redrawn in Fig. 1, shows a hexagonal phase Ta_2C having a very small composition range and a cubic TaC phase having a composition range of from 40 to 50 atomic pct C.

J. G. McMULLIN, Junior Member AIME, is associated with the General Electric Research Laboratory, Schenectady, and J. T. NORTON, Member AIME, is Professor of Metallurgy, Massachusetts Institute of Technology, Cambridge, Mass.

Discussion on this paper, TP 3602E, may be sent, 2 copies, to AIME by Dec. 1, 1953. Manuscript, April 15, 1953. Cleveland Meeting, October 1953.

This paper is based on a thesis by J. G. McMullin submitted in partial fulfillment of requirements for the degree of Doctor of Science in Metallurgy to the Massachusetts Institute of Technology, May 1952.

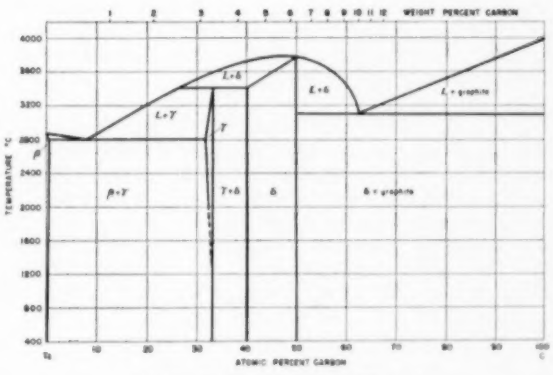

Fig. 1—Ta-C system after Ellinger.[1]

The authors made a separate determination of the composition range of TaC using lattice constant values and found the range to extend from 40 to 49.7 atomic pct C in good agreement with Ellinger's diagram.

Two determinations of the Ti-Ta system have appeared recently.[2,3] These two diagrams are in good agreement and show that β titanium and tantalum form a complete series of solid solutions.

The Ti-C diagram by Cadoff and Nielsen[4] shows a very limited solubility of carbon in both α and β titanium. The single carbide formed persists over a wide range of carbon contents. Several values for the upper limit of carbon content of this phase have been reported.[5-6] The highest value obtained in the M.I.T. Laboratory was 47.5 atomic pct C with a lattice constant of 4.328Å.[5] Fattinger[7] describes a gas carburization method which he claims produces stoichiometric TiC although he does not present any data showing that he actually had 50 atomic pct combined carbon. Several complete analyses on

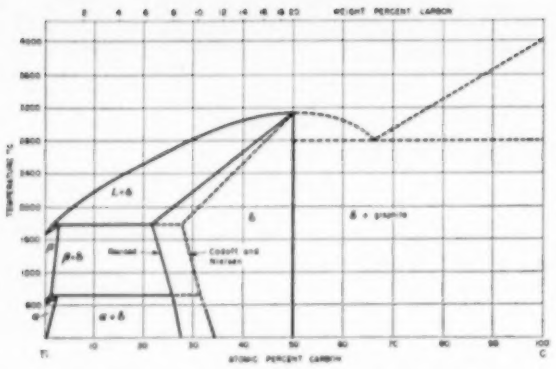

Fig. 2—Ti-C system tentative constitution diagram after Cadoff and Nielsen.[4]

commercially prepared titanium carbides have been made recently which have shown as high as 49.8 atomic pct combined carbon, and there seems to be no reason to doubt that the true upper limit of the phase is at 50 atomic pct. Cadoff and Nielsen[4] show the lower carbon limit of the δ phase to be about 27 atomic pct C at 1750°C. This is not in good agreement with the value of 22 atomic pct found by Ehrlich,[7] Rengstorff,[7] and Ragone.[8] The latter value was used in constructing the isothermal section shown in Fig. 3. No published data were available concerning reactions between TiC and graphite, but Stover[10] has observed a eutectic microstructure in melted alloys containing over 50 atomic pct C. Accordingly a eutectic is indicated in Fig. 2 although its temperature is not known.

Experimental Procedure

Alloy Preparation: All the alloys used in this program were prepared by powder metallurgy methods. The titanium and tantalum were added in the form of powdered metal hydrides, while carbon was added in the form of lampblack. The titanium hydride and tantalum hydride were carefully weighed out on an analytical balance in amounts calculated to give the desired atomic ratio of the two metals and the necessary amount of carbon was added. The powders were thoroughly mixed and cold-pressed into compacts about 25x6x6 mm.

The compacts were sintered 3 hr at 1820°C in a vacuum Arsem furnace with a vacuum better than one micron. The furnace cooled about 400°C in the first minute and was below 1000°C in 4 min. The cooling rate below the visible temperature range was slow because of the excellent vacuum in the furnace. A few specimens were cooled faster by filling the furnace with helium as soon as the power was shut off.

X-Ray Diffraction Methods: All specimens for X-ray examination were crushed and ground to −200 mesh. A suitable amount of the −200 mesh specimen was mounted on a glass microscope slide using collodion thinned with amyl acetate.

The X-ray diffraction patterns were made using a high angle X-ray spectrometer with copper radiation and a nickel filter. All lattice constant calculations were made using a value of 1.5405A for the wavelength of the Cu Kα1 line.

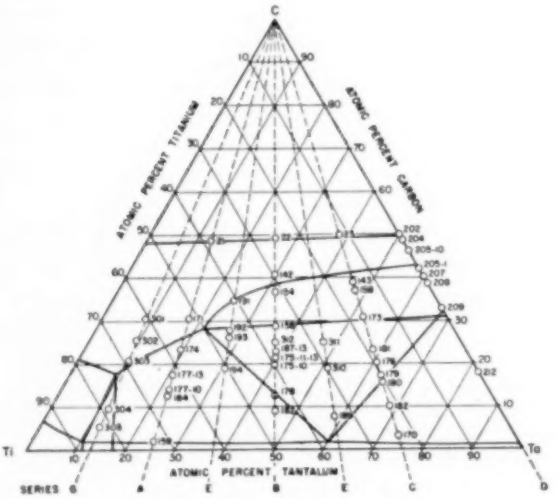

Fig. 4—Alloy compositions in atomic pct.

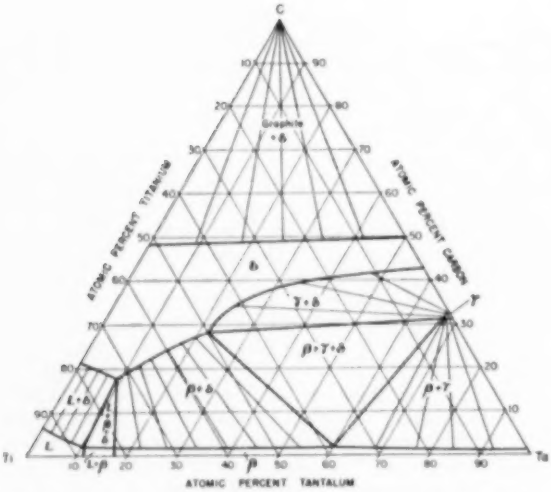

Fig. 3—Constitution of Ti-Ta-C alloys at 1820°C in atomic pct.

Chemical Analysis Methods: A carbon analysis was made on all samples. Total carbon analysis was made by combustion of the powdered carbide in a conventional carbon train.

Free carbon was determined by dissolving the carbide in a mixture of HF and HNO_3 and filtering. The residue on the filter was washed first with KOH, then with HCl and finally water. The residue was then ignited in the carbon train.

Combined carbon was determined by subtracting the free carbon from the total carbon analysis. A few analyses were made for titanium and tantalum and it was found that this ratio remained unchanged during the sintering. Fig. 4 shows the compositions of the alloys investigated.

The 1820°C Isothermal Section

The 1820°C isothermal section of the ternary diagram was chosen for extensive investigation for several reasons. It was desired to select a temperature which was below the solidus over most of the section but which was high enough to insure equi-

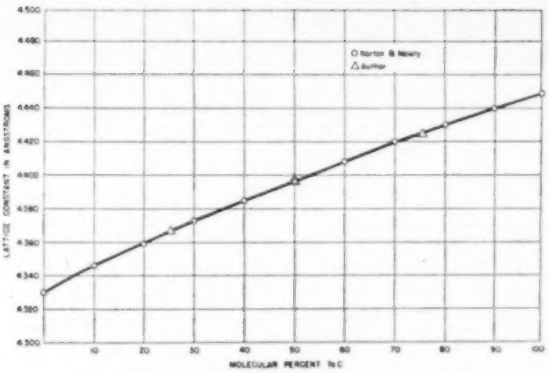

Fig. 5—Lattice constants of carbon-saturated δ phase.

librium in only a few hours at temperature. From the three binary diagrams it appeared that 1800°C would be an appropriate temperature. The particular temperature of 1820°C was chosen because the sintering furnace maintained this temperature very well but was difficult to control at 1800°C.

From the three binary diagrams it is apparent that five phases, liquid, β, γ, δ, and graphite (see Figs. 1 and 2) must be present at 1820°C. No other phases were observed at this temperature. With the δ phase extending across the diagram from TiC to TaC as shown by Norton and Mowry[11] and the boundary conditions imposed by the binary diagrams, it was evident that two three-phase fields must be present in the isothermal section. One of these, the liquid-β-δ field was not extensively investigated although its presence was definitely established. The β-γ-δ field was more thoroughly investigated and its boundaries located. Fig. 3 shows the 1820°C isothermal section as it was determined.

The β phase has a body-centered cubic structure with a comparatively narrow range of lattice constants.[5] In alloys containing less than 25 pct Ta the β phase transforms during cooling in a manner dependent on the rate. The small solubility of carbon in the β phase was not determined.

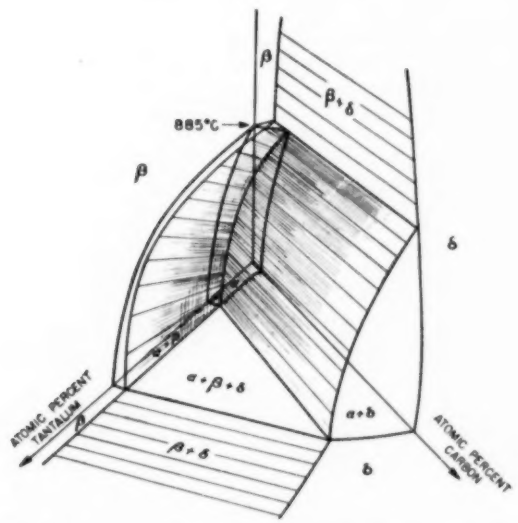

Fig. 6—Titanium-rich corner of the Ti-Ta-C ternary constitution diagram.

The δ phase has a face-centered cubic structure of the NaCl type. Fig. 5 shows the variation of lattice constant in carbon-saturated δ phase compositions between TiC and TaC. As the carbon content of the δ phase decreases, there is a marked decrease in the lattice constant.

The γ or Ta_2C phase was observed to have a hexagonal close-packed structure (a = 3.097Å, c/a = 1.595) as previously reported.[12] Since a pure Ta-C alloy (No. 209) containing 32 atomic pct C showed a trace of δ phase, it is apparent that the γ phase contains slightly less carbon than the stoichiometric Ta_2C. Its behavior is therefore exactly parallel to that of W_2C, with which it is isomorphous.[13] No shift in the high angle diffraction lines was observed in any specimen containing γ phase. This invariance of the lattice constants indicates that the composition range of γ phase is very small with respect to both carbon and titanium.

Because of this very small composition range of the γ phase the tie lines in the β-γ and β-δ fields can

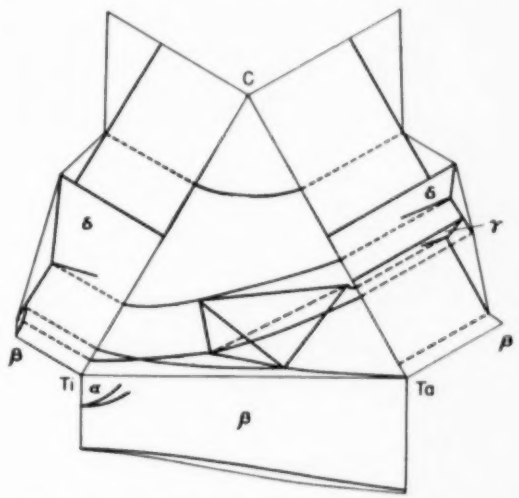

Fig. 7—Saturation lines in the Ti-Ta-C ternary constitution diagram.

be drawn in as shown. The δ phase lattice constants were used to locate the tie lines in the β-δ two-phase field.

Ternary Reactions

In the three binary diagrams there are six isothermal lines of two-fold saturation which must be considered in the ternary diagram.

The β Ti-α Ti-TiC peritectoid line probably moves in to the ternary as shown in Fig. 6 to form an α-β-δ three-phase field although this low temperature portion of the diagram was not investigated.

Two of these lines, the TiC-liquid-graphite eutectic and the TaC-liquid-graphite eutectic lines very probably join along a warped surface leaving a eutectic valley across the liquidus surface as indicated in Fig. 7.

The other three lines, the TiC-β Ti-liquid peritectic, the TaC-Ta_2C-liquid peritectic, and the Ta_2C-liquid-Ta eutectic could theoretically be joined on a four-phase invariant plane having either the eutectic or peritectic arrangement. A ternary eutectic plane would necessarily be at a temperature below the lowest binary reaction which in this case is the TiC-β Ti-liquid peritectic at about 1750°C. It is

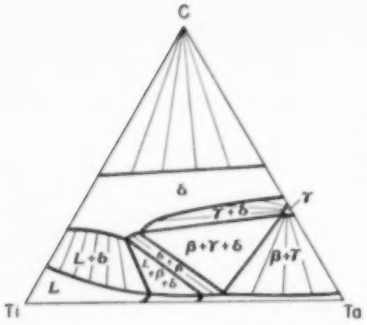

Fig. 8 (left)—Isothermal section at temperature below invariant plane.

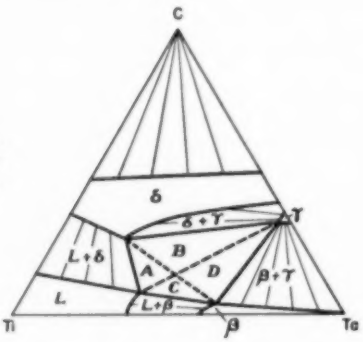

Fig. 9 (right)—Isothermal section at temperature of invariant plane.

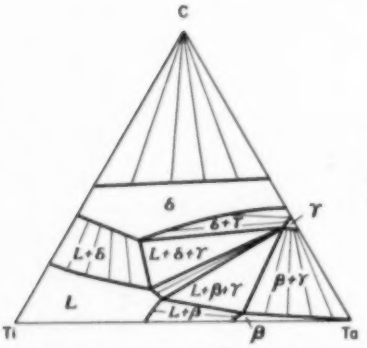

Fig. 10 (left)—Isothermal section at temperature above invariant plane.

evident from the 1820°C isothermal section shown in Fig. 3 that the ternary eutectic does not occur. With this possible arrangement eliminated, it was safe to assume that a ternary peritectic reaction occurred at some temperature above 1820°C and below the Ta_2C-liquid-Ta eutectic temperature of 2800°C.

To locate this temperature and the same time verify the assumed type of reaction, the following experiments were conducted. Several specimens of alloy No. 178 (43.1 pct Ti, 43.1 pct Ta, and 13.8 pct C) were prepared and sintered at 1820°C. After sintering, the specimens contained approximately equal amounts of β and δ phases in accordance with Fig. 3. Each of these specimens was given a short time anneal at successively higher temperatures above 1820°C and rapidly cooled with helium. Specimens annealed at temperatures up to and including 2020°C gave no evidence of melting. The X-ray pattern of the specimen annealed at 2020°C contained only β and δ X-ray lines. Specimen No. 178-17, heated to 2030°C and rapidly cooled showed physical evidence of partial melting by its rounded corners. The X-ray diffraction pattern of this specimen contained a substantial amount of γ phase as well as β and δ. Its microstructure gave definite evidence of melting. The appearance of γ phase and liquid was proof that the invariant temperature had been exceeded. Allowing for temperature measurement error, the temperature of the invariant plane is thus fixed at 2025° ± 15°C. On heating through this plane the so-called, "two over two" reaction of $\beta + \delta \rightarrow \gamma +$ liquid occurred. On rapid cooling some of the γ phase remained while the liquid decomposed to $\delta + \beta$.

As shown in Fig. 9, the invariant plane is divided into four quadrants; *A*, *B*, *C*, and *D*. The same reaction of $\beta + \delta \rightarrow \gamma +$ liquid occurs during the melting of alloys in all four quadrants although the phases present just above and below the invariant plane are different for each quadrant as shown by Figs. 8 and 10.

Summary

An isothermal cross section of the Ti-Ta-C alloy constitution diagram was determined. An invariant plane of four-fold saturation was found to occur at 2025°C. The reaction occurring at this temperature was $\beta + \delta \rightleftarrows \gamma +$ liquid.

No compounds or phases other than those occurring in the three binary constitution diagrams were observed.

The Ta_2C or γ phase was shown to be deficient in carbon containing only 31.5 atomic pct C instead of 33.3 pct. This carbon content appeared to be fixed and no solubility of titanium in Ta_2C was detected.

Titanium carbide and tantalum carbide formed a continuous series of solid solutions.

Acknowledgments

The authors wish to express their appreciation to Donald Guernsey for supervising the chemical analysis and to Kenneth Carlson for assistance in the experimental work. This project was sponsored by the Office of Naval Research under Contract No. N5ori-07817.

References

[1] F. H. Ellinger: The Tantalum-Carbon System. *Trans.* ASM (March 1943) **31**, p. 89.

[2] D. J. Maykuth, H. R. Ogden, and R. I. Jaffee: Ti-W and Ti-Ta Systems. *Trans.* AIME (1953) **197**, p. 231; JOURNAL OF METALS (February 1953).

[3] D. Summers-Smith: The Constitution of Ta-Ti Alloys. *Journal* Inst. Metals (October 1952) **81**, pp. 73-76.

[4] I. Cadoff and J. P. Nielsen: Ti-C Phase Diagram. *Trans.* AIME (1953) **197**, p. 248; JOURNAL OF METALS (February 1953).

[5] D. V. Ragone: Masters Thesis, Dept. of Metallurgy, Massachusetts Institute of Technology, 1951.

[6] G. A. Meerson and Ya. M. Lipkes: Study of Conditions of Carburization-Titanium. *Zhurnal Prikladnoi Khimii* (1941) **14**, No. 3, p. 291. (Brutcher translation 2099).

[7] V. Fattinger: Experimental Production of Pure TiC Powder by Means of Carburizing Gases. In *Physics of Powder Metallurgy* (1951) New York. McGraw-Hill Book Co.

[8] Ehrlich: On the Binary Systems of Titanium with the Elements Nitrogen, Carbon, Boron, and Beryllium. *Ztsch. anorg. allgem. Chemie* (1949) **259**, No. 1-4, pp. 1-21.

[9] G. P. W. Rengstorff: Masters Thesis, Dept. of Metallurgy, Massachusetts Institute of Technology, 1947.

[10] E. Stover: Personal communication.

[11] J. T. Norton and A. L. Mowry: Solubility Relationships of the Refractory Monocarbides. *Trans.* AIME (1949) **185**, p. 133; JOURNAL OF METALS (February 1949).

[12] H. J. Goldschmidt: The Structure of Carbides in Alloy Steels. *Journal* Iron and Steel Inst. (December 1948) p. 345.

[13] P. Rautala: Personal communication.

System Titanium-Chromium-Iron

by R. J. Van Thyne, H. D. Kessler, and M. Hansen

The phase diagram of the titanium-rich portion of the system Ti-Cr-Fe to 70 pct Ti was established by means of isothermal sections at 900°, 800°, 750°, 700°, 650°, 600°, and 550°C, using arc-cast alloys. An isotherm at 800°C was determined for the section bounded by Ti, $TiFe_2$, and $TiCr_2$. Micrographic analysis was employed as the principal method of investigation, supplemented by X-ray diffraction and incipient melting studies. A ternary eutectoid, $\beta \rightleftharpoons \alpha + TiCr_2 + TiFe$, occurs at approximately 8 wt pct Cr, 13 wt pct Fe, and about 540°C.

AMONG the first titanium-base alloys in commercial production were the Ti-Cr-Fe alloys. For this reason, the Materials Laboratory, Wright Air Development Center, sponsored an investigation of the system. No information on the constitution of the titanium-rich corner was available. Vogel and Wenderott studied titanium-poor ternary alloys.[1]

As part of this program, the binary systems Ti-Cr and Ti-Fe have been determined previously by the authors.[2] Other investigators have also studied the binary systems Ti-Cr,[3-7] Ti-Fe.[8, 8-10] Both of the binary systems are characterized by the eutectoid decomposition of the β phase.

Most of the effort of the present work has been concentrated on the titanium-rich corner with compositions of less than 30 pct total chromium and iron content. The determination of isothermal sections was the experimental approach used to obtain the ternary phase diagram. Vertical sections were used to check the consistency of the isothermal sections.

While this investigation was in progress, a study of the Ti-Mo-Cr system at Armour Research Foundation disclosed the existence of a high temperature modification of $TiCr_2$ above 1300°C.[11] This allotrope has a hexagonal structure of the $MgZn_2$ type, isomorphous with $TiFe_2$, whereas the low temperature modification of $TiCr_2$ is cubic,[6] of the $MgCu_2$ type. The existence of allotropy in $TiCr_2$ of course means a more complicated set of phase relationships in this general region than if the phase were monomorphic, as was first assumed.

Additional studies were made late in the investigation in order to clarify the part that the hexagonal $TiCr_2$ phase plays in the ternary phase relationships. These will be discussed in a separate section. Because they are of greatest practical significance, the phase relationships in the titanium-rich corner will be presented first, omitting the equilibria involving the hexagonal modification of $TiCr_2$ in an effort to simplify the presentation somewhat.

R. J. VAN THYNE is Associate Metallurgist, H. D. KESSLER, Junior Member AIME, is Supervisor, Nonferrous Metals Research, and M. HANSEN, Member AIME, is Chairman, Metals Research Dept., Armour Research Foundation of Illinois Institute of Technology, Chicago.

Discussion on this paper, TP 3603E, may be sent, 2 copies, to AIME by Dec. 1, 1953. Manuscript, April 20, 1953. Cleveland Meeting, October 1953.

Table I. Analyses of Impurities in Materials Used

Iron		Chromium	
Si	0.0093%	C	0.015%
Ni	0.012	O	0.066
P	0.0023	N	0.0022
S	0.013		
C	0.011		

Experimental Procedure

Materials: The titanium used in the preparation of the alloys was iodide crystal bar (99.9 pct pure) produced by the New Jersey Zinc Co. High purity chromium and iron were obtained from the National Research Corp. Table I gives the analyses of these materials.

Melting Practice: Over 100 alloy ingots weighing 10 to 20 g were melted in a nonconsumable electrode arc-melting furnace. As the techniques are identical to those reported previously,[12, 13] they will not be detailed here. The ingots were melted in the cavity of a copper melting block insert under a slight positive pressure of helium. No measurable hardness

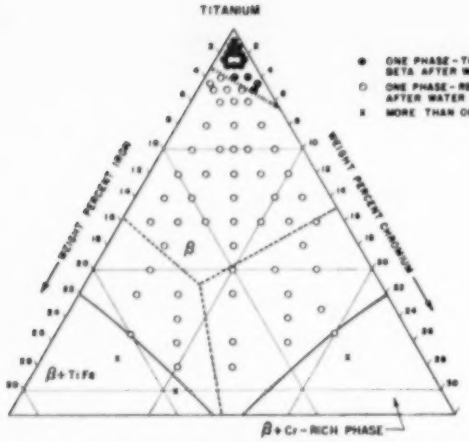

Fig. 1—Partial isothermal section at 900°C of the Ti-Cr-Fe system.

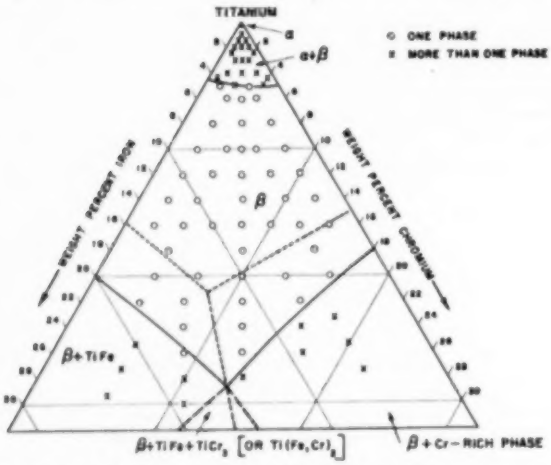

Fig. 2—Partial isothermal section at 800°C of the Ti-Cr-Fe system.

increase was found on remelting small control ingots of iodide titanium. To insure homogeneity of composition, each ingot was turned over and remelted four times without opening the furnace.

The alloy charges and resultant ingots were weighed to the nearest milligram. As the average weight losses on melting were small, the actual compositions were judged to be very close to the nominal compositions. Many check analyses, particularly for the binary alloys, substantiated the general use of nominal compositions.

Annealing Treatments: Annealing treatments of as-cast specimens were carried out in Vycor (to 1100°C) and quartz bulbs. The bulbs were sealed under vacuum for temperatures up to 1000°C; but for higher temperatures a partial pressure of argon was necessary to prevent their collapse. Information on the annealing times used for various temperatures is given in Table II. All samples heat-treated below 800°C were first annealed at 900°C for 2 to 8 hr and then slowly cooled to the temperature of final annealing. The furnace temperature control was within ±3°C of the reported temperatures below 1100°C, and about ±10°C for higher temperatures.

Coring was observed in some alloys containing over 5 pct total alloy content of chromium and iron. Therefore, these alloys were homogenization annealed at 1050°C for 24 hr prior to the regular isothermal anneals.

Melting Range Determinations: Metallographic analysis after isothermal annealing was used to outline the solidus surface. The annealing temperatures were selected by first determining the temperature of visible melting upon heating as described earlier.[13, 18] The samples for micrographic analysis were separated with molybdenum sheet during annealing to prevent contact in case of melting. The accuracy of these data is estimated to be ±10°C.

Table II. Annealing Conditions for Ti-Cr-Fe Alloys

Temperature, °C	Time, Hr	Temperature, °C	Time, Hr
1300	½	750	192-288
1200	½-15	700	192-288
1100	1-30	650	432
1050	24	600	576-600
1000	2-40	550	744
900	22-72	500	720
800	144		

Results and Discussion

The Phase Diagram: The constitution of the titanium corner of the Ti-Cr-Fe system is of the ternary eutectoid type. Curves of double saturation ($\beta \rightleftharpoons \alpha$ + $TiCr_2$ and $\beta \rightleftharpoons \alpha$ + TiFe) descend into the space

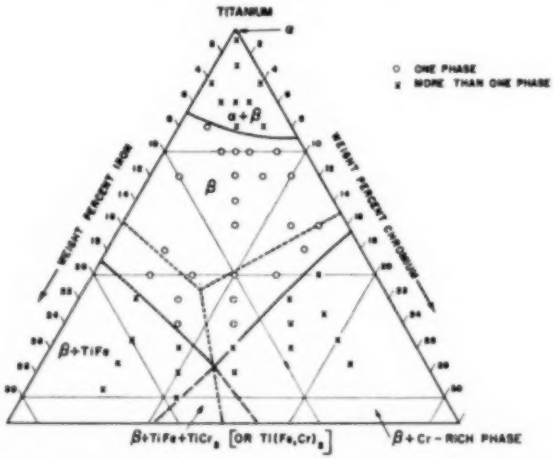

Fig. 3—Partial isothermal section at 750°C of the Ti-Cr-Fe system.

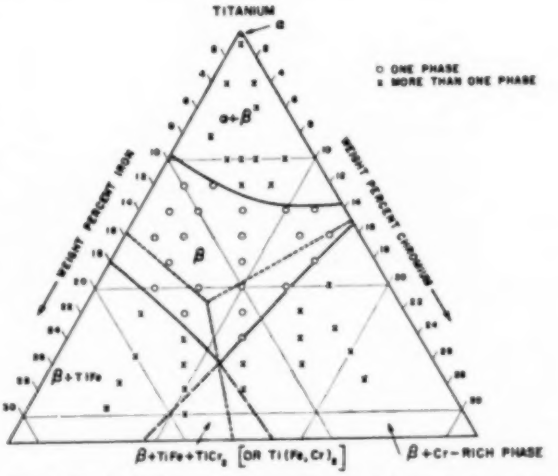

Fig. 4—Partial isothermal section at 700°C of the Ti-Cr-Fe system.

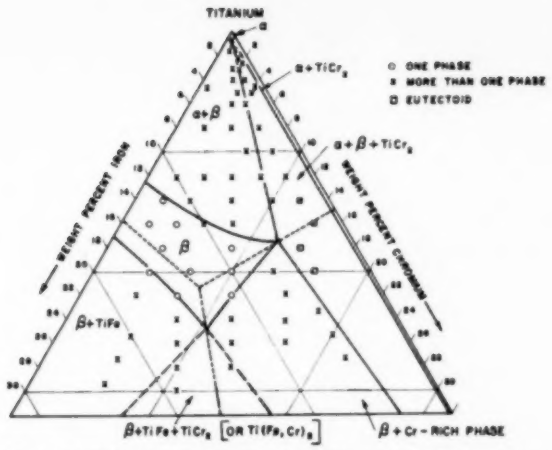

Fig. 5—Partial isothermal section at 650°C of the Ti-Cr-Fe system.

model from the two binary eutectoid points at 15 pct Cr, 685°C and 16 pct Fe, 585°C, respectively, along with that expressing saturation of the two compounds ($\beta \rightleftharpoons TiCr_2$ + TiFe). These three space curves meet to form a ternary eutectoid point ($\beta \rightleftharpoons \alpha$ + $TiCr_2$ + TiFe) at approximately 8 pct Cr, 13 pct Fe and 540°C.

Isothermal Sections: Isothermal sections at temperatures between 900° and 550°C are presented in Figs. 1 to 7. At 900°C, Fig. 1, the β field extends over almost the entire composition area shown. The transition from transformed to retained β after water quenching these alloys from the β state is shown as a shaded band. This appears to be a straight line joining the similar transition compositions in the binary systems; that is, between 3 and 4 pct Fe, and 6 and 7 pct Cr. The samples of lower alloy content transformed to an acicular product (α') partially or completely during water quenching, and those of higher alloy content consisted entirely of retained β. The position of the three space curves of double saturation have been shown as dotted lines on all of the isotherms.

Sections through the space model at 800°, 750°, and 700°C (Figs. 2 to 4) show the enlargement of the $\alpha + \beta$ and β + compound fields. In general, the limits of the β field in the isothermal sections were not determined by the data points obtained at a particular temperature alone. After the data had been obtained for all temperature levels (900° to 550°C), graphical interpolation, using the isothermal and vertical sections, was done, placing emphasis on the binary intercepts. Therefore, the isotherms shown are an integration of all the data.

The exact location of the sectional phase boundaries at 650°C and below (Figs. 5 to 7) was greatly impeded by the fact that the rate of diffusion at these temperatures is extremely low. As a consequence, the ternary β phase remains in a metastable state, and only in the alloys rich in chromium was microscopic evidence found of the reaction, $\beta \rightleftharpoons \alpha$ + $TiCr_2$.

The isothermal section for 650°C is presented in Fig. 5. With the eutectoid decomposition in the Ti-Cr system occurring at 685°C, the eutectoid decomposition of the ternary β phase ($\beta \rightleftharpoons \alpha$ + $TiCr_2$) would take place within a certain range of compositions along the entire Ti-Cr side of the system. However, as shown in Fig. 5, most of the hypoeutectoid alloys in the $\alpha + \beta$ + $TiCr_2$ field were actually found to be only two-phase ($\alpha + \beta$), even after 18 days of annealing. The fact that the eutectoid decomposition did not occur in the hypoeutectoid alloys of low alloy content at annealing temperatures fairly close to the eutectoid temperature, was also observed in the binary systems.[3]

Because of the reluctance of the eutectoid to develop, alloys with less than 12 pct Cr could not be used in positioning the boundary between the $\alpha + \beta$ and $\alpha + \beta$ + $TiCr_2$ fields at 650°C. However, as alloys of compositions near the space curve of double saturation showed eutectoid decomposition and the boundaries of the adjacent β field have to meet at the vertex of the $\alpha + \beta$ + $TiCr_2$ triangle, this point could be located at approximately 13 pct Cr and 5 pct Fe.

The isothermal section at 600°C (Fig. 6) is similar to that at 650°C, with changes only in the extent of the phase fields. Eutectoid decomposition was observed in a greater number of alloys on the chromium-rich side with falling temperature, although the β phase in samples of low alloy content continued to be metastable. As at 650°C, the vertex point of the $\alpha + \beta$ + $TiCr_2$ triangle was positioned using the intersection of the sectional phase boundaries

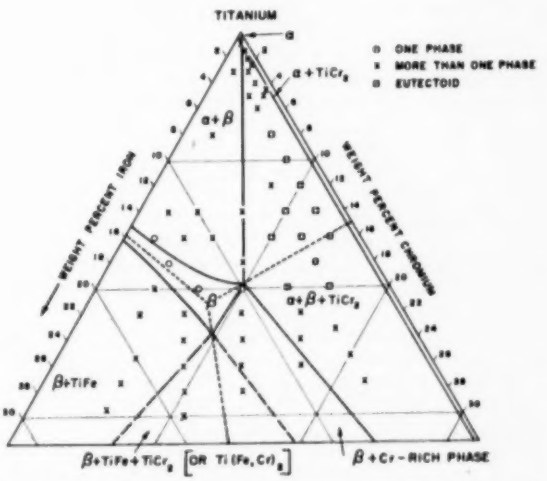

Fig. 6—Partial isothermal section at 600°C of the Ti-Cr-Fe system.

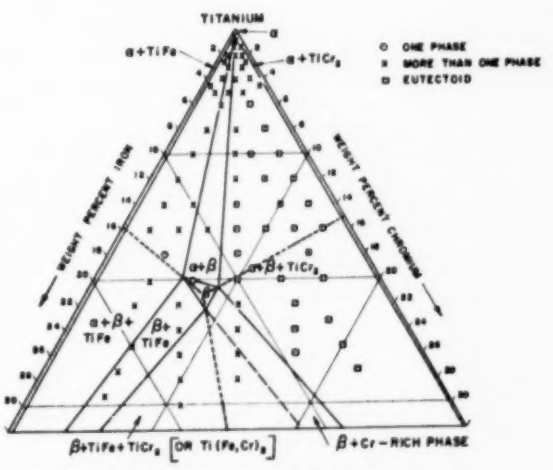

Fig. 7—Partial isothermal section at 550°C of the Ti-Cr-Fe system.

Fig. 8—Isotherms of the lower surfaces of the β phase space in the Ti-Cr-Fe system.

$\beta/\alpha + \beta$ and $\beta/\beta +$ Cr-rich phase in addition to the projection of the space curve of double saturation.

The section at 550°C (Fig. 7) is below the binary Ti-Fe eutectoid level, 585°C; therefore, the β + TiFe and $\alpha + \beta +$ TiFe fields should now be evident. It can be seen from the data points that no eutectoid structures were observed in ternary alloys on the iron side annealed at 550°C for 31 days although under similar annealing conditions the β phase of the binary Ti-Fe system started to decompose eutectoidally.[2] In the iron-rich ternary alloys, the eutectoid decomposition $\beta \rightleftharpoons \alpha +$ TiFe will start below the eutectoid temperature of the Ti-Fe system. It is not surprising, therefore, that at these low temperatures, equilibrium is approached only at a very low rate and that a definite indication of eutectoid was not observed.

The two curves of double saturation extending from the binary eutectoid points were positioned by the identification of either α or compound constituents in the microstructures of alloys lying on either side of the line. For example, at 550°C (Fig. 7), the microstructures of the 2 pct Cr-14 pct Fe and the 4 pct Cr-16 pct Fe samples consist of $\alpha + \beta$ and $\beta +$ TiFe, respectively. The 4 pct Cr-14 pct Fe alloy is single-phase (β), although the alloy is located in the $\alpha + \beta +$ TiFe phase field. The apparent anomaly is explained on the basis that the composition lies very close to the space curve of double saturation. Thus, no proeutectoid constituents would be expected in the microstructure, and the indicated β is metastable.

At 650° and 600°C, the β field is extensive enough

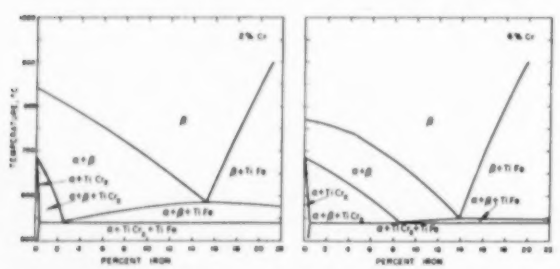

Fig. 9—Vertical sections of the Ti-Cr-Fe system at constant chromium contents.

that data points are available to accurately locate the limits of the β field and hence the other phase fields. However, at 550°C, the β field is very small and the data points on the isotherm alone did not permit the accurate placement of phase boundaries. A number of vertical sections were drawn, some of which will be presented later. From the extrapolation of data from higher temperatures, it was apparent that the β field was very restricted at 550°C and that the ternary eutectoid temperature occurs at approximately 540°C. Therefore, the β field has been constructed as very small with the limits located at points on the space curves of double saturation. The lines expressing double saturation intersect at the ternary eutectoid point; approximately 8 pct Cr and 13 pct Fe.

Although the data are not presented, alloys were annealed at 500°C for 30 days. In general, the microstructures were very fine and conclusive evidence of the binary Ti-Fe or ternary eutectoid decomposition was not observed in the ternary alloys. Several other techniques were tried to obtain the ternary eutectoid decomposition. A powder sample and a specimen that had been cold pressed were prepared. As slight amounts of contamination are known to greatly accelerate the reaction, an 8 pct Cr-13 pct Fe alloy was prepared using sponge titanium. These samples were annealed at 525°C

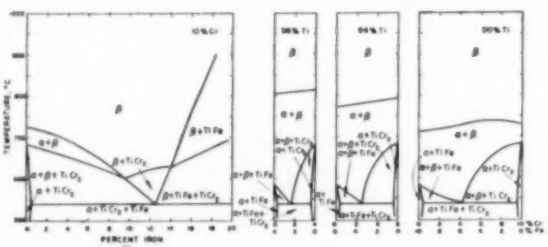

Fig. 10—Vertical sections of the Ti-Cr-Fe system at constant chromium and titanium contents.

for 12 days but no definite evidence of the ternary eutectoid decomposition either metallographically or by X-ray diffraction was found.

The solubility of chromium and iron in α titanium is less than 1 pct total alloy content. The curve of maximum solubility has been arbitrarily drawn at equal iron and chromium contents. Only a very narrow duplex phase space exists between α and $TiCr_2$, because of the restricted solubility of chromium and iron in α titanium. At equilibrium, the eutectoid reaction would be complete in this region, and β is consumed. No attempt was made to locate the extent of the $\alpha + TiCr_2$ or $\alpha +$ TiFe fields at high alloy contents because they apparently are very restricted.

Fig. 8, which is a composite of isotherms of the lower surfaces of the β phase space, illustrates the good correlation obtained on combining the results. Although not shown, additional alloys were prepared and annealed to more accurately locate the ternary eutectoid point. However, because of the very small size and small amounts of phases present in these microstructures, they could not be identified.

Vertical Sections: Vertical sections at constant chromium and titanium contents are illustrated in Figs. 9 and 10. The data used in preparing these curves were taken from the isothermal sections presented earlier. Excellent correlation of data was

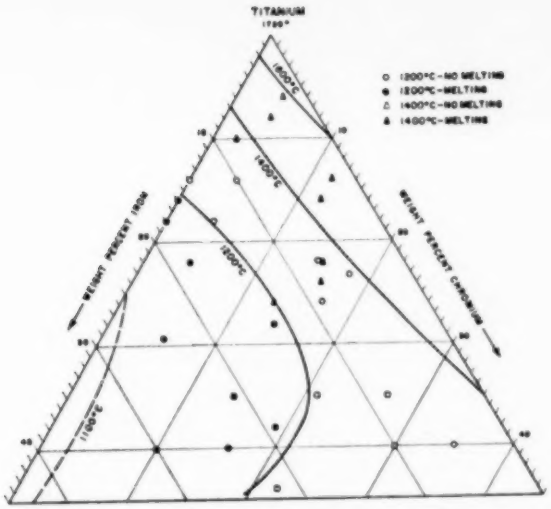

Fig. 11—Isotherms of the solidus surface of the Ti-Cr-Fe system.

obtained when plotting these sections and others that have been omitted due to space considerations.

Melting Range Determinations: The results of the solidus determinations are presented in Fig. 11; the data points shown were determined by metallographic examination of samples that were isothermally annealed and water quenched. The isotherms were drawn using previously determined solidus temperatures for the binary systems.[2] Incipient melting data were obtained for a number of alloys by visible sign of melting on heating and, in general, substantiated the isotherms illustrated. Annealing at 1100°C showed that only the binary Ti-Fe alloys were melted. Therefore, chromium additions raise the temperature of the binary Ti-Fe eutectic (1080°C).

Alloys Rich in Chromium and Iron: With the discovery of the hexagonal modification of $TiCr_2$, it became evident that at high temperatures a continuous series of solid solutions may exist between $TiCr_2$ and $TiFe_2$, which are isomorphous. At lower temperatures the cubic modification of $TiCr_2$ is stable. If a continuous single-phase field exists between $TiCr_2$ and $TiFe_2$ at high temperatures, it must continuously retreat away from $TiCr_2$ with falling temperature. This by itself would not necessarily affect the titanium-rich portion of the diagram that had been investigated. However, if the hexagonal phase extends into the ternary system and enters into equilibrium with β phase, the isothermal sections would then necessarily contain additional two and three phase regions.

To decide if the phase relationships mentioned above do exist, an X-ray pattern was obtained for a

Table III. X-Ray Diffraction Data for Alloys Lying on the Section $TiCr_2$-$TiFe_2$

Composition, Wt Pct			Annealing Treatment			Lattice Parameters of $Ti(Fe,Cr)_2$		
Ti	Cr	Fe	°C	Hr	Phases Observed	c(kX)	a(kX)	c/a
34	66	0	1300	½	$TiCr_2$ (Hex.)	7.987	4.919	1.624
			1200	½	$TiCr_2$ (Hex.)			
			1200	15	$TiCr_2$ (Hex.)			
			1100	1	$TiCr_2$ (Hex.)			
			1100	30	$TiCr_2$ (Hex.)			
			1000	2	$TiCr_2$ (Hex.) + $TiCr_2$ (Cubic)			
			1000	40	$TiCr_2$ (Cubic)			
			900	22	$TiCr_2$ (Cubic)			
34	63	3	800	144	$Ti(Fe,Cr)_2$ + $TiCr_2$	7.976	4.899	1.628
			700	288	$Ti(Fe,Cr)_2$	7.976	4.900	1.628
34	61	5	800	144	$Ti(Fe,Cr)_2$ + $TiCr_2$	7.983	4.899	1.630
			600	576	$Ti(Fe,Cr)_2$ + $TiCr_2$	7.971	4.900	1.627
			500	696	$Ti(Fe,Cr)_2$			
34	58	8	1000	30	$Ti(Fe,Cr)_2$	7.985	4.898	1.630
			800	170	$Ti(Fe,Cr)_2$	7.976	4.896	1.629
			700	288	$Ti(Fe,Cr)_2$	7.967	4.894	1.628
			600	576	$Ti(Fe,Cr)_2$	7.974	4.896	1.629
33	47	20	1000	30	$Ti(Fe,Cr)_2$	7.963	4.861	1.638
			800	170	$Ti(Fe,Cr)_2$			
			600	144	$Ti(Fe,Cr)_2$	7.968	4.862	1.639
32	36	32	1000	30	$Ti(Fe,Cr)_2$	7.925	4.839	1.638
			800	170	$Ti(Fe,Cr)_2$			
			600	144	$Ti(Fe,Cr)_2$	7.928	4.838	1.639
31	22	47	600	144	$Ti(Fe,Cr)_2$	7.869	4.812	1.635
30	10	60	600	144	$Ti(Fe,Cr)_2$	7.806	4.780	1.633
30	0	70	1000	30	$TiFe_2$	7.808	4.783	1.632
			800	170	$TiFe_2$			
			600	144	$TiFe_2$	7.806	4.780	1.633

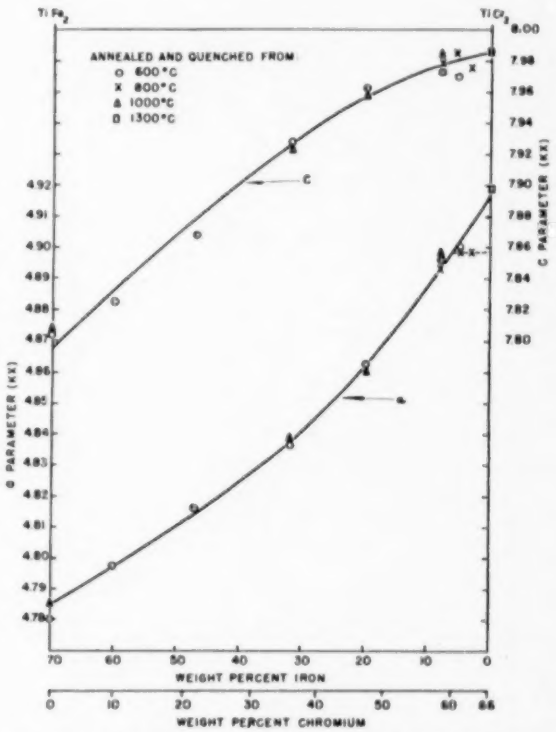

Fig. 12—Lattice parameters of the hexagonal $Ti(Fe,Cr)_2$ phase.

22 pct Cr-22 pct Fe alloy annealed at 800°C. This sample was found to contain β, TiFe, and the hexagonal modification of $TiCr_2$. Therefore, the hexagonal modification does enter into equilibrium with β. For this reason, the phase relationships concerning $Ti(Fe, Cr)_2$ (the designation $Ti(Fe, Cr)_2$ will be used to describe the ternary phase of hexagonal structure) were studied.

Over 20 samples of high alloy content, the compositions of which are shown as data points in Fig. 14, were annealed at several temperature levels between 1000° and 500°C. However, the 800°C isotherm will serve to illustrate the equilibria involved. As there are no metallographic differences between $TiCr_2$ or $Ti(Fe, Cr)_2$, X-ray diffraction was the principal method used to identify the phases. Micrographic analysis was used where it was helpful, such as for the identification of samples in the β + TiFe + $Ti(Fe, Cr)_2$ field.

X-ray diffraction data for the group of alloys with compositions spaced along a tie line between

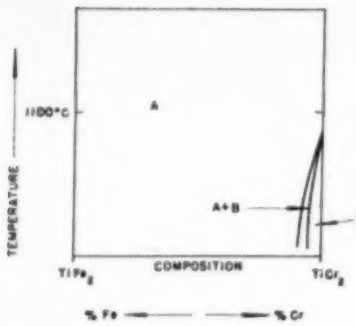

Fig. 13—Vertical section of the Ti-Cr-Fe system through $TiFe_2$ and $TiCr_2$. A—Ti(Fe, Cr)$_2$, hexagonal high temperature. B—$TiCr_2$, chromium-rich cubic phase.

$TiFe_2$ (70 wt pct Fe) and $TiCr_2$ (66 wt pct Cr) were obtained. Samples were annealed at temperatures between 1300° and 500°C for 30 min to 29 days. All alloys treated were found to consist of only the hexagonal phase, Ti(Fe, Cr)$_2$ at elevated temperatures. A summary of the lattice parameter measurements is shown in Table III. The polymorphic transformation of $TiCr_2$ was found to occur between 1000° and 1100°C.

The data shown in Table III are plotted in Fig. 12; smooth curves were obtained for both lattice parameter values at elevated temperatures. This proves the existence of a continuous series of solid solutions between $TiFe_2$ and hexagonal $TiCr_2$. Parameter values for a given alloy in the one-phase field at different temperature levels were in close agreement. A break occurs in the lattice parameter curves (particularly curve *a*) at the chromium-rich side with lowered temperature. This is due to the appearance of the two-phase field $TiCr_2$ + Ti(Fe, Cr)$_2$, and hence the composition of the hexagonal phase in equilibrium with the cubic phase remains the same. Fig. 13 schematically illustrates the vertical section through the two compounds.

The 800°C isotherm, given in Fig. 14, is based on X-ray data (Table IV) and metallographic observations. It is evident that the phase relationships are more complex than those shown in Fig. 2. They indicate that the β phase is in equilibrium with both $TiCr_2$ and Ti(Fe, Cr)$_2$ at 800°C. However, the location of the α, $\alpha + \beta$, and β spaces, on which most of the effort has been concentrated, is not affected by these findings.

The corners of the phase field β + TiFe + Ti(Fe, Cr)$_2$ are located at the saturated β phase, TiFe, and approximately 58 pct Cr-8 pct Fe, representing the Ti(Fe, Cr)$_2$ phase. The latter value was

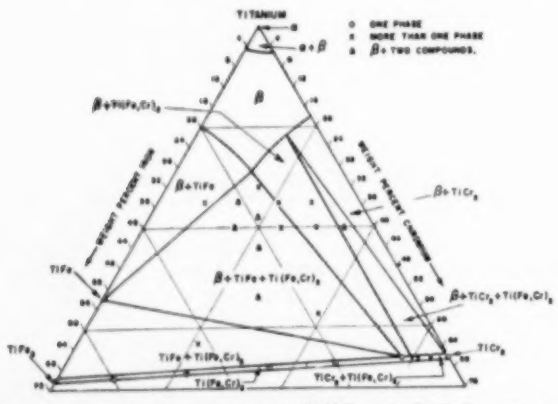

Fig. 14—Partial isothermal section at 800°C of the Ti-Cr-Fe system.

obtained by comparing the lattice parameters of the Ti(Fe, Cr)$_2$ phase of alloys in the three-phase field with those of the section $TiFe_2$-$TiCr_2$ (Fig. 12). The other three-phase field, β + $TiCr_2$ + Ti(Fe, Cr)$_2$, was located as shown, as the structure of the 35 pct Cr-5 pct Fe alloy was found by X-ray diffraction to consist of three phases.

Upon examination of the 800°C isotherm, it is recognized that additional phase relationships will occur below this temperature. No attempt was made to study these. For simplicity, it was assumed that the eutectoid decomposition of the ternary β phase involves the phases, α, TiFe, and $TiCr_2$. This would be true if a four-phase reaction, β + Ti(Fe, Cr)$_2$ $\rightleftharpoons$ TiFe + $TiCr_2$, takes place, eliminating equilibria involving Ti(Fe, Cr)$_2$ in alloys lying on the high titanium side of a tie line extending between TiFe and $TiCr_2$. However, it is realized that an alternate reaction, β + $TiCr_2$ $\rightleftharpoons$ α + Ti(Fe, Cr)$_2$, could proceed at a temperature between that of binary Ti-Cr eutectoid (685°C) and the ternary eutectoid (540°C). If this reaction should occur, the ternary eutectoid would consist of α + TiFe + Ti(Fe, Cr)$_2$.

Microstructures: Only a limited number of micrographs are presented as, in general, the microstructures observed were similar to those for the alloys of the binary systems. For typical microstructures representative of the various phase fields, the reader is referred to the binary systems.[2]

Table IV. X-Ray Diffraction Identification of Phases Present in Ti-Cr-Fe Alloys Annealed at 800°C

Composition, Wt Pct					Lattice Parameters of Ti(Fe,Cr)$_2$		
Ti	Cr	Fe	Annealing Time, Hr	Phases Observed	*c*(kX)	*a*(kX)	*c*/*a*
34	63	3	144	Ti(Fe,Cr)$_2$ + $TiCr_2$	7.976	4.899	1.628
34	61	5	144	Ti(Fe,Cr)$_2$ + $TiCr_2$	7.983	4.899	1.630
60	35	5	144	β + $TiCr_2$ + Ti(Fe,Cr)$_2$			
34	58	8	170	Ti(Fe,Cr)$_2$	7.976	4.896	1.629
60	30	10	144	β + Ti(Fe,Cr)$_2$			
60	24	16	144	β + Ti(FeCr)$_2$			
68	16	16	144	β + Ti(Fe,Cr)$_2$			
43	39	18	170	Ti(Fe,Cr)$_2$	7.999	4.893	1.635
33	47	20	170	Ti(Fe,Cr)$_2$			
65	14	21	144	β + TiFe			
56	22	22	144	β + TiFe + Ti(Fe,Cr)$_2$	7.988	4.905	1.630
32	36	32	170	Ti(Fe,Cr)$_2$			
37	21	42	144	TiFe + Ti(Fe,Cr)$_2$	7.904	4.849	1.631
30	0	70	170	$TiFe_2$			

The low solubility of chromium and iron in α titanium is shown by the duplex structure of Fig. 15. Fig. 16 illustrates the α + $TiCr_2$ eutectoid structure of the $\alpha + \beta$ + $TiCr_2$ space. As previously discussed in another section, no microstructural evidence of eutectoid decomposition in the $\alpha + \beta$ + TiFe space was observed. Also, no ternary eutectoid decomposition was noted at 500°C, although this temperature is below the ternary eutectoid plane. The Ti(Fe, Cr)$_2$ phase is illustrated in Fig. 17.

Fig. 18 shows the microstructure of an alloy annealed at 800°C in the β + TiFe + Ti(Fe, Cr)$_2$ space. An X-ray diffraction pattern of this sample confirmed the metallographic evidence of the two intermediate phases. To differentiate between the coexisting intermediate phases, staining etchants were tested. A 10 pct aqueous solution of various etchants was used. Of the many etchants tried, electrolytic etching with a $K_3Fe(CN)_6$ + NaOH solution was the most useful. The polished samples were etched first with a HNO_3 + HF + glycerine

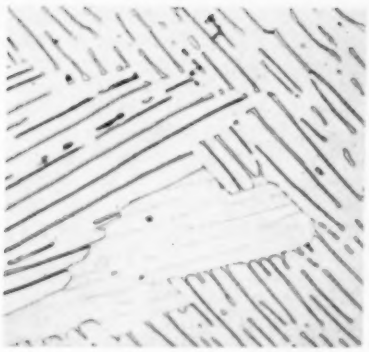

Fig. 15—A 0.5 pct Cr, 0.5 pct Fe alloy, water-quenched after annealing at 650°C for 432 hr. α + retained β (smaller amount). Etchant: HNO_3 + HF + glycerine. X500. Area reduced approximately 30 pct for reproduction.

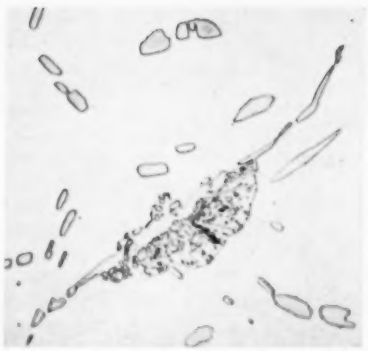

Fig. 16—A 12 pct Cr, 2 pct Fe alloy annealed at 650°C for 432 hr. Eutectoid (α + $TiCr_2$) and α in a matrix of retained β. Etchant: HNO_3 + HF + glycerine. X500. Area reduced approximately 30 pct for reproduction.

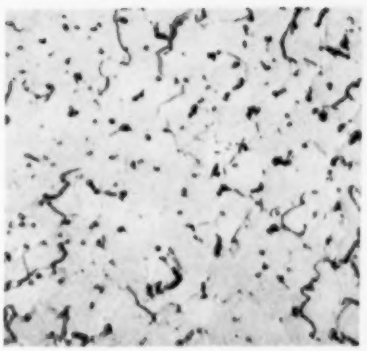

Fig. 17—A 47 pct Cr, 20 pct Fe alloy, water-quenched after annealing at 800°C for 144 hr. Nearly single phase, $Ti(Fe,Cr)_2$. Etchant: HNO_3 + HF + glycerine. X500. Area reduced approximately 30 pct for reproduction.

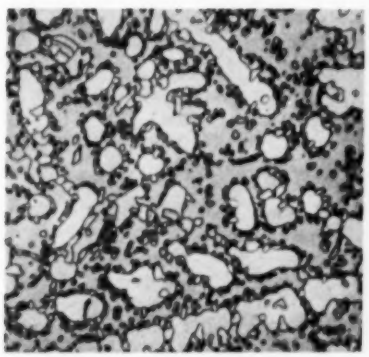

Fig. 18—A 22 pct Cr, 22 pct Fe alloy annealed at 800°C for 144 hr and water-quenched. $Ti(Fe,Cr)_2$ (larger crystals) and TiFe in a matrix of β. Etchant: HNO_3 + HF + glycerine. X750. Area reduced approximately 30 pct for reproduction.

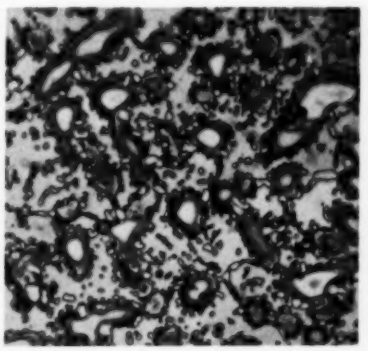

Fig. 19—The same microstructure as Fig. 18. $Ti(Fe,Cr)_2$ is now stained although TiFe is not. Etchant: electrolytic $K_3Fe(CN)_6$ + NaOH + H_2O superimposed upon the structure etched with HNO_3 + HF + glycerine. X750. Area reduced approximately 30 pct for reproduction.

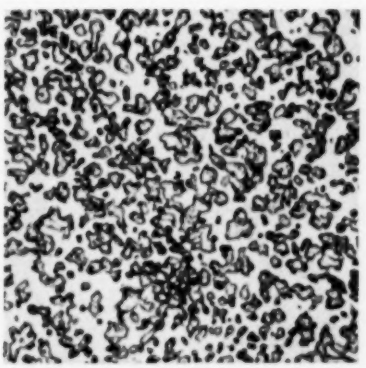

Fig. 20—A 50 pct Cr alloy, water-quenched after 24 hr at 1000°C. β and stained $TiCr_2$. Etchant: same as Fig. 19. X250. Area reduced approximately 30 pct for reproduction.

solution (Fig. 18) and were then electrolytically etched with the $K_3Fe(CN)_6$ + NaOH solution, preferentially staining $Ti(Fe,Cr)_2$ (Fig. 19).

A size difference may be noted in Fig. 18; $Ti(Fe,Cr)_2$ is larger with the smaller TiFe crystals surrounding it. In order to prove that the differential staining in Fig. 19 is due to the different phases present and not just size variations, binary alloys containing either $TiCr_2$ or TiFe were stain-etched. Both alloys were polished and etched under conditions identical to those used in the preparation of Fig. 19. Figs. 20 and 21 conclusively show that $TiCr_2$ is heavily stained whereas the TiFe is unaffected by the $K_3Fe(CN)_6$ + NaOH + H_2O etchant.

As another technique of differentiating between the two compounds, heat tinting was tried. With this method a sample previously polished is placed in a preheated furnace with an air atmosphere. At 700°C, the only temperature investigated, 40 sec appears to be the best time. Shorter times result in little tinting, whereas longer times produce deeper tints that mask the true structure.

Hardness: Vickers hardness data of Ti-Cr-Fe alloys annealed at and quenched from temperatures between 1000° and 650°C are presented graphically in Fig. 22. The alloys used are on the vertical section through the ternary system at the Cr:Fe ratio of 1:1. These alloys exhibit the same trends observed in the binary systems Ti-Cr and Ti-Fe.[8] The hardness curves for samples water-quenched from above 800°C reach a peak at about 5 pct total alloy content, which corresponds to the composition at which β is retained upon water quenching. Hardness peaks at 7 pct Cr and 4 pct Fe were obtained on quenching from the β field.

Annealing the ternary alloys at 650° or 700°C resulted in a linear increase in hardness with alloy composition up to 10 pct. Such alloys have α + β

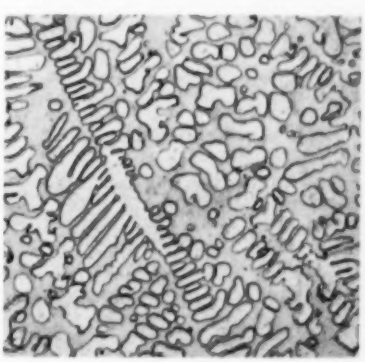

Fig. 21—A 40 pct Fe alloy annealed the same as Fig. 20. β and unstained TiFe. Etchant: same as Fig. 19. X250. Area reduced approximately 30 pct for reproduction.

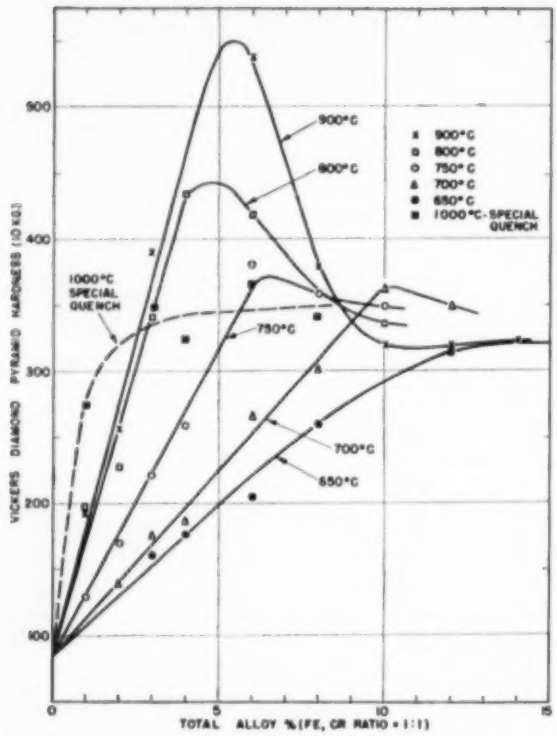

Fig. 22—Vickers hardness of Ti-Cr-Fe alloys (Fe, Cr ratio = 1:1).

structures, and are much softer than the product (β') obtained by quenching from above the transformation temperature. It can be seen from Fig. 22 that the hardness of alloys in the lower composition range, i.e., those in the commercial alloy region, may be very greatly changed by heat treatment. The hardness of the 5 pct alloy annealed at 650°C is 200 DPH, but quenching the same alloy from 900°C resulted in a hardness of over 500 DPH.

With very rapid quenching from the β field, the high hardness peak is eliminated. Samples were annealed at 1000°C for 15 min and rapidly quenched into an iced 10 pct NaOH solution. The specimen size was approximately 1/8x1/8x1/16 in. Temperatures as low as 100°C will age these metastable structures to much higher hardness.[14] Therefore, the hardness readings were obtained on unmounted samples. Similar results were obtained with binary Ti-Cr alloys. As the hardness peak obtained on quenching from the β field cannot be suppressed in samples a little larger than those described above, probably no commercial usage will be made of the phenomenon.

Summary

There is a continuous space of ternary β solid solution ranging from the Ti-Fe to the Ti-Cr system. Under equilibrium conditions, the following phase changes will occur with fall in temperature: According to the composition of the alloy, the ternary β phase starts to decompose by primary rejection of either one of the three phases, α, TiFe, or $TiCr_2$. This is followed by the eutectoid decomposition into $\alpha + TiCr_2$, $\alpha + TiFe$, or $TiFe + TiCr_2$, respectively, taking place within a temperature interval. The phase changes are terminated by the formation of the ternary eutectoid $\alpha + TiFe + TiCr_2$ at about 540°C. The ternary eutectoid is located at approximately 8 pct Cr-13 pct Fe. Whereas the precipitation of α, TiFe, and $TiCr_2$, respectively, takes place at a high rate, the "binary" and especially the ternary eutectoid decompositions, due to their low temperature of initiation, are extremely sluggish and can be enforced only by very long annealing times. Therefore, under ordinary conditions of heat treatment, the β phase remains metastable, similar to the conditions in the binary systems Ti-Fe and Ti-Cr.

A continuous series of solid solutions exists above 1100°C between $TiFe_2$ and the high temperature modification of $TiCr_2$. Solidus data are presented and show that chromium raises the binary Ti-Fe eutectic temperature (1080°C). Hardness data are presented and illustrate the pronounced effect of heat treatment.

Acknowledgments

The authors wish to thank the Materials Laboratory, Wright Air Development Center, who sponsored the work under Contract AF 33(038)-8708 for permission to publish this paper. The help of the many associates at Armour Research Foundation is appreciated. Special thanks are due to R. F. Domagala who was responsible for the heat treatment of the alloys; W. Rostoker, for the X-ray diffraction data; and C. A. Johnson, for the metallographic work.

References

[1] R. Vogel and B. Wenderott: The Constitution Diagram Iron-Chromium-Titanium. *Archiv Eisenhuttenwesen* (1940) **14**, p. 279.

[2] R. J. Van Thyne, H. D. Kessler, and M. Hansen: *Trans.* ASM (1952) **44**, pp. 974-989.

[3] C. M. Craighead, O. W. Simmons, and L. W. Eastwood: Titanium Binary Alloys. *Trans.* AIME (1950) **188**, pp. 485-513; JOURNAL OF METALS (March 1950).

[4] D. J. McPherson and M. G. Fontana: Preparation and Properties of Titanium-Chromium Binary Alloys. *Trans.* ASM (1951) **43**, pp. 1098-1125.

[5] M. K. McQuillan: A Provisional Constitutional Diagram of the Chromium-Titanium System. *Journal* Inst. Metals (1951) **79**, pp. 379-390.

[6] P. Duwez and J. L. Taylor: A Partial Titanium-Chromium Phase Diagram and the Crystal Structure of $TiCr_2$. *Trans.* ASM (1952) **44**, p. 495.

[7] F. B. Cuff, N. J. Grant, and C. F. Floe: Titanium-Chromium Phase Diagram. *Trans.* AIME (1952) **194**, pp. 848-853; JOURNAL OF METALS (August 1952).

[8] H. W. Worner: The Constitution of Titanium-Rich Alloys of Iron and Titanium. *Journal* Inst. Metals (1951) **79**, pp. 173-188.

[9] W. J. Fretague, C. S. Barker, and A. E. Peretti: Air Force Technical Report 6597, Parts 1 and 2 (November 1951-March 1952).

[10] A. D. McQuillan: The Application of Hydrogen Equilibrium-Pressure Measurements to the Investigation of Titanium Alloy Systems. *Journal* Inst. Metals (1951) **79**, pp. 73-88.

[11] B. W. Levinger: High Temperature Modification of $TiCr_2$. *Trans.* AIME (1953) **197**, p. 196; JOURNAL OF METALS (February 1953).

[12] M. Hansen, E. L. Kamen, H. D. Kessler and D. J. McPherson: The Systems Titanium-Molybdenum and Titanium-Columbium. *Trans.* AIME (1951) **191**, pp. 881-888; JOURNAL OF METALS (October 1951).

[13] M. Hansen, H. D. Kessler, and D. J. McPherson: The System Titanium-Silicon. *Trans.* ASM (1952) **44**, p. 518.

[14] W. M. Parris, L. L. Hirsch, and P. D. Frost: Low Temperature Aging in Titanium Alloys. *Trans.* AIME (1953) **197**, pp. 178-179; JOURNAL OF METALS (February 1953).

Plastic Deformation of Rectangular Zinc Monocrystals

by John J. Gilman

The data presented indicate that the critical shear stress and strain-hardening rate of a zinc monocrystal depend on the orientation of its slip direction with respect to its external boundaries. The tendency of a crystal to form deformation bands also depends on its shape.

THE plastic behavior of pairs of zinc monocrystals in which both members of the respective pairs had the same orientation with respect to the longitudinal axis, but each had different orientations with respect to their rectangular external shapes, were compared in this investigation. The purpose of the investigation was to see what influence the shape or surface of a zinc crystal has on its mechanical properties. In a previous investigation of triangular zinc monocrystals,[1] anomalous axial twisting was observed which seemed to be related to the triangular shape of the crystals.

Wolff,[2] in 400°C tensile tests of rectangular rock-salt crystals bounded by cubic cleavage planes, found that, of the four equivalent slip systems, the two with the "shorter" slip directions yielded and produced slip lines at lower stresses than the other two. This observation and the work of Dommerich[3] was formulated by Smekal[4] as a "new slip condition" for rock-salt: "among two or more slip systems permitted by the shear stress law, with reference to the formation of visible slip lines by large individual glides, that slip system is preferred which has the shortest effective slip direction."

More recently, Wu and Smoluchowski[5] reported essentially the same effect for ribbon-like (20x2x0.2 mm) aluminum crystals at room temperature.

Experimental

Chemically pure zinc (99.999 pct Zn), purchased from the New Jersey Zinc Co., was the raw material. Glass envelopes, containing graphite molds and zinc, were evacuated while hot enough to outgas the graphite but not melt the zinc. At a vacuum of about 0.2 micron the envelopes were sealed off and then lowered through a furnace at 1 in. per hr so as to melt and resolidify the zinc and produce monocrystals.

One-half of one of the molds is shown in Fig. 1a. Each mold consisted of four pieces from a cylindrical graphite rod that was split longitudinally and transversely at its midpoints. Rectangular milled grooves 0.050 in. deep and ⅜ in. wide formed the mold cavity when the split halves were assembled with twisted wires. Fig. 1b shows the specimen shape obtained when the top and bottom mold-halves were rotated 90° with respect to each other. Good fits prevented leakage and excess zinc was necessary to provide enough liquid head to fill the mold completely.

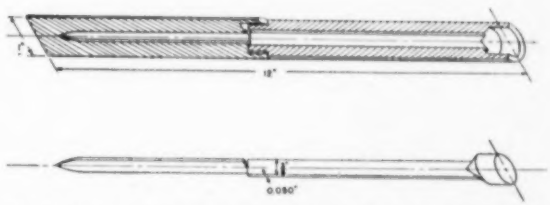

Fig. 1a (top)—Schematic drawing of one-half of the split graphite mold.
Fig. 1b (bottom)—Shape of monocrystalline specimens produced in molds like Fig. 1a.

In removing soft crystals from the molds it was impossible to avoid small amounts of bending. However, manipulations were carried out whenever possible with the crystals protected by grooved brass blocks. All specimens were annealed prior to testing.

From the top and bottom sections of each crystal, X-ray specimens and tensile specimens 7 to 8 cm long were sawed. The tensile specimens were annealed inside evacuated tubes for 1 hr at 375°C. Next the crystals were cleaned and polished by 2-min dips in a solution of 22 pct chromic acid, 74 pct water, 2.5 pct sulphuric acid, and 1.5 pct glacial acetic acid.[6] Cleaning was followed by a 10-sec dip in a 10 pct caustic solution, then washed in water and alcohol, and dried. This treatment results in a bright surface covered by an invisible oxide film.

The testing grips were a slotted type with set screws and were supported in a V-block during the mounting operations in order to avoid bending the crystals. A schematic diagram of the recording tensile-testing machine is shown in Fig. 2. The machine has been described elsewhere.[7] The head speed was 0.3 mm per sec for all tests.

The crystal orientations were determined by the Greninger X-ray back-reflection method with an estimated accuracy of ±1°.

Description of Crystal Geometry

A schematic picture of a rectangular zinc monocrystal is shown in Fig. 3. *ABD* designates the front edge of a basal plane (0001) of the crystal, the only active slip plane for zinc at room temperature. Of the three possible $(2\bar{1}\bar{1}0)$ slip directions, the active one is indicated by an arrow. Cartesian coordinates are taken parallel to the specimen edges. The normal, n, to the basal plane (n is parallel to the hexagonal axis) has the direction cosines α, β, and γ. $\chi_0 = 90 - \gamma$ is the angle between the longitudinal axis and

J. J. GILMAN, Junior Member AIME, formerly with Columbia University, is now associated with Metallurgy Research Dept., Research Laboratory, General Electric Co., Schenectady.

Discussion on this paper, TP 3571E, may be sent, 2 copies, to AIME by Dec. 1, 1953. Manuscript, Sept. 16, 1952; revision, Feb. 28, 1953. Cleveland Meeting, October 1953.

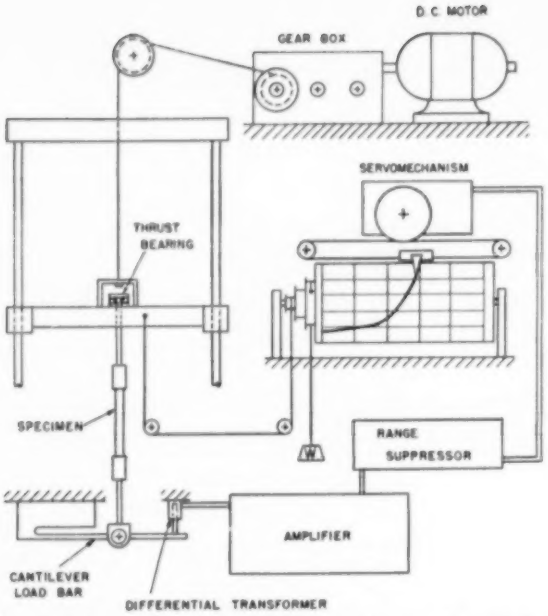

Fig. 2—Schematic drawing of the automatic recording tensile machine used for testing the specimens.

the basal plane, and λ_o is the angle between the longitudinal axis and the slip direction. The breadth and thickness of the specimen are b and t, respectively. θ is the angle between the projection of the slip direction into the cross-sectional plane and the normal to the wide side of the crystal. ξ and η are the angles between the surface traces of the slip plane and the x and y axes, respectively. ω is the angle between the slip direction and a line lying in the slip plane and perpendicular to $\overline{AB}$, its intersection with the side. δ is the angle between $\overline{AB}$ and $\overline{BD}$. s is the "length" of the slip direction and is the length of a unit slip (equal to the distance between atoms in the slip direction).

If α, ρ, γ, and λ_o are known, the other angular parameters, δ, θ, ω, ξ, λ, and η, may be calculated. However, they may be quickly measured on a stereographic plot of the specimen, so this was the method used here; a few calculations were made as checks.

The "length" of the slip direction, s, is found as follows:

$$s = \frac{GH}{\sin \lambda_o} = \frac{t}{\cos\theta \sin \lambda_o} \text{ or } \frac{b}{\sin\theta \sin \lambda_o} \qquad [1]$$

whichever is smaller. The area of the slip plane is:

$$a_o = \overline{AB}\ (\overline{BD} \sin \delta)$$

Since d_o is very small compared with b and t, the increase in surface area of the crystal per unit slip is

$$a' = 2\,c\,\overline{AB} + 2\,e\,\overline{BD}$$
$$= 2\left(\frac{cb}{\cos\xi} + \frac{et}{\cos\eta}\right)$$
$$= 2\,d_o\left(b\,\frac{\cos\omega}{\cos\xi} + t\,\frac{\sin\omega}{\cos\eta}\right) \qquad [2]$$

The perimeter of the slip plane is just

$$P = 2(\overline{AB} + \overline{BD}) = 2\left(\frac{b}{\cos\xi} + \frac{t}{\cos\eta}\right) \qquad [3]$$

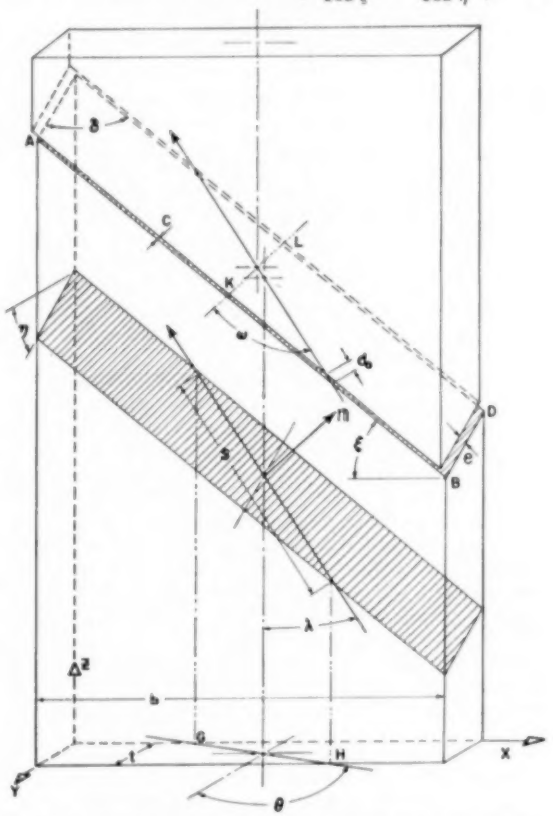

Fig. 3—Schematic geometry of a rectangular zinc monocrystal.

and the component of the perimeter perpendicular to the slip direction is twice the quantity in the brackets of Eq. 2. The quantities in Eq. 3 will be used in the discussion of the results.

Results

About thirty-five pairs of crystals were grown and tested. The growth technique yielded a majority

Table I. Reproducibility of the Stress-Strain Data for Pairs of Rectangular Zinc Monocrystals, with Zero Mold Rotation

Crystal Pair	Orientation Angles						Thickness, Mm	Gage Length, Cm	Resolved Shear Stresses, Elongation, Pct			Twinning	
	χ_o	λ_o	ξ	η	θ	ω			1/10	1	10	Stress, Kg per Sq Mm	Elongation, Pct
15T	9	11	74	79	3	69	1.25	8.3	36.3	58.6		1.12	5.7
B									36.5	59.5		1.16	5.8
16T	64	66	15	20	59	60	1.25	7.8	34.8	45.2	86.8		
B							1.04		34.0	42.1	80.0		
18T	12	12	52	78	16	54	1.25	7.7	38.7	54.1	156	0.91	1.6
B							1.04		38.3	51.5	154	0.97	1.7
20T	4	26	—	—	—	—	0.99	8.3	—	—	—	1.07	<0.1
B							1.02					1.03	

of crystals with low χ_o values, however, which slipped very little before they began to twin. For crystals which deformed by slip, it was considered that χ_o must be about 14° to 15°, if the orientation effects were not to be obscured by end effects. Crystals for which χ_o was less than 5° were considered to have deformed entirely by twinning. Crystals of intermediate orientations were not considered.

Slip: A major difficulty in experiments on the mechanical properties of monocrystals is that of obtaining reproducible results. In order to see how much reproducibility might be expected of the present crystals, four pairs were grown for which the top and bottom halves of the mold were given zero rotation. Data for these pairs are presented in Table I. For both slip and twinning the reproducibility was good. On the basis of Table I, the experimental error in stress-strain data is estimated to be 5 pct between two *crystals* of any pair. However, the differences between *pairs* of crystals were considerably larger, amounting to as much as 15 pct.

Table II lists data for pairs of crystals that were rotated 30° and 90° relative to each other in the mold. In most cases the θ values differ by just about this amount, but in some cases the difference is less than this because symmetry makes ($\theta = 90$) the same as θ. The resolved shear stresses are given at various percentages of elongations. These were calculated from the usual expression,

$$T = \sigma \sin \chi \cos \lambda$$

where σ is the tensile stress; χ, the instantaneous angle between axis and slip plane; and λ, the instantaneous angle between axis and slip direction.

The resolved shear stresses at 0.1 and 1.0 pct elongation are given as indices of the yield behaviors of the crystals. The difference between the shear stresses at 10 and 1 pct elongation, $T_{10} - T_1$, divided by the difference in corresponding shear strains, $\gamma_{10} - \gamma_1$, is a measure of the strain-hardening rate of a crystal. These values are listed in Table II after the critical shear stresses. Table II also lists the geometric parameters, s and a'.

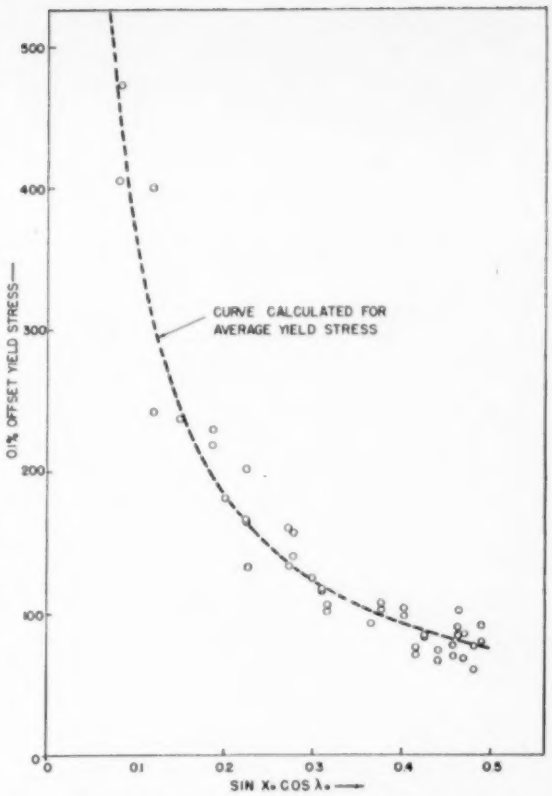

Fig. 4—Plot of 0.1 pct offset yield stress data listed in Table II.

The values of the resolved shear stresses differ considerably among crystals and pairs. This is shown graphically in Fig. 4 where the data are scattered about the curve calculated for the average resolved shear stress at 0.1 pct elongation; 37.0 g per sq mm. The reason for the scatter between castings is not known. Part of the cause was the

Table II. Tensile Test Data for Slip of Zinc Crystal Pairs

Crystal Pair	Orientation Angles						Gage Length, Cm	Resolved Shear Stress (G per Sq Mm) Elongation, Pct			Strain-Hardening $T_{10}-T_1$	Geometric Parameters	
	χ_o	λ_o	ξ	η	θ	ω		0.1	1.0	10	$\gamma_{10}-\gamma^1$	s, Mm	a^1 Sq Mm x 10^{-7}
2T	37	37	12	53	13	18	7.0	36.7	47.3	93.7	209	2.03	52.5
B			37	56	48	58		28.6	39.0	73.3	152	3.15	43.8
4T	34	34	54	24	62	74	2.9	38.3	51.8	—	—	4.83	30.9
B			48	49	32	55		42.9	53.8	—	—	2.36	50.8
7T	31	31	25	58	26	35	8.7	31.2	38.8	75.8	151	2.74	53.1
B			52	51	58	70		29.5	35.9	70.4	143	4.43	37.8
10T	35	42	32	52	70	69	7.4	34.7	43.7	87.5	176	5.46	31.4
B			3	56	38	22		35.1	45.1	104	242	2.03	50.9
11T	20	22	0	71	36	14	8.7	33.6	45.3	98.6	158	3.83	53.7
B			50	67	3	43		32.0	41.0	90.9	148	3.23	68.6
14T	29	31	13	60	32	28	8.9	29.4	36.6	76.6	156	2.77	52.0
B			48	54	62	71		31.3	39.5	71.9	122	5.25	35.5
17T	45	49	42	27	87	88	8.3	39.4	48.7	101	234	11.6	9.84
B			44	8	57	66		47.2	57.1	112	245	3.09	35.0
21T	34	34	12	56	2	9	3.2	39.9	53.1	109	—	2.17	53.0
B			26	56	38	42		41.2	52.4	109	—	7.36	48.5
23T	34	35	54	32	81	84	7.5	—	42.6	81.3	161	13.5	16.6
B			42	49	52	62		—	43.4	80.1	152	2.88	39.3
25T	63	65	22	14	37	42	3.6	40.2	53.2	106	—	1.73	45.3
B			13	16	2	7		38.4	52.3	119	—	1.34	52.5
27T	18	26	71	8	40	70	4.6	38.8	57.3	168	—	3.60	59.1
B			70	62	8	60		43.8	61.2	143	—	2.28	84.1
29T	14	21	73	56	68	82	8.2	31.6	45.6	113	145	9.03	35.5
B			65	74	79	83		37.6	50.9	119	144	18.3	38.5
32T	22	34	54	67	27	38	8.4	36.5	52.8	146	281	2.37	80.3
B			62	51	74	80		35.7	48.3	124	227	8.25	29.4
35T	22	37	20	66	64	52	5.5	37.1	50.9	133	242	4.73	46.0
B			68	34	46	64		37.7	55.3	147	271	3.04	66.5
37T	19	33	64	62	6	48	4.9	43.5	56.8	144	—	2.34	88.3
B			56	65	86	86		36.4	51.3	140	—	17.5	22.6
38T	55	55	18	32	18	24	4.2	40.0	48.6	89.7	—	1.53	51.7
B			32	21	73	76		32.0	42.0	73.8	—	4.14	19.9
39T	51	51	23	36	42	46	8.3	—	49.3	83.5	157	2.10	43.8
B			28	28	50	56		—	51.0	82.3	141	2.50	38.4

Fig. 5—Pair of rectangular zinc monocrystals which deformed by slip. $\chi_o = 31°$. $\lambda_o = 31°$.
a (top)—$\theta = 58°$. b (bottom)—$\theta = 26°$.

variable average θ values among the castings, but some of the scatter seems to have originated in the casting process.

The average value, 37.0 g per sq mm, of the critical resolved shear stress is not inconsistent with the value found by Jillson,[8] 18.4 g per sq mm. Jillson made his measurements at constant load-rate instead of constant elongation-rate so no direct comparison is possible, but, since his rate of resolved stress increase was 0.1 g per sq mm per min, the strain-rate must have been much lower than it was in the present tests. Furthermore, if the present data is extrapolated to 0 pct elongation, the extrapolated value falls between 15 and 20 g per sq mm in approximate agreement with Jillson's data.

There are several instances among the data of Table II where the shear stress values for a crystal pair differ by more than the 5 pct experimental error. Therefore, a shape or surface effect seems to exist for these crystals. Study of the data has indicated the following:

1—The harder crystal of a pair came from the top half of the mold about 50 pct of the time and from the bottom half about 50 pct of the time. Thus, the observed differences cannot be attributed to mold conditions.

2—Relatively large differences in the critical stresses for a pair of crystals were always associated with marked differences in the cross-sectional shape changes upon deformation. The shape changes are closely related to the θ values for the crystals. The relations may be simply expressed for the case of $\chi_o = \lambda_o$ as follows:

$$b' = b\left(1 + \frac{\Delta l}{l}\sin\theta\right),\ t' = t\left(1 + \frac{\Delta l}{l}\cos\theta\right)$$

where b' and t' are the breadth and thickness after deformation. Thus, if $\theta = 0$ a crystal thins without changing in breadth and if $\theta = 90°$ it narrows without changing in thickness. For all other θ values, the rectangular crystal becomes parallelepiped. A typical case is shown in Fig. 5 which is a photograph of pair 7. The top part (the right side in the figure) of this crystal pair thinned without changing much in breadth, while the bottom crystal (the left side in the figure) narrowed and thinned to form a parallelpiped.

Crystals which thinned more than they narrowed were harder than those which narrowed more than they thinned. Thus, the crystal in Fig. 5b was harder than the one in Fig. 5a.

3—For crystals free of end effects, the strain-hardening rate was greater for the crystal of a pair which was initially the hardest. The difference in strain-hardening rate was not great for any of the crystals. Short crystals (3 to 4 cm) did not adhere to this rule because more material is constrained at the ends of a crystal if θ is large than if θ is small. For a short crystal, this results in rapid apparent hardening.

4—The geometric parameters, s (slip length) and a' (slip plane area exposed) correlate fairly well with the tensile test data. The correlation with the slip plane perimeter is not as good. In general, it is found that the crystal of a pair which has the highest yield strength has a "shorter" slip direction, s, and forms more new surface area per unit slip, a', than the softer crystal. This is true for 13 out of 17 crystals of Table II (76 pct). In the exceptional cases, (crystals No. 11, 14, 25, 39), it is found that: first, all of the differences in the various quantities are small so that they may be attributed to experimental error; second, the crystal with small s and large a' strain-hardens more than its partner. This is significant because the strain-hardening rates are found from relative data and hence are subject to much smaller accidental errors than the shear stresses.

Although the data show too much scatter to allow a determination of the functional relations between the geometric parameters and the tensile data, large critical stress differences are associated qualitatively with large differences in s and a'.

Thus, for these zinc monocrystals at room temperature, crystals with small s and large a' had higher critical shear stresses and strain-hardened more rapidly than crystals of the same orientation but large s and small a'.

5—Examination of the deformed crystals has shown that those which have small θ values, and therefore tend to thin during deformation, have a greater tendency to form tensile kink bands than their opposites. In fact, crystals with θ near 90° often deform without forming any tensile kink bands, but those with θ near 0° seem never to deform without the formation of some kink bands. This may be one reason why the latter strain-harden more rapidly than the former. The crystals in Fig. 5 illustrate this point. Fig. 5b has a wavy surface because it contains many kink bands while the surface of the softer one, Fig. 5a, is smooth except for slip bands.

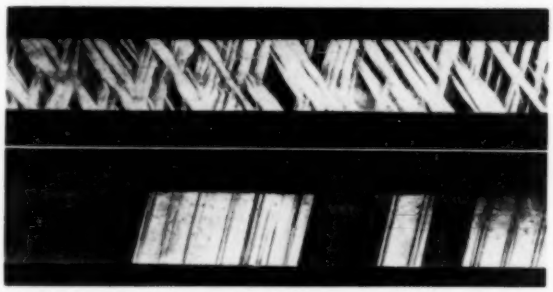

Fig. 6—Crystal pair No. 8 after deformation by twinning. ($\chi_o = 2°$. $\lambda_o = 17°$.) X1.5. Area reduced approximately 60 pct for reproduction.
a (top)—$\theta = 28°$, twinning stress = 1.19 kg per sq mm.
b (bottom)—$\theta = 1°$, twinning stress = 1.45 kg per sq mm.

Twinning: Nine specimens were grown for which χ_o was 5° or less. These deformed primarily by twinning. The crystal orientations and twinning stresses are listed in Table III and Fig. 6 shows the appearance of one of the crystal pairs after deformation. It may be seen in Fig. 6a that twinning sometimes (and in fact, usually) occurred on two sets of planes almost simultaneously. Therefore the value of calculations of resolved shear stresses is doubtful and these are not reported; rather, the tensile stress at first twinning is reported.

Twinning seems to be influenced by specimen

shape according to the data of Table III. Both halves of crystal-pair No. 20, which was grown in an unrotated mold, had nearly the same twinning stress, whereas marked differences are shown for most of the other pairs. These differences seem to correlate with the directions of twinning with respect to the external sides. When the twinning directions lay in a plane roughly perpendicular to the flat face of a crystal (as in Fig. 6b), the crystal showed a higher twinning stress than its mate with twinning directions lying more nearly parallel to its flat faces (as in Fig. 6a). This held true in six out of eight cases. In the exceptional cases (pairs No. 19 and 28) both crystals of each pair had nearly the same appearance after deformation so it could not be determined whether the above correlation is valid for them. However, the fact that no contradictions to the correlation were found tends to support its validity.

Although the crystal in Fig. 6b appears to have only one set of twin bands, actually it has two as shown by the appearance of its edges.

Discussion

It must be noted that the conclusions stated in paragraph 5 above appear to be in direct contradiction with the results of previous work on rock salt[3] at 400°C and aluminum at room temperature.[6] In these earlier studies it was found that "short" slip directions favored easy slip. In this investigation it was found that "long" slip directions favored easy slip. The reason for this contradiction is not known at present, but perhaps it is only apparent. Rock salt, aluminum, and zinc can hardly be called similar materials and there are other marked differences in their plastic behaviors.

On the other hand, the present results agree with what would be expected for a surface effect: That is, the crystals of each pair which led to larger increases in surface area during deformation, hence larger increases in surface energy, were more difficult to deform than their partners. The effect may not have been intrinsic, but the result of a surface film. From this point of view, the present results are complementary to the results of Roscoe,[9] Lichtmann and Rehbinder,[10] Ono,[11] and Makin and Andrade.[12] The last named authors found a marked increase in the strength of cadmium crystals with decreasing specimen diameters for diameters below about 0.5 mm. Ono found the same effect, but less marked, for aluminum crystals with diameters in the range 3 to 8 mm. The results of these authors contradict the observations on rock salt by Smekal and on aluminum by Wu and Smoluchowski, but they agree with the present results.

The interpretation of all of the known size or shape effects is difficult because they may either be bulk effects which depend on s or surface effects which depend on a' or some other surface parameter. Since s and a' are almost inversely proportional to each other it has not yet been possible to make an unambiguous distinction. Surface effect studies similar to those of Pfutzenreuter and Masing[13] may help to resolve the dilemma. They found that both anodic and cathodic polarization of metals in electrolytes may increase the flow rates. They interpret their results in terms of a'.

The observation that zinc crystals with small s tend more to form tensile kink bands than do those of the same orientation but large s is of some interest. Perhaps this means that aluminum crystals, which seem to form kink bands spontaneously, would not do so if they were tested in large sections.

Table III. Twinning of Pairs of Zinc Monocrystals

Crystal Pair	χ_o	λ_o	θ	Gage Length, Cm	Twinning Stress, Kg per Sq Mm
8T	2	17	20	8.8	1.19
B			1		1.45
13T	2	22	78	8.7	1.09
B			44		1.40
19T	1	25	57	7.6	1.20
B			80		1.42
20T	4	26	72	8.3	1.07
B					1.03
28T	4	4	72	8.1	1.45
B			40		1.25
30T	1	12	33	7.5	1.72
B			4		2.12
31T	5	15	32	6.6	1.00
B			1		1.30
33T	4	25	54	5.8	1.15
B			33		1.31
36T	2	20	28	6.9	1.30
B			58		1.27

Summary

By means of a special casting technique, it has been shown that zinc monocrystals, which have the same orientation with respect to the tension axis but different orientations with respect to their external sides, differ significantly in their plastic properties.

Rectangular monocrystals, having orientations such that they thin during a tensile test without changing in breadth, have higher critical shear stresses at room temperature and strain-harden more rapidly than crystals which become narrow during deformation without changing in thickness.

The geometric parameters, s, the "length" of the slip direction, and a', the ideal increase in surface area per unit slip, seem to correlate with the stress-strain data. Crystals with small s and large a' are harder initially and strain-harden more rapidly than crystals of the same orientation with respect to the tension axis but large s and small a'.

Zinc monocrystals with small s values tend to form tensile kink bands more rapidly than those with larger s values.

Crystals of twinning orientation twin at lower stresses when the twinning direction is roughly parallel to the flat faces of a rectangular crystal than when it is nearly perpendicular to the flat faces.

Acknowledgments

The author was assisted by A. Greene in the growth and preparation of the crystals. He is grateful to the General Electric Research Laboratory for aid in preparing the manuscript which J. C. Fisher kindly reviewed. This work was sponsored by the Office of Naval Research under Contract N6-onr-27128.

References

[1] J. J. Gilman and T. A. Read: Surface Effects in the Slip and Twinning of Monocrystals. *Trans.* AIME (1952) **194**, p. 875; JOURNAL OF METALS (August 1952).

[2] H. Wolff: Directional Dependence of the Slip Mechanism in Rock Salt Crystals at High Temperatures. *Ztsch. Phys.* (1934) **93**, p. 147.

[3] S. Dommerich: Directional Dependence of the Yield Point of Homogeneous, Cleaned Rock Salt Rods. *Ztsch. Phys.* (1934) **90**, p. 189.

[4] A. Smekal: A New Slip Condition. *Ztsch. Phys.* (1934) **93**, p. 166.

[5] T. Wu and R. Smoluchowski: A New Criterion for the Occurrence of Slip in Thin Single Crystals. *Physical Review* (1950) **78**, p. 468.

[6] J. Rodda: Private communication through M. Metzger.
[7] J. Gilman: A Simple Recording Tensile Machine for Metal Monocrystals. *Review of Scientific Instruments* (December 1952).
[8] D. C. Jillson: Quantitative Stress-Strain Studies on Zinc Single Crystals in Tension. *Trans.* AIME (1950) **188**, p. 1129; JOURNAL OF METALS (September 1950).
[9] R. Roscoe: The Plastic Deformation of Cadmium Single Crystals. *Philosophical Magazine* (1936) **21**, p. 399.
[10] V. I. Lichtman and E. K. Venstrom: Effect of Dimensions of Metal Single Crystals on the Shape of the Stress-Strain Diagram and on the Strength Lowering Effect of Adsorption. *Dokl. Akad. Nauk. SSSR* (1949) **66**, p. 881.
[11] A. Ono: On the Glide-Resistance of Aluminum. *Proc.* Third International Congress on Applied Mechanics (1930) **2**, p. 230.
[12] E. N. daC. Andrade: The Effect of Surface Conditions on the Mechanical Properties of Metals, Mainly Single Crystals. *Monograph No. 13* (1952) London. Inst. Metals.
[13] A. Pfutzenreuter and G. Masing: Increase of the Velocity of Plastic Flow of Metals in Electrolytes upon Electrochemical Polarization. *Ztsch. Metall.* (1951) **42**, p. 361.

Technical Note

Detection of Microcracks in Steel

by W. L. Jensen and R. F. Campbell

IT is not uncommon for martensitic high carbon steels having a coarse austenite grain size to exhibit microcracks when polished and etched and examined with a microscope, as described by Davenport, Roff, and Bain.[1] Whether such cracks exist before etching or are the result of acid attack during etching has been debated from time to time. Fig. 1 illustrates the effect of electrolytic polishing, mechanical polishing and etching subsequent to each polish on microcracks produced by oil quenching from 1800°F a steel containing 1.14 pct C, 0.23 pct Mn, 0.33 pct Si, and 0.45 pct Mo. The austenite grain size was 3-4 on the ASTM scale.

Grinding on lead laps followed by either electrolytic polishing with acetic anhydride-perchloric acid solution[2] or mechanical polishing with Linde "B" alumina on "microcloth" (sometimes referred to as Gamal cloth) revealed microcracks without conventional etching, as shown in Fig. 1a and b, respectively. These same fields, after subsequent etching with saturated picral, are shown in Fig. 1c and d, and the cracks are seen to be typical microcracks; moreover, the cracks appear to be broader and longer than before etching. Although the microcracks were revealed by electrolytic polishing alone, the possibility of acid attack was present; however, the mechanical polish was accomplished without any intermediate etching to remove disturbed metal, hence this is regarded as definite evidence that microcracks are present before etching.

W. L. JENSEN and R. F. CAMPBELL are associated with the Research Laboratory, United States Steel Corp., Kearny, N. J.
TN 178E. Manuscript, June 24, 1953.

[1] E. S. Davenport, E. L. Roff, and E. C. Bain: Microscopic Cracks in Hardened Steel, Their Effects and Elimination. *Trans.* ASM (1934) **22**, pp. 289-310.
[2] G. F. Meyer, G. D. Rahrer, and J. R. Vilella: Electrolytic Polishing of Steel Specimens. *Metals and Alloys* (1941) **13**, pp. 424-430.

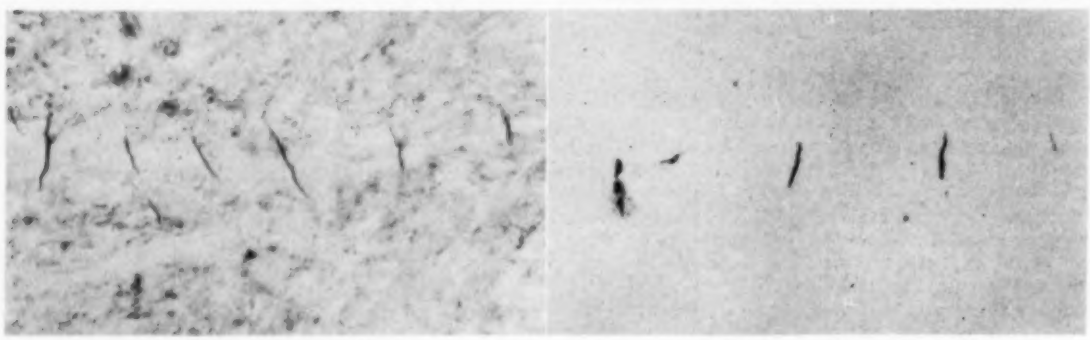

a—Electrolytic polish. Unetched.

b—Mechanical polish. Unetched.

c—Same field as Fig. 1a. Picral etch.

d—Same field as Fig. 1b. Picral etch.

Fig. 1—Microcracks as revealed by electrolytic and mechanical polishing and by subsequent etching. X750.

Variation of Plastic Properties with Annealing Procedure In Zinc Single Crystals

by Choh Hsien Li, J. Washburn, and Earl R. Parker

Yield stress in single crystals of zinc was shown to be dependent on prior annealing temperature and rate of cooling after annealing. Rate of strain hardening beyond the yield was not sensitive to annealing procedure. A tentative mechanism for the effect was discussed.

COMPARATIVE mechanical tests of metal single crystals generally show a large scatter of results. Many factors may contribute to this variation. The present investigation was undertaken to evaluate the influence of two factors not ordinarily considered of major importance—annealing temperature and cooling rate after annealing.

Since plastic properties of crystals are thought to depend on the presence of lattice imperfections, it follows that a variation in properties should result from differences in the distribution and density of these imperfections. Furthermore, in the light of current theories of interaction between edge dislocations and lattice vacancies,[1] it seems possible that annealing temperature and subsequent rate of cooling might play a part in this distribution. Analysis of the effect of these variables on plastic properties may lead to a better understanding of the annealed state.

Single crystals of zinc which have been strained in simple shear undergo complete recovery of mechanical properties upon subsequent annealing. This behavior is useful because a single specimen can be used repeatedly, thus eliminating the uncontrollable variables introduced by the use of many crystals. The test section of the crystals used for these experiments was a cylinder ⅛ in. thick with a cross-sectional area of about 1/3 sq in. The specimens were acid-machined from spherical single crystals 1 in. in diameter in such a way that the slip plane (0001) was at right angles to the axis of the cylinder. In testing, a shear stress was applied along one of the slip directions, $[2\bar{1}\bar{1}0]$ in the (0001) plane.[2] All crystals, unless otherwise noted, were grown in a helium atmosphere from molten 99.99 pct pure Horse Head Special Zinc.

Fig. 1 is a family of curves obtained from one crystal. Each curve was obtained by deforming the crystal to 10 pct strain at a rate of 3 pct per min, following an anneal of 1 hr at 260°C. The strain direction was reversed every other time so that no progressive change in shape of the specimen took place during the series of tests. Since the stress-strain curve was reproducible within a fairly narrow range under the same conditions of annealing, it was then possible to determine the effect of changes in annealing conditions. A crystal was tested repeatedly as previously described but the annealing temperature and rate of cooling preceding each test were varied (Fig. 2). Two cooling rates were used, approximately 30°C per min and 3°C per min. Annealing was conducted at three temperatures, 200°, 300°, and 400°C. For a given annealing time and rate of cooling the room temperature flow stress was higher the higher the annealing temperature. The increase in flow stress was small as the annealing temperature was increased from 200° to 300°C but rose rapidly when the annealing temperature was raised from 300° to 400°C. Faster cooling from the high temperature produced an even greater strengthening of the crystal. The curves were obtained in the order indicated by the numbers. The stress level associated with a certain annealing treatment was, within the limits of scatter, always the same regardless of the

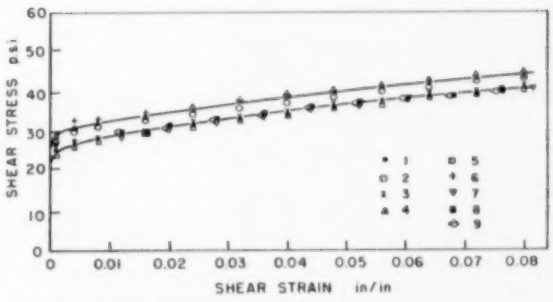

Fig. 1—Nine successive stress-strain curves from the same specimen showing complete recovery of mechanical properties—annealed 1 hr at 260°C before each test.

C. H. LI is Reseach Engineer, Institute of Engineering Research, and J. WASHBURN and E. R. PARKER, Member AIME, are Instructor and Professor in Metallurgy, respectively, University of California, Berkeley, Calif.

Discussion on this paper, TP 3600E, may be sent, 2 copies, to AIME by Dec. 1, 1953. Manuscript, April 16, 1953. Cleveland Meeting, October 1953.

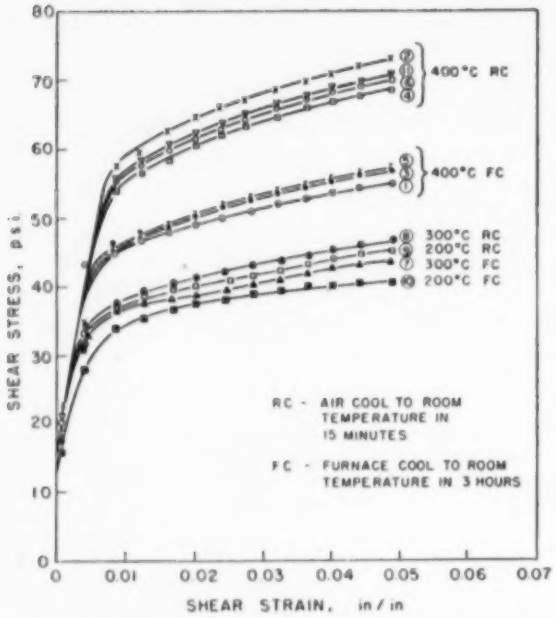

Fig. 2—Effect of annealing temperature and cooling rate on the initial part of the stress-strain curve of a zinc single crystal. Numbers indicate order of test.

penultimate treatment. This indicated that no continuous change in state of the crystal had occurred during the series of tests. Apparently the state at room temperature was characteristic of the annealing procedure. The two important differences observed in the stress-strain curve were: 1—change in the "yield stress" (or break in the stress strain curve), and 2—a change in amount of plastic flow prior to the break.

It seemed possible that these effects might be associated with the presence of impurities. This was a difficult question to settle because the effect might have been caused by a specific impurity.

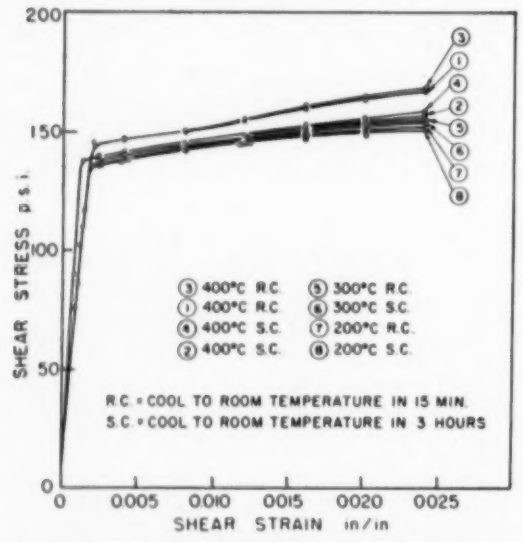

Fig. 3—Stress-strain curves after various annealing treatments of a zinc crystal containing 0.02 pct Cu in solid solution. Note change in shear stress scale for comparison with other figures.

Nevertheless, as a partial check on this possibility, some crystals were prepared containing a small amount of copper in solid solution while others were grown in a nitrogen atmosphere to introduce dissolved nitrogen. Results from one of the copper alloy crystals are shown in Fig. 3. The presence of copper in solid solution increased the "yield point" and the slope of the strain-hardening curve after the yield point by a factor of five, but the effect due to annealing temperature and cooling rate was no greater than for high purity crystals. Results from one of the crystals grown in nitrogen are shown in Fig. 4. The stress-strain curves for all annealing treatments were about the same as those for crystals grown in helium. Strain-aging characteristics

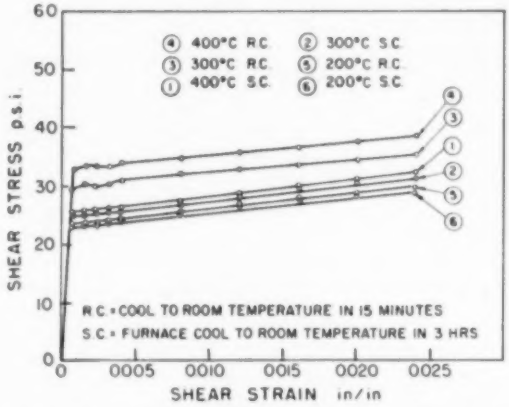

Fig. 4—Stress-strain curves after various annealing treatments of a zinc crystal grown in nitrogen atmosphere.

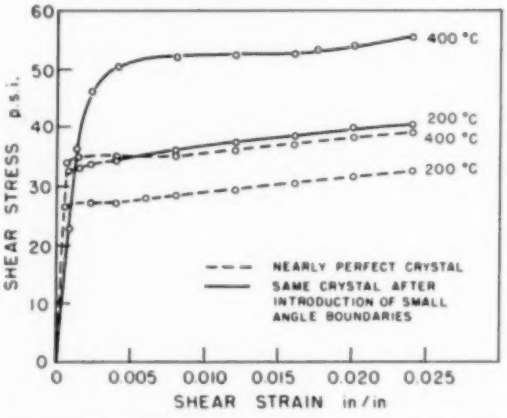

Fig. 5—Stress-strain curves of a 99.99 pct pure zinc crystal showing the effect of introducing a substructure of small angle boundaries. Specimen was cooled to room temperature in 15 min after each anneal.

were observed for the nitrogen-bearing crystals, as previously reported by Cottrell.[3] However, no increase in the annealing temperature effect was produced by the presence of nitrogen.

Thermal stresses as a possible cause of the annealing effect were excluded from consideration because no significant temperature gradients were found during furnace cooling.

The magnitude of the annealing temperature effect was found to vary considerably for different crystals. The first crystal (Fig. 2) showed a larger effect than any subsequently tested. It seemed

Fig. 6—Photograph of cleavage face showing system of small angle boundaries introduced during experiment of Fig. 5.

possible that this specimen might have been accidently damaged in such a way as to produce polygonized regions in the test section. Therefore, a substructure of small angle boundaries was intentionally introduced in a test specimen to investigate its influence on annealing characteristics. A series of curves was obtained from a single specimen both before and after introducing a substructure. The results are shown in Fig. 5. The system of small angle boundaries was made by applying a concentrated load acting in a direction parallel to the C axis. The specimen was at 350°C during this operation. After the subsequent anneals and tests, the specimen was cleaved through the gage section. Fig. 6 is a photograph of this cleavage face showing the network of boundaries introduced by the concentrated load. The presence of this substructure raised the yield stress of the crystal under all conditions of heat treatment and furthermore, greatly exaggerated the effect produced by the high temperature anneal. It caused little if any change in the rate of work hardening beyond the yield point.

Discussion

All crystals contain to a greater or lesser degree, regions of relatively perfect lattice which are slightly disoriented relative to one another. Substructures of macroscopic, microscopic, and submicroscopic proportions may be present. The nature of the boundaries between disoriented regions may be the same regardless of the scale of the substructure. Arrays of dislocations satisfy the geometrical conditions of the transition across boundaries. Furthermore, there is now direct evidence that small angle boundaries consist of arrays of dislocations.[4,5]

If most of the dislocations in an annealed crystal exist in the substructure boundaries, then the experiments described above suggest that the nature of these boundary regions between volumes of relatively perfect crystal may be extremely important in determining the stress at which slip is able to propagate entirely across the specimen. As shown in Fig. 5, the introduction of a network of dislocation boundaries of macroscopic proportions raised the stress at which the "yield-point" or break in the stress-strain curve occurred and also increased the amount of plastic strain which took place before the break. The rate of hardening or slope of the curve remained approximately the same both before and after the "yield-point" for the two conditions. In a recent photoelastic study of slip in sodium chloride crystals,[6] it was shown that plastic flow before the break in the stress-strain curve is associated with local slip processes which are not able to cross substructure boundaries. Thus it becomes evident that substructure boundaries play an important role in governing plastic properties of metals. Furthermore, the fact that annealing temperature and cooling rate become more important when a pronounced substructure is introduced suggests that the annealing effect is associated with subboundaries.

The results reported herein might be interpreted to mean that fairly rapid cooling from a high annealing temperature causes the boundaries to become more effective as barriers to slip. Just how this happens is not known but the following is a tentative suggestion: Huntington and Seitz have estimated that the equilibrium concentration of vacancies (in copper) at the melting point is of the order of 10^{-4} atomic pct.[7] The following possible disposition of these vacancies on cooling has been discussed by Seitz:[1] 1—condensation of vacancies on existing dislocations, and 2—condensation of vacancies to form new dislocation loops. The choice between these two alternatives was considered to depend on the density of existing dislocations.

If, near the melting point the equilibrium concentration of vacancies is as high as estimated, then on cooling, a large number of vacancies recombine with edge dislocations. It is conceivable that fairly rapid cooling may not allow time for recombination of vacancies in such a way that long segments of straight dislocation lines in the slip planes are retained. Rapid cooling may result in freezing in of numerous steps in the dislocation lines. Dislocation lines containing many segments which do not lie in the slip plane would be harder to move under stress than those which are wholly contained in a single slip plane. Therefore, a small angle boundary composed of such wavy dislocations might form a more effective barrier to the passage of other dislocations.

Acknowledgment

Support of this work by the Office of Naval Research and in particular, the interest and encouragement of Dr. O. Marzke and Dr. Julius Harwood is gratefully acknowledged.

References

[1] Frederick Seitz: On the Formation of Dislocations From Vacancies. *Physical Review* (1950) **79**, No. 5, p. 890.

[2] J. Washburn and Earl R. Parker: Deformation of Single Crystals. *Modern Research Techniques in Physical Metallurgy* (1952) ASM.

[3] H. L. Wain and A. H. Cottrell: Yield Points in Zinc Single Crystals. *Proc.* Physical Soc., London (May 1950) **63**, Sec. B, p. 339.

[4] J. Washburn and E. R. Parker: Kinking in Zinc Single-Crystal Tension Specimens. *Trans.* AIME (1952) **194**, p. 1076; JOURNAL OF METALS (October 1952).

[5] Choh Hsien Li, E. H. Edwards, J. Washburn, and Earl R. Parker: Stress Induced Movement of Crystal Boundaries. *Acta Metallurgica* (1953) **1**, No. 2, p. 223.

[6] P. L. Pratt: Strain Hardening of Single Crystals. A. E. R. E. Report M/R 883, Ministry of Supply, Harwell, Berks. (1952).

[7] H. B. Huntington and F. Seitz: Mechanism for Self-Diffusion in Metallic Copper. *Physical Review* (1942) **61**, p. 315.

Recovery in Single Crystals of Zinc

by R. Drouard, J. Washburn, and Earl R. Parker

Temperature dependence of the rate of recovery in zinc single crystals after a simple shear deformation at low temperature was investigated. Some tentative suggestions regarding the annealed and strain-hardened states of a crystal are discussed.

RECOVERY may be defined as the gradual return of the mechanical and physical properties of strain-hardened metal to those characteristic of the annealed material; an increase in temperature increases the rate of recovery. The annealing process in strain-hardened polycrystalline metals is complicated by the inhomogeneity of strain which always exists in aggregates. Polygonization in bent regions of the crystals and growth of new almost strain-free grains starting at points of severe local distortion[1-3] make it almost impossible to isolate and study the recovery process. Homogeneously strained single crystals, however, do not polygonize or recrystallize and hence they can be used advantageously to study recovery. In such crystals strain hardening is completely removed by recovery alone.

Since recovery is a process whereby certain lattice disturbances introduced by plastic flow are gradually reduced, a knowledge of the rate and temperature dependence of this process for various conditions of prestrain might be helpful in formulating a model of the strain-hardened state. For simplicity it seemed desirable to limit the type of prestrain to the simplest obtainable, i.e., simple shear strain.

In the experiments to be described, recovery was studied by observing changes in the stress-strain curve of prestrained zinc single crystals held for various times at temperatures above that employed for straining. Single crystals were grown from the melt by a modified Bridgeman technique from Horse Head Special zinc 99.99 pct pure, and from spectrographically pure zinc 99.999 pct pure. They were grown as 1 in. diameter spheres and acid-machined[4] to the final specimen contour. The test section was a cylinder about $\frac{1}{8}$ in. high and $\frac{3}{4}$ in. in diameter. The conical sections adjacent to the test section were cemented into the grips so the load could be transmitted to the crystal as uniformly as possible. The specimens were oriented so that in testing the maximum shear stress was applied along one of the slip directions, $[2\bar{1}\bar{1}0]$, in the (0001) plane. Details of the production and testing of such specimens have been presented.[4]

Each test was carried out according to the following schedule:

1—The crystal was strained at −50°C until it reached a maximum shear stress, σ_m. The strain rate was approximately 5 pct per min in all cases.

2—After straining, the crystal was unloaded before the temperature was changed. Unloading required about 3 min.

3—The temperature of the specimen was then increased from −50°C to the temperature, T, of recovery. This change in temperature was completed in a time of less than 2 min. The specimen remained at temperature, T, for a time, t, which differed for the various specimens.

4—Thereafter the temperature was again reduced to −50°C in approximately 3 min.

5—While at −50°C, the stress-strain curve after recovery was obtained.

6—The specimen was then unloaded and annealed for 1 hr at 375°C in a helium atmosphere to bring about complete recovery. Cooling to room temperature after anneal required 90 min.

7—The same crystal could be re-used for another test because the plastic properties after annealing closely duplicated those of the original crystal.

The specimen was immersed during the test in a bath of methyl alcohol which, through a system of tubes, could be pumped through either of two heat exchangers to regulate the temperature; this was accomplished by circulating the liquid through coils immersed in a bath of acetone and dry ice for cooling or in a bath of warm water for heating. Test temperatures were thus maintained constant within ±1°C. The −50°C temperature was low enough so that no measurable recovery occurred during unloading and reloading.

The stress-strain curve continued after recovery along a path below, but approximately parallel to, the path of a curve obtained in an uninterrupted test. Fig. 1 shows some of the results from a specimen of 99.999 pct Zn. The amount of downward displacement of the curve due to recovery was a

R. DROUARD, formerly Graduate Student, is now in Paris, France, and J. WASHBURN and E. R. PARKER, Member AIME, are Instructor and Professor of Metallurgy, respectively, University of California, Berkeley, Calif.

Discussion on this paper, TP 3591E, may be sent, 2 copies, to AIME by Dec. 1, 1953. Manuscript, April 14, 1953. Cleveland Meeting, October 1953.

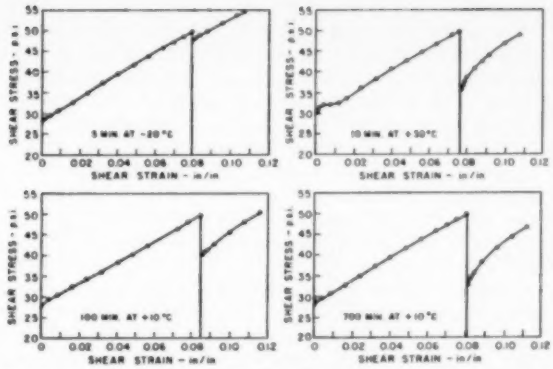

Fig. 1—Stress strain-curves at —50°C for a 99.999 pct Zn crystal showing drop in flow stress due to recovery for various times at higher temperatures.

function of both time and temperature. The quantitative measure of recovery which was adopted for comparison is illustrated in Fig. 2. $R = \frac{\sigma_m - \sigma}{\sigma_m - \sigma_o}$ is the ratio of the reduction in flow stress due to recovery to the total increase in flow stress due to strain hardening. The values of σ and σ_o were obtained by extrapolation of the linear part of the curve to the corresponding value of the stress for zero strain. This extrapolation avoided some secondary effects which caused changes in the shape of the initial portion of the curve. The sharpness of the yield after recovery varied considerably, being fairly sharp for the short times and low temperatures and somewhat rounded for high temperatures and long recovery times. Since this transient recovery effect became pronounced only at large values of R, it differed from the meta-recovery observed by Dorn et al.[2] in their studies of polycrystalline aluminum.

An attempt was made to reproduce exactly the prestrain portion of the stress-strain curve so that the recovery process could always be started with the crystal in the same state. However, small variations in the yield stress after annealing did occur. This made necessary the use of the above definition of recovery as a fraction of the amount of strain hardening. In addition to correcting for variations in stress, this definition was found to have validity

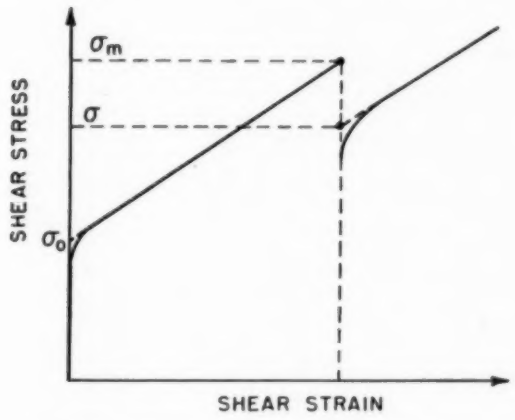

Fig. 2—Definition of recovery: $R = \frac{\sigma_m - \sigma}{\sigma_m - \sigma_o}$.

over a large range of prestrains, and for both 99.99 and 99.999 pct pure zinc. Most of the tests were made with a prestrain of about 8 pct but a few tests were made with 4 pct prestrain and others with 25 pct prestrain. The recovery as defined by R was apparently independent of the amount of prestrain because the points obtained in these tests were consistent with the data obtained for 8 pct prestrain. Large variations in yield stress σ_o were also produced by changing the temperature at which the crystal was annealed prior to some of the tests. The effect of annealing temperature on the stress-strain curve of zinc shear specimens is a complicated phe-

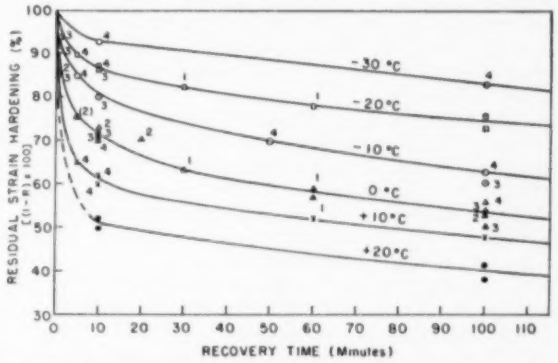

Fig. 3—Recovery of strain hardening as a function of time at various temperatures. Figures opposite experimental points indicate different specimens.

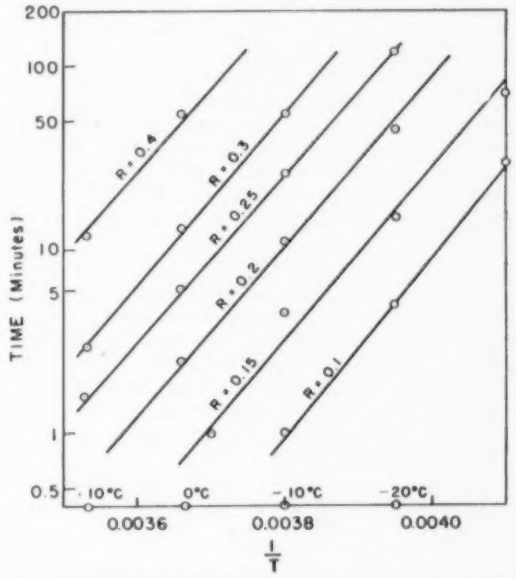

Fig. 4—Temperature dependence of the time required for various amounts of recovery.

nomena and will be discussed in detail in a separate publication.[6] Briefly, raising the annealing temperature above 200°C resulted in a raising of the yield point for the annealed crystal. However, the slope of the strain-hardening curve was not appreciably altered by change in annealing temperature. Recovery was found to be independent of stress level produced by these changes in annealing treatment. It seems, therefore, that recovery defined by $R = \frac{\sigma_m - \sigma}{\sigma_m - \sigma_o}$ is dependent only upon time and tem-

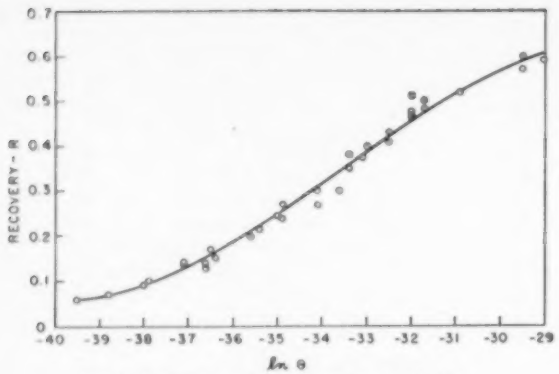

Fig. 5—Recovery — R vs ln $\theta = \ln t - Q/RT$.

perature and is independent of σ_∞ and σ_o. Results of tests for six different recovery temperatures are given in Fig. 3, where $(1-R)$ is plotted against recovery time.

Fig. 4 shows the temperature dependence of the time required to reach a given percentage of recovery. By plotting the natural logarithm of the recovery time against the reciprocal of the absolute temperature a series of straight lines was obtained corresponding to different fixed values of R. No consistent change in slope of the lines was detected with change in R from 10 to 40 pct. The average value of the slope or activation energy for the process was 20,000 cal per mol. The equivalence of temperature and time is further illustrated by Fig. 5 where recovery, R, for all the experimental points, including those tests where yield stress or prestrain was varied, is plotted as a function of temperature compensated time ($\ln t - Q/RT$). (Note: the R at the end of the preceding sentence and the last R in the caption for Fig. 5 refer to the gas constant rather than recovery as otherwise used in this paper.) By using the value of 20,000 cal per mol for Q all the points scatter fairly closely about a single curve.

Discussion

Since the activation energy for recovery after a simple shear deformation corresponds closely to that found by Miller and Banks[7] for self-diffusion in the C-axis direction in zinc ($[20.4 \pm 0.9] \times 10^3$ cal per mol) the results suggest that motion of lattice vacancies in the C-axis direction may be the rate-controlling factor during recovery.

The fact that recovery was independent of the yield strength apparently means that only those imperfections introduced by the strain are removed during this low temperature recovery. Although none of the tests were carried beyond 80 pct recovery, in most cases the crystal appeared to be approaching it immediately preceding the strain. Since both the initial yield strength of a crystal and the increase in strength attending strain are probably due to the presence of dislocations, it becomes important to consider the possible ways in which dislocations may be distributed.

Stress-strain curves for zinc single crystals deformed in simple shear (easy glide) show nearly the same rate of strain hardening beyond the yield regardless of the stress level at which yielding occurs.[8] The yield stress on the other hand is greatly affected by temperature of testing, prior annealing conditions, and geometrical perfection of the crystal. Therefore the shear strength of a crystal appears to be governed by two factors. 1—the initial structure of the crystal, and 2—the strain. The yield strength is characteristic of the annealed crystal. It is a reproducible value, determined for a given crystal largely by the annealing temperature. There seems to be little doubt that yielding depends to a great extent upon the nature of the substructure in the crystal,[4] whether it be macroscopic dislocation boundaries or submicroscopic mosaic blocks. Slip presumably increases the free energy of the structure by increasing the elastic strain energy in the system. Thus the altered structure is thermally less stable and tends to return to the lower energy state. The extent to which such strain-induced structural changes can be removed by recovery depends upon the test conditions, complete recovery at low temperatures being possible for simple shear but not for bending or for multiple slip such as usually occurs in cubic metals.

When a shear stress is applied to a crystal by a gradually increasing load, the process of slip is thought to begin by local shear displacements at many points throughout the crystal. When the yield stress is reached, the structural barriers provided by dislocation boundaries are penetrated. Slip on some of the slip planes then traverses the entire specimen and observable slip steps are formed at the surface. The growth of each elementary slip line presumably takes place in a short time and over a very narrow range of applied stress.[9] Once flow has ceased on a given slip plane it does not again become active in spite of considerable increase in applied stress. The reason for cessation of slip in an active slip line after a fairly definite amount of shear is still not clear. The most likely explanation seems to be that large numbers of lattice vacancies are produced by moving dislocations which, along with interactions between

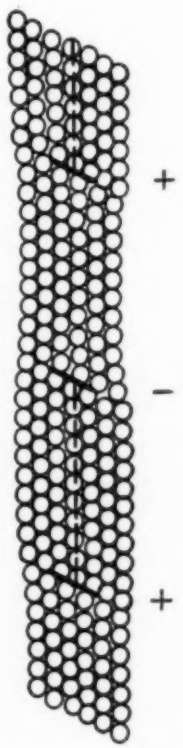

Fig. 6—Annihilation of edge dislocations. Condensation of lattice vacancies on the three dislocations shown would cause the central negative dislocation and the lower positive dislocation to move together by elimination of the extra partial plane of atoms between them. Escape of vacancies would cause the negative dislocation and the upper positive dislocation to annihilate each other in a similar way.

dislocations, bring slip to a halt.[9] The measured strain hardening should not be confused with this local hardening occurring in the immediate neighborhood of a slip line. Macroscopic strain hardening must be interpreted to mean that growth of each group of slip lines (slip band) across the crystal makes the next increment of slip a little more difficult. Therefore, measured strain hardening and the capacity of the strain-hardened crystal for recovery would seem to be greatly affected by the distribution of dislocations which became stuck primarily within the previously formed slip bands.

In the case where the shear stress acting in a crystal is uniform, i.e., where there are no shear stress gradients, it is to be expected that equal numbers of positive and negative dislocations would become trapped in each small volume of crystal. Elastic strain energy in the material between bands would be small and rate of strain hardening would be a minimum. On the other hand, when the stress system is such that local bending moments develop during deformation, positive dislocations tend to group themselves in some regions of the slip bands whereas negative dislocations collect in other parts. Groups of dislocations of like sign on neighboring slip bands tend to align themselves in an array at right angles to the active slip direction, thus forming small angle boundaries. The difference between simple shear deformation and other more complex deformations (for which the rate of strain hardening is greater) may be that in the former there is less tendency for groups of like dislocations to form.

The recovery characteristics are quite different for the two cases. If it is assumed that recovery is a return of the crystal to the structure it possessed before the deformation, then it involves a removal of lattice vacancies and bound dislocations introduced by the strain. Since it is not reasonable to suppose for the times and temperatures of these experiments that migration of vacancies over long distances can occur, then the changes taking place must be due to short range diffusion. For example, segments of edge dislocation lines having opposite signs, but existing on different parallel slip planes, can, by interaction with lattice vacancies, move onto the same slip plane and annihilate each other as illustrated in Fig. 6. Where each small volume of crystal within a slip band contains an equal number of positive and negative dislocations, this process for elimination of stuck dislocations during recovery seems reasonable. However, if dislocations are segregated into groups of like sign, low temperature recovery might be expected to cause some rearrangements (polygonization) but could not be expected to eliminate the dislocations introduced by the inhomogeneous strain.

The annealed or fully recovered state of a crystal then, is one in which all the existing dislocations are segregated into fairly widely spaced arrays of dislocations of like sign. Simple shear strain introduces equal numbers of positive and negative dislocations which may also concentrate at the existing substructure boundaries. Recovery returns the crystal toward its initial state by recombination of nearby positive and negative dislocation segments. Recovery after a nonhomogeneous strain, such as that occurring during deformation of a polycrystalline aggregate, would not be expected to return the crystal to its initial state since new widely separated arrays of dislocations of like sign are introduced by the strain.

The fact that zinc crystals subjected to simple shear do not show asterism even after large strains and that they recover completely at low temperatures suggests that both positive and negative dislocations are introduced by strain and that they are not concentrated into large widely separated groups of like sign.

Acknowledgment

Support of this work by the Office of Naval Research and in particular the interest and encouragement of Dr. O. Marzke and Dr. Julius Harwood is gratefully acknowledged.

References

[1] Von G. Tammann: The Result of Cold Working and Recovery of Metals from This State on Heating. *Ztsch. Metallkunde* (1936) **28**, pp. 6-17.

[2] T. V. Cherian, P. Pietrokowsky, and J. E. Dorn: Some Observations on the Recovery of Cold Worked Aluminum. *Trans.* AIME (1949) **185**, pp. 948-956; JOURNAL OF METALS (December 1949).

[3] N. Thorley: The Calculation of the Activation Energy of Recovery and Recrystallization from Hardness Measurements on Copper. *Journal* Inst. Metals (1950) **77**, p. 141.

[4] E. R. Parker and J. Washburn: Deformation of Single Crystals. *Modern Research Techniques in Physical Metallurgy* (1953) Cleveland. ASM.

[5] G. I. Taylor: The Mechanism of Plastic Deformation of Crystals. *Proc.* Royal Soc. (1934) **145A**, p. 362.

[6] Choh Hsien Li, J. Washburn, and Earl R. Parker: Variation of Plastic Properties with Annealing Procedure in Zinc Single Crystals. This issue, p. 1223.

[7] P. H. Miller and R. F. Banks: Self Diffusion in Zinc. *Physical Review* (1942) **61**, p. 648.

[8] A. F. Brown: Surface Effects in Plastic Deformation of Metals. *Advances in Physics* (October 1952) **1**, No. 4, pp. 427-479.

[9] N. F. Mott: A Theory of Work Hardening of Metal Crystals. *Philosophical Magazine* (1952) **43**, pp. 1151-1178.

Technical Note

Relation Between Initial Creep Rate and Resolved Shear Stress In Zinc Single Crystals

by N. Brown, J. Washburn, and Earl R. Parker

MOST previous quantitative work on creep of single crystals has been concerned primarily with developing empirical equations for the creep curve. Although the equations used by Cottrell and Aytekin[1] and Tyndall[2] represented the data quite well, it was often necessary to use different values of the constants for different specimens even though they were apparently tested under identical conditions. In the course of previous work on the effect of surface coatings on creep of zinc single crystals,[3] it was found that equal resolved shear stress frequently did not produce equal creep rates in different specimens. The work of Chalmers[4] in the very

N. BROWN is Assistant Professor, University of Pennsylvania, Philadelphia, J. WASHBURN is Instructor, and E. R. PARKER, Member AIME, is Professor, Dept. of Metallurgy, University of California, Berkeley, Calif.

TN 180E. Manuscript June 18, 1953.

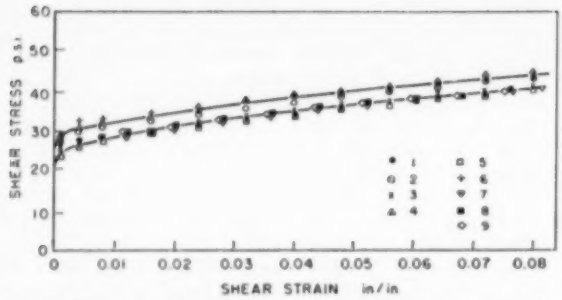

Fig. 1—Nine successive stress-strain curves from the same specimen showing complete recovery of mechanical properties. Annealed 1 hr at 260°C before each test.

low stress range appears to be the only data which shows a definite relation between initial creep rate and stress. In the microcreep range, where the creep process apparently consists only of a transient stage, initial creep rate was found to be directly proportional to stress.

The present work was undertaken in an attempt to establish some reproducible relation between initial creep rate and resolved shear stress at higher stress levels where the total creep strain is not limited. Many of the difficulties encountered when testing single crystals in tension[5,6] were avoided by the use of shear specimens. The production, mounting, and testing techniques used for achieving an essentially pure shear strain in these crystals have been discussed.[7] The purity of the zinc was 99.999. Fig. 1 shows a series of nine stress-strain curves from a single shear specimen. An anneal of 1 hr at 260°C prior to each deformation resulted in complete recovery of mechanical properties. No upward trend in the level of the curves was found since the ninth test was among the lowest of the series. The curves were essentially parallel, all the scatter being in the yield stress. From the results of another investigation,[8] the variation in yield stress has been found to be due to variations in annealing procedure. Even though reasonable care was taken in this case to keep the annealing conditions constant, a significant amount of scatter occurred.

Since single crystals creep at appreciable rates only for stresses above the yield stress, it seemed possible that the creep rate might correlate better with the increment of stress above the yield stress than with the total stress.

$$\dot{\gamma}_o = f\,(\sigma - \sigma_o) \qquad [1]$$

where $\dot{\gamma}_o$ is initial creep rate, σ is total stress, and σ_o is the yield stress. Consequently a method of applying the creep load was adopted which permitted recording of the stress-strain curve during loading. σ_o was difficult to establish experimentally, because of the curvature of the initial portion of the stress-strain curve. However, as shown in Fig. 1, the increment of stress above the yield stress is approximately proportional to the total strain,

$$\gamma \sim (\sigma - \sigma_o).$$

Thus it follows that a criterion nearly equivalent to that of Eq. 1 is

$$\dot{\gamma}_o = f\,(\gamma_o) \qquad [2]$$

where $\dot{\gamma}_o$ is initial creep rate and γ_o is the strain at the instant loading is completed.

The results of a number of tests on two different specimens are shown in Fig. 2, where initial creep rate is plotted as a function of initial strain, γ_o. Although large variations in σ_o resulted from annealing at widely different temperatures prior to testing, all of the experimental points fell along the same curve. Initial creep rate was found to increase linearly with initial strain and consequently with the increment of stress above the yield stress.

The yield stress σ_o may be the stress at which dislocations are able to break through substructure boundaries in a manner analogous to that recently observed for sodium chloride crystals.[9] This picture also seems to be consistent with the rather sharp transition from microcreep to macrocreep which occurred when a critical stress level was reached in Chalmers experiments.[4]

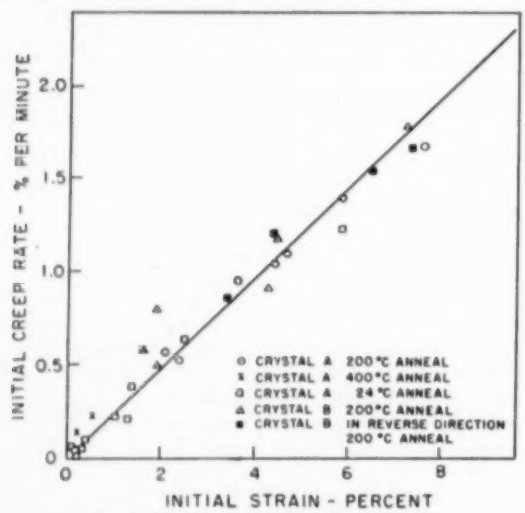

Fig. 2—Initial creep rate vs initial strain.

Acknowledgment

Support of this work by the Office of Naval Research and in particular the interest and encouragement of Dr. O. Marzke and Dr. Julius Harwood is gratefully acknowledged.

References

[1] A. H. Cottrell and V. Aytekin: Andrade's Creep Law and the Flow of Zinc Crystals. *Nature* (1947) **160**, pp. 328-329.

[2] E. P. T. Tyndall: Creep of Zinc Crystals. *A Symposium on the Plastic Deformation of Crystalline Solids.* Mellon Inst., Pittsburgh, May 1950. Under the Joint Sponsorship of the Carnegie Institute of Technology and the Department of the Navy, Office of Naval Research. p. 49.

[3] M. R. Pickus and Earl R. Parker: Creep Behavior of Zinc Modified by Copper in the Surface Layer. *Trans.* AIME (1951) **191**, p. 792; JOURNAL OF METALS (September 1951).

[4] B. Chalmers: Precision Extensometer Measurements in Tin. *Journal* Inst. Metals (1937) **61**, p. 103.

[5] J. Washburn and Earl R. Parker: Kinking in Zinc Single-Crystal Tension Specimens. *Trans.* AIME (1952) **194**, p. 1076; JOURNAL OF METALS (October 1952).

[6] R. W. K. Honeycomb: Inhomogeneities in the Plastic Deformation of Metal Crystals. *Journal* Inst. Metals (1951) **80**, p. 45.

[7] Earl R. Parker and Jack Washburn: Deformation of Single Crystals. *Modern Research Techniques in Physical Metallurgy* (1952) Cleveland. ASM.

[8] Choh Hsien Li, J. Washburn, and Earl R. Parker: Variation of Plastic Properties with Annealing Procedure in Zinc Single Crystals. This issue, p. 1223.

[9] P. L. Pratt: Strain Hardening of Single Crystals. A.E.R.E. Report, Harwell, Berks., M/R 883.

Plastic Deformation of Single Crystals of Copper

by J. J. Becker and J. N. Hobstetter

Slip lines in deformed copper single crystals exhibit very pronounced cross-slip and clustering if the stress axes are not too far from <100>. This orientation dependence seems to persist whether or not attempts are made to reduce the bending constraints of ordinary mechanical tests.

THE purpose of this paper is to report some microscopic features of the plastic deformation of copper single crystals.

The material used was OFHC copper obtained from the American Brass Co. Single crystals about 3 in. long and 5/16 in. in diameter were made by lowering graphite crucibles containing this copper out of the hot zone of a vertical tubular furnace at a rate of 1¼ in. per hr. The furnace atmosphere was nitrogen. The orientations of the crystals were determined by the back-reflection Laue technique.[1] The X-ray spots usually indicated a slight lineage structure of not more than a degree or two.

The crystallography of slip is discussed in Schmid and Boas.[2] The terms classical slip, cross-slip, and conjugate slip are used here with the same meanings as in ref. 3.

Compression

Specimen 17 (Fig. 1) was selected because the resolved shearing stresses on eight slip systems differed at most by a factor of 1.2. It was hoped that in this situation such effects as cross-slip might be made more prominent.

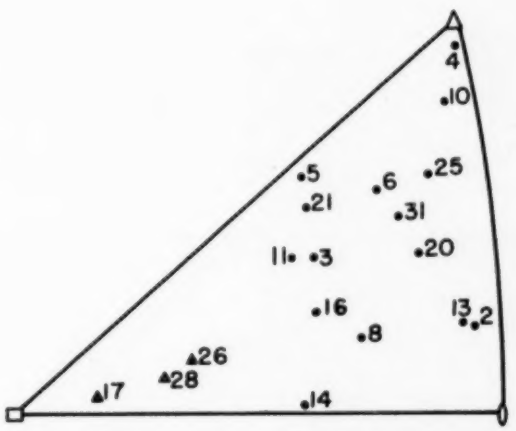

Fig. 1—Orientations of all specimens deformed. Triangles, specimens showing pronounced cross-slip.

Two intersecting planes parallel to the stress axis were ground on the crystal, using optical abrasive on a lead lap. The large plane was approximately perpendicular to the plane of the axis and the primary slip direction. Its exact orientation was determined by X-ray. The smaller made an angle of 49° with the larger, measured by reflecting a small light source. The specimen was etched with nitric acid until its diameter had been reduced 0.010 in., and then was given a metallographic polish and very

J. J. BECKER, Junior Member AIME, formerly Teaching Fellow, Dept. of Engineering Sciences and Applied Physics, Harvard University, is now associated with General Electric Research Laboratory, Schenectady, and J. N. HOBSTETTER, formerly Assistant Professor, Dept. of Engineering and Applied Physics, Harvard University, is now associated with Bell Telephone Laboratories, Murray Hill, N. J.

Discussion on this paper, TP 3592E, may be sent, 2 copies, to AIME by Dec. 1, 1953. Manuscript, April 15, 1953; revision, June 15, 1953. Cleveland Meeting, October 1953.

This paper is based on a thesis by J. J. Becker submitted in partial fulfillment of requirements for the degree of Doctor of Philosophy in the field of engineering sciences and applied physics to the Faculty of Arts and Sciences, Harvard University, January 1951.

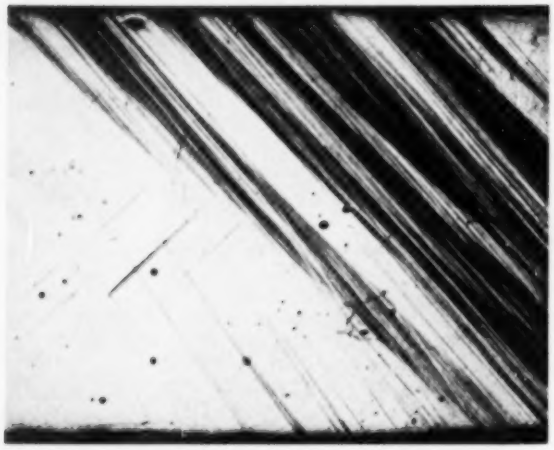

Fig. 2—Slip and cross-slip on specimen 17-A. Compressed 1 pct. Stress axis horizontal. X21. Area reduced approximately 50 pct for reproduction.

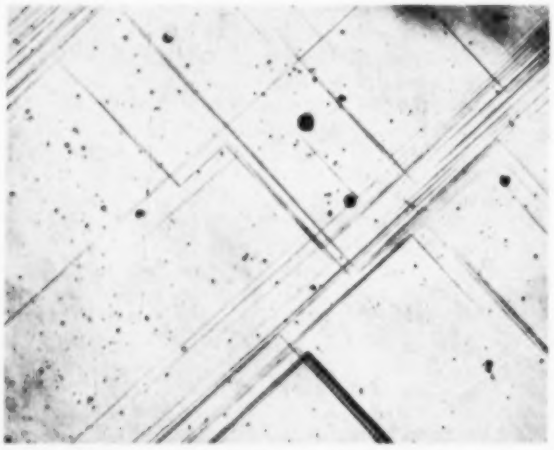

Fig. 3—Cross-slip on specimen 17-A. Compressed 1 pct. Stress axis horizontal. X75. Area reduced approximately 50 pct for reproduction.

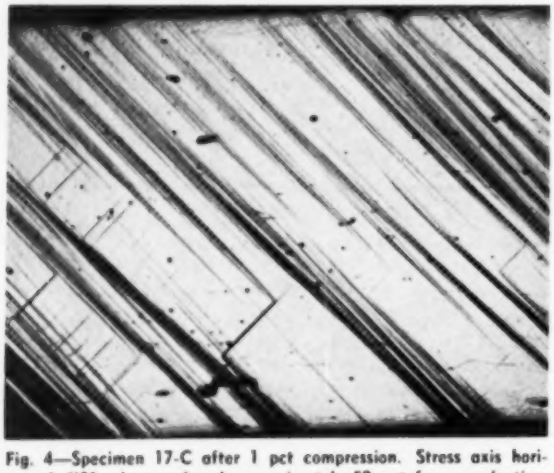

Fig. 4—Specimen 17-C after 1 pct compression. Stress axis horizontal. X21. Area reduced approximately 50 pct for reproduction.

Fig. 5—Specimen 17-C after 5 pct compression. Stress axis horizontal. X21. Area reduced approximately 50 pct for reproduction.

Fig. 6—Specimen 17-C after 10 pct compression. Stress axis horizontal. X21. Area reduced approximately 50 pct for reproduction.

heavily etched. The crystal was cut in thirds with a jeweler's saw and the ends faced on a lathe to the same length, 0.909 in. The flat surfaces were again polished and etched, the faced ends being protected from the etchant by paraffin which was then removed with xylol. This entire procedure did not change the nature of the X-ray diffraction spots.

The three specimens, 17-A, 17-B, and 17-C, were compressed 0.009 in., or 1 pct. 17-B and 17-C were then compressed to a total of 5 pct, and 17-C to a total of 10 pct. The strain rate was approximately constant and equal to about 0.001 in. per in. per min.

All three specimens showed very similar patterns of slip lines. A representative area from one of them is shown in Fig. 2, which shows about one quarter of the polished surface. Here, as in all the illustrations, the observation plane is perpendicular to the plane of the specimen axis and primary slip direction. A portion of this specimen, Fig. 3, shows many examples of the joining of slip and cross-slip lines at a corner. The cross-slip shown in these specimens is on an extremely large scale, compared with previous illustrations of the phenomenon.

Figs. 4 to 6 show the same region after 1, 5, and 10 pct compression. The most striking feature of these pictures is the accuracy with which the pattern of slip lines of the smaller deformation is pre-

Fig. 7—Slip on specimen 20. Deformed in shearing machine. Shear 0.5. Elongation, 27 pct. Stress axis horizontal. X75. Area reduced approximately 50 pct for reproduction.

served. Increasing the deformation by a factor of 10 results in the formation of heavy clusters of slip and cross-slip lines at the original slip and cross-slip lines. Regions which were practically free from slip lines remain conspicuously so. These figures also illustrate the very characteristic avalanching of slip lines, and avalanching of cross-slip lines as well. The boundaries of the clusters of slip lines go off at a slight angle to the lines themselves. Many examples could be seen of two slip lines which overlap for a considerable distance but are not connected by cross-slip. Deformations of single crystals are often specified in terms of "amount of shear" computed from geometry or from reorientation measured by X-ray. This computation assumes uniform shear on only one slip system, and is thus hardly applicable to complex cases such as specimen 17.

Attempts to Produce Slip on a Single System

The bending constraints imposed in the simple tensile test of a single crystal make such a test difficult to interpret. Attempts to eliminate these constraints were made by two methods, both of which have subsequently been described in the literature. One was to deform the specimen in a shearing machine essentially like that devised by Röhm.[4] The other was to use a tensile machine in which knife-edges at the grips provided a rotation axis through the midpoint of the first completely free glide ellipse at each end, the specimen being appropriately oriented about its own axis, precisely as described by Diehl and Kochendorfer.[5] Rosi[6] has also built a rotating-grip machine which provides two rotation axes instead of one.

Specimen 20 (Fig. 1) was tested in the shearing machine. It was given a deformation corresponding to an extension of 27 pct. This gives a geometrically computed overall shear of 0.5. The shear computed from the change in orientation of the center part of the crystal measured by X-ray was less than this. Since the specimen showed some bending at the ends, the reorientation of the center portion was

Fig. 8 (left)—Specimen 28 after 8 pct extension in rotating-grip machine. Stress axis vertical. X7.3.

Fig. 9 (right)—Specimen 31 after 11.8 pct extension in rotating-grip machine. Stress axis vertical. X7.3.

Fig. 10—Slip in specimen 31 after 11.8 pct extension in rotating-grip machine. Stress axis vertical. The faint vertical striations were present before deformation. X75. Area reduced approximately 50 pct for reproduction.

less than that deduced from simply measuring the angle from the new specimen axis to the original. Incidentally, since measurement of this angle was the method used by Röhm to find his shear strains, it is possible that the lowering of the shear stress-strain curves reported by him is due to the same cause.

Classical primary slip lines appeared very even and uniform during the process of deformation. None of the clustering, cross-slip, or other irregularities that specimen 17 showed could be seen in the center portion of the specimen. Premature conjugate slip was absent.

Fig. 7 shows the microscopic appearance of a typical portion of the center of the specimen. At the very ends of the specimen, where the bending was greatest, a little cross-slip could be seen. X-ray pictures showed no change in the nature of the diffraction spots.

Although the rotating-grip machine appears to accomplish the same results as the shearing machine, they are not entirely equivalent. The load applied by the rotating-grip machine is always axial. There is no externally applied bending moment. In principle, then, it might appear to be superior to the shearing machine. In practice, it was found difficult to use. Axiality of the knife edges was of the utmost importance. Although the machine was built with considerable care, the alignment of the specimens was not easy. After a number of trials, two tests were made which will be described here.

In the first test specimen 28 (Fig. 1) was used. It was given an extension in the machine of 8 pct. The grips rotated in the predicted direction, although one grip rotated somewhat more than the other. The unexpected appearance of the slip lines is shown in Fig. 8. The similarity of this to the specimen deformed in compression is striking. It shows exactly the same clustering of primary slip lines and cross-slip lines, and is the very opposite of what the machine was intended to do. An X-ray picture taken after the deformation showed a distinct spot structure but no asterism.

Another test was conducted on specimen 31 (Fig. 1). It was extended 11.8 pct, with quite different results. The overall appearance of its slip lines is shown in Fig. 9. Fig. 10 shows a region practically free from cross-slip at higher magnification. In general, there was very little cross-slip to be seen.

The completely different behavior of these two specimens led to a re-examination of all the specimens deformed during the course of this work. Their orientations are given in Fig. 1. A brief description of their deformation is given in Table I. Specimens 17, 26, and 28 showed similar patterns of very conspicuous cross-slip and clustering, and all have orientations near [100]. For the most part, specimens with orientations far from [100] did not show cross-slip, or showed it on a smaller scale. It seems as though the detailed nature of plastic deformation might depend more strongly on the orientation of the specimen than on the exact means of deforming it.

Table I. Deformation and General Appearance of Specimens

Specimen No.	Description
2	Slightly compressed. No cross-slip.
3	Slightly compressed. No cross-slip.
4	Heavily compressed. Two intersecting slip systems, heavy clustering but no cross-slip.
5	Sheared perpendicular to specimen axis. Three intersecting systems but no cross-slip as such.
6	Compressed. No cross-slip.
8	Compressed. No cross-slip.
10	Compressed, one end free to move transversely. Much overlapping of primary slip lines, but no cross-slip.
11	Deformed in shearing machine. Slipped out of lower grip. Overlapping primary slip lines but no cross-slip.
13	Deformed in shearing machine. Slipped out of upper grip. No cross-slip.
14	Rough tensile test. No cross-slip.
16	Sheared nearly perpendicular to axis. Three intersecting slip systems but no cross-slip.
17	Compressed (Section 3.2). Very pronounced cross-slip and clustering.
20	Deformed in shearing machine. No cross-slip.
21	Deformed in rotating-grip machine. Slight cross-slip.
25	Deformed in earlier model of rotating-grip machine. Some cross-slip.
26	Deformed in rotating-grip machine. Very prominent cross-slip.
28	Deformed in rotating-grip machine. Very prominent cross-slip.
31	Deformed in rotating-grip machine. Very slight cross-slip.

Conclusions

1—Plastic deformation in copper single crystals is complicated far beyond the naive idea of a "glide ellipse" on the classical slip plane. Clustering and avalanching are prevalent. Cross-slip and other unpredicted slips are frequent.

2—The occurrence of large-scale cross-slip seems to be favored by an orientation near [100] regardless of the way in which the crystals are deformed.

3—Large-scale cross-slip and severe clustering seem to be associated with each other.

References

[1] A. B. Greninger: Determination of Orientation of Metallic Crystals by Means of Back-Reflection Laue Photographs. *Trans.* AIME (1935) **117**, p. 61.

[2] E. Schmid and W. Boas: *Kristallplastizitat* (1935) Berlin. Julius Springer.

[3] R. Maddin, C. H. Mathewson, and W. R. Hibbard, Jr.: The Active Slip Systems in the Simple Axial Extension of Single Crystalline Alpha Brass. *Trans.* AIME (1949) **185**, p. 527; JOURNAL OF METALS (August 1949).

[4] U. Dehlinger: The Experimental and Theoretical Results of Plasticity at Normal Speeds of Strain. *Symposium on Plastic Deformation of Crystalline Solids.* (May 1950) pp. 19-20. Mellon Institute.

[5] J. Diehl and A. Kochendörfer: Zugverforming an Einkristallen mit Drehbaren Fassungen. *Ztsch. Angew. Phys.* (1952) **4**, p. 241.

[6] F. D. Rosi: Homogeneous Deformation of Single Crystals. *Review of Scientific Instruments* (1951) **22**, p. 708.

Orientation Relationships in the Recrystallization Of Deformed Copper Single Crystals

by J. J. Becker and J. N. Hobstetter

Deformed copper single crystals exhibited, upon annealing, a recrystallized twinned grain with a twin plane parallel to an active deformation plane, rotated approximately 22° about its pole, or else did not recrystallize at all. If extraneous deformation was not carefully removed, no simple orientation relationship was found.

RECRYSTALLIZATION textures have been a subject of practical interest for many years, but any real understanding of their formation will have to start with a study of the recrystallization of carefully deformed single crystals. Some efforts have been made in this direction,[1-4] but much more experimental information is needed before a satisfactory picture of the crystallography of recrystallization can be formed. This paper reports a few results in copper single crystals.

The crystals studied in this investigation were grown by the Bridgman method,[5] and their orientations determined by the back-reflection Laue technique.[6] Some specimens were simply deformed in compression, others were sheared, and still others tested in a rotating-grip device, in attempts to remove end constraints. The details of their deformation behavior are described elsewhere.[7] The deformed specimens were annealed and the orientations of the recrystallized grains were determined optically, as described by Barrett and Levenson.[8]

Compressed Specimens

Specimen 17-A, whose orientation is given in Fig. 1, was compressed to a total of 19 pct. As observed before,[7] increasing deformation took place by increasing density of slip lines in initially formed clusters, with little if any formation of new slip clusters in unslipped areas. The specimen was then etched in nitric acid until its length had been reduced from 0.766 to 0.735 in. It was annealed at 1000°C, in increments of a few minutes. After 63 min, two small grains had appeared in the center, Fig. 2. They were found to be twinned with respect to each other (*AB*, Fig. 4). After 30 min more, the specimen was completely recrystallized. A typical view of it is given in Fig. 3. A summary of all orientations found is given in Fig. 4, in which the prominent grain *G* is in (001) standard projection, and the poles of the active slip planes after deformation are indicated by SP (primary slip plane), CrSP (cross-slip plane), and CnSP (conjugate slip plane). All the orientations found were related through seven orders of twinning. A "family tree" of these twins is given in Fig. 5. Furthermore, the *BG* twin composition plane lies close to the cross-slip plane

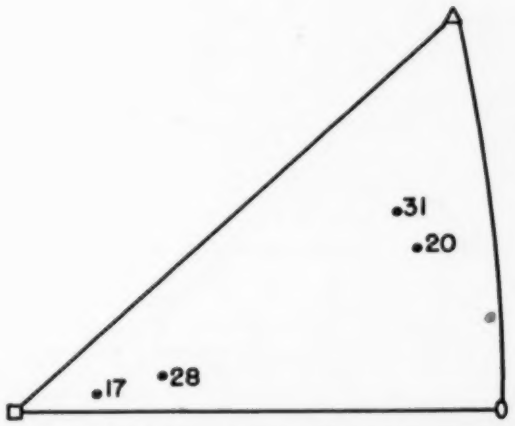

Fig. 1—Orientations of single crystals.

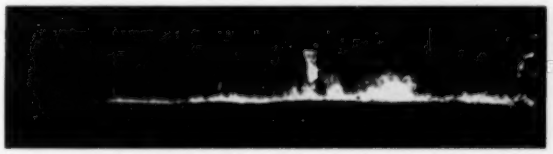

Fig. 2—Recrystallized grains beginning to form in specimen 17-A. X7.3. Area reduced slightly for reproduction.

Fig. 3—Specimen 17-A after complete recrystallization. X7.3. Area reduced approximately 50 pct for reproduction.

J. J. BECKER, Junior Member AIME, formerly Teaching Fellow, Dept. of Engineering Sciences and Applied Physics, Harvard University, is now associated with General Electric Research Laboratory, Schenectady, and J. N. HOBSTETTER, formerly Assistant Professor, Dept. of Engineering and Applied Physics, Harvard University, is now associated with Bell Telephone Laboratories, Murray Hill, N. J.

Discussion on this paper, TP 3593E, may be sent, 2 copies, to AIME by Dec. 1, 1953. Manuscript, April 15, 1953. Cleveland Meeting, October 1953.

This paper is based on a thesis by J. J. Becker submitted in partial fulfillment of requirements for the degree of Doctor of Philosophy in the field of engineering sciences and applied physics to the Faculty of Arts and Sciences, Harvard University, January 1951.

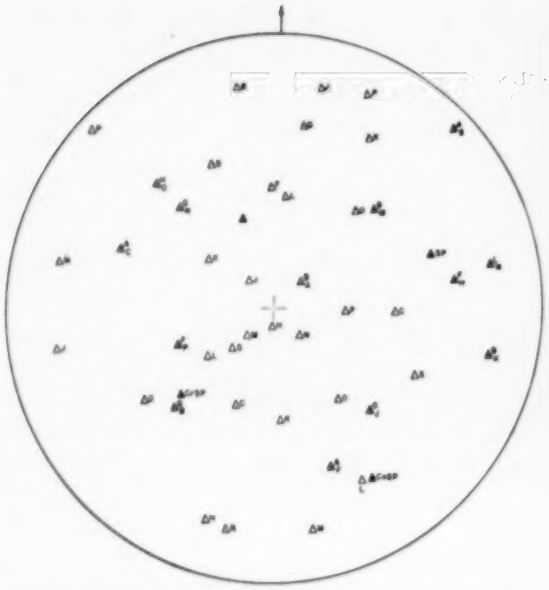

Fig. 4—Orientations of recrystallized grains in specimen 17-A.

Fig. 5—Twin relationships of recrystallized grains in specimen 17-A.

Fig. 6—BG twins in specimen 17-A. X4.8. Area reduced slightly for reproduction.

and the orientation of grain G is rotated approximately 24° in this plane. Fig. 6 was taken to show BG twins prominently. The dark grains are B, and the twins along the bottom of the picture are G.

Specimen Deformed in Shearing Machine

Specimen 20 (Fig. 1) was deformed 27 pct in a device designed to shear the specimen in such a way as to minimize the end constraints. It showed relatively uniform classical slip lines only. A piece about ½ in. long was removed from the center of this specimen with a jeweler's saw. This piece was etched until its thickness had been reduced 0.007 in. After 6 min at 1020°C, it showed no sign of recrystallizing. After another 15 min, it was entirely recrystallized. Figs. 7 and 8 show its appearance on opposite sides. Note that the orientations X and D, which are twins, occupy roughly the center two-thirds of the specimen. The orientations of these various grains are given in Fig. 9, in which the deformed crystal is in (001) standard projection. The XD composition plane is very close to the primary slip plane of the crystal.

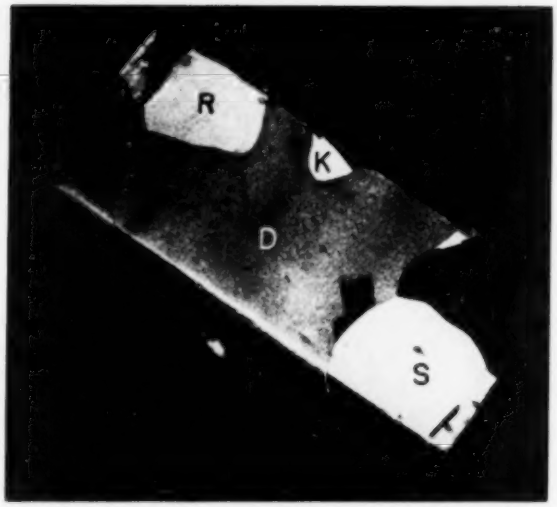

Fig. 7—Specimen 20 after recrystallization. X7.3. Area reduced slightly for reproduction.

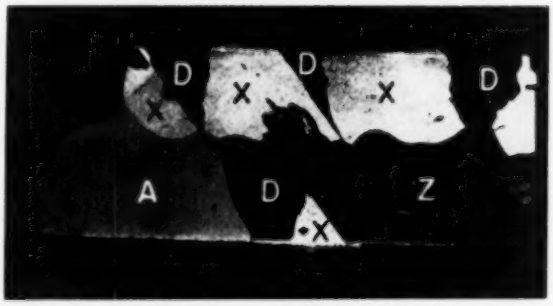

Fig. 8—Specimen 20 after recrystallization. X7.3. Area reduced slightly for reproduction.

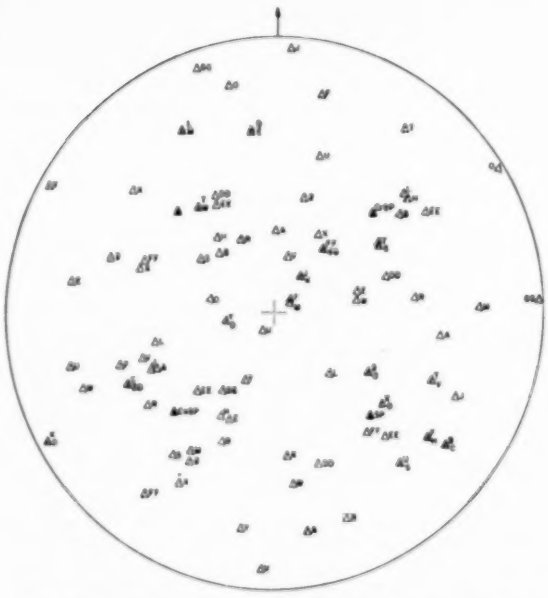

Fig. 9—Orientations of recrystallized grains in specimen 20.

Fig. 10 (left)—Recrystallized grains at end of specimen 31. X11.9. Area reduced slightly for reproduction.

Fig. 11 (right)—Recrystallized grains at end of specimen 31. X11.9. Area reduced slightly for reproduction.

No other close correlation appears. Furthermore, the orientation of X is related to the deformed crystal by a rotation of 22° about the pole of the classical slip plane.

Specimens Deformed in Rotating-Grip Machine

Specimen 28 was extended 8 pct in the rotating-grip machine, and specimen 31 was extended 11.8 pct. Their orientations are given in Fig. 1. Pieces about ½ in. long were cut from their centers with a jeweler's saw. The ends of these center pieces were ground with optical abrasive on a lead lap until their length had been reduced 0.050 in. They were etched in nitric acid until their lengths had been reduced another 0.016 in. The center of specimen 28 did not recrystallize after 75 min at 1000°C.

The center portion of specimen 31 was carefully placed in a copper foil capsule and annealed a total of 80 min at 1000°C plus 70 min at 1020°C. It did not recrystallize.

Gross recrystallization did not occur in either of the specimens deformed in the rotating-grip machine, even though one of them showed cross-slip and clustering and the other did not.

Effects of Random Nuclei

In all the instances that have been described here, in which distinctive orientation relationships were observed or recrystallization did not take place at all, the specimens had been considerably etched down after deformation and before annealing. This was done to remove the nuclei which might have been produced by saw cuts or by grips. A number of other specimens were annealed without this preliminary etch.

Specimen 17-C, with the same orientation as 17-A, was compressed 10 pct and recrystallized. The orientations of the recrystallized grains bore no obvious relationship to that of the deformed matrix. The end pieces of specimens 20 (deformed in the shearing machine) and 28 (deformed in the rotating-grip machine) were recrystallized as cut. In all cases recrystallization started under the grips and at the saw cut. No simple orientation relationship was found.

The ends of specimen 31 (deformed in the rotating-grip machine) were recrystallized without further treatment for 3 min at 1000°C. Both partially recrystallized. Two views of one of the recrystallized ends are given in Figs. 10 and 11. It would be expected that cutting a crystal with a saw would provide a multitude of nuclei in many orientations, among which those of certain orientations would grow most rapidly.[9] The large twinned grain in Fig. 11 corresponds to the conspicuous twinned grain at the bottom of Fig. 10, and illustrates this preferential growth. However, this does not result in a <111> rotation, or any other simple relationship. The orientations of these twins and of the deformed grain are given in Fig. 12. Selective growth, in this instance, does not lead to recognizable relationships.

Summary and Conclusions

Experiments are still needed in which geometrically simple deformation can be directly related to recrystallized orientations. The experiments reported here illustrate the following phenomena:

1—Whenever extraneous deformation was removed from the ends of deformed copper single crystal specimens, either they did not recrystallize at all, or else they exhibited a recrystallized twin plane parallel to one of the active deformation planes, with a rotation of about 22° about its pole. This same rotational relationship was found by Kronberg and Wilson[10] in the secondary recrystallization of copper. The identity of the twin plane

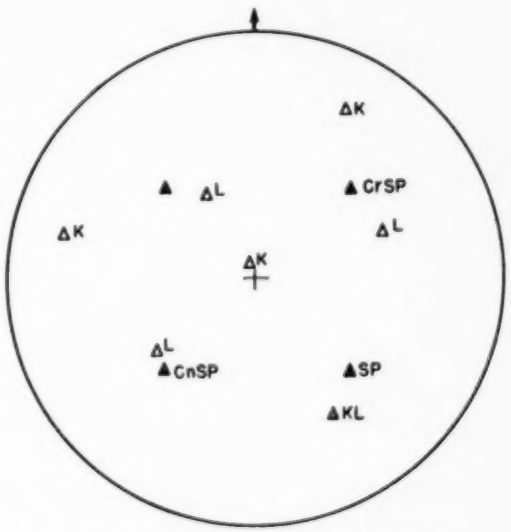

Fig. 12—Orientation of large grain in Figs. 10 and 11.

and the active slip planes was also found by Maddin, Mathewson, and Hibbard in the primary recrystallization of single crystals of α brass.[4]

2—When extraneous deformation was left in the specimens, and they recrystallized from grip marks or saw cuts, oriented growth could be observed, but it never resulted in a simple orientation relationship to the matrix.

References

[1] W. G. Burgers and P. C. Louwerse: Uber die Zusammenhang Zwischen Deformationsvorgang und Rekristallisationstextur bei Aluminium. *Ztsch. Phys.* (1931) **67**, p. 605.

[2] J. A. Collins and C. H. Mathewson: Plastic Deformation and Recrystallization of Aluminum Single Crystals. *Trans.* AIME (1940) **137**, p. 150.

[3] C. S. Barrett: Recrystallization Texture of Aluminum after Compression. *Trans.* AIME (1940) **137**, p. 128.

[4] R. Maddin, C. H. Mathewson, and W. R. Hibbard, Jr.: The Origin of Annealing Twins in Brass. *Trans.* AIME (1949) **185**, p. 655; JOURNAL OF METALS (September 1949).

[5] P. W. Bridgman: Certain Physical Properties of Single Crystals of Tungsten, Antimony, Bismuth, Tellurium, Cadmium, Zinc, and Tin. *Proc.* Amer. Acad. Arts and Sci. (1925) **60**, p. 305.

[6] A. B. Greninger: Determination of Orientation of Metallic Crystals by Means of Back-Reflection Laue Photographs. *Trans.* AIME (1935) **117**, p. 61.

[7] J. J. Becker and J. N. Hobstetter: This issue, p. 1231.

[8] C. S. Barrett and L. H. Levenson: Determination of Orientations by Etch Pits. *Trans.* AIME (1940) **137**, p. 76.

[9] P. A. Beck, P. R. Sperry, and H. Hu: The Orientation Dependence of the Rate of Grain Boundary Migration. *Journal of Applied Physics* (1950) **21**, p. 420.

[10] M. L. Kronberg and F. H. Wilson: Secondary Recrystallization in Copper. *Trans.* AIME (1949) **185**, p. 501; JOURNAL OF METALS (August 1949).

Technical Note

Thermal Conductivity, Electrical Resistivity, And Thermoelectric Power of Uranium

by W. W. Tyler, A. C. Wilson, Jr., and G. J. Wolga

THE physical properties of uranium have been reviewed by Katz and Rabinowitch.[1] Their review includes thermal conductivity data for temperatures above 375°K. Recently, Mendelssohn and Rosenberg[2] have published data on the thermal conductivity of uranium from 2° to 20°K. Our measurements indicate the temperature dependence of the thermal conductivity in the temperature interval from 20° to 300°K. Electrical resistivity and thermoelectric power were measured on the same sample.

The material studied was normal uranium which had been heated at 700°C in a lead bath for 10 min and then quenched in a water bath held at 50°C. From this material a rod ½ in. in diameter and 2½ in. long was machined. Two 0.040 in. holes were drilled into the rod 1¾ in. apart. Copper-constantan thermocouples for temperature and potential measurements were soldered to copper pins which were pressed tightly into these holes. Details of the equipment and experimental techniques used in making the measurements have been described elsewhere.[3]

Fig. 1 shows micrographs of a section of the sample studied. Fig. 1a was taken with unpolarized light and shows impurity inclusions, probably uranium carbide. Fig. 1b, showing the same field, was taken with polarized light and gives some indication of the grain size and twinning within the grains.

Experimental Results

Thermal conductivity and electrical resistivity data are shown in Fig. 2. Table I shows values of

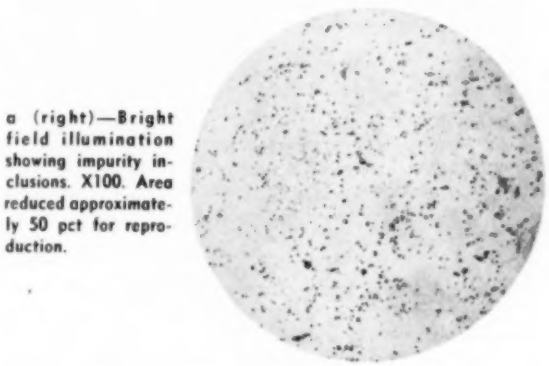

a (right)—Bright field illumination showing impurity inclusions. X100. Area reduced approximately 50 pct for reproduction.

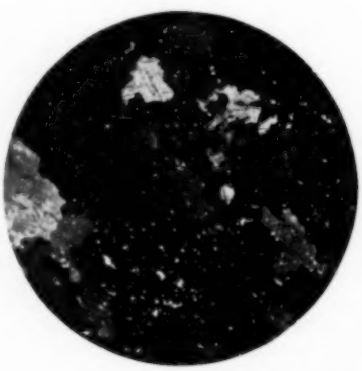

b (left)—Same field as in Fig. 1a but illuminated with polarized light showing microstructure. X100. Area reduced approximately 50 pct for reproduction.

Fig. 1—Micrographs of uranium.

W. W. TYLER and A. C. WILSON, Jr., associated with the Research Laboratory, General Electric Co., Schenectady, and G. J. WOLGA, associated with Cornell University, Ithaca, N. Y., were all formerly with Knolls Atomic Power Laboratory.

TN 169E. Manuscript, March 25, 1953.

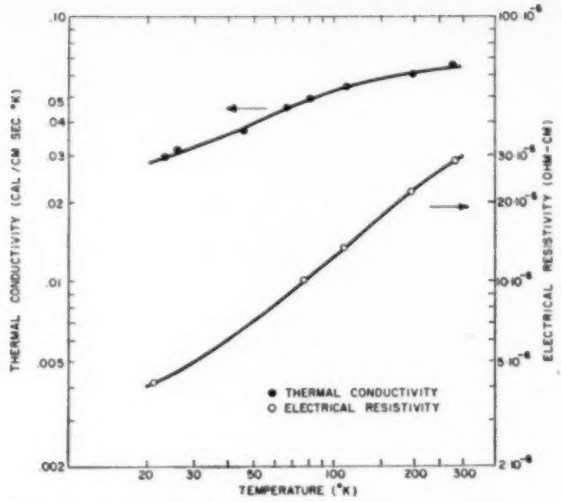

Fig. 2—Thermal conductivity and electrical resistivity of uranium.

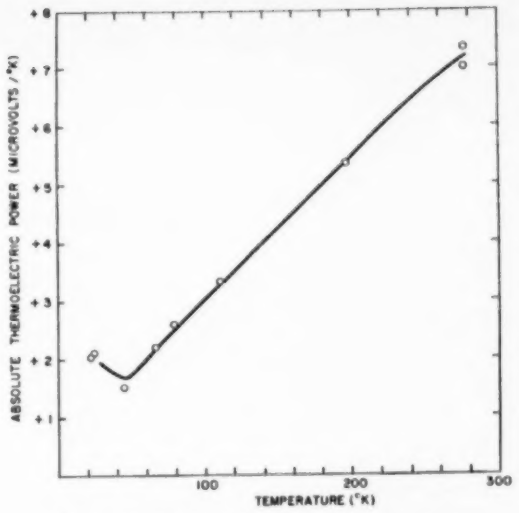

Fig. 3—Absolute thermoelectric power of uranium.

the Wiedemann-Franz ratio calculated from the smoothed curves of Fig. 2. Fig. 3 shows values of the absolute thermoelectric power of uranium obtained from measurements of thermoelectric power of a uranium-copper couple using data of Borelius[4] for the absolute thermoelectric power of copper.

The uncertainty in the magnitude of thermal conductivity data is estimated to be ±5 pct. Heat loss by heater and thermocouple leads was at the most 2 pct of the heat conducted by the specimen. Correction for this loss was made in a manner which has been described.[3] Errors due to thermal drift and radiation losses were at most 1 pct. A temperature-independent geometric error of about 2 pct resulted from the finite dimensions of the thermocouple contacts.

The accuracy of the electrical resistivity measurements was limited by the geometry of the sample. Due to the low values of the potential measured, the relative values of the resistivity data are uncertain by several percent in addition to the temperature-independent error due to form factor. Data points for electrical resistivity shown in Fig. 2 are averages of several points taken at approximately the same temperature. Assuming that the data of Borelius are applicable to the copper used in our couples, the thermoelectric power data are accurate to within 0.5 microvolts.

Discussion of Results

The values of the observed Wiedemann-Franz ratio vary from slightly below the free electron theoretical value of 2.45×10^{-8} (volts per degree)^2 at 20°K to slightly above the theoretical value at 300°K. The lattice does not contribute appreciably to thermal conductivity. This is in agreement with observations of Mendelssohn and Rosenberg[2] in the lower temperature range.

No maximum in the thermal conductivity characteristic of good electronic conductors[5] is observed for uranium. Extrapolation of our data gives somewhat higher conductivity at 350°K than indicated by data reported by Katz and Rabinowitch.[1] At 20°K, the conductivity of our sample is about 70 pct of that reported by Mendelssohn and Rosenberg. These differences, somewhat greater than experimental uncertainties, are probably due to differences in purity. The chemical purity of our sample is not accurately known and is not quoted for the other samples. Electrical resistivity data for our sample agree well with data quoted by Katz and Rabinowitch.[1] Their survey of available data indicates that the resistivity values depend upon purity and previous heat treatment.

Our value of absolute thermoelectric power at room temperature is in approximate agreement with values deduced from the data on thermoelectric power of uranium against copper and against platinum given by Ebert and Schulze.[6] The positive sign of the absolute thermoelectric power implies that conduction is predominantly due to holes.

Table I. Calculated Values

Temperature, °K	Wiedemann Franz Ratio (Volts/Degree)^2
20	2.34×10^{-8}
60	2.46×10^{-8}
100	2.75×10^{-8}
140	2.88×10^{-8}
180	2.88×10^{-8}
220	2.82×10^{-8}
260	2.73×10^{-8}
300	2.67×10^{-8}

The measurements reported were made at the General Electric Low Temperature Laboratory. We are indebted to J. E. Burke for his suggestion of this study and for his helpful discussion related to the interpretation of the micrographs.

References

[1] J. J. Katz and E. Rabinowitch: *The Chemistry of Uranium.* National Nuclear Energy Series (1951) Div. VIII, Vol. 5. New York. McGraw-Hill Book Co.

[2] K. Mendelssohn and H. M. Rosenberg: *Proc.* Physical Soc. (1952) **65**, 390A, p. 388.

[3] W. W. Tyler and A. C. Wilson, Jr.: *Physical Review* (1953) **89**, p. 870.

[4] G. Borelius: *Handbuch der Metallphysik* (1935) Vol. 1, pp. 181-485. Leipzig. Akad. Verlags. Gesellschaft.

[5] R. E. B. Makinson: *Proc.* Cambridge Philosophical Soc. (1938) **34**, p. 474.

[6] H. Ebert and A. Schulze: *Ztsch. Metallkunde* (1947) **38**, p. 46.

Age Softening of Beta Brass

by Harry Green and Norman Brown

The effect of quenching temperature and of aging temperature and time on compression stress-strain curves of β brass was investigated. Age softening occurs at a rate which decreases with decrease of quenching temperature below the critical temperature for ordering. The activation energy for softening is 15,400 cal per mol.

NO matter how rapidly β brass is quenched or what the temperature from which it is quenched, practically complete order is obtained at room temperature. It has been demonstrated that with respect to the specific heat,[1,2] electrical resistivity,[3] X-ray diffraction,[4] and microstructure, the slowly cooled and rapidly quenched specimens are the same and that complete long range order exists in both cases. However, Smith[5] showed that the hardness of β brass depended upon the cooling rate and the temperature from which β brass is quenched. Smith showed that the hardness was a maximum for specimens quenched from about 445°C and that the as-quenched structure softened at room temperature at a rate depending upon the temperature prior to quenching. This softening after quenching is in this paper referred to as age softening.

The results of this investigation are qualitatively the same as the findings of Smith. However, a more detailed analysis of these phenomena has been possible since the stress-strain curve offers a more sensitive index of the state of the metal than hardness. It is the purpose of this paper to show how the mechanical properties are related to the ordering of β brass.

A 200-lb ingot made from electrolytic copper and electrolytic zinc was extruded to ½-in. rod. Chemical analyses at frequent intervals along the rod showed that the alloy contained 51.5 pct Cu with the greatest impurity being iron, at 0.01 to 0.001 pct. To obtain a constant test material, the ½-in. extruded rod was warm-rolled to ⅜ in. diameter at 200°C and then recrystallized to a grain size of 2.0 mm.

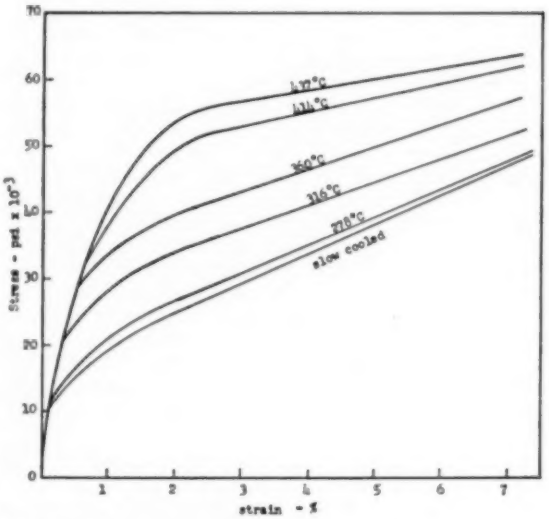

Fig. 1—Typical stress-strain curves showing effect of quenching temperature.

The specimens for the compression test were ⅜ in. high and ⅜ in. in diameter. The specimen ends were polished on 600 metallographic paper and coated with Molykote for a lubricant. The compression rig consisted of an anvil resting on the machined table of the Baldwin Southwark testing machine and a plunger fixed to the movable cross

H. GREEN is Metallurgist, Horizons Inc., Cleveland, and N. BROWN is Assistant Professor of Metallurgy, Towne Scientific School, University of Pennsylvania, Philadelphia.

Discussion on this paper, TP 3627E, may be sent, 2 copies, to AIME by Dec. 1, 1953. Manuscript, April 15, 1953. Cleveland Meeting, October 1953.

This paper is based on a thesis by H. Green submitted in partial fulfillment of requirements for a M. S. degree to the Graduate School, University of Pennsylvania.

head. For strains up to 7 pct, practically no barreling was observed.

The rate of strain for all tests was about 0.01 in. per in. per min. The change in length of the specimen was recorded automatically with the load upon a drum recorder. The change in length was indicated by a microformer unit placed along side the specimen under the cross head.

Experimental Results

All specimens were originally slowly cooled from 500°C to room temperature, putting them in a standard state of complete order. They were then reheated to various temperatures up to 500°C, and held 15 min at temperature prior to quenching in water. In order to determine whether equilibrium was achieved prior to quenching, a series of specimens were reheated to 500°C, rapidly cooled to a lower temperature, and then after 15 min water-quenched to room temperature. These different methods of approaching the quenching temperature had no effect upon the resulting mechanical properties.

Typical stress-strain curves for the states immediately after quenching are given in Fig. 1. Those states that exhibited higher flow stresses at low strains also work hardened at a slower rate so that all flow curves tend to converge at large strains.

The way in which the flow stress and the rate of work hardening depend on the quenching temperature is given in Fig. 2. The structure prior to quenching was shown to be at equilibrium with

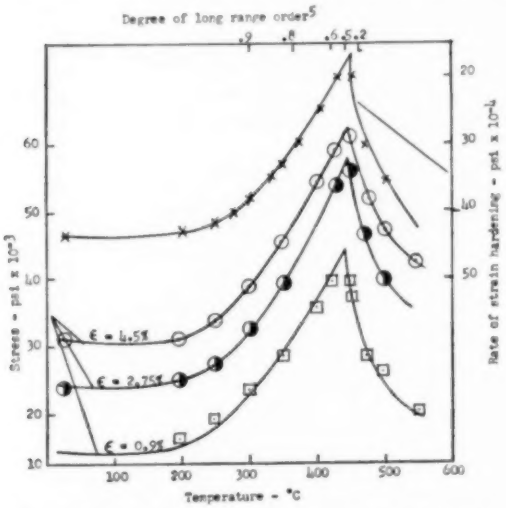

Fig. 2—Flow stress and rate of strain hardening vs quenching temperature.

respect to the resulting mechanical properties. Thus, the prequenched structure as represented by the degree of long range order prior to quenching has also been plotted along with the quenching temperature, Fig. 2. The data for the degree of order as a function of temperature was taken from the X-ray investigation by Warren and Chipman.[4] The maximum in the flow stress occurs when about 0.5 order existed prior to quenching. When the rate of work hardening as measured by the linear portion of the stress-strain curve is plotted against quenching temperature, the curve has a minimum at the same degree of order that the flow stress is at a maximum, Fig. 2. This behavior correlates with the rates of recovery to be presented later.

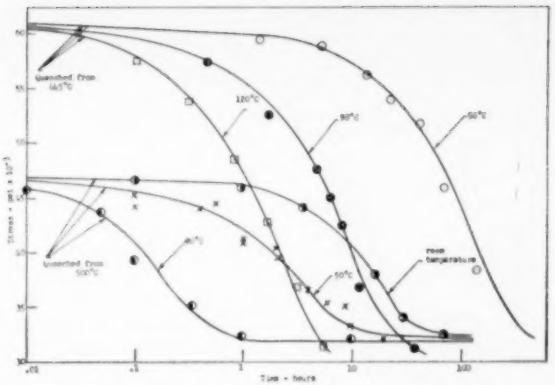

Fig. 3—Flow stress at 4.5 pct strain as a function of time at various aging temperatures for indicated quenching temperatures.

The as-quenched structure is unstable in the vicinity of room temperature and changes with time. The strength of all states decreases to the value characteristic of specimens slowly cooled to room temperature. This phenomenon will be called age softening. The way in which the age softening depends on time, aging temperature, and the temperature prior to quenching is shown in Fig. 3. The rate of softening as a function of the aging temperature was investigated by plotting the logarithm of the time against the reciprocal of the absolute temperature at which a given degree of softening was produced, Fig. 4. The slope of the resulting straight line was independent of the degree of softening and indicates that the age-softening phenomenon is a thermally activated process. An activation energy of 15,400 cal per mol is indicated by the slope of the straight line. This activation energy was found to be independent of

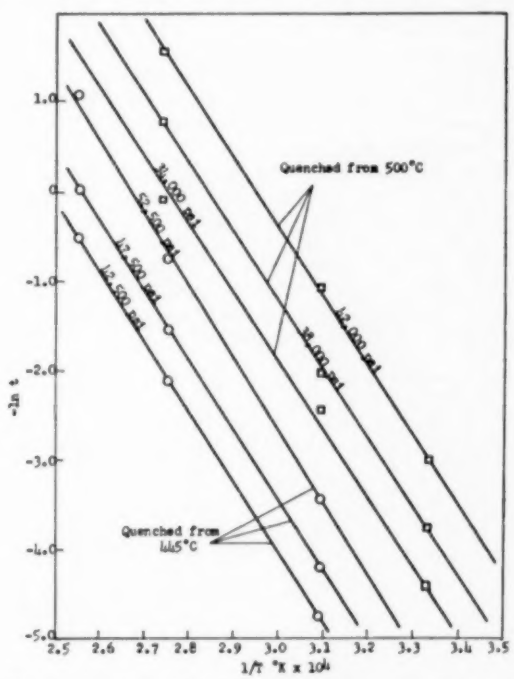

Fig. 4—Curves for determining activation energy for age softening.

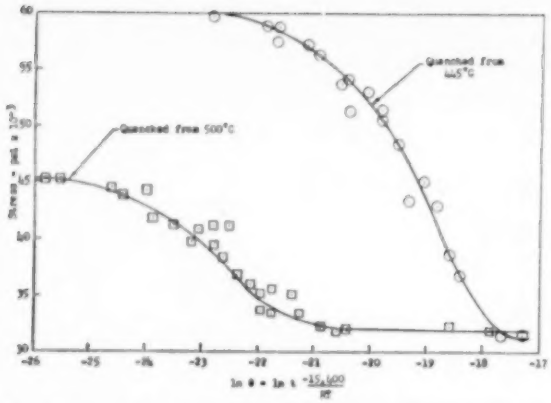

Fig. 5—Composite effect of time in hours and temperature in °K on aging of β brass quenched from indicated temperatures.

the temperature prior to quenching. The softening process is better described by using a temperature-modified time as shown in Fig. 5.

It was observed that the softening process following quenching displayed the following general characteristics:

1—The equilibrium value of the stress was the same for all quenching temperatures.

2—All curves had a delay time or incubation period before the softening was measurable.

3—The greater the delay time, the slower the rate of softening.

4—The softening curves were identical for specimens quenched from varied temperatures above the critical temperature of ordering.

5—For quenching temperatures below the critical temperature the rate of softening decreased as the quenching temperature decreased. These observations are based on Fig. 6, representing quenching temperatures ranging from 500° to 300°C. The aging temperatures ranged from 25° to 120°C and were chosen so that the aging times could be accurately measured and were not inconveniently long. Because it appeared to be more significant, the percentage of change in stress between the as-quenched and equilibrium state was plotted against the temperature-modified time.

It is to be noted that for quenching temperatures above 464°C, the critical temperature, the softening curves are identical. For a quenching temperature of 460°C, the rate of softening decreases abruptly and at the same time there is a pronounced scatter in the data. This scatter is significant because it means that in the range of temperature immediately below the critical it is difficult to reproduce the same structure. This is attributed to the fact that the degree of long range order changes very rapidly just below the critical temperature, and thus, very small differences in temperature produce very large differences in the degree of order. Similarly, since the critical temperature depends on composition, small differences in composition will produce large differences in the degree of order even if the difference between the quenching temperature was exceedingly small.

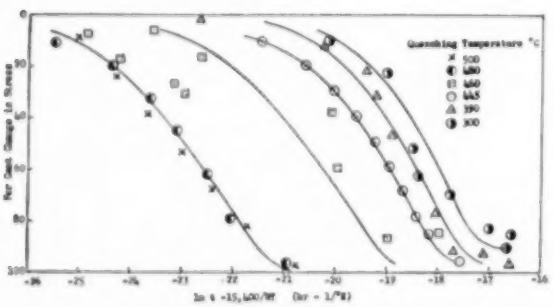

Fig. 6—The effect of quenching temperature on the age softening process. The aging temperatures ranged from 25° to 120°C.

As the quenching temperature is further decreased below the critical, the excessive scatter disappears, and the rate of softening decreases uniformly. Within the limits of the experimental error, all the curves in Fig. 6 have the same shape and the essential difference is based on their relative displacements along the time axis. This means that all the curves may be represented by a single empirical equation of the form

$$\frac{\sigma_i - \sigma_t}{\sigma_i - \sigma_E} = F(\ln t - 15{,}400/RT + \ln K) \qquad [1]$$

where σ_i is the initial stress; σ_E, equilibrium stress; σ_t, the instantaneous stress; t, the time; T, the absolute temperature; R, the gas constant; $\ln K$ = the relative displacement of the curves along the time axis in Fig. 6; and F is a function describing the shape of the curve. The value of K is a measure of the relative rates of age softening and is also a measure of the relative lengths of the delay times before any softening is measurable.

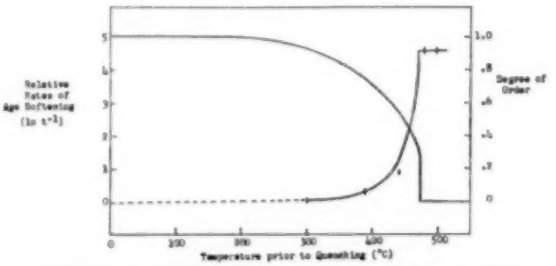

Fig. 7—Rate of age softening and degree of order prior to quenching as related to the quenching temperature.

The relationship between K and the quenching temperature is given in Fig. 7 where it is demon-

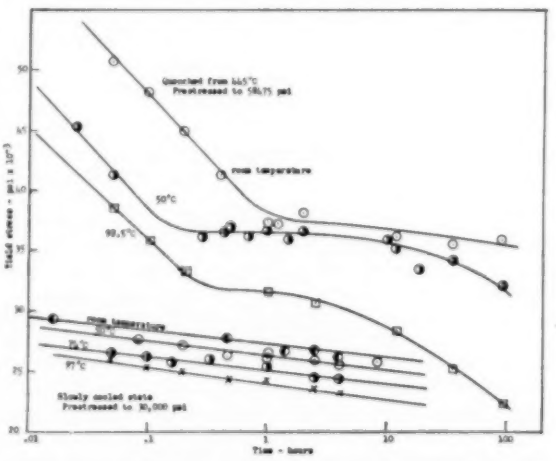

Fig. 8—Change in yield stress with time after prestraining. The recovery temperatures are indicated.

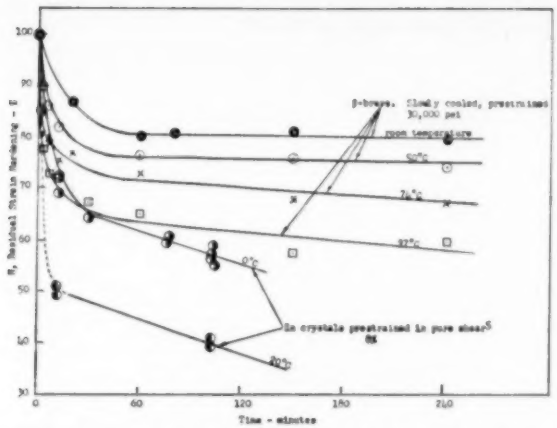

Fig. 9—Recovery of strain hardening as a function of time at various temperatures for slowly cooled β brass and for zinc crystals.[5]

strated that the rate of softening is constant down to the critical temperature, decreases sharply just below the critical temperature, and then appears to approach an equilibrium value. The functional relationship between the rate of age softening and the quenching temperature bears a strong resemblance to the functional relationship between the degree of long range order* prior to quenching and the quenching temperature, Fig. 7. The scatter in the data for the 460° quench is readily appreciated in the light of Fig. 7. The K values are such that a specimen quenched from above the critical softens about 200 times faster than one quenched from 300°C where the degree of order prior to quenching is about 0.92.

* The degree of order as a function of temperature was measured by Warren and Chipman[4] by means of a high temperature X-ray method.

The age-softening process was further investigated by giving the specimens a deformation prior to age softening. In order to determine the recovery effect without the presence of age softening, slowly cooled specimens were also used. The rate of softening after prior deformation is shown in Fig. 8. The recovery curves for the slowly cooled specimens have a different shape than those obtained from specimens quenched from 445°C. The slowly cooled specimens exhibit a recovery curve which is similar to the recovery of zinc[5] as shown in Fig. 9. In the case of the slowly cooled specimens, an activation energy of the recovery process was determined by plotting ln t against the reciprocal of the recovery temperature for a given degree of recovery. The slope of the straight line obtained in Fig. 10 corresponds to an activation of about 20,000 cal per mol for the recovery process. It should be pointed out that recovery of the strained β brass presumably involves a reordering of the lattice disordered by strain as well as the phenomena ordinarily associated with "recovery."

When the same procedure was used to obtain an activation energy for the recovery of specimens quenched from 445°C, a linear relationship was not obtained between ln t and the reciprocal of the recovery temperature as shown in Fig. 11. This is attributed to the age-softening process having a delay time whereas the maximum rate of recovery occurs at zero time. Thus age softening and recovery presumably are different processes.

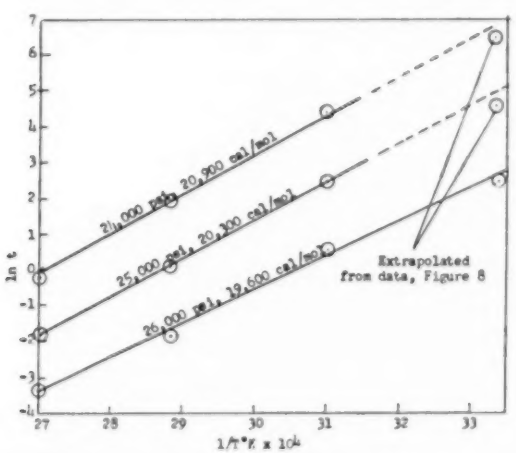

Fig. 10—Determination of activation energy for recovery after prestraining slowly cooled β brass.

Discussion

Although studies of the specific heat,[1,2] microstructure,[3] electrical resistivity, and X-ray diffraction showed no difference among specimens in the different mechanical states, some type of boundaries or crystal imperfections must be responsible for the variations in the mechanical properties. In accordance with current views by Barrett,[6] Smith,[8] and Cottrell[7] it is postulated that the difference in mechanical properties is caused by various configurations of the out-of-phase domains.

Warren and Chipman[4] attempted to determine whether there was any difference between a slowly cooled specimen and one quenched from 500°C. They decided that there was no difference with respect to out-of-phase domains, but their results are not conclusive because they polished and etched the specimen after quenching and they do not state what time elapsed between the quench and the X-ray examination. From the age-softening curves of Fig. 3, it is readily apparent that after such a history the specimen could have age-softened almost completely before the X-ray examination was made.

During the quench, the centers of short range

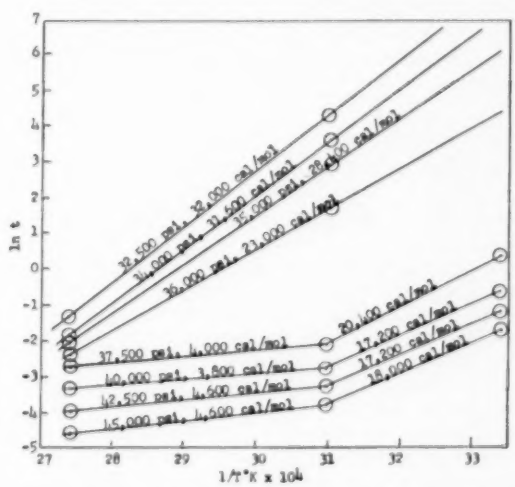

Fig. 11—Same as Fig. 10 except specimens were quenched from 445°C.

order nucleate the domains of long range order. If these domains are nucleated independently, then the superlattice sites occupied by the copper atoms in one domain will not always be the same sites occupied by copper atoms in the adjoining domains. This gives rise to out-of-phase domains in each of which complete long range order exists. During the age-softening process, these domains grow to a size limited by the grain boundaries. In the light of the low activation energy for age softening it is not surprising that β brass orders so rapidly. The observed value for age softening agrees closely with the activation energy for diffusion of 17,600 cal per mol.[8]

If the age-softening process is one of out-of-phase domain growth then some relationship must exist between the size of the domain and the percentage of change in stress. Although this relationship is not known, a general function may be assumed. Thus, Eq. 1 transforms to

$$\frac{dD}{dt} = g(D)\, Ke^{-Q/RT} \qquad [2]$$

where D is the domain size; g, the function of domain size; and Q, the activation energy. In general a growth process such as grain growth may be represented by

$$\frac{dD}{dt} = N \times M \qquad [3]$$

where N is a function related to the number of domains and M is a function of the rate of boundary migration. If the interfacial energy of the boundaries do not vary with domain size, then it may be assumed that M is independent of the quenching temperature. The differences in the rates of growth are attributed to differences in N. Therefore Eqs. 2 and 3 give the result that

$$K = N \qquad [4]$$

In Fig. 7 it is indicated that K depends upon the degree of order prior to quenching. This means that the degree of order prior to quenching determines the number of out-of-phase domains formed immediately after quenching. The relationship between K and the degree of order prior to quenching is given by the empirical equation

$$\ln K = 5.6(1 - S) \qquad [5]$$

where S is the degree of order prior to quenching. For all states the rate of age softening may be described by

$$\frac{d\left(\frac{\sigma_i - \sigma}{\sigma_i - \sigma_E}\right)}{dt} = H\left(\frac{\sigma_i - \sigma}{\sigma_i - \sigma_E}\right) e^{-15,400/RT}\, e^{5.6(1-S)} \qquad [6]$$

where H is a function related to the shape of the age-softening curve.

The nature of the interaction between the out-of-phase domain boundaries and dislocations is not certain. This effect is quite large as evidenced by the flow stress at 0.9 pct strain in the specimen quenched from 445°C, which is about three times the flow stress for the slowly cooled specimens. It is proposed that the density of trapped vacant lattice sites may be the cause. The aging process would then consist of the migration of vacancies to dislocations. This process would increase the length of dislocations and at the same time tend to remove jogs in the dislocations loop. It would be expected that such a process would produce a decrease in density during age softening. Since such a change in density is expected to be very small, the change in density is difficult to measure. A method has been devised using an electrical strain gage which detects changes in density on the order of 10^{-6}. An SR-4 strain gage was cemented on a specimen quenched from 445°C and the compensating gage was cemented in identical fashion on a slowly cooled specimen. The gages were balanced with an SR-4 type K strain indicator. After aging for two weeks at room temperature about a 10^{-4} change in strain was measured. Any drift in the indicator was minimized by using it only for the short time necessary to take a reading. The correlation between this density change and the change in mechanical properties is not definite because the rates are not the same. The change in density is slower and extends over a somewhat longer period of time. Further studies are being made of this density change. The presence of a large concentration of vacancies is consistent with the observation of a large Kirkendall effect in β brass.

Conclusions

1—The stress-strain curve of β brass depends on the temperature from which it is quenched. The greater the flow stress observed, the less is the rate of work hardening.

2—When about 50 pct order exists prior to quenching, a maximum in flow stress is obtained in the as-quenched state.

3—The as-quenched state is unstable and age-softens by a thermally activated process governed by an activation energy of 15,400 cal per mol.

4—The rate of age softening varies inversely with the degree of long range order existing prior to the quench.

5—Slowly cooled specimens of β brass recover after prior deformation with an activation energy of about 20,000 cal per mol.

Acknowledgment

The authors acknowledge the assistance of Marvin Herman throughout the work. The research was initiated by R. M. Brick who contributed greatly by his continued interest and discussions. The original ingot was made at Frankford Arsenal. The extrusion was done through the courtesy of the Bridgeport Brass Co. The research was supported by the Office of Ordnance Research, U. S. Army, under contract DA-36-034-ORD491.

References

[1] C. Sykes and H. Wilkinson: The Transformation in the Beta Brasses. *Journal* Inst. Metals (1937) **61**, p. 223.

[2] C. S. Smith: A Simple Method of Thermal Analysis. *Trans.* AIME (1940) **137**, p. 236.

[3] C. S. Smith: Hardness Changes Accompanying Ordering of Beta Brass. *Trans.* AIME (1943) **152**, p. 144.

[4] D. Chipman and C. Warren: X-ray Measurements of Long Range Order in Beta Brass. *Journal of Applied Physics* (1950) **21**, p. 696.

[5] R. Drouard, J. Washburn, and E. Parker: Recovery in Single Crystals of Zinc. This issue, p. 1226.

[6] C. S. Barrett: *Structure of Metals.* Second Edition (1952) p. 292. New York. McGraw-Hill Book Co.

[7] A. H. Cottrell: *Theoretical Structural Metallurgy* (1948) p. 222. London. Longmans, Green and Co.

[8] U. S. Lendergren and R. F. Mehl: Rates of Diffusion and Marker Movements in Beta Brass. JOURNAL OF METALS (February 1953) p. 153.

Plastic Deformation of Iron Between 300° and 77.2°K

by Donald F. Gibbons

THIS investigation was undertaken in order to gain further information on the mechanism of plastic deformation of iron at temperatures between room temperature and 77.2°K, and also to contribute to our understanding of the low temperature brittleness phenomenon that occurs in both the tensile and impact tests. It was decided to study as pure an iron as possible and to use the tensile test in order to simplify the problem as much as possible.

Two series of iron were used throughout the investigation: iron A, obtained from the National Research Corp. and supplied as gas-free, high purity iron; and iron B, obtained from Fast[1] and produced by melting iron under purified hydrogen. Typical analyses of samples of both irons, after fabrication, are given in Table I.

The main difference in composition of these irons is in their nickel and oxygen contents. Nickel has a very large solid solubility in iron. However, oxygen has an extremely small solid solubility. An attempt was made to reduce the oxygen content still further by remelting under purified hydrogen. This was successful in reducing the oxygen content to ~0.0006 pct. However, no results on tests of this iron are included, since difficulty was encountered in fabricating the ingot.

Wire specimens 1 mm in diameter were used for the investigation. The wires were produced from the ingots, as supplied, by cold rolling and swaging, with intermediate vacuum anneals at 700°C. Care was taken to reduce preferred orientation in the wires to a minimum by keeping the percentage of reduction in area between anneals of 30 to 40 pct. X-ray transmission photographs showed no indication of preferred orientation. The final grain size of iron A was 20 to 24 grains per linear mm and of iron B, 16 to 18 grains per linear mm.

All specimens were tested in the decarburized and denitrided condition unless otherwise stated. The procedure was to pass hydrogen, saturated with water vapor at 26°C, over the specimens at 730°C for 2 hr. The specimens were quenched in iced water and then annealed in a vacuum of ~ 5×10^{-4} mm Hg for one day at 560°C to remove hydrogen. Higher temperatures were used for the vacuum anneal but this temperature was found to be quite satisfactory in removing hydrogen. The specimens were slow-cooled after the vacuum anneal. Where it is stated that the specimens were carburized, the specimens were given an identical decarburizing treatment and then carburized by passing hydrogen, saturated with pure n-heptane vapor at 0°C, over the specimens at 730°C. The specimens were then homogenized at 730°C for 2 hr in dry hydrogen. After the carburizing treatment the specimens were given the same vacuum anneal as for the decarburized specimens. The carbon content was determined from the maximum value of the internal friction carbon peak.[2]

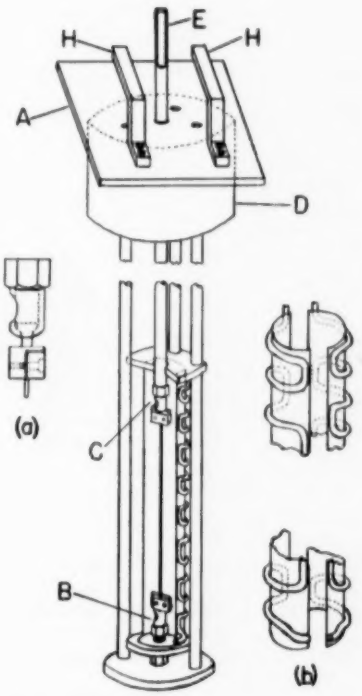

Fig. 1—Arrangement of the tensile apparatus and cooling coil for the low temperature tests.

Apparatus

Fig. 1 shows a diagram of the tensile apparatus, with half the cooling coil removed. The cooling coil enabled temperatures from 200° to 77.2°K to be obtained. The apparatus was designed to fit a standard Tinius Olsen Universal tensile machine.

The apparatus consisted of the rigid plate *A* which carried two carefully machined hooks *H*. These hooks attached the plate firmly to the moving crosshead of the tensile machine. The lower grip *B* was rigidly suspended from the plate *A* by three stainless steel rods. The upper grip *C* was joined to the upper grip of the tensile machine by the stainless steel rod *E*. The lower part of the apparatus was surrounded by a Dewar vessel, which was made a sliding fit inside the brass collar *D*. The specimen was held in a clamp which fitted into the grip, forming a ball and socket joint (see inset a). This was to attain as nearly pure

D. F. GIBBONS, Junior Member AIME, formerly the University of Chicago, is now Research Associate, Physics Dept., Royal Military College, Kingston, Ont., Canada.

Discussion on this paper, TP 3585E, may be sent, 2 copies, to AIME by Dec. 1, 1953. Manuscript, March 2, 1953; revision, May 19, 1953. Cleveland Meeting, October 1953.

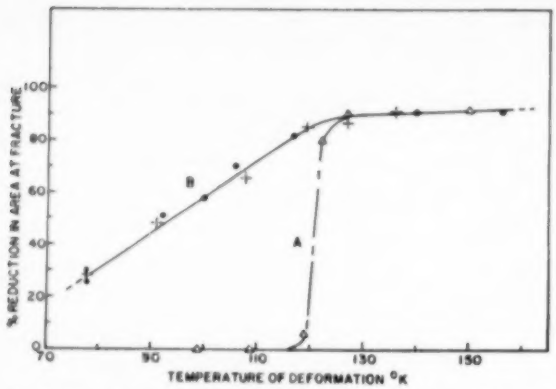

Fig. 2—Variation of the percentage of reduction in area at fracture with temperature of test.
Curve *A*—For specimens of iron A. Curve *B*—For specimens of iron B.

tension in the specimen as possible. The stress was applied to the specimen by lowering the crosshead, and so the lower grip *B*, at a constant speed of 0.05 in. per min.

The temperature of the specimen was controlled by the coil assembly shown in inset b. This was a split brass cylinder onto which ⅛ in. ID copper tube was soldered as shown. Cold evaporated nitrogen gas was passed through the assembly by immersing one end of the tube (this section of the tube was lagged) in liquid nitrogen. The other end of the coil was joined to the laboratory vacuum line by a Hooke valve. By setting this valve, the rate of gas flow and therefore the temperature could be controlled manually to within ±½°K with ease.

The temperature gradient along the specimen was checked by placing a dummy specimen in position, which had copper-constantan thermocouples soldered to it at 1-in. intervals. The gradient along the specimen was found to be 3°K with a maximum deviation from the mean of 1.75°K. This was regarded as being satisfactory for this investigation.

Experimental Results

Ductility: As the testing temperature of iron A specimens was decreased, the ductility, as measured by the percentage of reduction in area of fracture, remained nearly constant, until between 127° and 119°K it suddenly dropped to zero. Curve A, Fig. 2 shows the plot of the percentage of reduction of area vs testing temperature in this temperature range. Direct observation of the fractured surface on a specimen deformed below 124°K showed apparently a wholly cleavage type of fracture. However, if a longitudinal section was taken through the fracture, grain boundary failure as well as the cleavage failure could be seen. Fig. 3a shows the region adjoining a fractured surface in which fracture also started, it can be seen to follow the grain boundary. Fig. 3b shows a section through a fracture, which was nickel plated before sectioning, the intercrystalline as well as cleavage nature of the fracture can be seen clearly. This sudden onset of brittleness also occurred if the specimens were quenched from 700°C after the vacuum anneal instead of being slowly cooled.

As the testing temperature of iron B specimens was decreased there was no sudden loss in ductility corresponding to that in specimens of iron A. However, at approximately the same temperature the ductility started to decrease steadily. Curve B, Fig. 2 shows a plot of the percentage of reduction in area vs temperature of deformation for iron B.

Neumann Lamellae: Below 125°K the stress-strain curve became serrated and the deformation in this serrated region was accompanied by a series of characteristic "sharp" sounds, similar to a sharp rifle "crack." Curves a, b, and c of Fig. 4 show typical stress-strain curves in this temperature region. Metallographic examination of specimens after deformation revealed that below 125°K decreasing the temperature of deformation increased the number of Neumann lamellae. The end of the serrated region of the stress-strain curve was found to coincide with the cessation of the characteristic sound of deformation and there was no discernible increase in the number of Neumann lamellae present in the specimen after the end of the serrated region of the stress-strain curve.

The rate of work hardening of a specimen was affected quite markedly by the temperature of deformation below 125°K. Fig. 4, curves a, b, and c, shows stress-strain curves for specimens deformed at 77.2°, 96.5°, and 124°K, respectively. It can be seen that the lower the deformation temperature, and so the greater the amount of deformation occurring by the formation of Neumann lamellae, the greater is the rate of work hardening. It can also be seen from these curves that there is a change in the rate of work hardening coincident with the end of the serrated region. This change is more marked the lower the deformation temperature.

Fig. 5 shows a plot of yield stress, as defined by a 0.1 pct proof stress, vs temperature of deformation. The curve shows a definite approach to a constant value of the yield stress below 120°K.

If iron A was carburized to a value as little as 0.004 pct C, it no longer exhibited the sudden loss of ductility at 125°K. The curve of the percentage of reduction in area vs temperature of deformation followed that for iron B (curve B, Fig. 2). The curve for lower yield stress vs temperature of deformation was of the same form as for iron B. However, the curve was displaced along the stress axis toward higher stress due to the carbon content. The

Table I. Analyses of Iron Used

Iron	Analysis, Wt Pct											
	Al	Cu	Mg	Ni	Si	Ag	Mn	Co	Be	C	N	O
A	0.001	0.001	—	0.05*	0.008	—	0.001	—	—	0.005	0.0005†	0.021†
B	0.005	0.0008	0.0005	0.002	0.005	N.D.	N.D.	N.D.	N.D.	0.002	0.0005†	0.0034†

* Wet analysis.
† Vacuum fusion analysis. All other determinations spectrographic.
N.D. Not determined.
These analyses were made on specimens as tested, after all heat treatments were carried out.

Fig. 3a—Area near fracture in specimen of iron A tested at 105°K. X60. Area reduced approximately 60 pct for reproduction.

Fig. 3b—Section through fracture in specimen of iron A tested at 109°K. X200. Area reduced approximately 60 pct for reproduction.

removal of the sudden loss in ductility by carburizing occurred whether the carbon was retained in solid solution by quenching from 730°C, or precipitated as carbide, as determined by the disappearance of the carbon internal friction peak.

Lüders Bands: After complete decarburization a small yield point and yield point elongation could still be observed in specimens of both iron A and B tested at temperatures above 125°K, see Fig. 4 curve d for iron B. However, the yield point elongation was small, only ~ 1 pct, as compared with the carburized specimens which had a yield point elongation of 7 to 8 pct in this temperature range. This small yield point is attributed to oxygen in solid solution and confirms the observations of Boulanger.[5] Boulanger[4] has since shown the existence of an internal friction peak in iron due to oxygen which would also indicate that this yield point is due to oxygen in solid solution. No Lüders bands were detected in these specimens.

In specimens of iron A carburized to 0.006 pct C, the Lüders bands were very pronounced. Examination of specimens deformed above 125°K showed that a Lüders band was always initiated at each grip, the boundary between the deformed and undeformed regions being propagated toward the center of the specimen. However, during deformation below 125°K (the temperature for the onset of Neumann lamellae formation) the number of Lüders bands formed increased. Many Lüders bands were formed along the length of the specimen, in addition to those initiating at each grip. The stress-strain curve during the yield point elongation was also serrated, as was the case in the initial part of the stress-strain curves of iron B tested in this temperature range.

All the Neumann lamellae were found to be produced during the yield point elongation; there was no change in the number of Neumann lamellae present in specimens whose deformation was stopped at the end of the yield point elongation and those which were deformed until fracture occurred. Secondary evidence to support this conclusion is that the characteristic sound accompanying Neumann lamellae formation also ceased at the end of the yield point elongation.

Below 125°K the magnitude of the yield point elongation of carburized wires was found to decrease with decreasing temperature of deformation. The percentage of yield point elongation vs temperature of deformation is shown in Fig. 6. The form of this curve is similar to that of Fig. 2 (curve B) where the percentage of reduction in area vs temperature of deformation is plotted.

The yield point and yield point elongation occurring in decarburized specimens of iron B when tested above 125°K was completely removed when the specimens were tested below this temperature. This is illustrated by the stress-strain curves of Fig. 4.

Deformation of Single Crystals: A number of single crystals, 3 to 4 cm long, were grown in specimens of iron A by the strain-anneal method. The specimens tested, therefore, consisted of a number of single crystals in a "bamboo" type structure. In some cases the single crystals were separated by a large grained polycrystalline region approximately ½ cm in length.

After a standard decarburizing treatment the single crystals were found to be quite ductile down

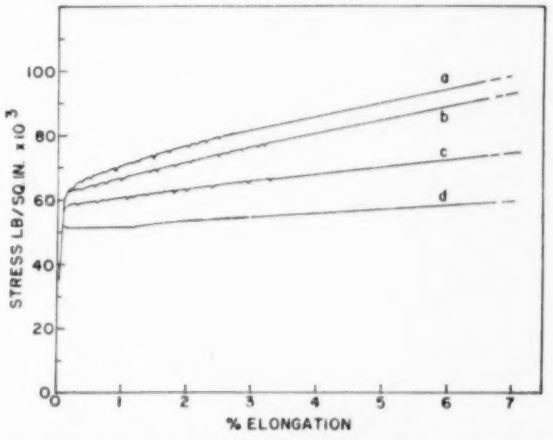

Fig. 4—True stress-strain curves for specimens of iron B tested as follows: *a*—77.2°K, *b*—96.5°K, *c*—124°K, *d*—150°K.

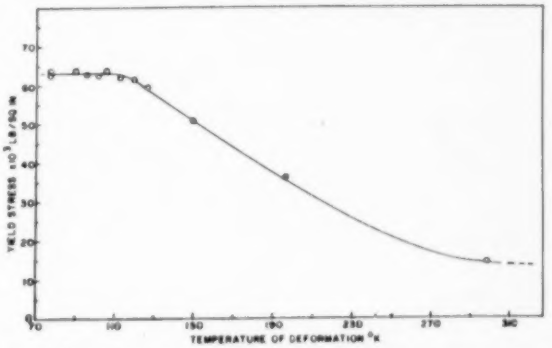

Fig. 5—Variation of yield stress with temperature of deformation for iron B.

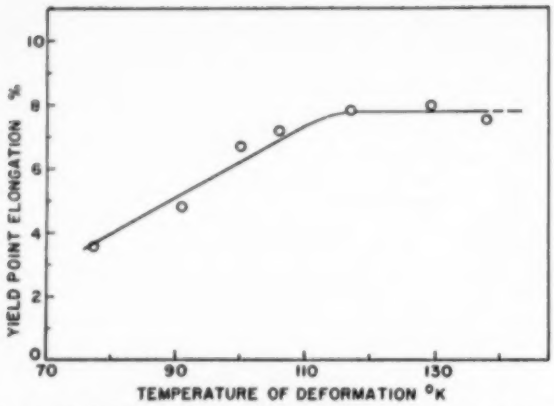

Fig. 6—Variation of percentage of yield point elongation with temperature of deformation for carburized specimens of iron A.

to 77.2°K and the stress-strain curve showed no evidence of a yield point. The fracture was a typical, single-crystal wedge-type fracture, the percentage of reduction in area at the fracture being ~ 95 pct. The stress-strain curve was serrated and the characteristic sound was emitted during the early stages of the deformation, as was the case in the polycrystalline specimens of iron B. Fig. 7 is a longitudinal section through a single crystal after deformation showing the Neumann lamellae.

Crystallographic Relations of the Neumann Lamellae: The orientation and crystallographic relationship of Neumann lamellae has been studied in silicon ferrite by Harnecker and Rassow[5] and Mathewson and Edmunds[6] by microscopic and X-ray reflection methods, respectively. However, it was felt that their evidence was inconclusive.

The crystallographic plane and direction of shear of the lamellae was determined from single-crystal wires and found to be the {112} ± ½° and <111> ± 4°, respectively. A technique similar to that used by Bowles,[7] to determine the crystallographic relationship of martensite, was used to determine the angle of shear and decide if the lamellae were twins. The angle was found to coincide within ± 3°, the angle predicted by twinning theory.*

* After this work was completed, Paxton[8] reported on a similar analysis which agrees with results given here.

Effect of Prior Deformation at Room Temperature: A specimen of iron B was elongated by 4 pct at 300°K and then tested immediately at 109°K. The stress-strain curve was quite smooth with no serrations and the noise during deformation was absent. A micrograph of such a specimen showed complete absence of Neumann lamellae. This phenomenon has been observed previously by Pfeil.[9] After annealing such a specimen for several days at room temperature, no Neumann lamellae were produced on deformation below 125°K. However, if the specimen was annealed at 100°C for 14 hr, after 4 pct elongation at 300°K, and then tested below 125°K, the Neumann lamellae formation partially returned. The serrations on the stress-strain curve and noise during deformation also returned.

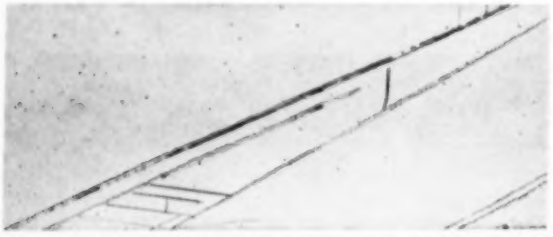

Fig. 7—Micrograph of Newmann lamellae in a single crystal of iron A tested at 77.2°K. X60. Area reduced approximately 60 pct for reproduction.

A specimen of iron A was deformed at 300°K prior to testing at 109°K and the specimen exhibited some ductility ~ 45 pct, as measured by the percentage of reduction in area at the fracture. As in the case of iron B there was no evidence of Neumann lamellae formation.

Discussion

In iron A, which exhibits the sudden onset of brittleness, fracture occurs by rupture, at least in part, along the grain boundaries. It has also been shown that a single crystal is completely ductile. It is evident, therefore, that the brittleness is intimately associated with the grain boundaries. As the two series of iron used only differ in their oxygen content, it seems justifiable to correlate the removal of this low temperature brittleness, in iron B, with the decrease in oxygen content. This agrees with the recent work of Rees and Hopkins[10] who found that intercrystalline failure started to occur if the oxygen concentration was greater than ~0.003 pct. This leads to the conclusion that the oxygen must be associated with the grain boundaries and in some manner cause failure along these boundaries. One question to be decided, therefore, is whether the oxygen at the grain boundary is in solid solution or present as a second phase.

The most recent value for the solid solubility of oxygen in α iron at 700°C is given as ~ 0.01 pct by Ziegler.[11] This value may be expected to be an over estimate, however, because it was near the limit of accuracy of his experimental procedure. This value for the oxygen solubility indicates that the oxygen concentration in iron B is below and that in iron A above the solubility limit. Oxygen may be expected to be present at the grain boundary as an oxide phase, therefore, in iron A.

Examination of metallographic specimens by the light or electron microscope showed no evidence of the existence of a second phase at the grain boundary. This, however, cannot be regarded as positive evidence that it was not present. An examination under the microscope of the fractured surfaces with polarized light, showed regions, on exposed grain boundaries, which exhibited bi-refrigence. These regions showed extinction at 90° intervals, which would correspond to Fe_2O_3.[12] However, since it was impossible to view a relatively large flat field, this extinction could have been spurious and due to geometric factors.

Positive evidence of a difference in the grain boundary behavior between the two irons was, however, given by internal friction measurements. The internal friction of the wires was determined using the torsion pendulum developed by Kê.[13] Curve A, Fig. 8 shows the grain boundary peak for a specimen of iron A which had been quenched from the decarburizing treatment. Curve B, Fig. 8 shows the peak obtained for iron B after an identical treatment. The temperature at which the maximum of the peak occurs has been shifted from 580°C in iron A to 460°C in iron B, and the magnitude of the peak lowered in the case of iron B. Due to the difference in grain size of the two irons, a small difference

in the temperature at which the maximum of the peak occurs would be expected.[14] However, this change should only be ~ 20° to 30°C and in the opposite direction to that in which it occurred.

The shift in the temperature at which the peak maximum occurs means that the time of relaxation for a shear stress across the grain boundary has been markedly altered. There is no way of calculating whether the shear stress relaxation time for an oxide-iron interface would be greater or less than that for an iron-iron interface; therefore, no quantitative deductions can be made from these internal friction measurements.

If the oxygen is present as an oxide at the grain boundary, there is no reason why the oxide alone should be responsible for the brittleness, because at temperatures down to 125°K the grain boundary has deformed "normally." The sudden onset of brittleness is, however, coincident with the beginning of deformation by twinning. It is suggested, therefore, that the combination of an oxide at the grain boundary and deformation by twinning may be necessary for the brittleness. A possible reason for this may be the rapid rate of formation of the twins, which would involve a rapid rate of deformation at the oxide-iron interface and so permit the formation of "microcracks." Whereas, when deformation occurs by glide there may be sufficient time for the stresses at the interface to be accommodated in the iron matrix. There is some indication that this may be the case, since when twin formation is suppressed by prior deformation at room temperature, specimens of iron A do exhibit some ductility below 120°K.

The mechanism by which carburizing iron A removes the brittleness is uncertain. If an oxide is either directly or indirectly, the cause of brittleness, there would have to be a solid state reaction between carbon and oxygen at the grain boundary at 730°C, the carburizing temperature. Whatever the mechanism, however, it must be reversible, since decarburizing the specimen makes it brittle again.

It has been suggested[15, 16] that, because of the similarity between the atom movements in slip and twinning, it is logical to expect twinning during deformation to occur by a dislocation mechanism also, for the same reasons that they were proposed for slip. Cottrell and Bilby[17] have postulated a dislocation mechanism for the growth of twins during deformation which involves the dissociation of a unit dislocation into two partial dislocations. This mechanism predicts that there should be a constant stress for the onset of twinning, being that stress required to form the initial interface. This has been shown to be the case, see Fig. 5, which shows that below the temperature at which twinning starts the yield stress becomes constant. In the case of one single crystal, which after deformation of about 1 pct exhibited only one active twinning system, it was possible to calculate the lower resolved critical shear stress for twinning, which was 37×10^3 lb per sq in.

The mechanism of Cottrell and Bilby also shows that twins could form in the order of microseconds, which has been shown to be the case experimentally for tin.[18] The serrations on the stress-strain curve and the "sound" during deformation are considered to be caused by bursts of twins forming rapidly within the specimen.

The dislocation mechanism also gives an explanation for prior deformation at room temperature suppressing the formation of twins. During plastic deformation at room temperature many dislocation lines will intersect each other, forming "jogs" in the dislocation line.[19] Also, as is evident from the wavy nature of visible slip lines, dislocations move out of one glide plane into a neighboring plane. Both of these factors inhibit the dissociation of a unit dislocation into partial dislocations. Therefore, the formation of twins, which requires this dissociation into partial dislocations, would be stopped. Annealing for 14 hr at 100°C would allow some recovery to occur and so permit the dislocations to dissociate once more. Since an anneal at 100°C for 14 hr only allows a partial return of twin formation it indicates that the activation energy for the process is much greater than would be expected by an interstitial atom diffusion, such as carbon.

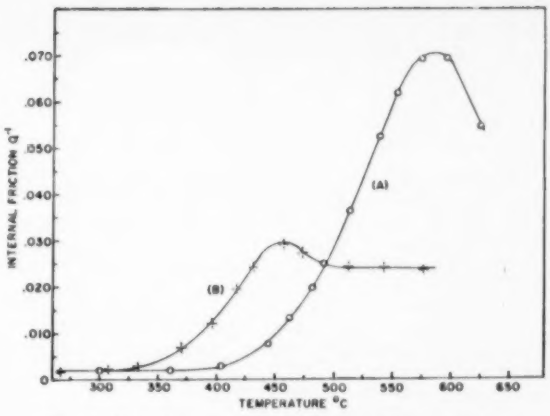

Fig. 8—Variation of internal friction with temperature. Curve *A*—For specimen of iron A. Curve *B*—For specimen of iron B.

Summary

A study was made of the tensile deformation, between 300° and 77.2°K, of two samples of iron, containing 0.0034 and 0.021 pct O, respectively.

Iron containing 0.021 pct O becomes completely brittle below 120°K, the fracture being a combined intercrystalline and cleavage type. Ductility can be restored by carburizing to 0.006 pct C.

Iron containing 0.0034 pct O remained ductile down to 77.2°K; however, the ductility slowly decreases between 125° and 77.2°K. At 125°K deformation starts to occur by the formation of Neumann lamellae, the number of lamellae produced increases with decreasing temperature.

Single crystals of iron containing 0.021 pct O are completely ductile down to 77.2°K.

Internal friction measurements on the grain boundary peak indicate a marked difference between iron containing 0.021 pct O and that containing 0.0034 pct O.

Deformation at 300°K prior to deformation below 125°K suppresses the formation of Neumann lamellae and restores ductility to iron containing 0.021 pct O.

The Neumann lamellae produced by deformation below 125°K are shown to be deformation twins.

It is considered that the brittle failure of iron containing 0.021 pct O is caused by a combination of the grain boundary oxide phase and deformation by twinning. The removal of twin formation by prior deformation can be explained by considering Cottrell and Bilby's mechanism for growth of deformation twins.

Acknowledgments

The author wishes to thank K. K. Ikeuye for pre-

paring the micrographs, E. D. Selmanoff for preparing the wire specimens, and A. Moskowitz for making the vacuum analyses.

References

[1] J. D. Fast: *Philips Research Reports* (1949) **4**, p. 370.
[2] L. J. Dijkstra: *Philips Research Reports* (1947) **2**, p. 357.
[3] C. Boulanger: *Revue de Metallurgie* (1950) **47**, p. 547.
[4] C. Boulanger: Private communication.
[5] K. Harnecker and E. Rassow: *Ztsch. Metallkunde* (1924) **16**, p. 312.
[6] C. H. Mathewson and G. H. Edmunds: *Trans.* AIME (1928) **80**, p. 311.
[7] J. S. Bowles: *Acta Crystalographica* (1951) **4**, p. 162.
[8] H. W. Paxton: *Acta Metallurgica* (1953) **1**, p. 141.
[9] L. B. Pfeil: *Journal* Iron and Steel Inst. (1926) **15**, p. 319.
[10] W. P. Rees and B. E. Hopkins: *Journal* Iron and Steel Inst. (1952) **172**, p. 403.
[11] N. A. Ziegler: *Trans.* Amer. Soc. Steel Treatment (1932) **20**, p. 73.
[12] *Metals Handbook* (1948) p. 449. Cleveland. ASM.
[13] T. S. Kê: *Physical Review* (1947) **71**, p. 533.
[14] T. S. Kê: *Physical Review* (1947) **72**, p. 41.
[15] J. Frenkel and T. Kontorova: *Journal of Physical Chemistry* (1939) **1**, p. 137.
[16] F. Seitz and T. A. Read: *Journal of Applied Physics* (1941) **12**, p. 470.
[17] A. H. Cottrell and B. A. Bilby: *Philosophical Magazine* (1951) **42**, p. 573.
[18] W. P. Mason, H. J. McSkimin, and W. Shockley: *Physical Review* (1948) **73**, p. 1213.
[19] F. Seitz: Advances in Physics. Quarterly Supp. *Philosophical Magazine* (1952) **1**, No. 1.

Technical Note

A Corrected Interpretation of the Mechanism of Growth Of Magnetite During Oxidation

by M. H. Davies, M. T. Simnad, and C. E. Birchenall

THE marker movements observed by Davies, Simnad, and Birchenall[1] during the growth of magnetite on wüstite have been misinterpreted. It is the purpose of this note to correct the original interpretation.

In that investigation wüstite specimens were prepared by oxidizing pure iron disks in water vapor until the iron was consumed. Argon was used as a carrier gas for the water vapor and on the complete conversion of the metal to its oxides ('FeO' plus a small amount (10 pct) of surface Fe_3O_4) the water supply was bypassed and the specimens were annealed in argon alone in order to equilibrate the wüstite with the overlying magnetite.

After cooling, the magnetite was ground off, a crude magnetic test being employed to determine its complete removal. Radioactive silver streaks were then applied to the surface and the specimen was oxidized completely in water vapor to prevent hematite formation. After complete oxidation the markers were found to enclose about 80 pct of the magnetite with the other 20 pct lying outside the markers. This observation was interpreted to mean that oxygen transport was four times as great as iron transport during the growth of the magnetite. The conclusion would have been correct if, as in the case of wüstite growing on iron, all the iron had started from one side of the marker and all the oxygen from the other side initially.

Actually a material balance is required. For simplicity, take wüstite to be exactly FeO, and magnetite to be Fe_3O_4. Then at the start of the reaction

$$3FeO + O \rightarrow Fe_3O_4$$

All of the iron and three-fourths of the oxygen of the final product will be within the marker interfaces. The other fourth of the oxygen is in the gas phase outside the marker.

From the experimentally determined final position of the markers simple calculation shows that one-fifth of the total iron has crossed the marker interface, while one-twentieth of the total oxygen has crossed in the reverse direction. The simplified result favors iron transport in the ratio four to one.

However wüstite is not stoichiometric FeO. At 900°C, the temperature of the measurement, the composition is about $FeO_{1.18}$. When the material balance for the same experimental result is repeated, assuming the product will be 1 mol of Fe_3O_4, it is found that 0.6 gram atoms of iron and 0.19 gram atoms of oxygen must have passed the marker *in the same direction*. (This is readily apparent from the reaction to form 1 mol of Fe_3O_4

$$3FeO_{1.18} \xrightarrow{+O_2} Fe_3O_4$$

The total oxygen supplied from the atmosphere is 0.61 gram atoms, but the iron which passes the marker interface, i.e., 0.6 gram atoms, requires 0.8 gram atoms of oxygen to convert it to Fe_3O_4.)

If all the transport during magnetite growth is due to iron ion diffusion, then the marker would enclose about 85 pct of the final magnetite and the original measurement is in error by about 5 pct. This error is probably less than the uncertainty in locating the markers by autoradiography. The possibility also exists that the starting wüstite was not quite saturated with oxygen and underwent further enrichment with consequent envelopment of the marker before magnetite caught up with the marker interface.

In any case it appears that these measurements actually favor iron ion diffusion in magnetite overwhelmingly as the factor controlling its growth, although further experimental measurements are needed to eliminate the error in material balance described. Such studies are planned.

M. H. DAVIES is Physical Metallurgist, Fulmer Research Inst. Ltd., Stoke Poges, Bucks, England, M. T. SIMNAD, Junior Member AIME, is a Member of Staff, Metals Research Lab., Carnegie Institute of Technology, Pittsburgh, and C. E. BIRCHENALL, Junior Member AIME, is associated with the James Forrestal Research Center, Princeton University, Princeton, N. J.

TN 175E. Manuscript, June 8, 1953.

[1] M. H. Davies, M. T. Simnad, and C. E. Birchenall: *Trans.* AIME (1951) **191**, p. 889; JOURNAL OF METALS (October 1951).

Rate of Propagation of Martensite

by R. F. Bunshah and R. F. Mehl

A fast amplifier technique has been developed for the measurement of the rate of propagation of martensite in an Fe-29.5 pct Ni alloy. The time of formation of one plate of martensite is 3×10^{-7} sec and the rate of propagation is 3300 ft per sec approximately.

IT has been known for some time that the plate-like structural unit of martensite forms from austenite with great rapidity. Wiester[1] and Hanemann, Hofmann, and Wiester[2] took motion-pictures of the transformation as it occurs in a 1.65 pct C steel; they demonstrated that a single plate formed fully in the time interval between successive frames, viz., 1/20 sec, thus setting an upper limit. Förster and Scheil,[3] using an Fe-Ni alloy with 29 pct Ni, recorded the sonic characteristics of the process electrically, upon an oscillograph, setting the upper time limit at 0.002 sec. Förster and Scheil,[4] measuring the change in electrical resistance in the same alloy upon a cardiograph, set a limit of 0.02 sec. Förster and Scheil[5] later, employing the same alloy, improved their technique, reporting an upper limit of 7.10^{-5} sec. In studying signals of such short duration, it is an important question whether the frequency response of the electrical system used is high enough compared to frequency of the pulse measured, or, put differently, whether the system is able to reproduce without distortion the signal arising, in this case, from the formation of a single martensite plate. Förster and Scheil (referring only to their last paper) obtained signals of a frequency of 30 kilocycles (hereinafter kc); this was about the frequency response of the equipment used; thus, if the signal had a frequency higher than 30 kc, it would still appear as a signal of frequency 30 kc. All of these results thus provided upper limits only.

Recent developments in electronics have made available equipment with very high frequency response, very high sweep-speeds, high gain, etc. The electrical characteristics of such equipment, used in the present study, are given in Table I. Such equipment offers obvious attraction in the study of the rate of propagation of a martensite structural unit—and perhaps of other structural alterations proceeding at a very high rate.

This paper reports an attempt to develop a technique employing such equipment to measure the time of propagation of a martensite structural unit and the variation of this with temperature, with the mode of formation—athermal and isothermal—in both polycrystalline and single-crystal samples; and from such measurements to obtain the rate of propagation. As will be seen, the results obtained are useful theoretically.

R. F. BUNSHAH, Junior Member AIME, is Research Associate, Metals Research Laboratory, and R. F. MEHL, Member AIME, is Head of Dept. of Metallurgical Engineering and Director, Metals Research Laboratory, Carnegie Institute of Technology, Pittsburgh.

Discussion on this paper, TP 3604E, may be sent, 2 copies, to AIME by Dec. 1, 1953. Manuscript, April 13, 1953. Cleveland Meeting, October 1953.

This paper is based on a thesis by R. F. Bunshah submitted in partial fulfillment of requirements for the degree of Doctor of Science to Carnegie Institute of Technology, June 1952.

Materials

All data presented here are for an Fe-Ni alloy of the following analysis: 29.5 pct Ni, 0.027 pct C, 0.135 pct Mn, 0.094 pct Si, balance Fe. There were several reasons for choosing this alloy: 1—it is substantially the one used by previous investigators; 2—it exhibits both the athermal[6] and the isothermal[7] mode of formation of martensite, both studied in detail by Machlin and Cohen; 3—the subzero temperatures of transformation in this alloy are experimentally very convenient; 4—it exhibits the "burst phenomenon";[6] 5—the change in electrical resistance upon the formation of martensite, a decrease, is great, approximately 50 pct.[6]

The polycrystalline specimens were in the form of wires of 0.025 in. diameter; the single crystals were $1 \times \frac{1}{4} \times \frac{1}{4}$ in.

Experimental Methods

Electrical Apparatus: Fig. 1 is a schematic drawing of the electrical circuit used. The principle used in these measurements is the same as that used by Förster and Scheil.[5] A small direct current, about 1 to 2 amp, is passed through the sample. When a martensite plate forms, the resistance of the sample changes and a high frequency signal is generated. This signal is picked up by the probes attached to the sample, fed into the bank of amplifiers and thence to the vertical deflection plates of a cathode-ray oscilloscope. The signal itself triggers the oscilloscope trace which flashes across the tube face and is photographed by means of a 35 mm movie camera at the end of a light-tight hood. The camera has no shutter. As soon as the signal flashes

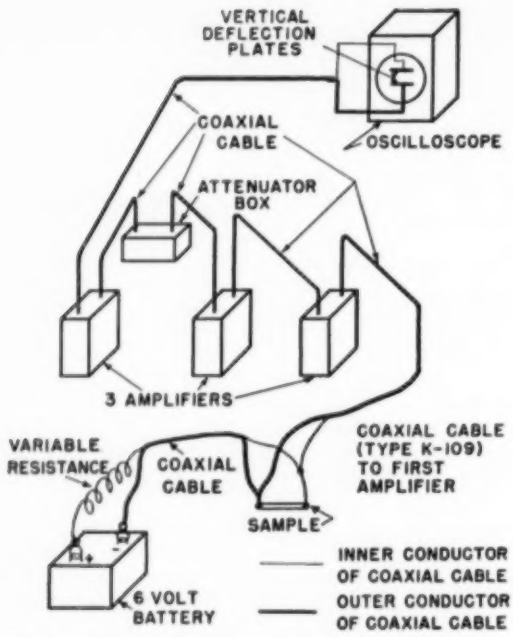

Fig. 1—Schematic representation of the electrical circuit.

across the screen, it is photographically recorded, and the film is moved one frame forward by the experimenter, so that the set-up is ready for recording the next signal. The movie camera used in this single-shot fashion is very convenient for the purpose of recording transient signals occurring in very rapid succession. Appendix I deals with the electrical apparatus and its workings in greater detail.

Metallurgical Apparatus and Procedure: The temperature range for the formation of martensite in this alloy is −20° to −200°C. Athermal martensite was formed in the apparatus shown in Fig. 2. The sample resting in one of the lucite holders was lowered gradually toward liquid nitrogen in the bottom of a Dewar flask. The temperature of this sample could not be measured directly, since a thermocouple circuit attached to the sample would completely upset the electrical circuit; accordingly, an identical dummy sample, resting in the twin lucite holder, positioned similarly with respect to the bath served this purpose, with the temperature

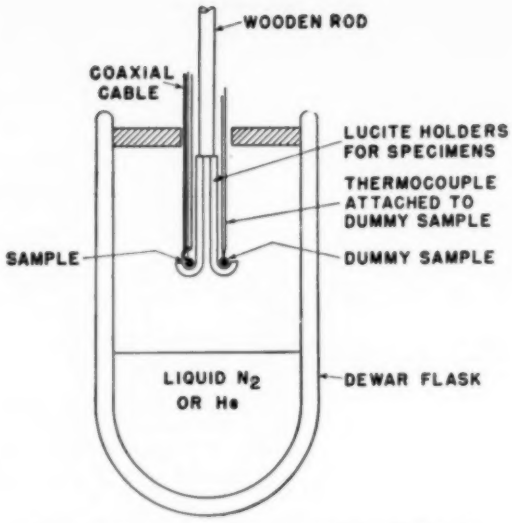

Fig. 2—Apparatus for subzero temperature experiments.

measured by a copper-constantan thermocouple; a check experiment showed the temperatures of the two samples to differ by no more than 3°C. The apparatus used to study the formation of isothermal martensite was similar to that employed by Das

Table II. Austenitizing Treatments and Resulting Grain Diameters in an Fe-30 Pct Ni Alloy

	Austenitizing Time, °C	Austenitizing Time, Hr	Resultant Average Grain Diameters, In.
A	1300	18	0.01
B	1100	2	0.005-0.007
C	900	½	0.001

Gupta and Lement;[9] it is essentially a nichrome-wound furnace with liquid nitrogen on the outside, maintaining the outside temperature at −196°C; the specimen was inserted in an inner tube containing iso-pentane (melting point −155°C); the generation of heat by the nichrome winding is thus set against the loss of heat to the liquid nitrogen; the temperature can be raised, or lowered, or maintained constant.

Table I. Electrical Characteristics of the Equipment Used

	Chain Pulse Amplifier Type 202	Chain Pulse Amplifier Type 214	Oscilloscope Type 517
Manufacturer	Spencer-Kennedy Labs. Cambridge, Mass.	Spencer-Kennedy Labs. Cambridge, Mass.	Tektronix, Inc. Portland, Oregon
Band-width (frequency response)	40 kc to 80 mc	100 kc to 200 mc	200 cycles — 75 mc
Gain	30 db ± 215 db	20 db ± 1 db	
Sweep speeds			20 microseconds per cm to 10 millimicroseconds per cm
Accelerating potential			24,000 v

Definitions of Symbols:

kc = kilocycle; mc = megacycle = 10^6 cycles = 1000 cycles
db = decibels
1 microsecond = 10^{-6} second; 1 millimicrosecond = 10^{-9} second

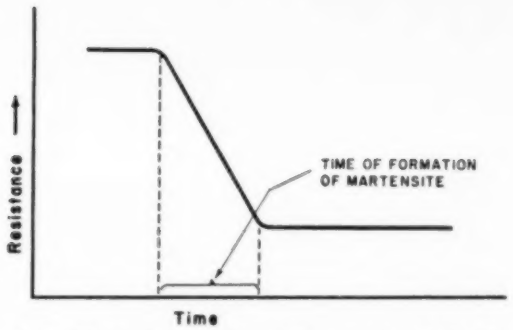

Fig. 3—Idealized picture of an oscilloscope trace during the martensite transformation.

Samples of the alloy wire were cut into 2-in. lengths and sealed in Vycor tubes in purified argon. These samples were austenitized at the temperatures and at the times shown in Table II; they were then water-quenched, and were found to be completely austenitic. The diameters of the austenite grains were measured, and are recorded in Table II.

Experimental Results

General Observations: The resistance of the martensite is lower than that of the austenite in an Fe-30 pct Ni alloy. The signal resulting from the unit martensitic transformation should thus be negative, as shown in Fig. 3, i.e., the resistance decreases with time. Strangely enough, this was never observed. Fig. 4 shows a photograph of the signal resulting with the sweep-speed set at 50 millimicroseconds per cm and the trigger on "positive signal." It is seen that the resistance of the sample first increases to a maximum and then decreases to a value lower than the initial ambient level. In order to determine whether this initial increase in resistance during the transformation is actually a part of the process of formation of a structural unit of martensite or is some other effect not connected with the martensitic transformation, the following experiment was performed: The oscilloscope was set to trigger on "negative signal" and the signals resulting from the martensitic transformation photographed, an example of which is shown in Fig. 5, which shows two consecutive traces on one frame of the film. It may be noted that the initial part of the signal consisting of the increase to the maximum and the subsequent decrease to the initial ambient level is missing. The signal triggered the sweep only on going negative. Thus the initial increase is not a characteristic of the apparatus *per se*.

It may be concluded that the signal resulting from the formation of a martensite plate in an Fe-30 pct Ni alloy consists of an initial increase in resistance of the sample up to a maximum value and a subsequent decrease to a value below its initial ambient level. Hereinafter, the term "pulse cycle" will refer to the complex signal described above.

The time of formation of a plate of martensite corresponding to one pulse cycle is 1.10^{-7} sec from Fig. 4.

Figs. 6, 7, and 8 show signals resulting from the martensitic transformation with sweep speeds varying from 50 to 200 millimicroseconds per cm and "positive signal" trigger setting. These figures show a large number of pulse cycles following each other;

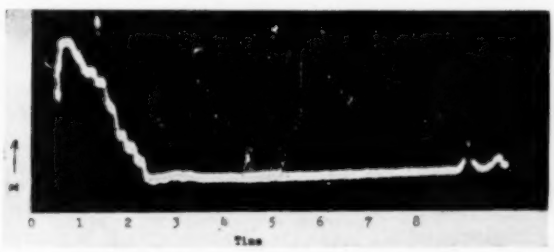

Fig. 4—Photograph of the oscilloscope screen during the martensite transformation. Each division corresponds to 50 millimicroseconds. Positive signal trigger.

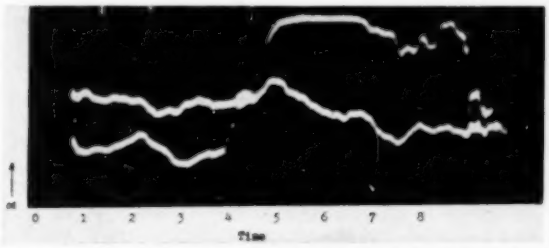

Fig. 5—Photograph of the oscilloscope screen during the martensite transformation. Each division corresponds to 100 millimicroseconds. Negative signal trigger.

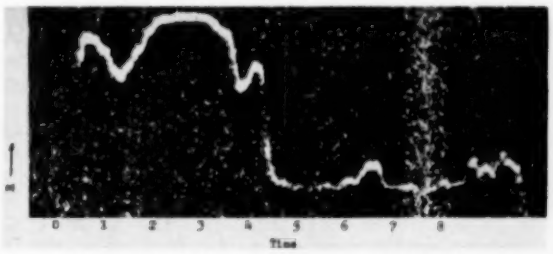

Fig. 6—Photograph of the oscilloscope screen during the martensite transformation. Each division corresponds to 50 millimicroseconds. Positive signal trigger.

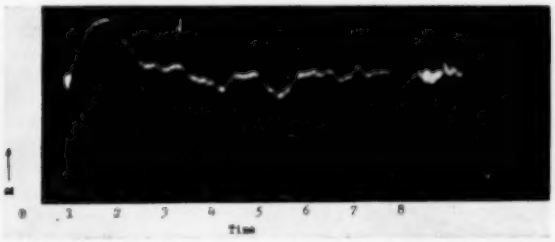

Fig. 7—Photograph of the oscilloscope screen during the martensite transformation. Each division corresponds to 100 millimicroseconds. Positive signal trigger.

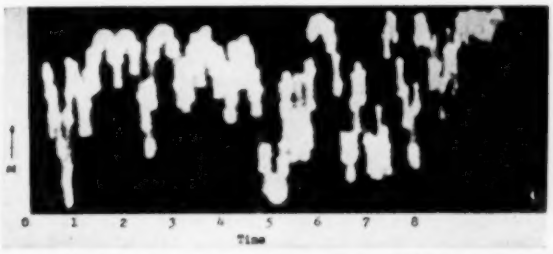

Fig. 8—Photograph of the oscilloscope screen during the martensite transformation. Each division corresponds to 200 millimicroseconds. Positive signal trigger.

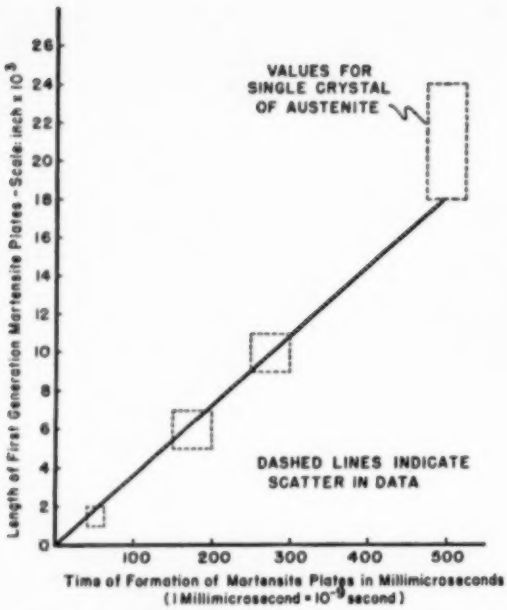

Fig. 9—Plot of first generation martensite plates vs their time of formation.

in most cases, the pulse cycle due to one martensite plate is superimposed in time on the one from the previously formed plate. The error due to this superposition is about $\pm 0.3 \times 10^{-7}$ sec, as can be seen from the fairly steep slopes of the traces. From an analysis of about 200 such oscilloscope traces, the time of formation of a plate of martensite varies from 5.0×10^{-7} to 0.5×10^{-7} sec depending on the size of the martensite plate formed, as will be seen.

These signals correspond to a frequency of 10 megacycles. From Table I, it can be seen that the system responds to frequencies up to 75 megacycles. Thus, the signals resulting from the martensitic transformation are well within the frequency response of the apparatus used and represent an undistorted or true value for the time of formation of martensite, i.e., this is the first measurement of the lower limit in time. The experimental error in measurement due to the electrical measuring system is ±5 pct.

Thus far, it has been tacitly assumed that each pulse cycle corresponds to the formation of one structural unit of martensite. The large number of pulse cycles observed and their superposition in time may be considered as indirect evidence of this. The following type of critical experiment was performed to check the validity of this assumption. The martensite transformation in a large-grained austenitic sample was allowed to proceed until only a very small amount of martensite had formed, with further transformation prevented by "upquenching" to room temperature. The entire sample (1 in. long and 0.025 in. in diameter) was polished across the medial longitudinal section and etched and the number of martensite plates counted. A count of the number of pulse cycles in the oscilloscope photographs taken was also made. The two counts differed by about 3 to 4 in a total of about 20. This appears to be fairly satisfactory evidence that each pulse cycle corresponds to a single martensite plate. More direct proof though possible would be unwarrantedly laborious.

Interrelationship Between Size of Martensite Plates, Their Time of Formation, and Signal Strength: As is well known, the first generation of martensite plates traverse the entire austenite grain (provided it is not large) until their growth is stopped at discontinuities of the lattice-like grain boundaries, twin interfaces, and inclusions, etc.

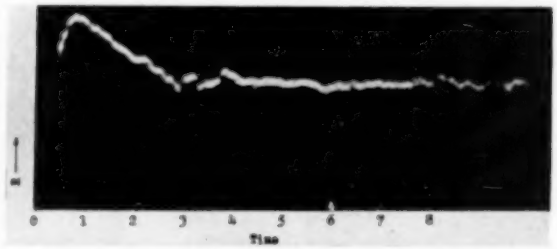

Fig. 10—Photograph of the oscilloscope screen during the martensite transformation. Each division corresponds to 100 millimicroseconds. Positive signal trigger. Isothermal run at —90°C.

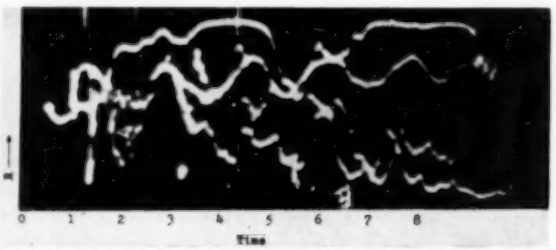

Fig. 11—Photograph of the oscilloscope screen during a "burst" in polycrystalline and single crystal specimens. Each division corresponds to 100 millimicroseconds. Positive signal trigger.

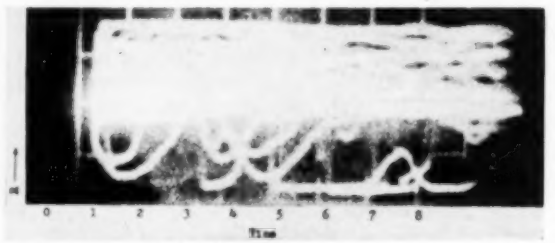

Fig. 12—Photograph of the oscilloscope screen during a "burst" in polycrystalline and single crystal specimens. Each division corresponds to 200 millimicroseconds. Positive signal trigger.

Thus, it may be assumed that the length of the martensite plate is approximately the same as the diameter of the austenite grain for the first generation of martensite plates. Austenitic samples of this alloy with grain diameters varying from 0.001 to 0.01 in. were prepared by the heat-treatments given in Table II. They were transformed to martensite and the time of formation of the first generation martensite plates measured. Single-crystal austenite specimens were also transformed and the time of formation of first generation plates measured. (It may be noted that there appears to be a limiting size to the martensite plates formed in a single crystal of austenite, as has been also observed by Kurdjmow[15] and Machlin and Cohen.[5] Fig. 9 shows a plot of length of first generation martensite plates vs their time of formation. It may be noted that the plot is linear, thus indicating that the overall process of the propagation of martensite is a constant velocity process. The experi-

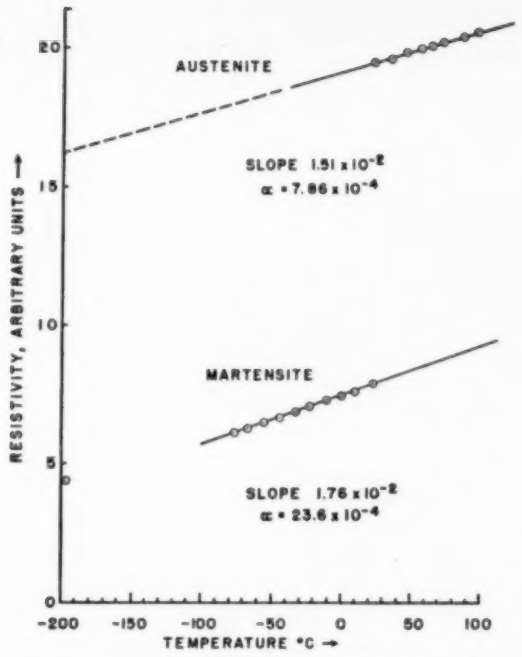

Fig. 13—Resistivity of a 71 pct Fe-29 pct Ni alloy as a function of temperature.

mental scatter is $\pm 0.25 \times 10^{-7}$ sec on the time scale and 1.10^{-3} in. on the length scale, as may be seen from Fig. 9.

The average slope of the straight line drawn through the data which is a measure of the rate of propagation of martensite is 3300 ft per sec or 100,000 cm per sec, approximately. The maximum error in the rate of propagation due to the scatter in data is about ±20 pct.

It was also observed that the signal strength resulting from the martensite transformation varies directly with the size of the martensite plate formed.

Influence of Temperature on the Athermal Transformation: The time of formation of a martensite structural unit was measured from −20° to −195°C and was found to be of the order of 10^{-7} sec throughout this temperature range. The variation was from about 3.10^{-7} sec at −20°C to 0.5×10^{-7} sec at about −195°C for specimens with initial austenite grain size 0.01 in. This does not represent a change in the velocity of propagation however. It may be seen from Fig. 9 that this decrease in the time of formation at lower temperatures can be accounted for by the decrease in size of the martensite structural units with decrease in temperature as a result of the partitioning of the parent austenite by the prior formation of martensite. Thus the velocity of martensite propagation is independent of the temperature of transformation within the temperature range −20° to −195°C; the maximum error due to the scatter in experimental data is ±20 pct.

Isothermal Transformation: The time of formation of isothermal martensite at four different reaction temperatures, −60°, −90°, −105°, and −195°C was measured, and found to be of the order of 10^{-7} sec. About 10 runs were made at each temperature. Fig. 10 shows a photograph of the oscilloscope trace during an isothermal run at −90°C. The pulse cycle has identical characteristics with those occurring during the athermal transformation.

The Burst Phenomenon: Machlin and Cohen[8] define the burst phenomenon as a large amount of martensite (>½ pct) forming in the time interval of an audible click. This phenomenon was observed and photographs of the oscilloscope screen taken during a "burst" are shown in Figs. 11 and 12. The very large number of pulse cycles on one frame of the movie film show very graphically that the "burst" consists of a large number of martensite structural units forming in a very small period of time, the reaction occurring in a cataclysmic or autocatalytic fashion; presumably the stresses caused by the formation of one plate nucleate the succeeding ones.

Discussion

On the Nature of the Pulse Cycle: The pulse cycle corresponding to the formation of a plate of martensite consists of an initial increase of the resistance to a maximum followed by a subsequent decrease to below the initial level. The initial increase is new. The overall decrease in resistivity is in accord with expectations for this alloy. Several explanations may be advanced for the initial anomalous increase:

1—The austenite-martensite transformation is accompanied by the evolution of heat. The resistance of a metal characteristically increases with

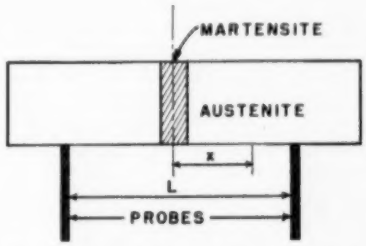

Fig. 14—Representation of boundary conditions for problem considered in Appendix II.

increasing temperature; thus, the sudden release of the latent heat in the localized region of the specimen transformed to martensite might account for this initial increase in the resistance of the sample.

This argument would be valid only if the amount of heat liberated would be sufficient to cause the observed increase in resistance, and if the flow of heat from the localized region was rapid enough to account for the subsequent decrease in resistivity.

Smithells[10] gives the latent heat of transformation of austenite to martensite in a 0.9 pct C steel as 500 cal per gram-atom, and that of the transformation of $\gamma \rightarrow \alpha$ iron at 720 cal per gram-atom. For an Fe-30 pct Ni alloy, it will be assumed that the latent heat of transformation is 720 cal per gram-atom or 13 cal per gram as an upper limiting value. The specific heat of this alloy is 0.119 cal per gram per °C.[11] Thus, the temperature rise corresponding to the liberation of 13 cal per gram-atom is 13/0.119, or roughly 110°C.

Fig. 13 shows the resistivity vs temperature curves for samples of Fe-30 pct Ni alloys in the 100 pct austenitic and martensitic (about 90 pct

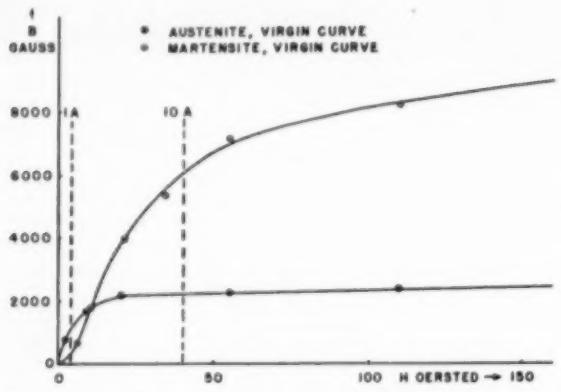

Fig. 15—Magnetization curves for a 71 pct Fe-29 pct Ni alloy.

martensite) states.[12] It will be assumed that a martensite plate forms completely across the cross section of the wire as shown in Fig. 14. This assumption is obviously biased to favor the argument. From Fig. 13, it may be seen that the increment in resistance of the newly formed martensite structural unit on being raised in temperature by 110°C would not even increase its resistance to a value corresponding to that of the same volume of the austenite, whereas an overall increase in resistivity is observed. A rough calculation based on the slope of the plots in Fig. 13 and the pulse cycle shows that a heating of about 1500°C would be required to validate the argument. Thus, the localized liberation of latent heat of transformation to the martensite unit alone cannot account for the initial increment of resistance observed.

It may be argued that the flow of heat from martensite to austenite would account for the subsequent decrease observed in the pulse cycle, since the temperature coefficient of resistance of austenite is one-third that of martensite. However, as the slopes of the resistivity vs temperature plots for austenite and martensite and their relative specific heats are almost the same, the decrement in the resistance of the sample due to a fraction of the heat flowing from the martensite to the austenite would approximately balance the increment of the resistance of the austenite caused by this heat transfer. Thus, the decrease in resistance observed in the pulse cycle cannot be explained as due to the flow of heat from martensite to austenite, even in the very small time observed for this decrease, viz., 10^{-7} sec. The calculation illustrated in Appendix II shows that the decay time, τ, for one-half of the initial quantity of heat to flow past the probes is 41 sec which is much too long for the time observed for the decrease in resistance, viz., 10^{-7} sec.

Thus the localized heating of the martensite structural unit formed cannot account for the pulse cycle observed for the formation of this structural unit of martensite.

2—Stresses increase the electrical resistance of metals and alloys. Wheeler and Jaswon[13] have estimated an average value of 93 tons per sq in. for the microstresses in a structure consisting of martensite and retained austenite in Fe-C alloys. It might be argued that the very high microstresses occurring during the formation of martensite cause the initial "anomalous" increase in resistance of the sample, and that these stresses are subsequently relieved by the plastic flow of the matrix thus permitting the resistance to decrease to the level for martensite.

From Fig. 13, it is seen that the resistance of austenite is 2 to 3 times greater than that of martensite, the variation depending upon the temperature. From the pulse cycle, it may be observed that the initial increment in resistance is roughly of the same order of magnitude. Thus it appears rather unlikely that the stresses due to the formation of one structural unit of martensite could increase the resistance of the sample by 4 to 6 times the value of the resistance of martensite.

3—It has been suggested, on the basis of rough calculations, that this initial increase may be due to a part of the sample going from a very low ferromagnetic state (austenite) to one which is highly ferromagnetic (martensite). As this transformation occurs in a very short time interval, the sudden change in the distribution of the magnetic lines of force causes a temporary apparent increase in the resistance of the sample, which may account for the initial increase in resistance observed in the pulse cycle. The following critical experiments led to the abandonment of this possibility:

Fig. 15 shows the B-H curves of fully austenitic and fully martensitic (90 pct martensite approximately) for an Fe-30 pct Ni alloy as obtained in this laboratory by the use of a Koepsal permeameter.[12] It may be noted that the curves cross each other, i.e., below a field strength of about 15 oersteds austenite has a greater permeability ($\mu = B/H$) than martensite and above 15 oersteds the reverse is true. Thus, the conditions necessary for the effect postulated would exist in the latter situation (above 15 oersteds) and not for the former. The field strength within the sample can be varied by varying the current passing through the sample. Thus, for wire specimens (diameter of 0.025 in.) a current of 1 amp produces a field strength of 4 oersteds and a current of 10 amp produces a field strength of 40 oersteds. The pulse cycles resulting from the martensite transformation at field strengths 4 and 40 oersteds in the samples show identical characteristics. Pulse cycles observed at intermediate values of field strengths also showed the same characteristics. Thus this possibility is excluded.

4—Of the many publications on the crystallographic nature of the transformation of the face-centered cubic (austenite) lattice to the body-centered cubic (or body-centered tetragonal martensite) lattice, all have found it necessary to assume the process to occur as a result of two shearing or distortion processes. Since other possibilities seem excluded above, it appears that the form of the pulse cycle observed is experimental confirmation of such a two-stage distortion process. The form of the pulse cycle cannot be taken as evidence for a complete separation in time of the two distortions; though the two distortions are sequential in time, there is doubtless overlap; indeed the roundness of the maximum suggests overlap; the absence of a truly horizontal plateau at the maximum would appear to demonstrate that the two stages are not separated in time; Machlin and Cohen[14] have speculated on the sequence and the overlap of two distortions.*

* It may be possible to explain the nature of the pulse cycle on the basis of a shear-like distortion and subsequent stress-relieving slip or twinning mechanism proposed by Geisler (*Acta Metallurgica* (1953) Vol. 1, No. 3); whether this mechanism can account for the very small times observed awaits further consideration.

Correlation of the Velocity of Martensite Propagation and Elastic Wave Propagation: The slope of the plot in Fig. 12 gives the velocity of martensite propagation, estimated to be 3300 ft per sec. The velocity of elastic wave propagation in a solid is given by

$$v = \sqrt{\frac{G}{d}}$$

where v is the velocity of elastic wave propagation in the solid; G, the modulus of rigidity; and, d, the density of solid. The values of G and d for an Fe-30 pct Ni alloy are[11]

$$G = 8{,}600{,}000 \text{ psi}$$
$$d = 510 \text{ lb per cu ft.}$$

This gives a value of 9925 ft per sec as the velocity of propagation of elastic waves in an Fe-30 pct Ni alloy.

McReynolds[8] has shown that for an Fe-30 pct Ni the value of G and d are invariant with temperature at subzero temperatures. Thus the velocity of elastic wave propagation in this alloy should also be invariant with temperature below room temperature. The results of this investigation show that the velocity of martensite propagation is constant in the temperature range −20° to −195°C.

Thus, it may be concluded that the martensite transformation is an elastic-wave-like propagation in the solid. The apparent discrepancy between the velocity of martensite propagation (3300 ft per sec) and that of elastic wave propagation (9925 ft per sec) may be reconciled if it is considered that the martensite transformation consists of two stages sequential in time, but each proceeding possibly with the velocity of elastic waves, thus decreasing the overall velocity of martensite propagation from 9925 to 3300 ft per sec. This is in good accord with the strain-wave model of martensite propagation.

Concerning Theories on the Martensite Transformation: During the past five years, two theories have been proposed for the martensite transformation. Kurdjmow and coworkers[15, 16, 17] and Fisher, Hollomon, and Turnbull[18] have applied a modified version of regular nucleation and growth† kinetics to the martensite transformation. Scheil[19] in 1929 proposed that the transformation occurs by nucleation and a subsequent very rapid propagation of the martensite phase into the parent austenite in the manner of a strain-wave, to form a fully grown martensite plate. Machlin and Cohen[7] have put this theory on a more quantitative footing. The two theories essentially differ in one important respect; i.e., the rate equation for the nucleation and growth theory contains a term

$$e^{-Q/RT}$$

where Q is the activation energy for growth, which is absent from the rate equation of the propagation theory. This difference has fundamental significance however. The term Q represents the activation energy for the growth of a nucleus to the final martensite plate by a process of atom-by-atom transfer across the austenite-martensite interface. For transformation propagated as a strain-wave, the activation energy for growth should be virtually zero.[7] Machlin and Cohen[7] in an elegant critical experiment showed that martensite formed with its characteristic high velocity of propagation even at 4°K on deforming a specimen of an Fe-29 pct Ni alloy, as evidenced by the audible clicks. This would be impossible according to the nucleation and growth theories, as, even if new nuclei are formed as a result of the deformation, their growth rate would be inappreciable. On the other hand, the strain-wave propagation theory would predict that as soon as the nuclei are formed by the applied stress, they grow to full-size plates.

According to the nucleation and growth theories, the activation energy for growth of martensite is 500 to 2000 cal per mol. For an activation energy of 500 cal per mol,[17] the ratio of the velocity of propagation at 250°K to that at 80°K is calculated to be about 8. For an activation energy of 2000 cal per mol this ratio is 3000.[18]

The results of this investigation demonstrate that this ratio is unity with the maximum possible deviation due to experimental scatter raising this ratio to about 2. Thus the activation energy for the propagation of martensite is very small, virtually zero, neglecting frictional effects.

The strain-wave propagation theory does not distinguish between the athermal and isothermal modes of the martensite propagation. The results of this investigation show that the characteristics of the pulse cycle are identical for both modes of transformation.

In general, this investigation has yielded results which are in excellent agreement with the strain-wave propagation theory and differ with the concept of growth of martensite plates by an atom-by-atom transfer across the moving interface.

† In this discussion, the term "growth" refers exclusively to the conventional atom-by-atom growth process across the interface.

Summary

1—An experimental technique has been established capable of measuring accurately phenomena of very short duration occurring in metals and alloys.

2—The time of formation of a plate of martensite 0.01 in. long in an Fe-30 pct Ni alloy is 3.10^{-7} sec; this represents perhaps the most accurate value reported for the propagation of martensite.

3—The rate of propagation of martensite is 3300 ft per sec or 100,000 cm per sec approximately, and is independent of temperature in the range −20° to −195°C in this alloy.

4—Thus, the "activation energy" for the propagation of martensite is virtually zero.

5—It may be concluded from 3 and 4 that the concept of martensite formation by a process of atom-by-atom growth is incorrect. On the other hand, these results are in very good accord with the strain-wave propagation theory proposed for the martensite transformation.

6—The characteristics of the transformation, viz., the time of formation of martensite units, and the general nature of the pulse cycle resulting from the martensite transformation are independent of whether the transformation occurs athermally or isothermally.

7—The time of formation and the signal strength vary directly with the size of the plate formed.

8—The velocity of martensite propagation is of the same order of magnitude as the velocity of elastic wave propagation in the solid.

9—From considerations on the nature of the pulse cycle, it may be concluded that the martensite propagation consists of two stages proceeding with the velocity of elastic wave propagation in the solid.

10—This technique is ideally suited for the study of rapidly occurring phenomena in metals and alloys such as slip, twinning, cleavage, etc. Such investigations are underway in this laboratory.

Acknowledgments

This research work was sponsored by the Office of Air Research and carried out under Contracts AF 18 (600) — 161 and AF 33 (038) — 10218. Our thanks are also due to Professor E. M. Williams and coworkers of the Department of Electrical Engineering for their extended assistance with the complex electronics equipment. Our appreciation is also extended to Eliel Lahteenkorva for his able assistance in the laboratory.

Appendix I

The following major pieces of electrical equipment were used in this investigation: Two of Type 202P Spencer-Kennedy Chain-Pulse amplifiers; one of Type 214 Spencer-Kennedy Chain-Pulse amplifier; and a Cathode Ray Oscilloscope, Tektronix, Type 517. Some of the characteristics of these apparatus are given in Table I. A 160-ohm impedence cable, No. K 109 of the Federal Telephone and Radio Corp. is used to connect the various parts of the circuit, excluding the battery loop.

The following special characteristics of the cathode-ray oscilloscope should be noted:

1—Accelerating potential of 24,000 v. In making a photographic record of very fast transient signals flashing across the face of a cathode-ray tube (of the order of 0.1 microsecond), it is obvious that there is no control over the exposure time of the film. Thus the intensity of the light emanating from the face of the tube must be very high. This is accomplished by having a very high accelerating potential of 24,000 v on the cathode-ray beam, since the intensity of the light varies better than linearly as the velocity of the electron beam or the accelerating potential on the tube. A metallized 5XP cathode-ray tube with a P11 phosphor (which emits blue light) in conjunction with Eastman Linagraph Pan 35 mm Film developed in Developer SD 19 (a) (Ref. Kodak Formulary) permits a satisfactory photographic record of the oscilloscope trace.

2—The oscilloscope can be set to trigger on either a positive or negative signal.

Appendix II

The problem under consideration is the time necessary for the latent heat liberated in a martensite plate to flow out of the entire sample past the probes, see Fig. 14.

The specific resistivity of a homogeneous sample is linear with temperature. Moreover, at the temperatures under consideration the specific heat is nearly independent of temperature. Therefore, if a quantity of heat is suddenly generated within the sample, the decay time of the voltage signal due to this heating is determined by the time needed for the heat to flow out of the sample.

It is assumed that at time $t = 0$, an amount of heat ν is generated instantaneously in a thin cross section of a long cylindrical wire and is distributed uniformly in that cross section. Neglecting radial heat transfer, the problem reduces to a simple one-dimensional case, whose solution is

$$T = \frac{1}{\sqrt{4\pi\alpha t}}\, e^{-x^2/4\alpha t}$$

where T is the absolute temperature at time t and position x, α is the thermal diffusivity of the material; x is measured from the cross section at which ν was generated. The integral

$$\int_{-x'}^{x'} T dx = \frac{2}{\sqrt{\pi}} \int_{0}^{x'} \frac{2}{\sqrt{\pi}}\, e^{-\left(\frac{x}{\sqrt{4\alpha t}}\right)^2} d\left(\frac{x}{\sqrt{4\alpha t}}\right)$$

$$= erf\left(\frac{x'}{\sqrt{4\alpha t}}\right)$$

is proportional to the heat remaining between points $-x'$ and x' at any given instant t. Since $erf\ (\infty) = 1$, the interval τ during which $\nu/2$ flows beyond $-x'$ and x' is determined by the condition

$$erf\left(\frac{x'}{\sqrt{4\alpha\tau}}\right) = \frac{1}{2}$$

From tables of the error function, this is the case when

$$\frac{x'}{\sqrt{4\alpha\tau}} = 0.477$$

If the leads of the signal circuit are attached symmetrically at $x = -L/2$ and $x = L/2$, (see Fig. 14), the decay time is

$$= 0.477^{-2}\, \frac{L^2}{16\alpha}$$

For $\alpha = 0.027$ sq cm sec^{-1} and $L = 2$ cm

$$\tau = 41 \text{ sec}$$

It is thus seen that decay times of this order of magnitude are very much longer than the observed time interval corresponding to the decrease, viz., 10^{-7} sec.

References

[1] H. J. Wiester: *Ztsch. Metallkunde* (1932) **24**, p. 276.
[2] H. Hannemann, W. Hofmann, and H. J. Wiester: *Archiv. Eisenhuttewesen* (1932-1933) **6**, p. 199.
[3] F. Förster and E. Scheil: *Ztsch. Metallkunde* (1936) **28**, p. 295.
[4] F. Förster and E. Scheil: *Naturwissenschaften* (1937) **25**, p. 439.
[5] F. Förster and E. Scheil: *Ztsch. Metallkunde* (1940) **32**, p. 165.
[6] E. S. Machlin and M. Cohen: *Trans.* AIME (1951) **191**, p. 746; JOURNAL OF METALS (September 1951).
[7] E. S. Machlin and M. Cohen: *Trans.* AIME (1952) **194**, p. 489; JOURNAL OF METALS (May 1952).
[8] A. W. McReynolds: *Journal of Applied Physics* (1949) **20**, p. 896.
[9] S. C. Das Gupta and B. S. Lement: *Trans.* AIME (1951) **191**, p. 727; JOURNAL OF METALS (September 1951).
[10] C. J. Smithells: *Metals Reference Book* (1949) pp. 418-421.
[11] J. S. Marsh: *Alloys of Iron and Nickel* (1938) McGraw-Hill Book Co.
[12] E. E. Lahtenkorva, R. F. Bunshah, and R. F. Mehl: Unpublished research, Carnegie Institute of Technology, 1952.
[13] J. A. Wheeler and M. A. Jaswon: *Journal* Iron and Steel Inst. (1947) **157**, p. 161.
[14] E. S. Machlin and M. Cohen: *Trans.* AIME (1951) **191**, p. 1019; JOURNAL OF METALS (November 1951).
[15] G. V. Kurdjmow: *Journal of Technical Physics* U.S.S.R. (1948) **18**, No. 8, p. 999.
[16] G. V. Kurdjmow and O. P. Maksimova: *U.S.S.R. Academy of Sciences Report* (1948) **61**, p. 53.
[17] G. V. Kurdjmow and O. P. Maksimova: *Ibid.* (1950) **73**, No. 2, p. 95.
[18] J. C. Fisher, J. H. Hollomon, and D. Turnbull: *Trans.* AIME (1949) **185**, p. 691; JOURNAL OF METALS (October 1949).
[19] E. Scheil: *Ztsch. anorg. allgem. Chem.* (1929) **183**, p. 98.

Decay of Lattice Defects Frozen into an Alloy by Quenching

by A. E. Roswell and A. S. Nowick

Anelastic measurements of atomic mobility in an Ag-Zn substitutional solid solution, make possible a study of the rate of decay of lattice defects frozen into the alloy by quenching.

A WIDE variety of experimental evidence has accumulated recently in support of the belief that atomic mobility or diffusion in face-centered cubic lattices occurs principally through the movement of lattice defects, as contrasted to a mechanism by which two or more atoms directly exchange lattice positions. The most direct evidence, summarized in a recent review,[1] includes the Kirkendall-effect measurements and anelastic measurements on quenched alloys. Theoretical calculations[2] have focused attention on the lattice vacancy as the defect probably responsible for diffusion in the common metals. Later calculations[3] have also shown the possible importance of combined pairs of vacancies in producing diffusion. The only defect that has been considered seriously, in addition to the vacancy and combination of vacancies, is the "interstitialcy" (an atom which has left its normal lattice position and entered an interstitial position); the calculated energy of formation of an interstitialcy in a close-packed lattice is too large to permit a reasonable probability for the occurrence of this defect.[2] In view of these calculations it may be tentatively concluded that the defects producing atomic movements are single or multiple vacancies.

Anelastic measurements of atomic mobility in substitutional solid solutions provide a valuable method for the study of lattice defects. By means of this method it was first demonstrated[4] that defects may be frozen into a lattice by rapid quenching from high temperatures. (It was subsequently shown[5] that resistivity measurements may also be capable of detecting the presence of frozen-in defects.) A summary of the principles involved in these anelastic measurements will now be presented.

The anelastic method is based on a relaxation phenomenon in substitutional solid solutions, first discovered by Zener[6] in α brass and subsequently investigated extensively in a series of Ag-Zn solid solutions.[7] This relaxation effect may be observed in the usual way[6] either dynamically, as a peak in

A. E. ROSWELL, Student Associate AIME, and A. S. NOWICK, Junior Member AIME, are Graduate Student and Assistant Professor, respectively, Dept. of Metallurgy, Yale University, New Haven, Conn.

Discussion on this paper, TP 3619E, may be sent, 2 copies, to AIME by Dec. 1, 1953. Manuscripts April 13, 1953. Cleveland Meeting, October 1953.

the curve of internal friction vs temperature, or statically as a stress relaxation or elastic after-effect phenomenon. A simple interpretation of these anelastic effects is suggested by Zener,[9] who focuses attention on pairs of solute atoms in the substitutional solid solution. Thus, suppose that the solute atoms have a larger atomic diameter than the solvent atoms. The application of a tensile stress to the solid solution will then result in a preferential alignment of pairs of solute atoms along those crystallographic directions that lie nearest to the tensile axis, since such redistribution of atoms acts to relieve the stress. Since the rate of this reorientation of solute atom pairs depends on the rate of atomic diffusion, the application of stress will produce typical anelastic behavior with a relaxation time closely related to the mean atomic jump time in the solid solution.

It is pointed out by one of the authors[7,9] that Zener's pair reorientation mechanism is a special example of stress-induced ordering, where the application of stress to an initially random solid solution produces preferential atomic rearrangements accompanied by anelastic strain. Furthermore, it is argued that since a large solute concentration (usually greater than 15 pct) is required in order that the effects be observable experimentally, most solute atoms will have at least two nearest neighbors that are solute atoms. The concept that isolated solute atom pairs are the unit which undergoes ordering therefore seems to be an oversimplification. Investigation of the orientation dependence of the anelastic effects in single crystals, which are now under way, should lead to a more accurate picture of the relaxation process. It is important to note, however, that regardless of the relaxation mechanism, the experimentally measured relaxation time, τ, represents the time for atomic redistribution under an applied stress and is therefore of the same order of magnitude as the mean jump time of an atom in the lattice. (Because diffusion takes place through the movement of defects, the rate of movement of solute and solvent atoms is not generally the same; under these conditions the mean jump time of the slower atomic species should determine the measured relaxation time.[7,9]) It is therefore possible, by the use of relaxation measurements in appropriate substitutional solid solutions, to measure atomic mobility at temperatures far below those at which ordinary diffusion experiments can be carried out. Such measurements make possible a demonstration[4,10] that an excess of defects may be frozen into the lattice of an alloy by quenching to produce abnormally short relaxation times at low temperatures. (Evidence is presented[10] to rule out the possibility that the observed effects can be attributed to quenching stresses.)

The earlier investigation[10] of the freezing-in of lattice defects utilized almost entirely an Ag-Zn solid solution containing 30 atomic pct Zn. Decay curves, which show the variation of the relaxation rate (i.e., of atomic mobility) with time after quenching, were obtained at different temperatures. The precise form of the decay curves could not be obtained because of the rapidity of the rate of decay. During these measurements on the 30 atomic pct Ag-Zn alloy, preliminary experiments were also conducted on a solid solution containing 33.5 atomic pct Zn. These experiments showed that the decay rates for the latter alloy were considerably slower than for the 30 pct alloy and that, consequently, more precise decay curves could be obtained. The present paper describes detailed experiments of this type carried out with the 33.5 pct solid solution. Inasmuch as equilibrium measurements of atomic mobility for this solid solution had not been carried out previously, such measurements are also included.

The theory required for the interpretation of the measurements has been presented in the earlier papers.[7,10] For the sake of completeness, the basic equations are briefly outlined below.

Theory

The rate of relaxation, τ^{-1}, is determined by the product of the concentration of defects, c, (expressed as an atom fraction) and the rate of jump of defects, or

$$\tau^{-1} = Ace^{-\Delta H_j/RT} \qquad [1]$$

where ΔH_j is the heat of activation for movement of a defect and A is a frequency factor. The defects may be considered to be vacancies, in order to be specific. If the two component atoms of the binary solid solution do not jump into a vacancy at the same rate, then, as mentioned in the previous section, the quantity ΔH_j should correspond to the slower moving component, i.e., ΔH_j is the larger of the two heats of activation for vacancy jump. Under conditions of thermal equilibrium, the vacancy concentration is given by $\bar{c}$, where

$$\bar{c} = Be^{-\Delta H_f/RT} \qquad [2]$$

The dimensionless quantity B is related[10] to the entropy of formation of a defect, while ΔH_f is its heat of formation. Thus, the equilibrium value of τ may be written

$$\bar{\tau} = \bar{\tau}_0 e^{H_r/RT} \qquad [3]$$

where H_r is the composite "activation energy" for relaxation, given by

$$H_r = \Delta H_j + \Delta H_f \qquad [4]$$

The value of H_r may not be precisely the same as the "activation energy" obtained from a diffusion experiment if the two component atoms diffuse at different rates. The quantity $\bar{\tau}_0$ is equal to $(AB)^{-1}$.

In a quenched specimen, the concentration of defects, c, to be inserted in Eq. 1 is much greater than the equilibrium value, and decays in time toward $\bar{c}$. In general, the function is written $c = c(t)$, with $c(0)$ for the concentration frozen in by quenching. From equilibrium measurements of $\bar{\tau}$ as a function of temperature, and from measurements of $\tau(0)$, the value obtained immediately after quenching, as a function of temperature, the quantity $c(0)$ may be estimated. The freezing-in temperature, T_r, defined as the temperature at which $\bar{c} = c(0)$, is then given by

$$c(0) = Be^{-\Delta H_f/RT_r} \qquad [5]$$

The freezing-in temperature can be less than or equal to the quenching temperature. The decay curve, which shows the variation of τ^{-1} with time after quenching at constant temperature, is also a measure of the time variation of the concentration of defects at the temperature of measurement, since from Eq. 1

$$\frac{\tau^{-1}(t)}{\tau^{-1}(0)} = \frac{c(t)}{c(0)} \qquad [6]$$

Eq. 6 is only valid as long as one type of defect is operative.

Specimens and Procedure

The Ag-Zn specimens used in this investigation were prepared by melting electrolytic silver and high purity zinc in a graphite crucible under charcoal. The casting was homogenized at 650°C, after which it was reduced in diameter by rolling and swaging. Finally, it was cold drawn to a diameter of 0.032 in. In order to grow coarse grains (to avoid complications due to grain boundary relaxation[11]) the drawn wire was sealed under vacuum in a quartz tube and heated to 650°C where it was held for five days. The final specimens contained 33.5 atomic pct Zn.

The relaxation time is obtained either from the position of an internal friction peak (when $\tau < 1$ sec) or from measurements of elastic after-effect (when τ is in the range between 10 and 10,000 sec). For the internal friction measurements, if T_m is the temperature of maximum damping, the relaxation time, $\tau(T_m)$ at this temperature, is obtained[8] from the equation

$$\tau(T_m) = (2\pi f)^{-1} \qquad [7]$$

where f is the vibration frequency. For an elastic after-effect measurement, the wire specimen is twisted through a desired angle for an appropriate length of time, then, upon release of the applied torque, the residual (anelastic) strain is measured as a function of time. A plot of the anelastic strain against the logarithm of the time shows an inflection point at a time τ_i, called the "time to inflection." Under equilibrium conditions, when the relaxation time τ is not changing with time, this quantity τ_i is equal to τ. For the quenching experiments, on the other hand, where τ is a function of time, a correction is required to relate the measured time to inflection to the appropriate relaxation time.[10] This correction was important in the earlier experiments, where the decay rates were so rapid that the change in relaxation time between successive measurements was large. In the present experiments the decay rates are much slower, so that τ_i is equal to τ without significant correction, and the use of the symbol τ_i is therefore superfluous.

In the quenching experiments, the specimen, supported against a heavier wire, is held at 400°C in a nitrogen atmosphere for 4 min, then allowed to fall freely into a tube containing water at room temperature. (It has been shown[10] that the results obtained are independent of the annealing time at the quenching temperature.) After this quenching operation, the specimen is mounted in the measuring furnace which is at the desired temperature. The time of relaxation is determined as a function of the total time at temperature from a series of elastic after-effect measurements. Inasmuch as the decay at room temperature is negligible over a period of several hours, the total time may be measured from the time of insertion of the specimen into the measuring furnace. The error due to the time required for the wire to reach temperature and to the time for the furnace temperature to become stabilized, means that the first relaxation measurement is often less reliable than the rest. Except for this initial instability, the temperature is held to ± ½°C by means of an electronic proportioning temperature controller.

Table I. Principal Numerical Results of Measurements and Calculations

Measured Quantities	
H_τ, kcal per mol	30.5 (±0.5)
log τ_0 (sec)	−14.1 (±0.3)
ΔH_f, kcal per mol	18.6 (±0.8)
log $Ac(0)$ (sec^{-1})	10.0 (±0.5)
Deduced Quantities	
ΔH_f, kcal per mol	11.9
$c(0)$	2.5×10^{-4}
c(m.p.)	7×10^{-3}
T_T	360°C
N	10^6

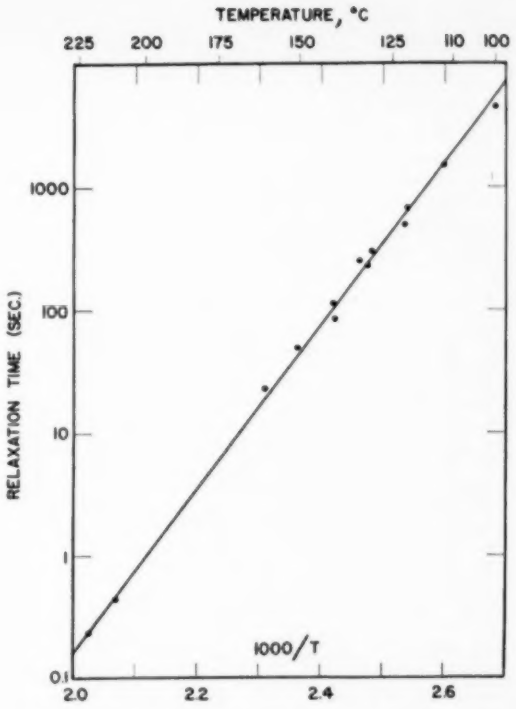

Fig. 1—Variation of the equilibrium time of relaxation with temperature, corresponding to a composite "activation energy" of 30.5 kcal per mol.

Equilibrium Measurements

The relaxation time under equilibrium conditions, for the 33.5 pct Ag-Zn alloy, is shown as a function of temperature in Fig. 1. The two points at the high temperature end of the curve are obtained from internal friction peaks at two different frequencies; the remaining points are obtained from the elastic after-effect measurements. Although a straight line is obtained in Fig. 1, previous measurements[7] on Ag-Zn alloys of lower zinc concentration have shown that when the data are extended to higher temperatures by the use of high frequency internal friction measurements, the plots of log τ against T^{-1} show a small but definite curvature. This result implies that the quantity H_τ (Eq. 3) is a

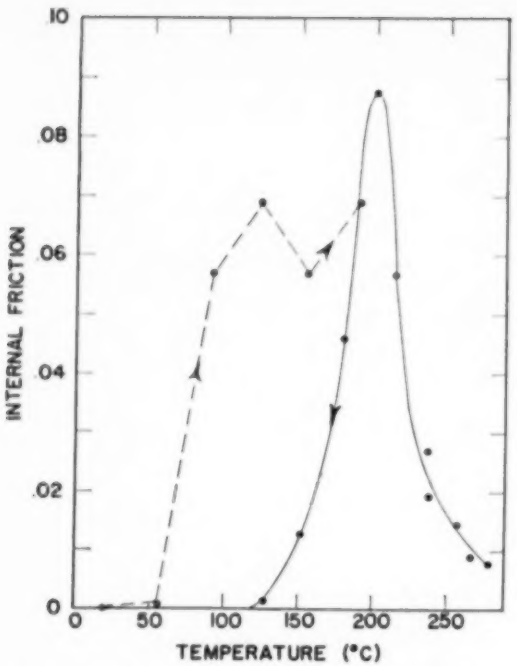

Fig. 2—Internal friction (Q^{-1}) during rapid heating (open circles) and cooling (solid circles) of the quenched Ag-Zn alloy. The solid curve represents the equilibrium internal friction peak. Frequency of vibration is 0.18 sec^{-1}.

slowly-varying increasing function of temperature. In the range of Fig. 1, however, appreciable deviation from a straight line is not detectable. The best values of the parameters in Eq. 3, obtained from Fig. 1, are $H_r = 30.5$ kcal per mol and $\log \bar{\tau}_o = -14.1$. These values, together with their estimated reliability, are listed in Table I.

Nonequilibrium Measurements

As in the earlier experiments, quenching a specimen from 400°C into water at room temperature results in abnormally short relaxation times at low temperatures. A specimen slowly cooled or dropped out of the furnace into still air shows no such effects, and is therefore assumed to be more nearly in equilibrium than the water-quenched specimen. The effect of varying the quenching temperature has already been observed;[10] in the present experiments the quenching temperature is always 400°C.

Static measurements (e.g., elastic after-effect measurements) are better suited to the study of quenched specimens than internal friction measurements because the latter must be measured at higher temperatures where the rate of decay of the quenching effects becomes very large. It was felt, however, that internal friction measurements on a quenched specimen might be very illustrative, qualitatively, of the effects of quenching. According to the interpretation given to these measurements, the atomic jump time, and therefore the relaxation time, is decreased by quenching because of the abnormally high defect concentration. For a given vibration frequency, it follows from Eq. 7 and the temperature dependence of τ that the effect of quenching is to shift the peak to lower temperatures. Due to the rapid decay of the effects of quenching at temperatures near the internal friction peak, it is expected that the peak will be moving toward higher temperatures during attempts to measure it. Accordingly, the quenched specimen was heated as quickly as possible while measurements of internal friction and temperature were taken in rapid succession. When the temperature reached 280°C, the furnace power was shut off and cooling data taken in a similar fashion. The results are shown in Fig. 2, where each measured value of internal friction is plotted against the average temperature during the measurement. The results show that the peak was constantly moving to the right during the course of the measurements, so rapidly in fact, that it was not possible to climb over the peak until a temperature of 190°C had been reached. Beyond this point, the data follow the solid curve, which represents the equilibrium internal friction peak, both on heating and cooling. When the same experiment was carried out with a slower rate of heating of a quenched specimen, similar results were obtained, but the values of internal friction attained in the vicinity of 100° to 150°C were not as high as in Fig. 2 and equilibrium was attained at a lower temperature. Thus, nonequilibrium internal friction effects must be measured very rapidly, with a resulting loss in ability to follow the approach to equilibrium. Such experiments, however, are of qualitative value in demonstrating that the relaxation peak is moved to a lower temperature by quenching, and therefore that the atomic mobility is increased.

By means of static measurements, it becomes possible to study the approach to equilibrium quantitatively. Fig. 3 shows the variation of τ with time after quenching, obtained by means of elastic after-effect measurements at 69°C. This figure is essentially a decay curve, as defined earlier, except that the ordinate is τ in place of τ^{-1}. Extrapolation of Fig. 1 shows that the equilibrium value of the relaxation time at 69°C is about 2×10^5 sec. The initial relaxation time after quenching, $\tau(0)$, obtained by extrapolating the data of Fig. 3 to zero time, is about 75 sec. The data of Fig. 3 are represented closely by two straight lines, with a sharp break at about $\tau = 800$ sec. Beyond this break, data are observed to fall along the second straight line out to 5000 min (i.e., well beyond the range shown in Fig. 3). The

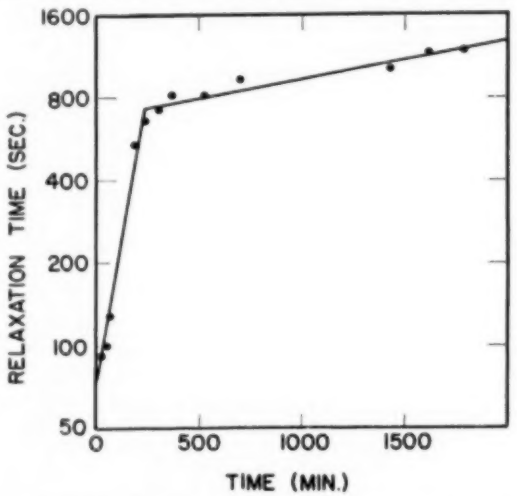

Fig. 3—Variation of the relaxation time with total time at 69°C for a quenched specimen. Equilibrium relaxation time equals 2×10^5 sec.

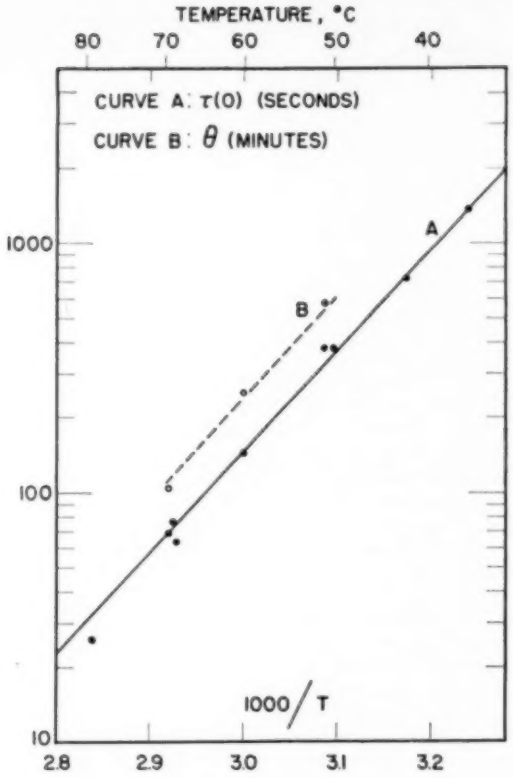

Fig. 4—Curve A: Initial relaxation time after quenching as a function of temperature of measurement. Curve B: Variation of the decay time with temperature for stage I.

occurrence of such breaks will be discussed further below. It should be noted here, however, that the abrupt decrease in the rate of decay cannot be attributed to the fact that the relaxation time is approaching its equilibrium value, since the break occurs when the relaxation time is still about 250 times smaller than the value of τ for this temperature.

From a series of decay curves at different temperatures, similar to that of Fig. 3, values of the initial relaxation time, $\tau(0)$, may be obtained as a function of temperature; the results are given in Fig. 4, curve A. The higher the temperature, the less accurate the extrapolation to zero time; the 80°C point is therefore considered the least reliable. Below 50°C the rate of attainment of equilibrium is too slow to permit the measurement of decay curves. However, additional points are obtainable below 50°C, since the initially measured relaxation time at these temperatures may be taken equal to $\tau(0)$ with negligible correction. From Eq. 1 with $c(0)$, the initial concentration of defects directly after quenching, substituted for c, it is clear that the slope of the straight line of Fig. 4A yields the quantity ΔH_f, while the product $Ac(0)$ is obtained from the intercept. The values obtained and their estimated reliability are listed in Table I. From H_r and ΔH_f, the quantity ΔH_f may be obtained,† Eq. 4. It is also possible to obtain $c(0)$ as follows. The quantities $Ac(0)$ and $AB(=\tau_\infty^{-1})$ are already known experimentally, while B can be estimated from theoretical considerations[10] to have a value of 3.0 (probably to within a factor of 2). The concentration of imperfections trapped by quenching, $c(0)$, is therefore estimated to be 2.5×10^{-4}. This value is probably reliable to within a factor of 5, in view of the uncertainties in the quantities from which it is calculated. The value of the equilibrium concentration of vacancies at the melting point (the solidus temperature) of the alloy is readily obtained from Eq. 2, to be

$$\bar{c}\ (\text{m.p.}) = 7\times10^{-3}$$

to within a factor of about 2.5. In the calculation of this quantity, no account is taken of the possible dependence of ΔH_f on temperature. If such a correction were required, however, a still larger value would be obtained for $\bar{c}$ (m.p.). The above value is larger than the equivalent quantity for pure copper calculated theoretically.[9]

The freezing-in temperature, T_r, defined by Eq. 5 may also be calculated from the results reported thus far. The value obtained is 360°C, and is probably reliable to about ± 40°C. This result is therefore consistent with the fact that the quenching temperature is 400°C. There is no reason to require that T_r be equal to the quenching temperature, i.e., that all defects present at the quenching temperature be frozen in. On the contrary, the earlier experiments,[10] which determined the dependence of initial relaxation time at a given temperature of measurement on the quenching temperature, show that defects present at the quenching temperature are not completely frozen in. These various deduced quantities, $c(0)$, $\bar{c}$(m.p.), and T_r, are listed in Table I.

The most significant results obtained from these experiments are the decay curves. In view of Eq. 6, the ratio $\tau(0)/\tau(t)$ represents the concentration of defects at any time t relative to the value $c(0)$ frozen in by quenching. When this ratio is plotted on a logarithmic scale against the time, the curves obtained may be represented by two intersecting straight lines, as shown in Fig. 5. (In some of the runs, however, a slight negative curvature is indicated at the start of the decay curves.) The occurrence of a sharp break was already noted in the case of the 69°C measurements given in Fig. 3.

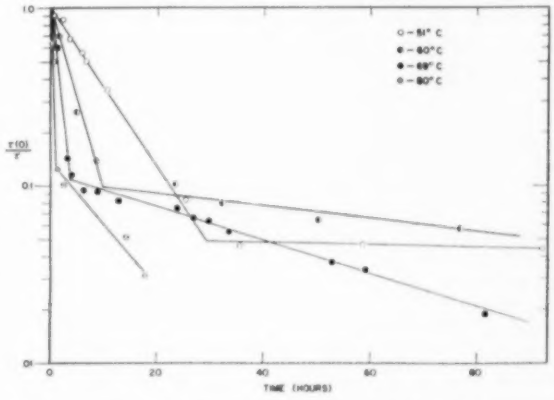

Fig. 5—Decay curves showing the variation of the reciprocal of the relaxation time (relative to its initial value) with total time at four different temperatures of measurement.

† As noted in the previous paper,[10] the quantities H_r and ΔH_f are measured in different temperature ranges. Since H_r is known to be a function of temperature, this calculation of ΔH_f is not strictly valid. The error resulting from the failure to take this temperature dependence into account is probably small, and such as to yield a value for ΔH_f smaller than that calculated here.

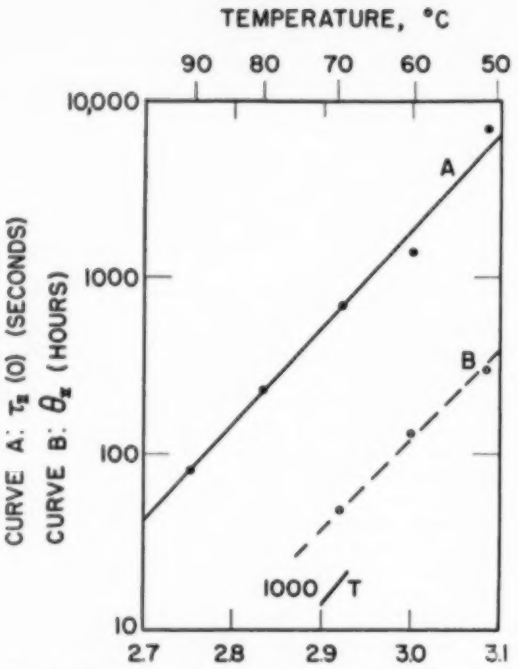

Fig. 6—Dependence of the parameters of stage II of the decay curves on the temperature. Curve A: Initial relaxation time, $\tau_{II}(0)$ Curve B: Decay time, θ_{II}.

The decay curves of Fig. 5 are suggestive of the occurrence of two stages in which there is a distinct difference, either in the manner by which relaxation is produced or in the mechanism of the decay of imperfections. The early portion of the decay curve, before the sharp break, will be designated "stage I," and the later portion, "stage II," for convenience in future reference. The slope of the decay curve in stage I may now be obtained as a function of temperature. Since the curve is approximately a straight line, it may be represented as

$$\tau(0)/\tau = e^{-t/\theta} \qquad [8]$$

where θ may be termed the decay time. The temperature dependence of θ should be of the form

$$\theta = \theta_0 e^{\Delta H'_I/RT} \qquad [9]$$

The quantity $\Delta H'_I$, which is an effective heat of activation for the decay of defects in stage I, may not be the same as the quantity ΔH_I, derived from the variation of $\tau(0)$ with temperature. A difference may be expected, first because the rate of relaxation is controlled by the slower moving atomic species of the binary solid solution, as already mentioned in the theory section, while the rate of migration of defects is controlled by the faster moving component. This factor acts to make $\Delta H'_I$ smaller than ΔH_I. On the other hand, the rate of atomic mobility has been shown[7] to be strongly concentration dependent; it is therefore to be expected that defects, in moving through local variations in concentration in the alloy, will be held up for relatively long periods in certain regions, i.e., where the heat of activation for jump is larger than the average value. The decay rate is controlled by the rate of jump in these special regions. This factor acts to make $\Delta H'_I$ larger than ΔH_I. In view of these two opposing factors, it is not clear as to whether $\Delta H'_I$ should be smaller or larger than ΔH_I.

Experimental values of θ as a function of temperature are given in Fig. 4B. It is difficult to obtain a precise value of $\Delta H'_I$, since measurements are limited to a narrow temperature range. In addition, as already shown in the previous work,[10] the decay rate is structure sensitive; a small amount of cold working changes this rate appreciably. In the present experiments the wire specimen, used for the series of runs of Fig. 5, was accidently dropped and bent before the 80°C run, but after measurements had already been obtained at 51°, 60°, and 69°C. It is found that the slope of the 80°C decay curve does not fall into agreement with the corresponding values at 50° to 70°C given by Fig. 4B, but instead, the 80°C value of θ is about a factor of 1.9 too small. Correspondingly, repetition of runs at 50° and 70°C shows that the value of θ at these temperatures subsequent to the accidental bending, is lower by about the same factor.‡ Annealing at 400°C for 15 min does not seem to produce recovery of the original decay rate. The three determinations of θ before the 80°C run are plotted in Fig. 4B; they indicate a value of $\Delta H'_I$, possibly slightly larger than the quantity ΔH_I obtained from Fig. 4A. Since any difference in slope of the two lines is within experimental error, it seems that, pending further measurements, $\Delta H'_I$ may be considered to be equal to ΔH_I for this solid solution. It should be noted that in the earlier measurements on the 30 pct alloy,[10] it appeared that $\Delta H'_I$ may be about 2 to 3 kcal per mol less than ΔH_I (just outside of experimental error).

‡ The authors are not completely certain that the bending of the specimen was entirely responsible for the subsequent change in decay rates. Other changes in the specimen, not as clearly defined, may have occurred at about the same time.

Under the assumption that the two straight lines of Fig. 4 are parallel, the value of $\theta_0 = 10^{-8}$ sec is obtained for the temperature independent factor of Eq. 9. The value of θ at the freezing-in temperature (360°C) is then found to be 0.03 sec. This decay time is in good agreement, in order of magnitude, with the anticipated time of quenching, and therefore serves as a check on the self-consistency of the results of these experiments.

It is useful to estimate the mean number of jumps, N, of a defect (for stage I) before it is rendered inactive. For this purpose, the ratio of the decay time, θ, to mean jump time of a defect must be obtained. The mean jump time will be assumed to vary with temperature with the same heat of activation, $\Delta H'_I$, as the decay time (Eq. 9). Since the temperature-independent factor of the decay time is $\theta_0 = 10^{-8}$ sec, and the corresponding temperature-independent factor for the mean jump time is of the order of magnitude 10^{-14} sec (see ref. 10), the estimated value of N, obtained from the ratio of these two quantities is 10^6 jumps.

For the interpretation of the sharp break in the decay curves, it is important to know the value of the activation energy associated with stage II. A heat of activation may be obtained both from the dependence of the intercept and of the slope (decay time) of the straight line of stage II on the temperature of measurement, in a way analogous to Fig. 4. The results are given in Fig. 6. Besides the points derived from the decay curves of Fig. 5, an additional run at 90°C is included; this run was not included in Fig 4 because at this temperature the decay rate in stage I is too rapid to allow a precise determination of $\tau(0)$. From the data for the intercept of the straight lines of stage II, a heat of activation to 25 kcal per mol is obtained. This result is

greater than the value of ΔH_f obtained from stage I by an amount which seems to be well outside of experimental error. The decay times in stage II (Fig. 6B) give a heat of activation of 23.5 kcal per mol, but the uncertainty in this value is large.

Although the heats of activation associated with stages I and II differ, the magnitude of the relaxation effects are not detectably different in the two stages. This result is significant, since it indicates that the nature of the atomic rearrangement produced by the application of stress to this alloy is the same in both stages.

Comparison with Previous Results

The previous experiments[10] on the freezing-in of defects were conducted on an Ag-Zn alloy containing 30 atomic pct Zn, as contrasted to the present 33.5 atomic pct solid solution. A comparison of the principal results of the two sets of experiments seems desirable at this point.

The equilibrium measurements on the two alloys show that relaxation takes place more rapidly for the 33.5 pct alloy. This difference is attributed to the fact that H_r is 1.0 kcal per mol larger for the 30 pct alloy. This small but experimentally significant change of H_r with zinc concentration is in keeping with earlier equilibrium measurements on a series of Ag-Zn alloys.[7] The nonequilibrium measurements for the 30 pct alloy seem to show that this difference in H_r enters entirely into the term ΔH_f, and that the values of ΔH_f are the same for the two alloys. In view of the uncertainties in the determinations of ΔH_f, however, it is probably more likely that the 1 kcal per mol difference in H_r is taken up by both ΔH_f and ΔH_f. The value of ΔH_f obtained in the present experiments is more reliable than that obtained for the 30 pct alloy because of the wider range of measurement and the greater precision in the determination of $\tau(0)$. The estimated values of $c(0)$, $\bar{c}$(m.p.), and T_F are consequently more reliable in the present experiments, although their values are in agreement within experimental error with the same values for the 30 pct alloy.

The most important difference in the nonequilibrium behavior of the two alloys is in the decay rates. The value of θ (for stage I) for the present alloy at 60°C is 250 min, while the equivalent value observed for the 30 pct alloy at the same temperature is about 58 min. The decay rate is, therefore, more than four times greater in the 30 pct alloy, in spite of the fact that the equilibrium atomic mobility is actually lower in this alloy. Thus the ratio $\theta/\tau(0)$ is about 100 in the present case, and only 14 in the earlier work. There are two possible explanations for this large difference: First, the structure sensitivity of the rate of decay, as illustrated[10] by the fact that a small amount of cold working results in a change in decay rate of almost a factor of two, suggests a possible difference in dislocation density in the two alloys. Second, the measurements on the 30 pct alloy indicate that the heat of activation, $\Delta H'_f$, which controls the decay rate, may be somewhat lower than ΔH_f. In the present experiments, however, Fig. 4 shows that $\Delta H'_f$ is at least as large as ΔH_f, if not larger. Thus, in spite of the more rapid equilibrium relaxation in the 33.5 pct alloy, the value of $\Delta H'_f$ may be larger in this case than in the 30 pct alloy. In order to determine which of these two explanations best explains the large differences in the rate of decay of defects in the two alloys, further experiments are necessary.

Discussion

The self consistency in the interpretation given to these experiments is indicated by the reasonable values obtained for three of the quantities deduced from the experimental results: the freezing-in temperature T_F, the value of θ at T_F, and the equilibrium defect concentration at the melting point $\bar{c}$ (m.p.).

The most striking result is the form of the decay curves; the remainder of this discussion will therefore be devoted to this subject. It is noteworthy that the decay curves in both stages I and II obey a simple exponential of the form of Eq. 8 within experimental error (except for a slight curvature at the start of some of the curves, as reported above). The linearity of the decay curves indicates that the process of decay is similar to a first-order reaction, i.e., that the defects are annihilated or rendered ineffective at fixed points in the crystal. An alternative possibility, that the defects combine to form pairs, would result in a curve that corresponds to a second-order reaction, the decay rate then decreasing proportionately to the time. The present data are not in agreement with this latter possibility.

From the number of jumps, N, made by a defect in stage I before it becomes inactive, it is possible to test the hypothesis that vacancies and similar lattice defects are brought to equilibrium principally at edge dislocations[12,13] in this stage. If it is assumed that the dislocation density has the reasonable value of 10^{7} cm^{-2}, then one lattice site in 10^{8} lies on a dislocation line, in agreement with the calculated value of N (Table I). The fact that the decay is a first-order reaction is consistent with the belief that the defects terminate at dislocations. Finally, the previous demonstration,[10] that cold working produces an increase in the decay rate in the early stage, is also in accordance with this belief. In view of the calculated result that $c(0)$ is of the order of 10^{-4}, it becomes difficult to understand why annihilation of defects is not accomplished by their combination to form pairs (in the form of a second-order reaction), which would require, at the outset, only 10^{4} jumps instead of the 10^{8} required to reach a dislocation trap. If combination to form defect pairs results in a lowering of the energy of the system (as indicated[8] at least for the combination of single vacancies to form divacancies) this implies an attractive force between individual defects at close range. It does not follow, however, that there may not be a long-range repulsion between defects which would greatly lower the probability of their combination. This question deserves further theoretical investigation.

The tendency for the decay rate to decrease sharply, when the relaxation time reaches about ten times its initial value, $\tau(0)$, is reported[10] on the basis of the earlier quenching experiments on the 30 pct Ag-Zn alloy. In view of the slower decay rates in the present 33.5 pct alloy, and consequently the higher precision attainable, it is shown that the decay curves break more sharply than had been suspected from the earlier measurements; in fact, the curves reported in this paper can usually be represented as two intersecting straight lines, within experimental error. The authors have considered several possible explanations for this sharp break and will outline these below.

One possible explanation, proposed earlier,[10] is the exhaustion of the dislocation sites or other sinks at which defects are absorbed, i.e., it is assumed that these sites have only a limited capacity for the

absorption of defects and that once these sites are filled the decay rate of defects will be greatly decreased. If this hypothesis were correct, a gradual rather than an abrupt decrease in decay rate would be anticipated. Furthermore, the activation energy associated with stage II should then be the same as that of stage I, in contradiction to the present experimental results.

A second explanation is based on the existence of local regions in which the mobility of a defect is considerably slower than in the bulk of the lattice. Such regions are referred to here as *S*-regions. Since it has already been shown[7] that the average mobility in a series of Ag-Zn alloys depends strikingly on the composition, it is clear that within a solid solution both the probability of finding a defect and the mobility of a defect will fluctuate considerably from one lattice position to another. *S*-regions may therefore exist due to these fluctuations in composition. Another possibility is that lattice positions near dislocations may serve as *S*-regions. It then seems reasonable that in stage I the defects present in the bulk of the lattice directly after quenching control the rate of atomic movement, while in stage II relaxation is controlled by those defects released from *S*-regions. The higher activation energy in stage II is thus readily explained. In order to account for the sharpness of the break in the decay curve, it is necessary to assume a high degree of similarity in the various *S*-regions throughout the lattice. It is also necessary that the capacity of these *S*-regions for defects be very large, to account for the continuance of the straight line of stage II out to long times, as observed experimentally.

The final explanation, proposed to account for the sharp breaks in the decay curves, is the existence of two types of defect present in nonequilibrium quantities upon quenching, each capable of producing atomic mobility independently of the other. The decay curve may be described as due to the predominance of one defect in producing relaxation in stage I, and to the predominance of the second defect when the concentration of the first is greatly decreased, in stage II. The sharpness of the break is then a consequence of the logarithmic scale, in much the same way as the sharp break obtained in the plot of log D (diffusion coefficient) against T^{-1} when both volume and grain-boundary diffusion occur simultaneously.[14] This hypothesis also provides a natural explanation for the different activation energies associated with the two stages. In accordance with this hypothesis, an equation analogous to Eq. 1 may be written for the defect responsible for stage II. The results of Fig. 6A then indicate that the quantity $Ac(0)$ for stage II is about 10^{19} (or 100 times larger than the corresponding quantity for stage I). This means that either A or $c(0)$ for stage II defects is much larger than the same quantity for stage I. It is not reasonable to expect much more than a concentration of 10^{-4} for stage II defects, but it is possible that the frequency factor A is 100 times larger than for stage I if a large positive entropy of activation were associated with the movement of the stage II defect.

In view of the above discussion, it seems that only the first of the three proposed explanations for the break in the decay curve is inconsistent with the present experimental results.

Summary

A study is made of atomic mobility, in an Ag-Zn solid solution containing 33.5 atomic pct Zn, by means of anelastic methods. Measurements are made both under conditions where lattice defects are in equilibrium and in the presence of a large excess of defects frozen into the lattice by quenching. The quenching experiments make possible the separation of the composite "activation energy" for atomic mobility under equilibrium conditions into a heat of activation for movement of a defect, equal to 18.6 kcal per mol, and the heat of formation of a defect, equal to 11.9 kcal per mol. It is estimated that about 0.03 atomic pct of defects are frozen in by quenching from 400°C into water.

The decay curve, which is essentially a plot of the logarithm of the atomic mobility as a function of time after quenching (at constant temperature), is closely represented by two intersecting straight lines; the sharp break occurs when the mobility reaches about one-tenth its initial value after quenching. Various possible explanations are given for the existence of two distinct stages in the decay process.

Acknowledgments

The authors wish to express their appreciation to W. Heller for stimulating discussions and criticism, to the Higgins Fund which financed the basic equipment used in these experiments, and to the Office of Ordnance Research for their sponsorship of this work.

References

[1] A. D. LeClaire: Diffusion in Metals. *Progress in Metal Physics* (1953) **4**, p. 265. London. Pergamon Press Ltd.

[2] F. Seitz: Fundamental Aspects of Diffusion in Solids. *Phase Transformations in Solids* (1951) p. 77. New York. John Wiley and Sons. See also the original calculations by H. B. Huntington and F. Seitz: *Physical Review* (1942) **61**, pp. 315, 325.

[3] J. H. Bartlett and G. J. Dienes: Combined Pairs of Vacancies in Copper. *Physical Review* (1953) **89**, p. 848.

[4] A. S. Nowick: The Production and Detection of a Non-Equilibrium Number of Vacancies in a Metal. *Physical Review* (1951) **82**, p. 551.

[5] J. W. Kauffman and J. S. Koehler: Quenching in of Lattice Vacancies in Pure Gold. *Physical Review* (1952) **88**, p. 149.

[6] C. Zener: Internal Friction of an Alpha Brass Crystal. *Trans.* AIME (1943) **152**, p. 122.

[7] A. S. Nowick: Anelastic Measurements of Atomic Mobility in Substitutional Solid Solutions. *Physical Review* (1952) **88**, p. 925.

[8] C. Zener: *Elasticity and Anelasticity of Metals* (1948). Chicago, Univ. Chicago Press; Stress Induced Preferential Orientation of Pairs of Solute Atoms in Metallic Solid Solution. *Physical Review* (1947) **71**, p. 34.

[9] A. S. Nowick: Internal Friction in Metals. *Progress in Metal Physics* (1953) **4**, p. 1. London. Pergamon Press Ltd.

[10] A. S. Nowick and R. J. Sladek: Anelastic Measurement of Atomic Mobility Under Non-Equilibrium Conditions. *Acta Metallurgica* (1953) **1**, p. 131.

[11] T. S. Kê: Experimental Evidence of the Viscous Behavior of Grain Boundaries in Metals. *Physical Review* (1947) **71**, p. 533.

[12] F. R. N. Nabarro: Deformation of Crystals by the Motion of Single Ions. *Report on a Conference on Strength of Solids* (1948) p. 75. London. The Physical Society.

[13] F. Seitz: On the Formation of Dislocations from Vacancies. *Physical Review* (1950) **79**, p. 890.

[14] D. Turnbull: Grain Boundary and Surface Diffusion. *Atom Movements* (1951) p. 129. Cleveland. ASM.

Measurement of Approximately Cylindrical Particles In Opaque Samples

by Robert L. Fullman

Relationships are derived between average dimensions measured on a polished cross section and the spatial dimensions of particles dispersed as uniform cylinders. The equations are applicable to the measurement of rods or plates without the stipulation that they be extremely thin.

QUANTITATIVE analysis of the elements of microstructures has been limited by a lack of knowledge concerning the relationships between observations on plane surfaces and the spatial nature of the structure. This paper is an extension of previous efforts to establish equations suitable for the quantitative investigation of microstructures. The equations derived fill two gaps in the range of particle shapes for which measurements may be required, namely those shapes lying between extremely thin plates and equiaxed particles (approximately spherical), and those intermediate between equiaxed particles and extremely thin rods or needles.

In a previous paper[1] equations were developed relating dimensions measured on a polished cross section to the average spatial dimensions of particles in the form of spheres, extremely thin plates, and extremely thin rods. For extremely thin rods the dimensions measured on a polished cross section were found to depend on the radius only, so that no information concerning the rod lengths or number of rods per unit volume could be obtained from observations on a cross section. In this paper equations are derived relating dimensions measured on a polished cross section to the spatial dimensions of particles in the form of identical cylinders. These equations may be used to evaluate the dimensions of rods, as well as the dimensions of plates, without the stipulation that the plates or rods be extremely thin. The impossibility of evaluating the length of extremely thin rods from planar measurements appears as an increase in the amount of data required for a given precision, as the length-radius ratio increases.

Consider a sample containing particles of a phase in the form of cylinders of uniform radius r and height t. If the cylinders are randomly oriented, as in a sufficiently large sample of a fine grained polycrystalline material, area and lineal analysis may be carried out with parallel cross-sectional planes and lineal traverses. If the cylinders are not randomly oriented, it is necessary to randomize the orientations of the cross-sectional planes and traverse lines. Let a unit cube be cut from the sample, and a cross-section plane be passed through the cube parallel to one of the cube faces. The number of particles N_A cut by the cross-sectional plane per unit area is equal to the number of particles N_v per unit volume times the probability p_i of a plane intersecting a single randomly positioned and randomly oriented cylinder in the cube. Let J be the maximum cylinder dimension in the direction normal to the cross-section planes, as shown in Fig. 1. Since, of the various possible positions for the cross-sectional plane over the unit length from top to bottom of the cube, only those positions existing over the length J

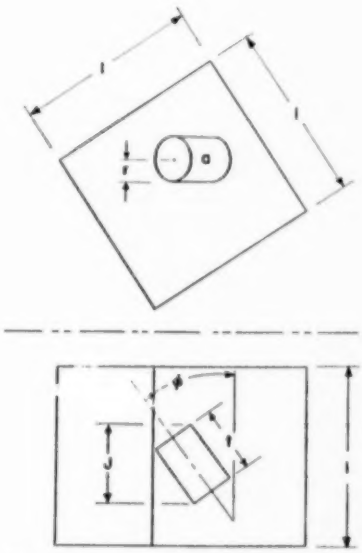

Fig. 1—Diagram of a cylindrical particle in a unit cube.

R. L. FULLMAN, Junior Member AIME, is associated with the Research Laboratory, General Electric Co., Schenectady.

Discussion on this paper, TP 3597E, may be sent, 2 copies, to AIME by Dec. 1, 1953. Manuscript, April 15, 1953. Cleveland Meeting, October 1953.

would lead to the plane intersecting the cylinder, the probability of intersecting a single cylinder is equal to $\bar{J}$, the mean value of J for all possible orientations of the cylinder.

Let ϕ be the angle between the cylinder axis and the normal to the cross-sectional planes, and let $p_\phi d\phi$ be the probability that a cylinder orientation is described by an angle between ϕ and $\phi + d\phi$. Then for randomly oriented cylinders $p_\phi = \sin \phi$. Let $p_J dJ$ be the probability that a given particle has a maximum dimension between J and $J + dJ$ in the direction perpendicular to the cross-section planes. Referring to Fig. 1,

$$J = 2r \sin \phi + t \cos \phi.$$

$$p_J = p_\phi \left| \frac{d\phi}{dJ} \right| = \frac{\sin \phi}{2r \cos \phi - t \sin \phi}.$$

The average value of J is equal to the integral, over all possible orientations, of the product of J and its probability.

$$\bar{J} = \int_0^{\pi/2} J p_J dJ =$$

$$\int_0^{\pi/2} (2r \sin \phi + t \cos \phi) \sin \phi d\phi = \frac{1}{2} (\pi r + t).$$

$$N_s = N_V p_\phi = N_V \bar{J} = \frac{N_V}{2} (\pi r + t). \qquad [1]$$

Combining Eq. 1 and the equality of volume and area fractions f, a relationship is obtained between the average area $\bar{s}$ of particles intersected by a random cross section and the particle dimensions.

$$f = N_V V = N_s \pi r^2 t = N_s \bar{s} = \frac{N_V}{2} (\pi r + t) \bar{s}.$$

$$\bar{s} = \frac{2\pi r^2 t}{\pi r + t}. \qquad [2]$$

Eq. 2 may be compared with the equations derived previously, Eq. 1, for extremely thin plates and rods. If $r >> t$, Eq. 2 reduces to $\bar{s} = 2rt$, as was found for very thin plates. If $r << t$, Eq. 2 reduces to $\bar{s} = 2\pi r^2$, as was found for very thin rods.

If randomly placed lines are passed through the unit cube parallel to an edge, the number N_L of particles per unit length intersected by the lines is equal to the number of particles per unit volume times the probability p_a that a line will intersect a single randomly positioned and randomly oriented cylinder in the cube. Let a be the area of the projection of a cylinder on the plane perpendicular to the traverse lines, as shown in Fig. 1. Since, of the various positions for the traverse line over the unit area of the cube top, only those positions within the area a would lead to the line intersecting the cylinder, the probability of intersecting a single cylinder is equal to $\bar{a}$, the mean value of a for all possible orientations of the cylinder.

Cauchy[2,3] has shown that the average projected area of a convex particle* is equal to one-fourth the particle's surface area. Therefore, $p_a = \bar{a} = \pi(r^2 + rt)/2$.

$$N_L = p_a N_V = \frac{\pi}{2} N_V (r^2 + rt). \qquad [3]$$

Combining Eq. 3 with the equality of volume and lineal fractions f, a relationship is found between the average traverse length $\bar{l}$ and the particle dimensions.

$$f = N_V V = N_V \pi r^2 t = N_L \bar{l} = \frac{\pi}{2} N_V (r^2 + rt) \bar{l}.$$

$$\bar{l} = \frac{2rt}{r + t}. \qquad [4]$$

Eq. 4 may be compared with the equations previously derived for extremely thin plates and rods. If $r >> t$, Eq. 4 reduces to $\bar{l} = 2t$, as was found for very thin plates. If $r << t$, Eq. 4 reduces to $\bar{l} = 2r$, as was found for very thin rods. Before applying Eqs. 2 and 4 to the analysis of moderately thick plates or rods, it is desirable to estimate the degree to which the equations are sensitive to the precise shape assumed, i.e., circular cylinders. If, for approximately equiaxed cylinders, the equations correspond to those previously found for spheres,[1] they may be applied with confidence to plates and rods that depart significantly from extreme thinness. Eq. 2 corresponds to that for a sphere ($\bar{s} = 2\pi r^2/3$) for $t = \pi r/2$, and Eq. 4 corresponds to that for a sphere ($\bar{l} = 4r/3$) for $t = 2r$. Both of these relationships correspond to roughly equiaxed cylinders.

In order to find the particle dimensions in terms of the average particle area $\bar{s}$ and average traverse length $\bar{l}$, or in terms of the volume, area, lineal, or point fraction f of the phase and the area and lineal counts N_s and N_L, Eqs. 2 and 4 or 1 and 3 may be combined.

$$r = \frac{\pi \bar{s} \pm \sqrt{\pi^2 \bar{s}^2 - 2\pi(\pi - 1) \bar{l}^2 \bar{s}}}{2\pi \bar{l}}. \qquad [5]$$

$$t = \frac{\bar{l}(\pi \bar{s} \pm \sqrt{\pi^2 \bar{s}^2 - 2\pi(\pi - 1) \bar{l}^2 \bar{s}})}{2(\pi \bar{s} \pm \sqrt{\pi^2 \bar{s}^2 - 2\pi(\pi - 1) \bar{l}^2 \bar{s} - \pi \bar{l}^2})}. \qquad [6]$$

$$r = \frac{\pi N_L \pm \sqrt{\pi^2 N_L^2 - 2\pi(\pi - 1) f N_s}}{2\pi N_s}. \qquad [7]$$

$$t = \frac{f(\pi N_L \pm \sqrt{\pi^2 N_L^2 - 2\pi(\pi - 1) f N_s})}{2N_L(\pi N_L \pm \sqrt{\pi^2 N_L^2 - 2\pi(\pi - 1) f N_s} - \pi f N_s)}. \qquad [8]$$

In Eqs. 5 to 8, the positive sign is used before the radical for particles in the form of plates, and the negative sign for particles in the form of rods.

Conclusions

Equations have been derived permitting the evaluation, from measurements on polished cross sections, of the dimensions of particles dispersed as uniform cylindrical plates or rods. The validity of the equations is not limited to extremely thin plates or rods nor to particles of exactly cylindrical shape. The relationships do not appear sufficiently simple to encourage their extension to the analysis of nonuniform particles.

References

[1] R. L. Fullman: Measurement of Particle Sizes in Opaque Bodies. *Trans.* AIME (1953) **197**, p. 447; JOURNAL OF METALS (March 1953).

[2] A. Cauchy: Memoires sur le rectification des courbes et la quadrature des surfaces courbes. (1832) Paris.

[3] V. Vouk: Projected Areas of Convex Bodies. *Nature* (1948) **162**, p. 330.

* A convex body, in the sense used here, is one whose surface cannot be pierced in more than two places by any straight line.

The Following Books Are Offered Less 30 Pct to AIME Members

BASIC OPEN HEARTH STEELMAKING

(A Completely Revised Edition)

Prepared by the Physical Chemistry of Steelmaking Committee, AIME
Sponsored by the Seeley W. Mudd Memorial Fund

In 22 chapters, the best in open hearth practice and principles, written and edited by a committee of the foremost steel plant operating and metallurgical authorities. Each chapter considers a specific factor or operation in steel production, and describes methods, practices, and the latest metallurgical knowledge on the subject.

1951 • 960 Pages • $8.00

Part I—Practice

- Basic Open Hearth Furnaces
- Survey of Operations
- Open Hearth Refractories
- Fuels, Combustion, Instrumentation
- Raw Materials
- Slag Control
- Charging and Melting
- Refining
- Finishing and Deoxidizing
- Molds and Pouring
- Ingot Structure, Segregation
- Nonmetallic Inclusions
- Properties of Steel

Part II—Principles

- Chemistry of High Temperature Reactions
- Kinetics of Metallurgical Processes
- Chemistry of Liquid Steel
- Chemistry of Slag-Metal Reactions
- Chemistry of Open Hearth Refractories
- Thermal Changes in Melting and Refining
- Gas Flow and Heat Transfer
- Combustion and Utilization of Fuel
- Rates of Open Hearth Reactions

Solidification of Metals and Alloys . . .

A Symposium by the AIME's Institute of Metals Division

A publication on the subject of major significance to metallurgists, by four of the nation's outstanding authorities. Three papers cover ferrous and nonferrous metals solidification and discuss many of the phenomena of metal freezing.

1951 • 75 Pages • $3.00

Nucleation of Solids, J. H. Hollomon and D. Turnbull

Growth of Metal Crystals, R. F. Mehl

Solidification of Steel Ingots, B. R. Queneau

Preface, Cyril Stanley Smith

OTHER METALS BRANCH BOOKS

Transactions, Vols. 185 ('49), 188 ('50), 191 ('51)	$7.00
75 Years of Progress in Iron and Steel, 1948	1.50
Bergwerk und Probierbuchlein, 1949	5.00
Stress Corrosion Cracking of Metals, 1944	5.00
Brief History of Science of Metals, 1948	1.50
Nonferrous Rolling Practice, 1948	4.00
Rod and Wire Production Practice, 1949	3.00
Proceedings	
Electric Furnace Steel, 1947-1951	$10.00 Ea.
Blast Furnace, Coke Oven and Raw Materials, 1946, 1947, 1951	10.00 Ea.
Open Hearth 1944-1947, 1950	10.00 Ea.

AIME 29 W. 39th St., New York 18, N. Y.
Please send me the books listed below. Enclosed is Check ☐; Money Order ☐ for $..... (AIME members may be billed.)
• AIME Members, 30% Discount on All Books.

1. ..... 3. .....

2. ..... 4. .....

Name .....

Address .....

City and Zone ..... State .....

Nonmember Foreign Orders, Add 50c for Mailing.